

THE CONCEPT, DESIGN AND EXPERIMENTAL
EVALUATION OF AN
"ACOUSTIC SUB-SEABED INTERROGATOR"

VOLUME I.

TEXT

This document was produced
by scanning the original publication.

Ce document est le produit d'une
numérisation par balayage
de la publication originale.

JACQUES YVES GUIGNÉ

OPEN FILE
DOSSIER PUBLIC
1518
GEOLOGICAL SURVEY
COMMISSION GEOLOGIQUE
OTTAWA

THE CONCEPT, DESIGN AND EXPERIMENTAL EVALUATION
OF AN
"ACOUSTIC SUB-SEABED INTERROGATOR"

Submitted by

Jacques Yves Guigné

for the degree of Ph.D of the
University of Bath - England

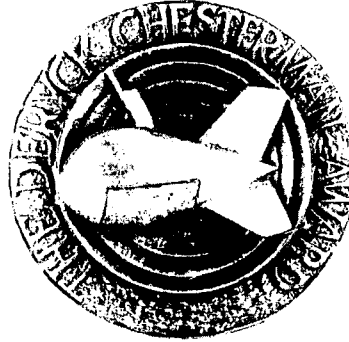
1986

COPYRIGHT

Attention is drawn to the fact that copyright of this thesis rests with its author. This copy of the thesis has been supplied on condition that anyone who consults it is understood to recognise that its copyright rests with its author and that no quotation from the thesis and no information derived from it may be published without the prior written consent of the author.

This thesis may not be consulted, photocopied or lent to other libraries without the permission of the author or NORDCO Ltd. of Newfoundland, Canada, for two years from the date of acceptance of the thesis.

SCHOOL OF PHYSICS



UNIVERSITY OF BATH

DERYCK CHESTERMAN
MEMORIAL MEDAL

Professor Deryck Chesterman, 1912–1978
Professor of Geophysics
University of Bath
1969–1978

Designed by JOHN HUGGINS
Made by DAVID TUCKER
1979

Awarded to
Jacques Yves A.F. Guigné
1986

This medal was commissioned for presentation to outstanding postgraduate students in the School of Physics, University of Bath, as planned by Professor Chesterman as his retirement gift.

The commission was funded through the generosity of his many friends and colleagues.

The medal depicts a towed body used for sonar surveys of the seabed.

ACKNOWLEDGEMENTS

The author wishes to express his thanks to Professor H. O. Berktaf of the University of Bath, England for providing the opportunity to undertake this study in the School of Physics and to Dr. Nicholas Pace, also of the same university, for supervising the project. Dr. Pace offered direction and help in all stages of the Ph.D. His indepth instruction in acoustical modelling and his constructive review of the original manuscript kept the project tightly on schedule. Equally acknowledged is the support provided by NORDCO Ltd. of Newfoundland. This study would not have been possible without the flexibility and entreprising spirit shown by its Chief Executive Officer, Mr. Frank Smith. Likewise the inspiration for the topic belongs to Dr. David I. Ross, Acting Director of the Atlantic Geoscience Centre (AGC) Canada, who acted in the capacity of external supervisor. His dedicated guidance throughout the course of the work is sincerely appreciated.

The experimental testing took place in the deep water tank of the Ocean Engineering Group at Memorial University of Newfoundland. Dr. Derek Muggerridge was instrumental in making these excellent facilities available along with providing whenever possible the services of the machine shop.

The research was financed through NORDCO Ltd.'s internal funds supplemented by two Industrial Research Assistance Program (IRAP) agreements administered by the National Research Council (NRC) of Canada. In addition, the Atlantic Geoscience Centre provided two research contracts from the Panel on Energy Research and Development (PERD). It is important to note that the signal processing developed during the experimentation was specifically made possible through an extension of PERD support. In this context, the author wishes to emphasize the assistance of Mr. Gordon Cross (NRC), Mr. Steve Blasco (AGC) and Dr. David I. Ross (AGC) in helping to secure these funds for the project.

Dr. John Ross of the Department of Defense (Canada) followed the research from its conceptual stage. Discussions held with him were always fruitful and fitting. Scientific exchanges were also held with Dr. Larry Mayer of Dalhousie University and Dr. Peter Simpkin. Both are thanked for their advise. The author's director, Dr. Jack Clark, Centre for Cold Ocean Resources Engineering (C-Core, Newfoundland) encouraged the development of the "Acoustic Core" product, in particular the hypothesis advanced at the end of the thesis to correlate elastic properties from an acoustic response.

Finally, special mention must be given to my colleagues, Mr. Voon Hong Chin, Mr. Bill Bushman and Mr. Keith Mews, who provided technical assistance at critical stages of the research. The author is also grateful to Mr. Robert Trépanier of Bruel and Kjaer (Canada). His company's signal analyser was used in the post-processing of the experimental data. The final typing of the manuscript was professionally executed by Mrs. Levinia Vatcher. Help on the drafting of the figures came from Mr. Damien Morrissey and Mrs. Joan Butler.

ABSTRACT

This research study is centered around the design and experimental development of a unique subbottom profiler concept called an "Acoustic Sub-seabed Interrogator" (acronym ASI). The objectives behind the concept deal with the creation of a remote sensing probe that is capable of interrogating complex lithologies of a seabed. Through its use, it should become possible to precisely map and interpret variations found within sedimentary sequences, especially within complex sediment mixtures typical of glacial drift deposits and of permafrost structures.

The concept of the ASI revolves around the optimization of lateral and temporal components which define the criterion of resolution. The ASI amalgamates fully the benefits of a terminated Parametric Source while operating in a stationary mode. The parametric approach provides an ease in manipulating a wide band of frequencies, while the stationary base allows for geometrical manipulations of the transmitters and receiving arrays.

An optimized acoustic propagation of an ASI signal travelling within a structurally complex sediment model was theoretically appraised in terms of Signal-to-Noise Ratio and Signal-to-Reverberation Ratio. The theoretical modelling also concentrated on developing an interrogation ability to extract sub-seabed information from the returning signals. A product called the "Acoustic Core" was created. The logic of the core design controls the cross correlation routines envisioned for the ASI. The Hilbert Transform was integrated into the logic.

The results obtained in the experimental simulations support the ASI philosophy and highlight the versatility of the "Acoustic Core". Although scaled the simulations are considered representative; providing a sensitive test of the ideas as they apply to one of the worst scanning cases; a glacial till matrix. An indepth insight into the model's physical and spatial variations was attained by directing the interrogations on the acoustic properties of velocity and of absorption. Their statistical distribution emphasized the depositional processes that were involved in the creation of the layer. It is believed that the fundamental internal information defined by the ASI for the pseudo till structure and illustrated in the "Acoustic Core" cannot be attained using existing geophysical and geotechnical techniques.

Finally, the "Acoustic Sub-seabed Interrogator" may provide a means of defining a first estimate of the elastic nature of soils from its calibrated acoustic response. It is hypothesized that the correlation of attenuation data with rigidity may establish an indirect but precise mensuration of shear-wave velocity.

TABLE OF CONTENTS

	<u>Page</u>
ACKNOWLEDGEMENTS	ii
ABSTRACT	iii
TABLE OF CONTENTS	iv
LIST OF FIGURES	viii
LIST OF PLATES	xii

VOLUME I - TEXT

1.0 INTRODUCTION	1
2.0 HISTORICAL BASIS FOR AN "ACOUSTIC SUB-SEABED INTERROGATOR" CONCEPT	8
2.1 General Discussions	8
2.2 Review of Potential Acoustic Techniques and Approaches	15
2.2.1 Source Position: Lateral Resolution and Signal Strength	15
2.2.2 Synthetic Aperture	21
2.2.3 Vertical Resolution	23
2.2.4 Parametric Approach	29
2.3 Conclusion	35
3.0 ASI MODEL DEVELOPMENT	37
3.1 "Is it possible to get a signal back?"	37
3.2 Stratigraphic Sediment Modelling	39
3.2.1 The Glacial Sediment Models	41
3.2.2 The Project Model	46
3.3 Signal Loss in a Sedimentary Structure	49
3.3.1 Absorption	56
3.3.2 Reflection	63
3.3.3 Scattering	68
3.4 Analytical Appraisal of a Terminated Parametric Source in Reference to a Conventional System	74
3.4.1 Evaluation of Signal Loss in the Sediment Model	78
3.4.2 Evaluation of Source Level	83
3.4.3 Evaluation of Pressure, of Centre Frequency, and of Bandwidth beyond the Water/Seabed Interface	91
3.4.4 Evaluation of Temporal Resolution Versus the Model's Stratigraphic Depth	106

	<u>Page</u>
3.4.5 Evaluation of Signal-to-Noise Ratio	109
3.4.5.1 Ambient Noise	111
3.4.5.2 Target Strength	117
3.4.5.3 Echo Level	120
3.4.5.4 Signal-to-Noise Ratio	122
3.4.6 Evaluation of the Basal Till Backscatter	123
3.4.6.1 Derivation of an Expression for Target Strength of Reverberation	125
3.4.6.2 Calculation of the Scattering Volume ..	130
3.4.6.3 Modelling of a Realistic Basal Till Composition and Structure	139
3.4.6.4 Evaluation of each Layer's Reverberation Level	141
3.5 Synopsis	144
4.0 EXTRACTION OF SUB-SEABED INFORMATION FROM THE RETURNED SIGNALS	146
4.1 Foreword	146
4.2 Detection of Primary Reflections using a Moveout Technique	148
4.2.1 Establishing an Interrelationship between θ , t and z	149
4.2.2 Developing a Procedure to Systematically Identify True Echos from Multiples	152
4.2.3 Deriving a Velocity Value for each Layer	158
4.3 Horizontal Location of Arriving Echos using a Spatial Coherency Approach and a Focussing Application	161
4.3.1 Assembling a Spatial Offset Network	161
4.3.2 Engaging a Focussing Approach	163
4.4 Specific Applications of the Hilbert Transform	166
4.4.1 Describing the Hilbert Transform	166
4.4.2 Identifying Sub-seabed Lithologies	168
4.5 Development of an "Acoustic Core" Product	170
4.5.1 Designing the Three Dimensional Logic of the Dynamic "Acoustic Core"	170
4.5.2 Applying the "Acoustic Core" Product to the Stratigraphic Model	176
5.0 PREPARATIONS FOR THE ACOUSTIC EXPERIMENTS	179
5.1 Pre-amble	179
5.2 Experimental Objectives	179
5.3 Scaling Factor	180
5.3.1 Discussion	182
5.3.2 Summary	184

	<u>Page</u>
5.4 Experimental Details	186
5.4.1 Acoustic Tank and Positioning System	186
5.4.1.1 Description of Setup	187
5.4.1.2 Carriage Tracks	190
5.4.1.3 Transmitter Carriage	190
5.4.1.4 Fixed Positioning Bracket	190
5.4.1.5 ASI Simulator	191
5.4.1.6 Transmitter Rotation Apparatus	192
5.4.1.7 Hydrophone Carriage	193
5.4.2 Transmitting Instrumentation	193
5.4.2.1 General Application Transducers	194
5.4.2.2 Primary Transducer	195
5.4.2.3 Electronic Circuitry	197
5.4.3 Receiving Instrumentation	202
5.4.4 Sediment and Acoustic Propagation Modelling	203
5.4.4.1 Acoustic Simulation Parameters	204
5.4.4.2 Sediment Preparation	211
5.4.4.3 Supporting Containers	212
5.5 Experimental Compendium	214
6.0 LABORATORY SIMULATION EXPERIMENTS	216
6.1 Scope	216
6.2 Hypotheses to be Tested	217
6.3 Nomenclature and Setting Used	218
6.4 Simulation Results	218
6.4.1 Establishing the Initial Character of the Water/Sediment Interface	221
6.4.2 Appraising the Internal Dimensions of the Pseudo-Glacial Till Structure	229
6.4.3 Quantifying and Illustrating the Coherency between the Two Spatial Scanning Rings	240
6.5 Final Interpretation	247
6.5.1 Appraising the Bathymetric and Thickness Contours	247
6.5.2 Appraising the Velocity and Attenuation Contours	256
6.5.3 Summary	258
7.0 TRANSFORMING ACOUSTIC RESPONSES INTO DISCRETE PHYSICAL AND ELASTIC PROPERTIES	259
8.0 FINAL DISCUSSION AND CONCLUSION	267
8.1 Acoustic Criteria for the Concept	267
8.1.1 Lateral Resolution	268
8.1.2 Temporal Resolution	268
8.2 ASI Model Development	269
8.2.1 The Project Model	270
8.2.2 Signal-to-Noise and Signal-to-Reverberation Evaluation	270

	<u>Page</u>
8.3	Extracting Sub-seabed Information 272
8.3.1	Detection of Primary Reflections Using a Moveout Technique 272
8.3.2	The Spatial Offset Network 273
8.3.3	The Hilbert Transform Approach 273
8.4	Results of the Experimental Simulations over a Pseudo-Glacial Till 275
8.4.1	Time History Data using the Hilbert Transform 275
8.4.2	Statistical Evaluation of the Pseudo-Glacial Till's Homogeneity Character 276
8.4.3	The "Acoustic Core" Product 277
8.5	Attenuation Loss Approach to Measure and Monitor Changes in Shear-Wave Velocity 278
8.5.1	Elastic Equations 278
8.5.2	Correlating Attenuation Losses with Rigidity ... 279
8.6	Future Direction 280

VOLUME II. REFERENCES AND APPENDICES

LIST OF REFERENCES	282
APPENDIX A - Summary of Conclusions of the Geonautic's Boulder Detection Study	297
APPENDIX B - Difference Frequency Pressure	300
APPENDIX C - Experimental Data Digest for the Outer and Inner Scanning Circles	302
PLATES - 1 A to 1d ₁ : Pre-measurement Setting	303
PLATES - 2 A to 2d ₁ : Time History Data	320
PLATES - 3 A to 3d ₁ : Envelope of the Time Signals	337
PLATES - 4 A to 4d ₁ : Instantaneous Frequency	354
APPENDIX D - Confidence Levels Associated with In-Situ Attenuation Measurements	371

LIST OF FIGURES

<u>Figure</u>	<u>Page</u>
Chapter 1.0	
1.1 High Resolution Seismic Record Collected in the Vicinity of the Scotian Shelf	3
1.2 Particularly Strong Subbottom Reflector	4
Chapter 2.0	
2.1 Evaluation of Seismic Systems in Field Conditions	10 and 11
2.2 Observed Performance of Seismic Devices	12
2.3 Fresnel Zones	18
2.4 Comparison of Seismic Profiles and Reflection Coefficients	25
2.5 Profiling Case of a Till Lense	27
2.6 Examining the Signals from Reflectors (a) and (b)	28
2.7 Potential Advantages of the Parametric Source for Echo Ranging	32
Chapter 3.0	
3.1 Sedimentation from Floating Ice or Ice Fronts	42
3.2 Moraine Forms	45
3.3 Depositional Chronology for the Project's Stratigraphic Sediment Model	48
3.4 Porosity Versus Mean Grain Size	52
3.5 Rigidity Modulus Versus Mean Grain Size	53
3.6 Sound Speed - Porosity Relationships	55
3.7 Mean Grain Size and Porosity Versus k in $\alpha = Rf'$	62
3.8 Interpreted Seismic Profiles, 1982 Raleigh Site, Davis Strait	64
3.9 Sediment Impedance, Reflection Coefficient and Bottom Loss at Normal Incidence	67

	<u>Page</u>
3.10 Conceptual Illustration of Scattering	73
3.11 Stratigraphic Model Reference and Terminology	76
3.12 Optimization of a Terminated Parametric Array	88
3.13 Values for Af_1 , Af_2 , and Af_{max}	94
3.14 Principles of Newton's Methods	103
3.15 P/P_{max} versus f at Different Values of A	104
3.16 Comparison between the Terminated Parametric Array and the Conventional Source Models	107
3.17 Temporal Resolution with Depth for a Terminated Parametric Array and for a Conventional Source	110
3.18 Composite Ambient Noise Spectrum	114
3.19 Signal-to-Noise Ratio with Depth for a Terminated Parametric Array and for a Conventional Source	124
3.20 Truncated Conical Volume Geometry as it Applies to the Stratigraphic Model	131
3.21 Approximate Beam Pattern Versus Height above the Seabed and Radius of Transducer	133
3.22 Approximate Beam Pattern Versus Frequency	134
3.23 Functional Behaviour Curves for a Conventional Source and for a Terminated Parametric Array	136
3.24 Calculated Beam Patterns for a Conventional Source and for a Terminated Parametric Array	137
3.25 RL for the Four Case Histories	142
3.26 EL, DNL and RL Evaluations Versus Depth	145
Chapter 4.0	
4.1 Geometry used in the Normal Moveout Calculations	150
4.2 Primary Reflection and 1st Order Multiple Ray Geometry as Applied to the Stratigraphic Model	153

	<u>Page</u>
4.3 Results of the Analytical Model Simulation	157
4.4 Configuration of the Spatial Offset Network	162
4.5 Engaging a Focussing Approach	164
4.6 Qualitative Sketch of a Focussed Profile Over a Bouldery Structure	165
4.7 Flow Diagram Illustrating the Interrogation Logic	171
4.8 "Acoustic Core" Product	175
4.9 Computer Simulation of an "Acoustic Core"	177
 Chapter 5.0	
5.1 Water Tank Geometry and Limitations	188
5.2 Experimental Layout of the ASI Simulator and Sediment Model	189
5.3 Primary Transducer Dimensions	196
5.4 Complex Impedance Measurements	198
5.5 Inverse Ricker Wavelet	200
5.6 Transmitting and Receiving Instrumentation Schematic	201
5.7 Cummulative Distribution Curve for the Physical Model and its Corresponding Scaled Up Case	207
5.8 Comparing the Grain Size Distribution for the Laboratory Model and for the Full Scale Model	208
5.9 Acoustic Water Tank, Sediment Model Tank and Control Core Dimensions.	213
5.10 Overview of the Experimental Setting	215
 Chapter 6.0	
6.1 Spot Profiling Positions in Context to the Sediment Tank and to the Inner and Outer Scanning Rings	219
6.2 Terminology and Ray Path Geometry used in the Experimental Simulation Trials	220
6.3 Statistical Data Digest	243

	<u>Page</u>
6.4 Bathymetry Isolines	248
6.5 Thickness Isolines	249
6.6 Velocity of Sound Isolines	250
6.7 Attenuation Coefficient Isolines	251
6.8 Qualitative 3-Dimensional Distribution of Thickness	252
6.9 Qualitative 3-Dimensional Distribution of Velocity	253
6.10 Qualitative 3-Dimensional Distribution of Attenuation Coefficients	254
6.11 Reference Chart	255
Chapter 7.0	
7.1 Attenuation Loss versus Shear Wave Velocity Hypothesis ...	264

LIST OF PLATES

<u>Plate No.</u>	<u>Page</u>
1. Premeasurement Settings	222
1A - Position A - Outer Scanning Circle	304
1A ₁ - Position A ₁ - Outer Scanning Circle	305
1B - Position B - Outer Scanning Circle	306
1B ₁ - Position B ₁ - Outer Scanning Circle	307
1C - Position C - Outer Scanning Circle	308
1C ₁ - Position C ₁ - Outer Scanning Circle	309
1D - Position D - Outer Scanning Circle	310
1D ₁ - Position D ₁ - Outer Scanning Circle	311
1a - Position a - Inner Scanning Circle	312
1a ₁ - Position a ₁ - Inner Scanning Circle	313
1b - Position b - Inner Scanning Circle	314
1b ₁ - Position b ₁ - Inner Scanning Circle	315
1c - Position c - Inner Scanning Circle	316
1c ₁ - Position c ₁ - Inner Scanning Circle	317
1d - Position d - Inner Scanning Circle	318
1d ₁ - Position d ₁ - Inner Scanning Circle	319
2. Time History Data	224
2A - Position A - Outer Scanning Circle	321
2A ₁ - Position A ₁ - Outer Scanning Circle	322
2B - Position B - Outer Scanning Circle	323
2B ₁ - Position B ₁ - Outer Scanning Circle	324
2C - Position C - Outer Scanning Circle	325
2C ₁ - Position C ₁ - Outer Scanning Circle	326
2D - Position D - Outer Scanning Circle	327
2D ₁ - Position D ₁ - Outer Scanning Circle	328
2a - Position a - Inner Scanning Circle	329
2a ₁ - Position a ₁ - Inner Scanning Circle	330
2b - Position b - Inner Scanning Circle	331
2b ₁ - Position b ₁ - Inner Scanning Circle	332
2c - Position c - Inner Scanning Circle	333
2c ₁ - Position c ₁ - Inner Scanning Circle	334
2d - Position d - Inner Scanning Circle	335
2d ₁ - Position d ₁ - Inner Scanning Circle	336

LIST OF PLATES

<u>Plate No.</u>		<u>Page</u>
3.	Envelope of the Time Signals	232
3A	- Position A - Outer Scanning Circle	338
3A ₁	- Position A ₁ - Outer Scanning Circle	339
3B	- Position B - Outer Scanning Circle	340
3B ₁	- Position B ₁ - Outer Scanning Circle	341
3C	- Position C - Outer Scanning Circle	342
3C ₁	- Position C ₁ - Outer Scanning Circle	343
3D	- Position D - Outer Scanning Circle	344
3D ₁	- Position D ₁ - Outer Scanning Circle	345
3a	- Position a - Inner Scanning Circle	346
3a ₁	- Position a ₁ - Inner Scanning Circle	347
3b	- Position b - Inner Scanning Circle	348
3b ₁	- Position b ₁ - Inner Scanning Circle	349
3c	- Position c - Inner Scanning Circle	350
3c ₁	- Position c ₁ - Inner Scanning Circle	351
3d	- Position d - Inner Scanning Circle	352
3d ₁	- Position d ₁ - Inner Scanning Circle	353
4.	Instantaneous Frequency	238
4A	- Position A - Outer Scanning Circle	355
4A ₁	- Position A ₁ - Outer Scanning Circle	356
4B	- Position B - Outer Scanning Circle	357
4B ₁	- Position B ₁ - Outer Scanning Circle	358
4C	- Position C - Outer Scanning Circle	359
4C ₁	- Position C ₁ - Outer Scanning Circle	360
4D	- Position D - Outer Scanning Circle	361
4D ₁	- Position D ₁ - Outer Scanning Circle	362
4a	- Position a - Inner Scanning Circle	363
4a ₁	- Position a ₁ - Inner Scanning Circle	364
4b	- Position b - Inner Scanning Circle	365
4b ₁	- Position b ₁ - Inner Scanning Circle	366
4c	- Position c - Inner Scanning Circle	367
4c ₁	- Position c ₁ - Inner Scanning Circle	368
4d	- Position d - Inner Scanning Circle	369
4d ₁	- Position d ₁ - Inner Scanning Circle	370

Cette thèse est dédiée à ma femme
Anna, à mes deux fillettes, Françoise et Simone,
et à Maman et Papa!

VOLUME I

TEXT

1.0 INTRODUCTION

Offshore high resolution seismic reconnaissance has as its primary objective to clearly define the structure lithology of the seabed for possible hazards and anomalies. The identification of these hazards is important in exploratory drilling to install efficiently the initial casing and to establish safe drilling procedures in the early phases of the program. The presence of boulders, hydrate and gas accumulation, permafrost, faulting, major scarps and softer sediments such as ooze are all potential drilling hazards especially if these are not expected at the time of their encounter. They also become hazards to the safety of the platform if not adequately identified before the production facility is positioned over the site.

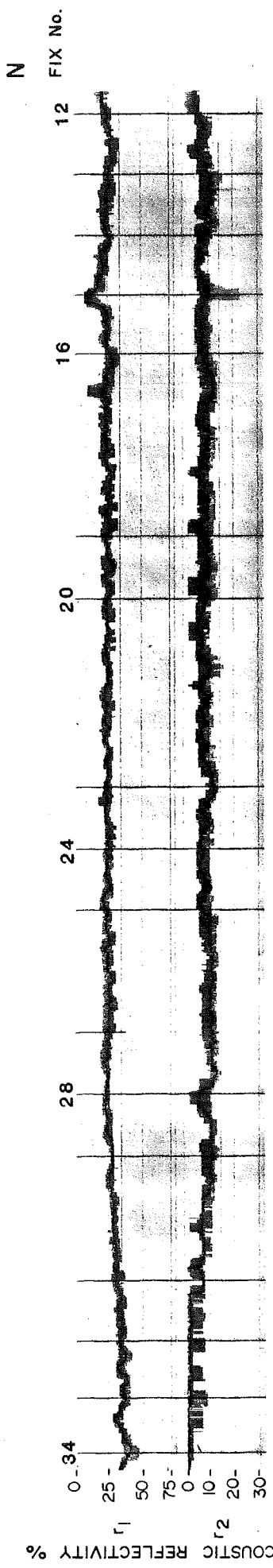
The geophysical seismic profilers available today are able to provide reliable predictions on the general occurrence of such hazards. By seismically mapping the reflections from interfaces between formations in a continuous manner, their physical properties can be geologically interpreted. It is thus possible to produce structural maps of any geological horizon which yields reflections. Nevertheless, the sediment themselves cannot be identified without independent geological information such as might be obtained from borehole studies (Dobrin 1976).

Most seismic profiling systems are capable of recording sufficient information in areas where the seabed is largely composed of acoustically transparent sediments such as silts, and/or clays.

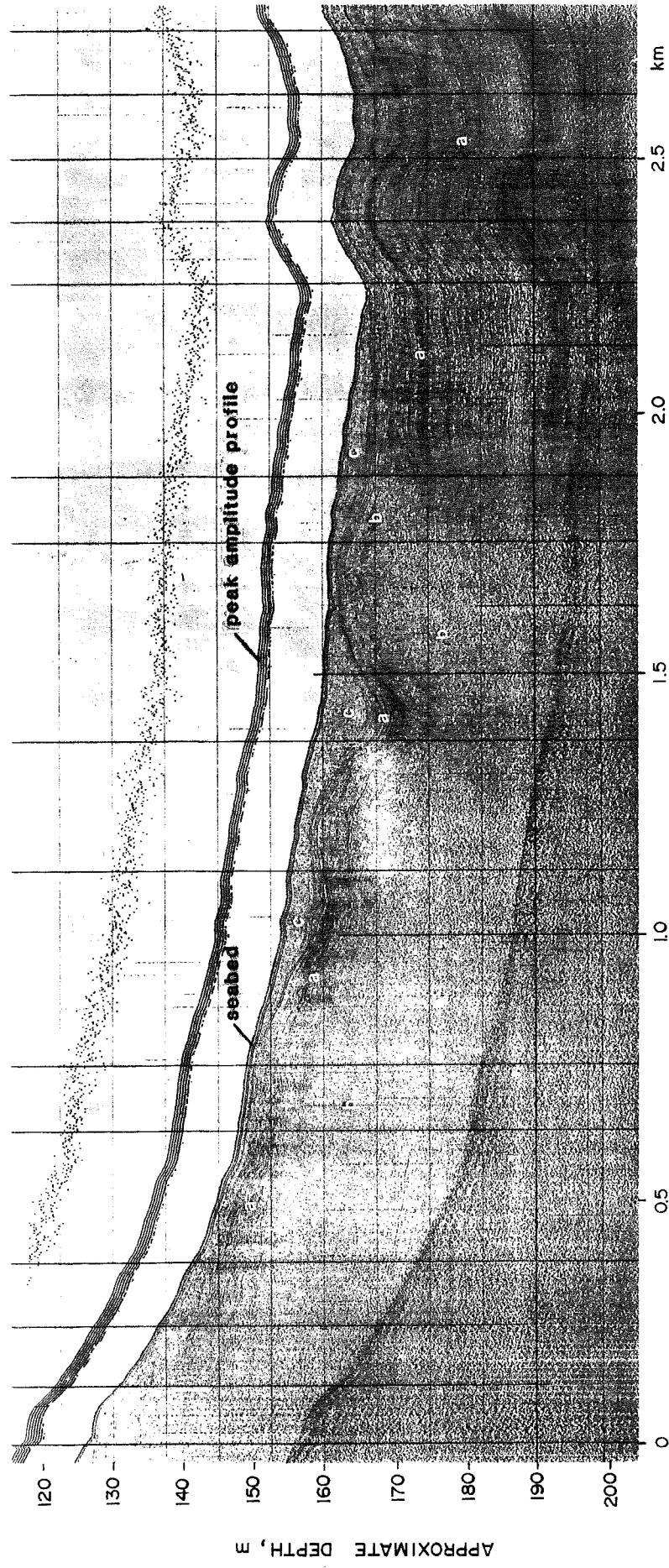
However, in a seismically hard environment such as those off the East Coast of Canada where the seismic energy is redistributed in the seabed in various forms of attenuation and of scatter, transmissions tend to show limits in penetration and continuity and therefore provide reflection data of restricted usefulness. For example, Figure 1.1 illustrates a section of a high resolution seismic record collected in the vicinity of the Scotian Shelf. This profile outlines a stratigraphy which may contain a possible till tongue complex. The record clearly differentiates the small deposits of the more acoustically transparent Emerald Silt from the underlying subglacial Emerald Silt unit. However, the digitation of the subglacial Emerald Silt abruptly truncates with another unit believed to be a glacial till lense. Very little structural information can be extracted in the area associated with this glacial till unit. The contact with the Emerald Silt and with the subglacial Emerald Silt is indistinct.

In certain cases it is important to be able to identify the exact nature of a particularly discontinuous and strong sub-bottom anomaly. The seismic section presented in Figure 1.2 is an example of a situation where the interpretive scope is very broad. The prominent reflector seen on this figure, has been interpreted to be one of the following: (Guigne 1984 - in preparation; this profile was collected during a 1982 reconnaissance survey in the Davis Strait).

- i) gas in the sediment
- ii) a rough portion of the Ordovician Limestone beds which are believed to be the dominant bedrock type near the seabed surface.
- iii) a Precambrian bedrock inlier exposure.

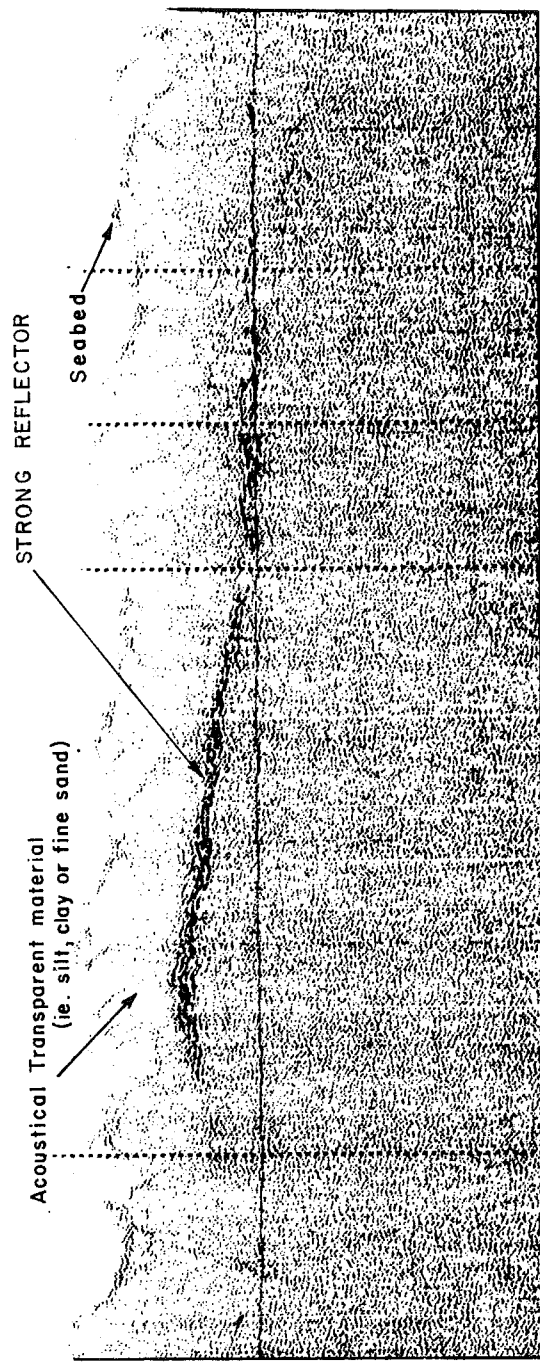


WEST ESPERANTO SCOTIAN SHELF SEISMIC LINE IO



Huntec DTS data showing acoustic reflectivities, peak amplitude profile and seismic section over an Emerald Silt deposit on line IO which shows a possible till tongue complex. Subglacial Emerald Silt (a) digitates with a unit believed to be glacial till (b). A small deposit of Emerald Silt (c) lies on top of the subglacial Emerald Silt Unit. Vertical exaggeration = 15X.

FIGURE 1.1 High Resolution Seismic Record Collected in the Vicinity of the Scotian Shelf (illustration was released for this thesis by Petro-Canada).



(Guigné 1984)

Possible Interpretation :

- i) Gas in the sediment.
- ii) A rough portion of the Ordovician limestone beds which are believed to be the dominant bedrock type near the seabed surface.
- iii) A Precambrian bedrock inlier exposure.

FIGURE 1.2 Particularly Strong Subbottom Reflector.

Since all three explanations are significantly different, this particular site could pose a serious problem if drilled. While offshore exploration continues, spurred on by the new hydrocarbon discoveries in the vicinity of the Beaufort Sea, Grand Banks, and the Scotian Shelf, strong demands are being placed to develop better remote sensing acoustical tools for more reliable seabed interpretations. The subject of this thesis is specifically oriented to meet that criteria and introduce to the geophysical/geological community a new concept in ground truth control which complements and enhances existing geophysical mapping.

This study experimentally develops a high resolution deep penetrating acoustic spot probe called an "Acoustic Sub-seabed Interrogator"*. Through its use, it should become possible to precisely map and interpret variations found within sedimentary sequences, especially within complex sediment mixtures typical of glacial drift deposits and of permafrost structures. Of special interest to the project is the modelling of sediment structures found in the Canadian Arctic waters particularly the ability of the "Acoustic Sub-seabed Interrogator" to define lenses of cobbles or boulders within a column of sediment and to detect the nature or presence of sub-bottom permafrost. In addition, the analytical modelling techniques developed for the evaluation of the concepts can be applied to other remote mapping seabed methods. This aspect is of

* The name "Acoustic Sub-seabed Interrogator" and its shortened title of ASI are interchangeable. They refer to the concept developed in this thesis of a high resolution stationary probe that can intelligently interrogate the acoustic responses coming off sedimentary structures.

special importance to the offshore engineering community who require realistic performance appraisals of their profiling systems under specific conditions.

The following chapters describe the design parameters involved in the development of the ASI with particular attention placed on the analytical and experimental derivations. For example, Chapter 2.0 reviews the acoustic theory associated with seabed profiling. Spatial and temporal resolution are highlighted in the discussions as the two restrictions crucial to the successful mapping of morainal seabeds. Chapter 3.0 is a comprehensive analytical study into acoustic signals travelling within structurally complex sediments. The primary objective in this chapter is to establish the feasibility of using non-linear acoustics for the ASI transmission by testing it over a multi-layered seabed. A highly scattering and attenuating Basal Till model is theoretically developed for the seabed structure.

From the model development of Chapter 3.0, the succeeding chapter concentrates on the conceptual probe's ability to extract sub-seabed information from the returning signals. A product called an "Acoustic Core" is introduced. The logic of the core design controls the cross correlation routines envisioned for the "Acoustic Sub-seabed Interrogator".

Chapters' 5.0 and 6.0 experimentally prepare and test the concepts of the previous three chapters. Although scaled, the simulations are considered representative. They provide a real insight into the

performance of the concepts and ideas as they apply to an actual scanning of a pseudo glacial till matrix.

The last two chapters synthesize the results of the theoretical analyses with the data collected experimentally. Arguments are presented which suggest a correlation can be established between attenuation losses and elastic properties. It is recommended that the next phase of research test acoustically a wide range of soil types of known geotechnical property to verify the validity and sensitivity of the correlation. A programmable monitoring - ASI simulator is suggested for this new venture.

2.0 HISTORICAL BASIS FOR AN "ACOUSTIC SUB-SEABED INTERROGATOR" CONCEPT

2.1 General Discussion

General acoustic sounding used in structural studies and in vertical profiling of highly scattering media such as over a morainic drift, are restricted by factors involving impedance mismatches between the different sediment densities, sound attenuation or extinction due to the scattering nature of its path and source constraints of long pulse lengths, wide beam spreads. Penetration improvements in high resolution equipment generated by a variety of independent researchers, industrial and academic, have been limited in success when tried over these seismically hard seabeds. One of the objectives of the thesis is to establish the acoustic theory associated with seabed profiling in a comprehensive realistic manner. This would therefore provide an effective means to optimize existing sensing systems as well as to efficiently develop a new probe.

In an attempt to select the best geophysical tool or combination of systems which would meet frontier survey requirements, various investigations have taken place to test and compare the capabilities of different sources off the East Coast of Canada. A joint venture in 1976 between CFP (Compagnie Francaise des Petroles), IFP (Institut Francaise du Petrole) and SNEA (P) (Societe-Nationale Elf-Aquitaine-Production) associated in the GERTH (Groupement Europeen de Recherches Technologiques sur les Hydrocarbures) with the EEC (European Economic Community) support, decided to run such a study. This survey was

specifically designed to critically examine the largest possible variety of seismic data acquisition devices and methods available at that time (des Vallieres et al 1978). Nine seismic sources, five types of streamers and seven different recorders were tested in a morainic environment off the East Coast of Canada on an acreage held by the Labrador Group of Companies of which Eastcan was the primary operator. The observed performances of the tested seismic devices are summarized in Figures 2.1 and 2.2.

The main conclusions from this investigation were as follows (see des Vallieres et al 1978):

- i) Use of combined instruments is necessary to obtain an overall and detailed sub-seabed knowledge.
- ii) The mini-flexichoc appeared to have the deepest penetration of more than 200 ms, while still maintaining a high resolving capability of approximately 15 ms.
- iii) Bottom-towed sparker was considered to be most efficient in terms of penetration/resolution ratio (15 ms/1 ms). The subtow sparker also appeared efficient with a 2 ms resolution capability and deeper penetration.
- iv) Bottom-towed boomer had the highest resolution (0.5 ms) although its penetration was considerably more limited than the bottom-towed sparker.
- v) The multi-electrode sparker was assessed to have a 5 to 10 ms resolution and a penetration in the order of 150 ms bridging the gap between shallow penetration, high resolution systems with deep penetration, low resolution approaches.
- vi) Enhanced results can be obtained using digital data acquisition systems (6/12 channels) at a very high sampling rate (1/8 ms). Digital multitrace recording allows true amplitude recovery, velocity analysis, CDP stacking, migration and impedance approximation.
- vii) Processing procedures used in deep seismic were proven feasible and showed substantial progress in enhancement of penetration and resolution as well as in structural and lithological determination.

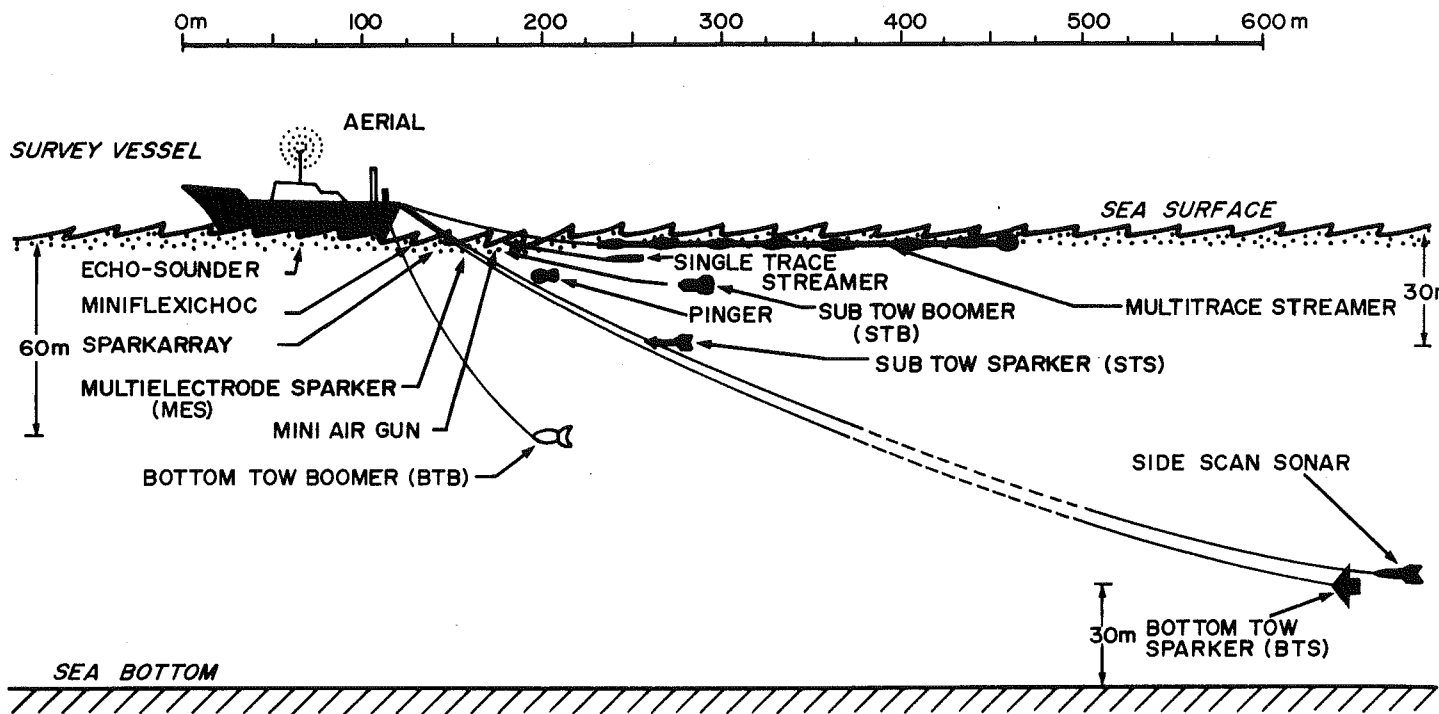


FIGURE 2.1 a - Tow Configuration of the Source-Receiver Assembly.

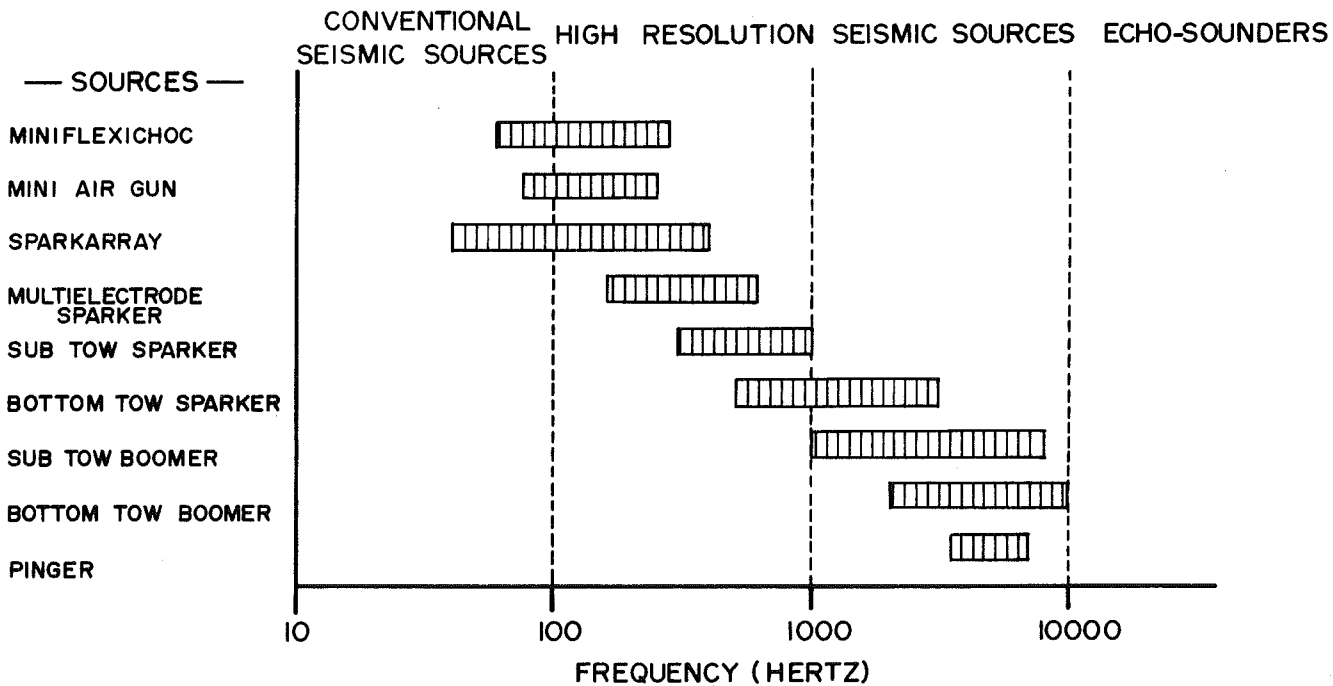


FIGURE 2.1 b - Frequency Range of the Seismic Source in Field Conditions (from des Vallieres, 1978)

FIGURE 2.1 Evaluation of Seismic Systems in Field Conditions

ADVANTAGES

DISADVANTAGES

TESTED SYSTEMS

- EASY IMPLEMENTATION
- EASY POSITIONING
- NO RESTRICTION CONCERNING THE ENERGY OF THE SOURCE
- MULTITRACE RECORDING

- AFFECTED BY SEA CONDITIONS
- VERTICAL RESOLUTION LIMITED BY GHOST REFLECTION
- ENERGY LOSS IN WATER COLUMN
- SHIP NOISE

- MINIFLEXICHOC
- MULTIELECTRODE SPARKER
- SPARKARRAY
- MINI AIR-GUN

- NOT AFFECTED BY SEA CONDITIONS
- REDUCED WATER COLUMN
- BETTER RESOLUTION (DECOUPLING OF THE GHOST FROM PRIMARY REFLECTION)

- PENETRATION LIMITED BY SURFACE GHOST
- NEED FOR A DEPTH/HEAVE COMPENSATION SYSTEM
- LIMITED SOURCE POWER (ENERGY LOSS IN THE TOW CABLE)

- SUB TOW SPARKER (NO DEPTH COMPENSATION)
- SUB TOW BOOMER (NO DEPTH COMPENSATION)

- VERY SMALL WATER COLUMN
- NO GHOST REFLECTION
- GOOD HORIZONTAL RESOLUTION (LESS DIFFRACTIONS CAUSED BY SHARP TOPOGRAPHY)
- SIGNAL CONTRACTION DUE TO HYDROSTATIC PRESSURE

- REDUCED PENETRATION (STRONG ENERGY LOSS IN THE TOW CABLE)
- POOR POSITIONING
- NEED FOR A DEPTH/HEAVE COMPENSATION SYSTEM

- BOTTOM TOW SPARKER
- BOTTOM TOW BOOMER

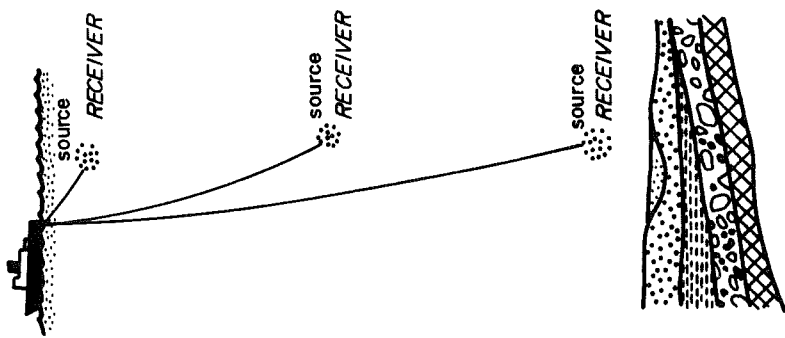


FIGURE 2.1c - Advantages and Disadvantages in Connection with the Immersion of the Source - Receiver Assembly (from des Vallieres, 1978)

FIGURE 2.1 continuation: Evaluation of Seismic Systems in Field Condition

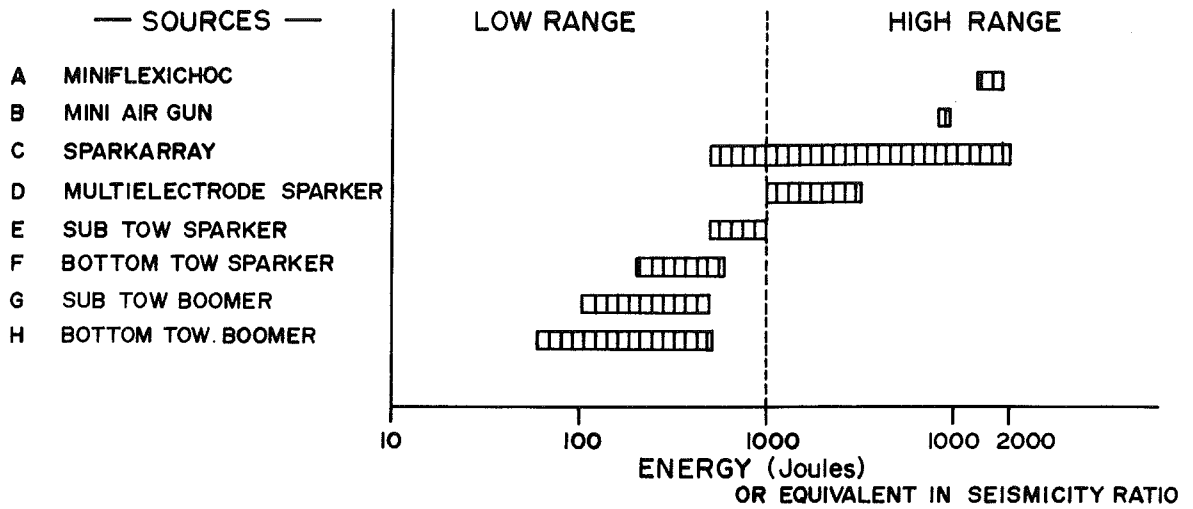


FIGURE 2.2a Energy Range of the Seismic Source in Field Conditions.

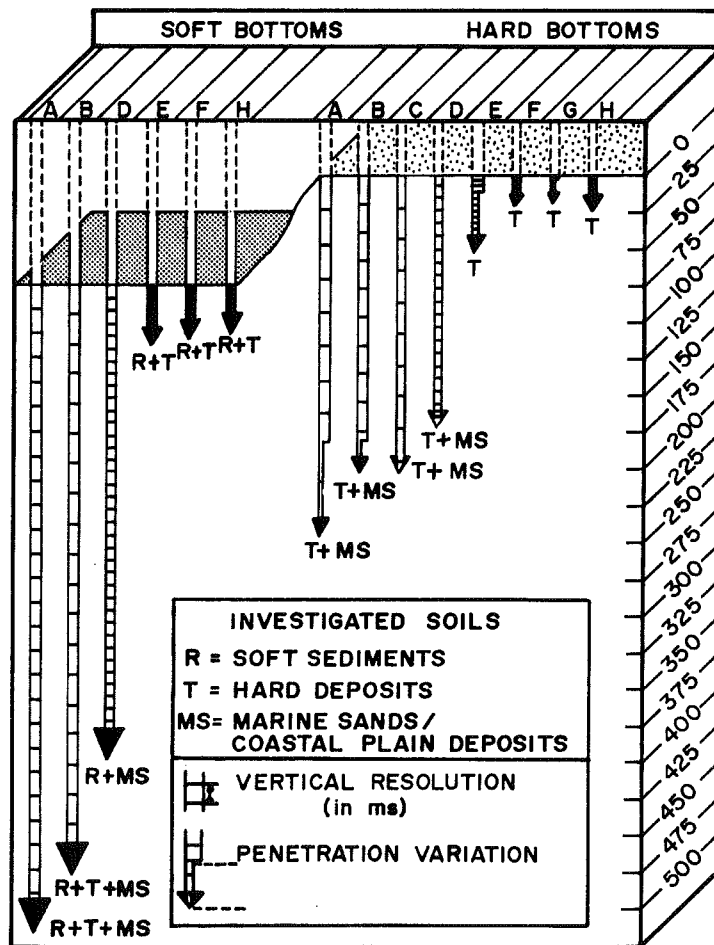


FIGURE 2.2 b Penetration of the Various Tools Tested (from Analog Records)

FIGURE 2.2 Observed Performances of Seismic Devices. (from des Vallieres, 1978)

In 1981, Geonautics Limited reviewed the Labrador Sea Soil Survey 1976 investigation and undertook a further paper study of the boulder detection problem this time for the Davis Strait region of the Eastern Arctic. Their main objective was to thoroughly assess the quality of shallow seismic data from three data sources:

- i) Four Industry Wellsites
- ii) Bedford Institute of Oceanography - Open File Data
- iii) Labrador Sea Soil Survey 1976.

This data was examined in light of potentially identifying boulder or cobble characteristics by considering such aspects as penetration, horizontal and vertical resolution, Signal-to-Noise and seismic event continuity. However in their final analysis, the detection of boulders and cobbles remains difficult to interpret unless preconceived knowledge of the geology is available to help identify true signals scattered off boulders from the rest of the redistributed energy (refer to Appendix A for a summary of their conclusions).

Adjunct to this investigation, Geonautics Limited initiated a small study to quantify the effect of attenuation by the sediment on the reflected signal through the use of sonogram analysis (Geonautics 1983). This is interlinked with the research of Dodds (1980, 1981); Parrott et al (1980); and Cochran and Dunsiger (1979) who demonstrated that valuable information could be extracted from the incoherent signals received with the HUNTEC Deep Towed Seismic System. Dodds (1980) developed a synthetic sonogram modelling technique whereby

acoustic returns due to acoustic energy reflected from the seabed can be distinguished from the energy that is reflected from within the sediment column (as a result of internal scatters within the sediment). An assessment of HUNTEC DTS records was undertaken in close proximity to the Leif Wellsite on Hamilton Bank (Labrador Sea) and the Cabot Wellsite on Saglek Bank (Labrador Sea). The aim was to delineate local areas where the sonogram modelling could be performed as a preliminary test of the techniques for the detection of areas of high internal scatter within the sediment.

Although no ground truthing is available, there appears to be a reasonable match between sonograms generated from field data and synthetic sonograms for both sites. There are some problems in the proper evaluation of volume scattering without actual information on bottom roughness or surface scattering. As well, information on the internal variability of the sediment may almost be considered as a prerequisite in order to fully appreciate and correctly interpret the results of the sonograms. Nevertheless with a better ground truthing transmitter source, this technique could potentially provide an efficient approach to assess the volume and the surface scattering characteristics of the seabed. For instance, appreciating the lack of geotechnical support data in the Geonautics 1983 study, the interpretation suggests the following conclusions:

"-At the Cabot Wellsite the synthetic sonogram modelling indicates that a large component of the acoustic returns is due to scattering from the seabed and that volume scattering has a significant effect on the acoustic returns.

-At the Leif Well site the synthetic sonogram modelling indicates that the acoustic returns are almost entirely the effect of scattering from the seabed. A small component may be attributed to volume scattering."

(Geonautics 1983)

2.2 Review of Potential Acoustic Techniques and Approaches

Although the use of combined instruments with overlapping spectrum performances, such as recommended in the GERTH 1976 study (ie: Miniflexichoc, Multielectrode Sparker, and Subtow Sparker), does significantly improve the interpretive quality of the combined records, it will not provide a comprehensive nor detailed sub-seabed picture in a hard morainic bottom. The primary strength of all these systems is in their continuous mode of operation which allows them to map the continuity of interface reflectors. The coherent portion of the signal is recorded and interpreted while the incoherent portion is discarded or filtered out. Unfortunately in an area characterized by high levels of volume and/or surface scatter the continuity of reflectors are often non-existent. The information relating to the sediment properties is therefore found within the incoherent "noise".

2.2.1 Source Position: Lateral Resolution and Signal Strength

The lateral or spatial resolving ability and the signal strength of a sound source are affected by its scanning height above the seabed and by its horizontal multiplicity of data. To obtain maximum information on sediment properties under specific survey conditions the transducer should be placed as low as possible to the seafloor and

towed over the surface at a very low speed. This would allow for the best integration of returns which in turn would provide additional signal enhancement. A high order of lateral resolution is essential when a target echo is to be extracted or accentuated from a scattering background.

The footprint size of a propagating signal upon the seafloor is proportional to the height of the transmitter above the bottom. Depending on the width of the sound beam and the distance to the seafloor, the sound energy transmitted will irradiate a specific area of the seabed. The portion of the illuminated area represented in the returned signal is determined by constructive interference of the reflected waves and is known as the Fresnel area. Effectively it is that portion of a reflecting interface where the energy will be received within the first half-cycle. This constructive interference is often used to delineate a horizontal resolution cell because the Fresnel area generally dictates the size of the objects which can be detected or discriminated.

The Fresnel area also decreases the rate of overrun or of multiplicity of data required to attain a specific level of lateral resolution. The spatial coherency and/or continuity of a profile is governed by the proximity of the horizontal resolution cells recorded. Using the following equation, we can estimate the Overrun Factor for different conditions: (from Van Overeem 1977).

$$\text{Overrun Factor } F = \frac{\text{sum of all Fresnel areas}}{\text{area covered by Fresnel}}$$

(2.1)

which can be restated as $\frac{1/2 \pi r_f}{s}$ where;

r_f = radius of the Fresnel circle

s = horizontal distance covered by the source between two successive pulses.

From Clay and Medwin (1977), the approximate radius of the Fresnel circle can be solved for r as a function of the relative phase differences $\Delta\Phi$. Considering that we are interested in the situation where the reflector is many wavelengths from the source and where h is the height above the reflector then (refer to Figure 2.3)

$$\Delta\Phi \approx \frac{2\pi r^2}{h\lambda}$$

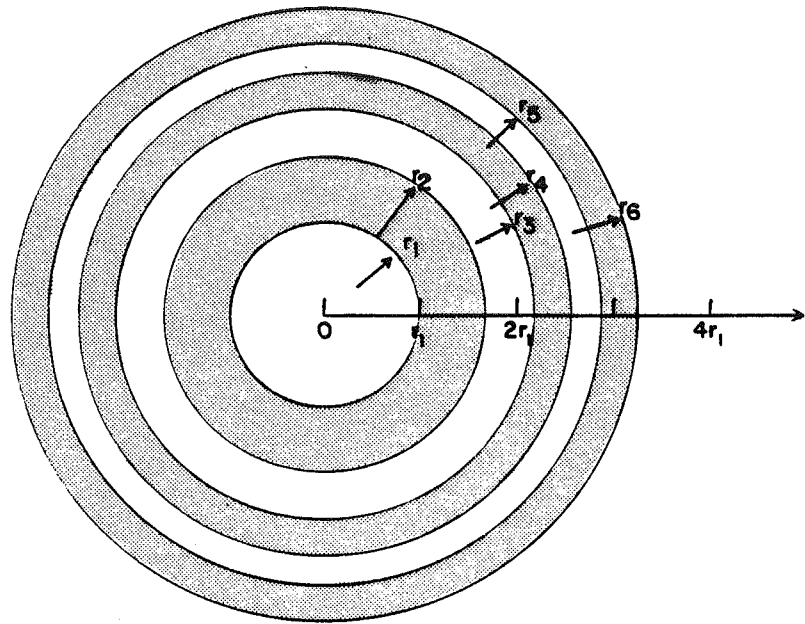
(given $\lambda \ll h$) (2.2)

The contributions are positive for different elements in the scattering area at radii such that $\Delta\Phi$ is in the range $0 \leq \Delta\Phi \leq \pi$. This range is the first phase zone also known as the first Fresnel zone. In the range $\pi \leq \Delta\Phi \leq 2\pi$, the contributions are negative. Letting $\Delta\Phi$ be $n\pi$, the phase changes the sign at radii

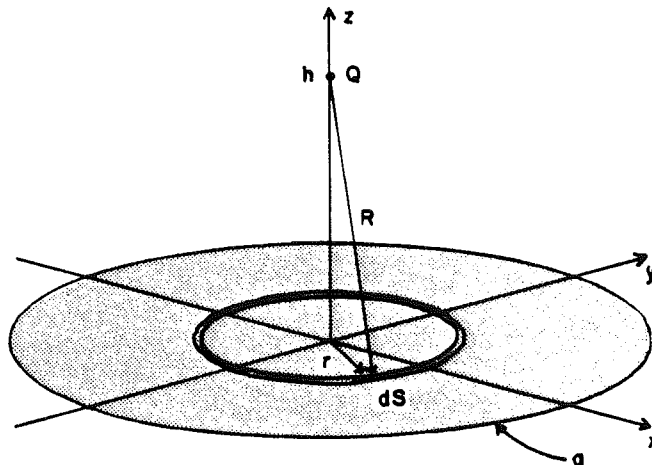
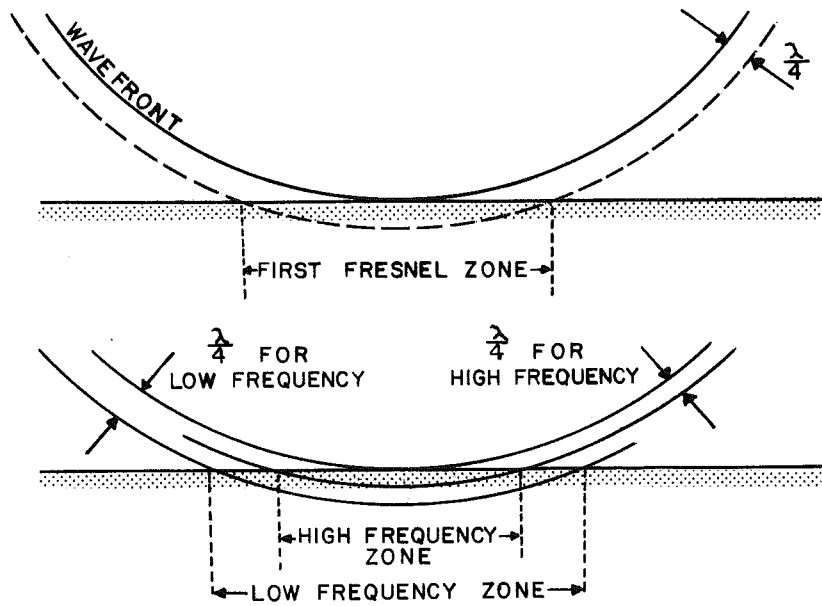
$$r_n \approx \frac{(\lambda h)^{1/2} n^{1/2}}{2}$$

(2.3)

Since a signal reflected at a disk having the radius of the first zone r_1 (i.e: the central circle) given when $n = 1$ has a maximum value, the first Fresnel zone will be used to define r_f . The subsequent



Fresnel or phase zones for reflection.



Reflection geometry for a plane area πa^2 . Receiver and source are at the same place Q; dS is an element of area at radius r .

FIGURE 2.3 Fresnel Zones (reproduced from Clay and Medwin 1977 and Sheriff 1978)

Fresnel zones will not be considered in the calculations because their contribution are in all practical purposes negligible. For instance the reflected energy from the second and subsequent Fresnel zones is delayed by a half to one cycle. A cancelling effect will thus take place. The effect of the second zone will nearly cancel that of the third. Subsequent zones will also nearly cancel each other out. The overall effect is the first Fresnel zone (refer to Figure 2.3). This phenomena is well documented and understood in the field of optics.

Two cases are described to illustrate the relationships between the Overrun Rate, the Fresnel area (for a given frequency and depth) and the distance between successive shots:

Case I

The reflected signal of a 5 kHz frequency will have an approximate Fresnel radius of $r = 3.9$ metres at a height above the seabed of $h = 100$ metres. This will in turn yield an Overrun Rate of $F = 24.5$ when the distance between successive shots is $S = 0.25$ metres. If S is increased (i.e. much faster ship speed) to $S = 1.25$ metres than $F = 4.9$. Changing the height above the seabed to a lower level, $h = 25$ metres, will produce an Overrun Rate of $F = 11.9$ when $S = 0.25$ metres. Likewise $F = 2.4$ when $S = 1.25$ metres.

Case II

Given the situation of a lower frequency, a frequency of 800 Hz will derive a Fresnel radius of $r = 9.7$ metres at a height above the seabed of $h = 100$ metres. This will in turn yield an Overrun Rate of $F = 60.9$ when the distance between successive shots is $S = 0.25$ metres. If S is increased to $S = 1.25$ metres than $F = 12.2$. Lowering the height above the seabed to $h = 25$ metres, will produce an Overrun Rate of $F = 30.2$ when $S = 0.25$ metres. Likewise $F = 6.0$ when $S = 1.25$ metres.

From this relationship it is clear that the shorter the distance between successive shots, (ie. slower vessel speed), the greater rate

of overrun for a given frequency and depth. Therefore while the placement of a transmitter over the seafloor should be kept to a minimum distance to derive a small Fresnel area and thus enhance the discrimination potential of smaller targets such as boulders, the horizontal distance between successive shots should also be kept short, thereby increasing the Overrun Rate. This latter point should be useful in data processing using averaging or vertical stacking techniques. This understanding and consideration of the Fresnel zone was a fundamental omission in the Gerth 1976 investigation.

Having the transmitter too close to the bottom may introduce some problems. For instance, ringing from the transducer may interfere with the returning signals especially where shallow sediment structures exist. In addition there is a greater possibility of multiple returns between the transducer and the seafloor. Keeping the Fresnel area at the seabed small by reducing the height above the bottom of an acoustic source, does not prevent the transmission beam from diverging. Spherical spreading will continue to occur and therefore will still make small horizontal detection of targets at depth below the seabed difficult. There are other practical problems to consider such as the vertical stability of a towed transmitter. If the transmitter height fluctuates, the transmission path the energy will follow will have an angular displacement resulting in loss of coherent energy in the desired scanning direction. This will tend to be more important for a given small change when near the seabed than if the source was flying higher in the water column where the Fresnel zone at the seabed is already large.

2.2.2 Synthetic Aperture

Horizontal discrimination of reflecting interfaces can in principle be enhanced by employing a radar technique called "Synthetic Aperture". The technique of aperture synthesis utilizes a line array concept whereby the elements of the array are a single transducer moved through the water acting as both source and receiver. By combining the individual returns a focussing effect results, behaving much like a very long virtual array. Although the uses of synthetic aperture techniques in radar are commonplace, largely developed through the work of such authors as Cultrona et al (1961, 1962, 1966, 1970, 1975); Harger (1970); Brown et al (1962) and T. Sato et al (1973, 1977); the application to underwater acoustics has been slow in acceptance and application. In the earlier studies on "Synthetic Aperture Sonar", there were difficulties encountered in avoiding large ambiguities due to the very high order of magnitude difference in the propagation speeds of radar electromagnetic signals as compared to sonar acoustic signals (Cultrona 1975). However, in recent years procedures have been developed which now make it possible for "Synthetic Aperture Sonar" systems to achieve desired resolutions without ambiguities. Cultrona (1975) describes such a procedure. He is able to avoid the ambiguity problems by controlling the projector pattern and the projector's horizontal aperture and by radiating a multiplicity of beams when required.

The synthetic approach eliminates the requirement for a large physical aperture and therefore may be a useful tool for the detection

of large subbottom scatterers such as boulders and cobbles. Where the ambient noise and turbulence of the medium could degrade the imagery, effective preprocesses could be used employing correlation methods. Ikeda and Sako (1980) have examined the effectiveness of such preprocessing for a "Synthetic Aperture Sonar" in a turbulent medium and concluded:

- i) Both multiplicative and additive noises deteriorate the Signal-to-Noise Ratio of the image in the same way;
- ii) The Signal-to-Noise Ratio of the image improves with an increase in the number of sampling points;
- iii) Correlation preprocessing is fairly effective for reducing the effects of multiplicative noises such as the turbulence of the medium.

In practical terms applying this technique to subbottom profiling would require careful consideration to multipath, to path stability and to refraction. These will seriously restrict the achievable resolution of the system. Cultrona (1975) indicates also that motion compensation is much more severe or important in a sonar application than in a radar system since the time required to translate a sonar system over a distance equal to the synthetic aperture length is much longer than for radar. However in comparing a "Synthetic Aperture Sonar" to a conventional sonar system, the along track resolution has been noted by various investigators to be independent of range for the "Synthetic Aperture Sonar" instead of the more linear resolution which will become coarser with range in a conventional system. A further advantage to the aperture techniques is that the seafloor geometry has only a minor effect on the area coverage rate. Ultimately, these advantages are at

the cost of relatively large amounts of processing and of preprocessing as seen in Ikeda and Sako's work, demanding trajectory control of a quality compatible with the resolution to be achieved.

2.2.3 Vertical Resolution

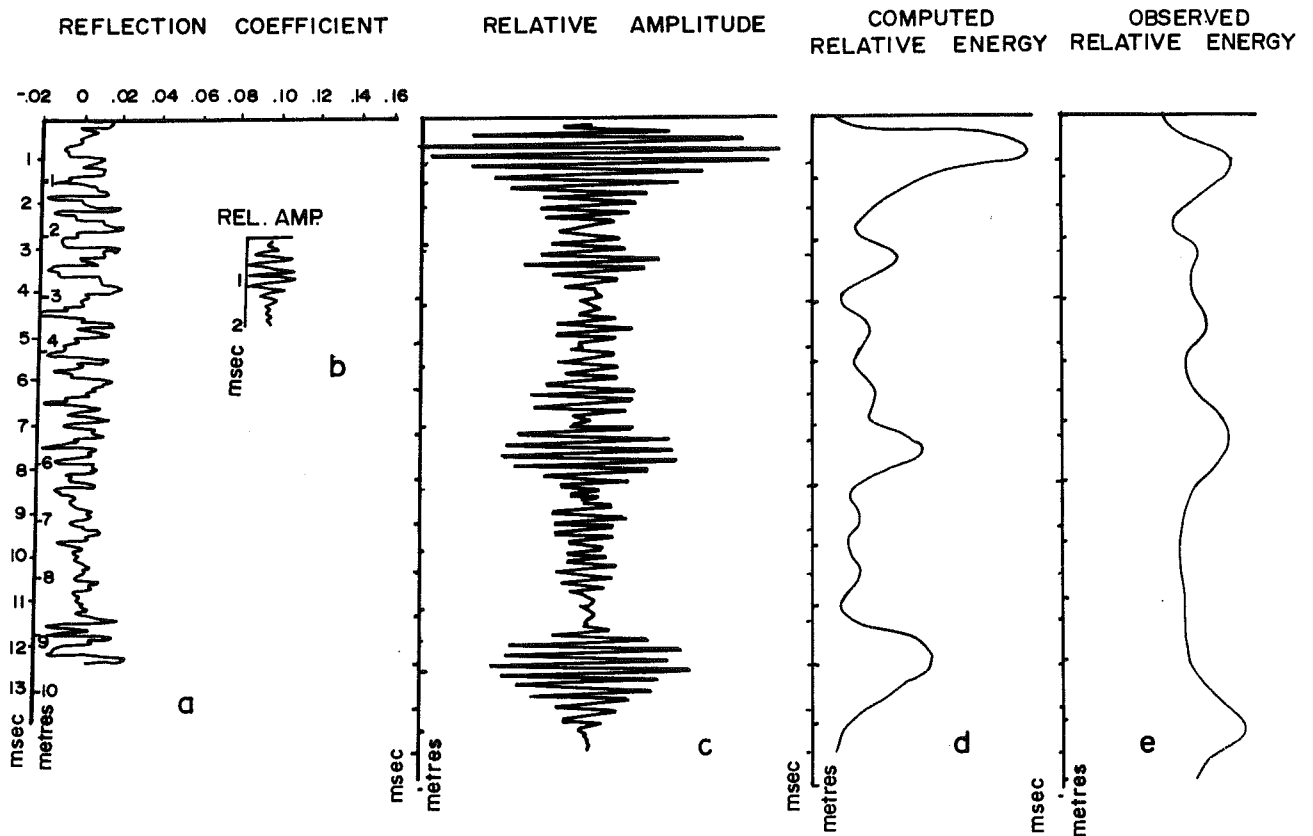
Another criterion to consider is vertical resolution. The length of the acoustic pulse will determine the vertical discrimination ability of the sound source. This is particularly important in situations where the energy is being scattered off thin sediment and/or glacial till layers. For example, if the pulse length is too long in relation to the sequence of true reflectors, a masking effect will occur. This inability to acoustically resolve these layers is often illustrated in acoustic-stratigraphic studies where Reflection Coefficient horizons derived off seabed cores rarely correlate with the seismic horizons observed. On the Scotian Shelf for instance, the fine layer stratigraphy believed to exist within the LaHave Clay province as interpreted from shallow high-resolution subbottom records does not appear to exist in the cores recovered for the site (L. King, G. Fader, 1983 communication).

Similarly, through various investigations of the acoustic properties of carbonates, Mayer (1979 and 1983) has enhanced our understanding of the problems that arise when the shape of the outgoing pulse is not compatible with the structures being sensed. While no correlation (or very little) was found between his seismic profiles and corresponding Reflection Coefficients, a high degree of correlation was

determined between the original seismic profiles and the synthetic seismograms generated by convolving the outgoing pulse with the impulse response (Mayer and LeBlanc 1983)(refer to Figure 2.4). As this outgoing pulse encountered and interacted with the fine scale layering of the sediment column some form of interference was generated. Therefore, to accurately represent true subsurface geology using acoustic profiling techniques it is paramount that the temporal resolution be sufficiently high to prevent interference within the layers. This essentially means an infinitively sharp change in amplitude such as in a step function. In the time domain this would require an infinitely short pulse.

It is not always feasible however to have such a short pulse using conventional acoustical techniques. The length of the outgoing signal is a function of the pulse bandwidth. The pulse bandwidth determines the sharpness of the amplitude change with frequency near resonance or Q of the system. As the bandwidth is increased, the pulse length will shorten and the Q of the system will lower. Unfortunately a decrease in Signal-to-Noise power ratio will also occur proportionally to the shortening of the pulse length; efficiency being a function of Q . An increase in bandwidth will also engender an increase in ambient noise (see Section 3.4.5). Since the Absorption Loss in a sedimentary structure is dependent on frequency, a decrease in Signal-to-Noise is a serious constraint on the frequencies available in the propagation.

If the nature of the sedimentary structure is considered seismically hard whereby its composition includes angular particle shapes, rather high grain size distributions and variable porosity, the



LEGEND: (a) Reflection coefficient log. (b) Digitized outgoing 4-kHz pulse of Deep-Tow (c) Output of convolution (amplitude). (d) Output of convolution (e) Deep-Tow 4-kHz reflection profile. (reproduced from Mayer and LeBlanc, 1983)

FIGURE 2.4 Comparison of Seismic Profiles and Reflection Coefficients.

resultant attenuation at high frequencies will be large. If the profiler does not have a broad bandwidth transient signal and a high Signal-to-Noise Ratio, its resolution and penetration potential will be seriously limited.

Consider the profiling case of a glacial till lense. The thickness of the layer can be expressed as a range difference ΔR , between an upper and lower boundary. The difference in travel times of the sound scattered at the upper reflector (a) and at the lower reflector (b) is:

$$\Delta t' = \frac{2\Delta R}{c} \quad (2.4)$$

given that c is the speed of sound. Refer to Figure 2.5 which illustrates the propagation geometry.

If the transient signal width is Δt , then given the condition where $\Delta t \ll \Delta t'$ the boundaries of the layer are potentially resolvable. However, if $\Delta t' = \Delta t$ it would be very difficult to differentiate between the reflectors. Since the temporal resolution of the system depends on the bandwidth and not the carrier frequency then the minimum bandwidth Δf required to detect the horizons separated by Δt can be determined through the close approximation of:

$$\Delta f \Delta t' \geq 1 \quad (2.5)$$

using $\Delta f \Delta t = 1$ as a lower limit and defining Δf by the -3dB points as seen in Figure 2.6.

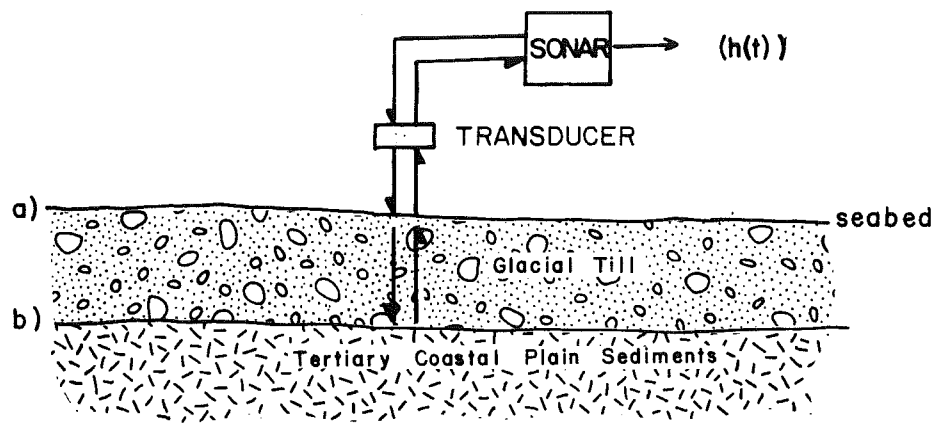


Fig 2.5a Geometry

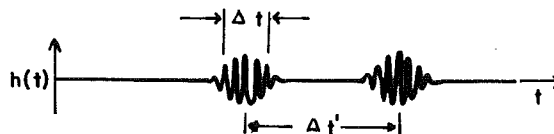


Fig 2.5 b Separated Returns ($\Delta t \ll \Delta t'$)



Fig. 2.5 c Echoes are Merging, Difficult to Resolve ($\Delta t = \Delta t'$)

FIGURE 2.5 Profiling Case of a Till Lense
(modified from Clay and Medwin, 1977)

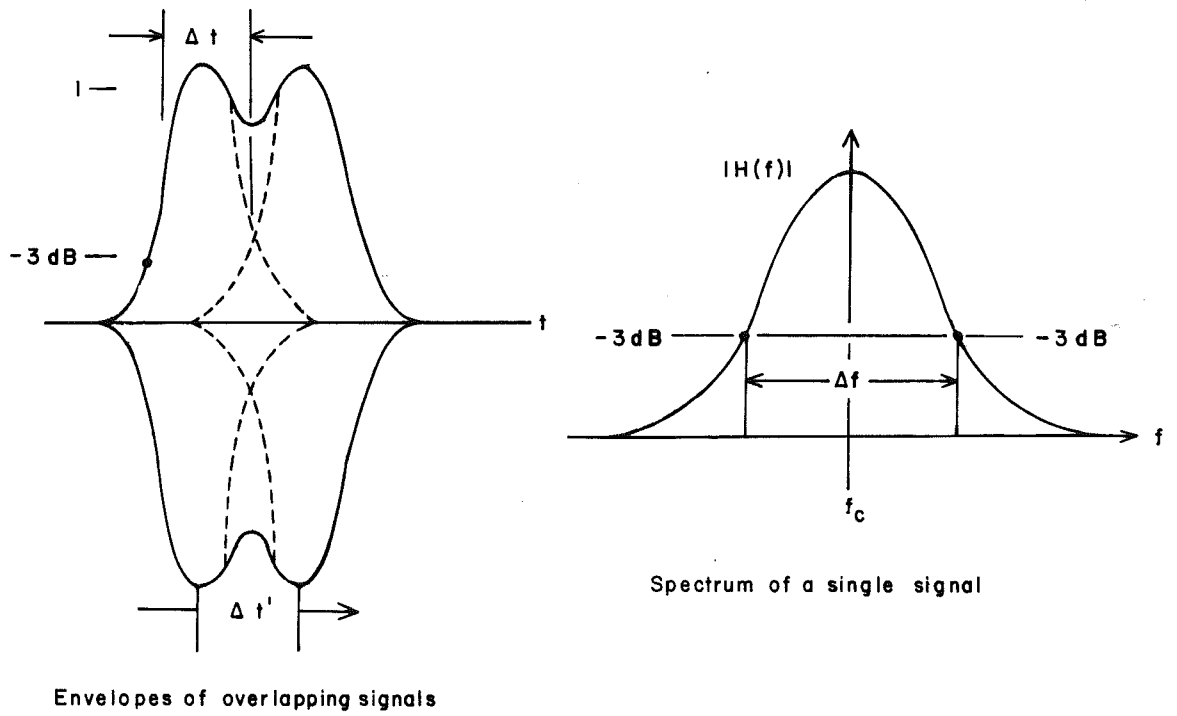


FIGURE 2.6 Examining the Signals from Reflectors (a) and (b) (modified from Clay and Medwin, 1977)

Addressing this to the till layer, we can calculate the minimum bandwidth required to resolve the layer thickness. Resolution for a two way passage is $\frac{c\Delta t}{2}$ metres. If the layer is 0.45 metres between the upper and lower boundaries then applying expression (2.4) defines

$$\Delta t' = \frac{2(0.45)}{1500} \text{ thus } \Delta t' = 6 \times 10^{-4} \text{ seconds}$$

The minimum bandwidth where $\Delta t' = \Delta t$ would therefore become:
(using expression 2.5)

$$\Delta f = (\Delta t)^{-1} = \underline{1,667} \text{ Hz (0.6 msec pulse duration)}$$

However, if the till layer thickness was 0.25 metres the minimum bandwidth requirement would have to be much broader; i.e. 3000 Hz (0.3 msec pulse duration).

2.2.4 Parametric Approach

A wide bandwidth at low frequencies with a narrow beam pattern can be attained by employing the recently recognized technology of non-linear acoustics. The Parametric Array uses non-linear acoustic effects to create a low frequency narrow beamwidth. For example, when the transducer operating in a non-linear medium is energized with two slightly different high frequencies, two collinear acoustic beams are formed. A parametric beam at the difference or secondary frequency can

then be produced from the interaction of the beams of the two primary frequencies in the non-linear medium (e.g. the water column). The resultant secondary beam has the characteristics of an exponentially tapered end fire array, the exponential taper being caused by the water attenuation at the primary frequency and the end fire array is formed in the narrow water column below the transducer.

Since Westerwelt's early work (1957) which introduced this phenomenon of scattering of "sound by sound", a number of scientists have successfully applied his predictions. One potential application which has been widely discussed by many authors as being quite attractive is the use of a Parametric Source for bottom and subbottom profiling. Berktaf et al (1979) best summarizes the main attributes of applying non-linear acoustic techniques for high resolution sub-bottom profiling by stating:

- i) A narrow beamwidth at a low frequency can be achieved using a relatively small transducer.
- ii) The low frequency used can be varied over a wide range with ease and simplicity.
- iii) Wide bandwidth signals can be used in order to obtain high range resolution.
- iv) The primary frequency returns can be used to provide a high frequency narrow beam echo sounder which determines the positions of the sea bottom accurately, even for soft sediments.

In addition, the short clean transmit pulse that can be achieved is also an advantage when scattering is a problem (Konrad 1979). This last point may be of particular importance in the remote sensing of a

bouldery layer where high levels of volume scattering exist. It is well documented now that the unique beam pattern of the Parametric Source provides a distinct improvement in the performance of active sonar under reverberation limited conditions (e.g. Berktaf 1967, Westervelt 1963, Tucker 1965, Horton 1974, Kritz 1977, Konrad 1979, and Quazi 1977). Two examples are described by Konrad (1979) to illustrate the potential advantages of the Parametric Source for echo ranging in shallow or surface waters. He states:

"... A comparison was made of conventional and parametric systems in an experiment at NUSC's Millstone Quarry Facility in 1971; each system used the same projector. The transducer depth was 4.5 m and the range to the target was 36 m. The source level was the same in each case. The target in each case was an LC-10 hydrophone (7.8 cm long by 1.3 cm diameter) target strength was -35 dB. Note that the narrow parametric beam eliminates surface reverberation and the target is unobscured" (Figure 2.7A).

"... on a larger scale, [Figure 2.7B] displays a return from a 5 dB target at a range of 8.7 Kyd in Seneca Lake. The difference frequency was 12 kHz with a source level 221 dB re 1 μ pa at 1 m and a conical 3° beam. Reverberation is just above the noise level for the parametric source. The much higher reverberation completely obscures the target for the conventional source".

Likewise, work performed by Muir, et al, (1974, 1975, 1979); on propagation models for Parametric Sources in shallow waters have provided comparisons of mean propagation curves for linear and non-linear sources. When the problem of echo to reverberation becomes important the high directivity of the Parametric Source has been noted to weigh favourably against equivalent broad beam linear sources. Wide bandwidth capabilities for signal processing as well as Doppler considerations also appear to favour Parametric Sources (Muir, et al

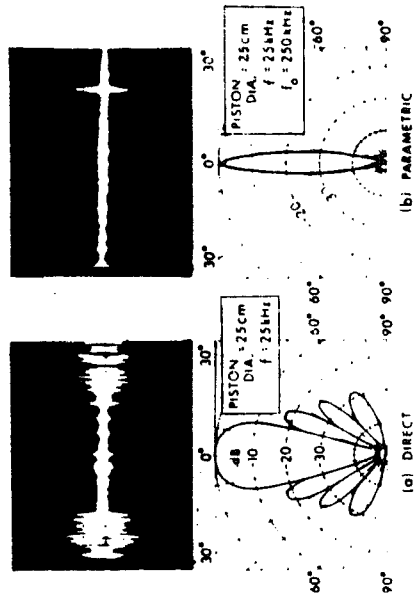


Fig 2.6 a Echo Ranging Performance

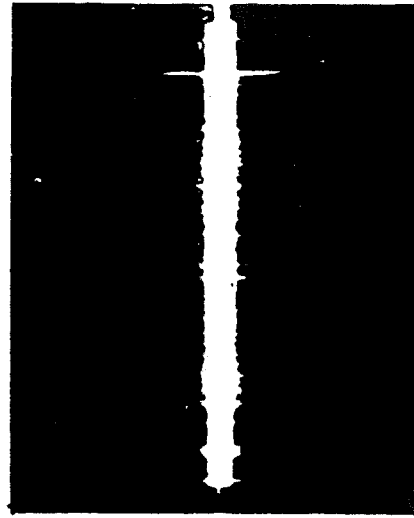


Fig 2.6 b Parametric Return 5 dB Target

FIGURE 2.7 Potential Advantages of the Parametric Source for Echo Ranging (from Konrad, 1979)

1976). As well Bjorno, et al (1977, 1979); have shown encouraging qualitative results for the operation of a parametric system in a temperature and salinity stratified shallow water region of the Baltic Sea.

Similarly, the use of Parametric Arrays in direct acoustical investigations of marine sediments, be it in the laboratory or in-situ has yielded interesting observations. Muir (1973) describes the results of such an experiment where the transmission of sound into a sediment layer could be studied in greater detail using a Parametric Array than with a Conventional Source. In fact the absorption over the refracted path significantly reduces the refracted amplitude. Likewise an evanescent wave which has been predicted to propagate parallel to the interface with an exponential decay with depth in the sediment was found to be a relatively insignificant factor (Muir 1973).

Research performed in Bath by Pace and Ceen (1980, 1982) on the "Terminated Transient Parametric Array" has also provided an insight into the situation where the parametric source volume is truncated in the region of the transmitting transducer nearfield/farfield boundary coinciding with the water/sand interface. Their experimental results have shown that the terminated Parametric Array as seen from a point in the water may be considered as consisting of two directive sources, one located at the transducer and the other at the termination. Concordantly Muir (1973) also indicated that the difference frequency radiations from Parametric Arrays while they did not possess minor

lobes in their radiation patterns, such lobes did appear to be present in the truncated parametric field transmitted into the sediment.

The relative amplitudes and spacing of the two directive sources referred to by Pace and Ceen as seen from below a plane water/sand interface were recorded to effectively change. Furthermore, unlike a conventional acoustic beam there was no sudden reduction in the acoustic intensity at a point in the sand as the critical angle was passed. Instead they observed a shift in the peak energy arrival time whilst the amount of energy which arrived at the field point increased with a decrease in the centre frequency of the acoustic pulse. This effect was not found to be simply due to lower attenuation in the sand at lower frequencies but caused by a composite relation to given geometry. (Pace and Ceen 1982).

Unfortunately, these attractive virtues of the Parametric Source are bought at the cost of very low power efficiency. Clay and Medwin (1977) affirm that the efficiency is generally a fraction of 1%. This value can be altered in the optimization of the acoustic transmission parameters. For example by increasing the difference frequency, the efficiency augments. Likewise, a positive influence on the energy transformation will occur if the beamwidth is decreased by lowering the primary frequency within a constant primary beam area. Regrettably these approaches erode the advantages of the non-linear source unless higher levels of primary power are applied. However, there are finite limits to the amount of power that can be engaged, largely dictated by saturation effects and cavitation which occur at high intensities (Clay and Medwin 1977).

In summary, the application of a Parametric Source does appear to have favourable subbottom profiling attributes which could prove advantageous over a morainic bottom. Fine resolution capabilities and potential for deep penetration could eventuate through the wide bandwidth inherent in the source. The Parametric Source's narrow beamwidth is only of use if the transmission path is coherent and has a stability comparable to that of the precision of the narrow pencil beam produced. The limitations of this technique's very low power efficiency and requirement for stability may be met by having the transducer fixed to a given spot over the seabed. A vertical profile would emanate as the integration of several returns would raise the level of Signal-to-Noise sufficiently to obtain unambiguous records.

2.3 Conclusion

The requirement to measure with precision the physical parameters of complex sedimentary structures such as of glacial drift deposits and lenses has outlined specific acoustic sensing criteria. Sound propagation constraints due to the medium's high volume scattering, to temporal distortions by multipath reflections, to rather high energy reflection levels off distinct layers of differing impedances and rapid attenuation of frequencies by coarse particulate size sediments in the surficial zones, are difficult conditions to meet in designing an effective seismic profiler. The technique suggested for the "Acoustic Sub-seabed Interrogator" to address these points, amalgamates the benefits of a Parametric Source in a fixed stationary mode of

operation. The parametric design envisioned takes full advantage of the wide band of frequencies that can be formed by a single transducer along with its consequential short clean transmit pulse. Being stationary, a stable base can be established for enhanced information extraction through precise geometrical manipulations. As well, signal discrimination, signal recovery and enhancement processing can be efficiently achieved, given the high order of stability provided by the coherent scans.

Ultimately, an attempt is made in this Ph.D. thesis to develop for the marine geoscience community, an acoustic spot profiling concept which would have the ability to intelligently interrogate signal and noise responses off the unconsolidated sediments of the Canadian Continental Shelf.

3.0 ASI MODEL DEVELOPMENT

3.1 "Is it possible to get a signal back?"

A theoretical investigation into the behaviour of signals travelling within structurally complex sediments is undertaken in order to efficiently develop the acoustic parameters required for the design of the "Acoustic Sub-seabed Interrogator". The proposed use of non-linear acoustics as suggested in Chapter 2.0 is very attractive, especially since the mode of operation is meant to be stationary. This use of a Parametric Array would potentially provide for a wide bandwidth capability, a short adjustable transmit pulse and a narrow beamwidth. The objective of this chapter is to quantify these aspects in relation to a conventional system while addressing the intrinsic question;

"Is it possible to get a signal back from a highly attenuating and scattering medium using a shallow high resolution profiler?"

In order to formulate a reply, a comprehensive sub-seabed model is designed in Section 3.2. The historical basis for a Basal Till structure is examined and its complex composition is specifically highlighted. Section 3.3 theoretically derives and appraises the energy losses that would occur in the sediment model. This in turn establishes the individual acoustic character of each layer in terms of attenuation, of scatter and of reflection. A series of evaluations are then performed in Section 3.4 on the signals projected from a truncated

Parametric Source and from a Conventional System onto the model.

Temporal Resolution, Signal-to-Noise, and Signal-to-Reverberation form the skeletal framework of this analysis while the computation criteria used involves parameters relating to the sonar equation. For example, such aspects as Source Level, receiver and transmitter Directivity Index, Transmission Spreading Losses, Ambient Noise, Absorption and Target Strength are considered in the final definition of Signal-to-Noise Ratio (SNR). The Signal-to-Reverberation Ratio (SRR) is defined in a similar manner but focusses on the high volume scattering effect of the model's Basal Till. The two sonar equations used are:

$$\text{SNR} = \text{SL} - (\text{TL}_D + \text{TL}_U) - \text{ABS} - (\text{NL} - \text{DI}_R) + \text{TS} \quad (3.1)$$

and

$$\text{SRR} = \text{TS} - \text{TSR} \quad (3.2)$$

where:

- SL is the Source Level (dB re 1μ Pa @ 1m)
- TL_D is the Geometrical Spreading Losses going down through the medium (dB)
- TL_U is the Geometrical Spreading Losses going up through the medium (dB)
- ABS is the losses due to Absorption (dB)
- NL is the ambient Noise Level (dB re 1μ Pa)
- DI_R is a Directivity Index (dB) on reception

- TS is the Target Strength of the basement reflector
(dB re 1m^2)
- TSR is the Target Strength of the till's layer reverberation
(dB re 1m^2)

A synopsis of the evaluations is presented in Section 3.5 and the results are discussed in detail. From this, another question emerges and is posed:

"What sub-seabed information can be extracted from the returned signals?"

An answer to this question is articulated in Chapter 4.0.

3.2 Stratigraphic Sediment Modelling

Determination of the changes in the wave shape seen in seismic data is the fundamental basis of seismic stratigraphic analysis. By mapping the configuration of reflection interfaces, the geological structure of an area can be inferred. As an interpretative tool some form of modelling is employed to aid in the assessment of the character inherent in the reflections. Sheriff (1980) best describes the all encompassing nature of modelling by defining it as:

"Modelling invariably involves a concept, an idea of a relationship between cause and effects. Sometimes it involves an actual physical model and the concept that effects will be scaled according to the ratio of model dimensions to actual dimensions. More commonly, modelling is done by manipulation of numbers in a digital computer according to a set of rules that incorporate the modelling concepts. Sometimes a model is only a mental concept that we use in thought processes".

Two types of modelling are instigated in the study to best direct an analytical appraisal of the ASI concept.

- i) Forward Modelling
- ii) Inverse Modelling

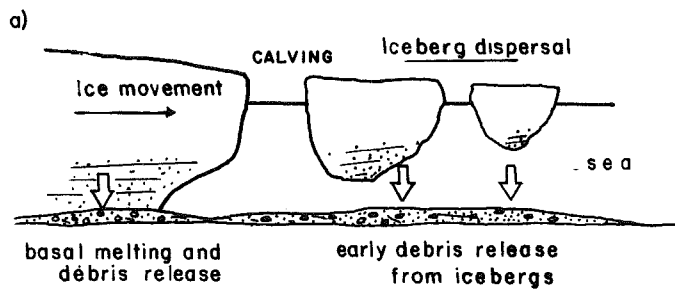
In theory, seismic Forward Modelling establishes a geological lithology which is then associated with a calculated reflection trace. When applied, the seismic effects of a stratigraphic change can be predicted. Although Inverse Modelling also involves a similar construction and use of a model, the direction this time is to examine the seismic effects and then postulate a potential lithology. Such aspects as the variations in acoustic impedance found on the seismic traces would be equated to a corresponding stratigraphy. While a model is designed to represent the important aspects of a geological sequence and of the seismic traces, the representation may not be precise or even resemble actual cases observed. The focus however of each model is to design a criterion which can provide a realistic basis for the interpretation of geological processes and/or for the existence of the observed seismic traces.

Since the analytical appraisal of the potential ASI concept depends on the evaluation of various transmission loss factors, the Forward Modelling approach will initially be used to define the system requirements based on a specific seabed model. The geological model that would best qualify as a control in this evaluation is one which incorporates the processes of glacial deposition in the sea.

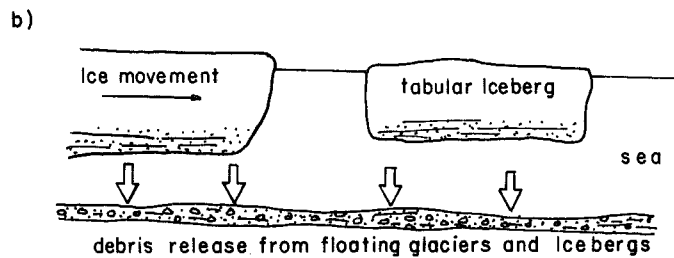
3.2.1 The Glacial Sediment Models

Sedimentation from grounded and floating ice is specifically applicable to the more northerly waters off the east coast of Canada. Unfortunately, little is readily known of this active type of sedimentation. There is little scientific data available on actual sediment deposition rates originating from icebergs and ice flows coming off Northern Ellesmere Island and North West Greenland resulting in numerous unsubstantiated hypotheses. On a larger extent, glacio-marine sediments of a post-glacial time are better known and documented. Goodell et al, (1968), and Olausson (1972) have indicated the extent of such sediments throughout the Arctic and Antarctic Oceans, the North Sea and Norwegian Sea. Their age can also vary extensively. For instance, Andrew (1970), relates the age of the uppermost tills of the Hudson Bay region to a date of about 7,800 BP which is considered to be the approximate time of catastrophic ice sheet disintegration when the ice was lifted from its bed by impounded meltwater (Sugden and John 1976).

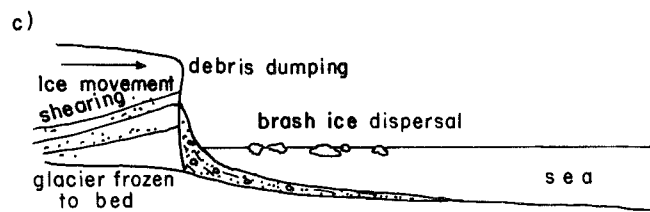
Ice melting and ablation by seawater are the primary glacial processes of deposition which concern this study. (Refer to Figure 3.1). In the case of grounded ice, the slow moving sheets of meltwater will slowly erode at the ice and gradually extract debris which will then settle to the seabed. Where the ice is afloat, the actions of melting and ablation will release material directly into the sea through wave action. The natural settling that follows will to a minor extent sort out the various particulate sizes. For instance, boulders



Warm-based glacier is standing in deep water in a calving bay.



Cold glacier or ice shelf is afloat in very deep water.



Cold-based glacier is standing in shallow water or on a beach.

FIGURE 3.1 Sedimentation from Floating Ice or Ice Fronts (modified from Sugden and John, 1977)

and cobbles may be deposited on to the seabed first, followed by coarser sands then silts and clays because of suspension selectivity. The fine fraction of silts and clays could thus remain quite long in suspension depending on the sea's temperature, salinity and turbulence which prevails at the time of settling. However, since the erosional conditions tend to be near continuous, a constant input of material is fed into the water. The sorting that would take place can therefore be considered minor.

Since it is well known that bottom currents do alter the sedimentation pattern of a seafloor it is conceivable that they may also act directly onto the freshly deposited glacial sediments. Hartshorn and Ashley (1972) state that secondary structures could be created if turbidity currents operated near enough to the seafloor. Therefore potential shear planes, folds, and involuted structures could result in sizes that are quite substantial.

Sediment characteristics in the till are strongly influenced by the nature of glacier calving (Sudgen and John 1976). If a glacier snout extends far out into deep water before calving, very large tabular bergs will be produced. When tabular bergs which traverse across the Davis Strait encounter the shallower waters of the Canadian Continental Shelf their keels may strike the seafloor. If the iceberg does impinge on the sea bottom, debris entrapped in the ice may become dislodged. Clusters of erratic boulders and significantly large patches of till can be deposited onto the seabed in this manner. Sonar

records collected in the Davis Strait and in the Strait of Belle Isle substantiate this depositional process (Guigné 1983).

The rate of till sedimentation is a function of the local conditions and the nature of the transporting ice mass. If a particular glacier is heavily charged with debris, several metres of till may be created in a short period of time. For example the Sefstrom glacier in Spitsbergen has been recorded to deposit 30 metres of till in a ten year period (Flint 1971). Glacier advances can also create spectacular push moraines. Sugden and John (1976), explain the most important effects of an advancing snout from the point of view of deposition to be:

- i) the bulldozing of previously pro-glacial material, including frozen blocks of silt and sandur sands and gravels, peat and slabs of bedrock.
- ii) the recycling of material (mostly till) being delivered to the snout englacially and supra-glacially by the normal mechanisms of transport.

Most of the morphology observed on the Eastern Canadian Continental Shelf relating to glacial till accumulations are derivations of morainic structure. Figure 3.2 summarizes in table form the different types of moraines that are to be found.

Glacial till deposits can be defined as a non-sorted agglomeration of particles of all sizes. Although, freshly deposited glacio-marine sediments may have larger void ratios and lesser bulk densities than terrestrial tills, (Easterbrook 1964) they can still be grouped together

Linear features		Non-linear features
Parallel to ice flow (controlled deposition)	Transverse to ice flow (controlled deposition)	Lacking consistent orientation (controlled or uncontrolled deposition)
Subglacial forms with streamlining: (a) Fluted and drumlinized ground-moraine (b) Drumlins and drumlinoid ridges (c) Crag and tail ridges	Subglacial forms: (a) Rogen or ribbed moraine (b) De Geer or washboard moraine (c) Kalixpinno hills (d) Subglacial thrust moraines (e) Sublacustrine moraines Ice-pressed forms: minor transverse squeezed ridges and corrugated moraine	Subglacial forms: (a) Low-relief ground moraine (b) Hummocky ground moraine
Ice-pressed forms: longitudinal squeezed ridges	Ice-pressed forms: minor transverse squeezed ridges and corrugated moraine	Ice-pressed forms: random or rectilinear squeezed ridges
Ice marginal forms: lateral and medial moraines, some interlobate and kame moraines	Ice front forms: (a) End moraines (b) Push moraines (c) Ice thrust/shear moraines (d) Some kame and delta moraines	Ice surface forms: (a) Disintegration moraine (controlled) (b) Disintegration moraine (uncontrolled)

FIGURE 3.2 Moraine Forms (modified after Prest, 1980)

in terms of composition. Goldthwait (1971) describes diagnostic features of till as follows:

- i) It is poorly sorted and often has clasts of many sizes (including boulders) in a variable finer matrix;
- ii) It tends to be massive in structure, without smooth lamination or graded bedding;
- iii) It is composed of mixed minerals and rock types, some of which are far-travelled;
- iv) It generally has a proportion of striated stones and micro-striated grains;
- v) It may have a common orientation of elongated particles;
- vi) It may be more compact than neighbouring sediments, due to the great pressures exerted during deposition;
- vii) It may rest upon a striated rock or sediment basement;
- viii) Its component clasts are predominantly sub-angular, due to frequent breakage during transport and partial smoothing by abrasion.

In addition, Dreimanis and Vagners (1971) concluded from their investigation on particulate size breakdown in tills that there are sorting or separating mechanisms which occur similar to what would occur under laws of crushing. In other words some form of compression and/or minor sorting can be expected in their makeup.

3.2.2 The Project Model

Our understanding of the geomorphological processes which have taken place along the Eastern Canadian Shelf has been very limited by the scarcity of data collected and the difficulty in its interpretation. The construction of a useful stratigraphic model

incorporating till can reasonably be made by inferring from processes which have occurred in other glaciated environments as well as from the generally accepted knowledge of the character of till composition and of till distributions. The exact reproduction of an actual site is not necessary. However, the model specifically designed for this project will take into account the conditions of a seismically hard seabed through the emplacement of till sheets (ground moraine) within a series of finer sediment layers.

The formulation of this pseudo-seabed is based on a drift section in Midlothian Scotland as described by Kirby (1969). The Pleistocene stratigraphic sequence expressed in it provides for a realistic representation of sedimentary sequences of varying particulate size beds. The actual model structure enlarges on the section by increasing the thicknesses of each sequence and including a surface layer of acoustically transparent material as a cap. In addition, a strong base reflector will terminate the model.

Details of the stratigraphy are illustrated in Figure 3.3. Its composition consists of a 40 metre deposit over a Tertiary Coastal Plain Sediment Base. The depositional chronology starting from the Tertiary bedrock appears as follows:

- A basal till (10 metres) is overlain by a gravel cover (10 metres) then a fine sand layer (8.4 metres) which in turn is covered by a sequence of four beds, each 0.4 metres in thickness of alternating fine sand and till.
- The top half of the section will consist of 10 metres of acoustically transparent silt-clay.

Section at Park Burn, Midlothian Scotland showing the alternation of Till and Fluvio-glacial deposits. (after Kirly, 1969)

Project's Stratigraphic Model

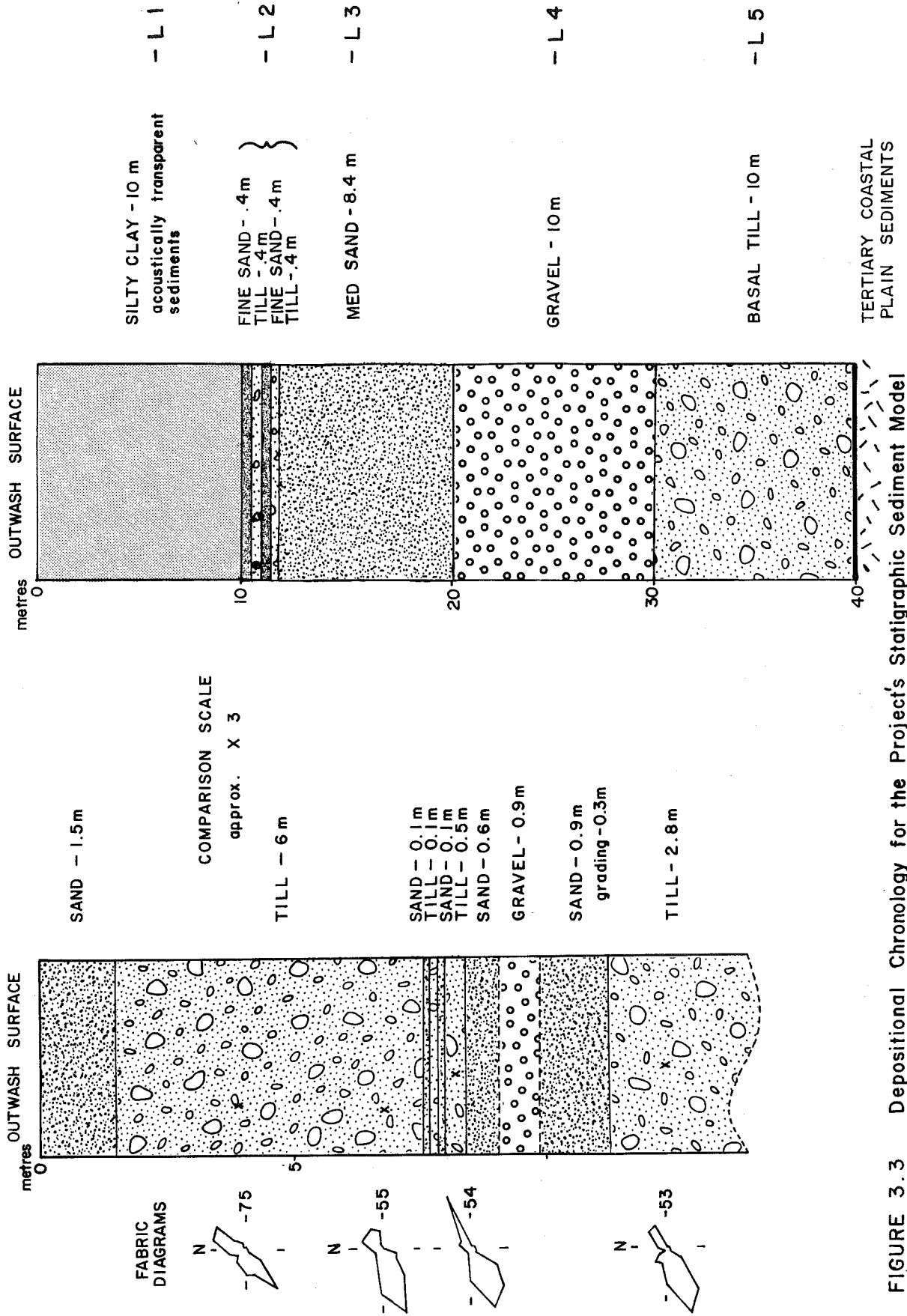


FIGURE 3.3 Depositional Chronology for the Project's Stratigraphic Sediment Model

A performance analysis can now be undertaken for the ASI in relation to this complex multi-layered seabed model. To initiate the evaluation, the following section (Section 3.3) examines the mechanical properties of seafloor sediments and their effect on the acoustic propagation.

3.3 Signal Loss in a Sedimentary Structure

It is not surprising that the prediction of signal loss as sound encounters the seabed is often difficult to quantify when one considers the internal complexity of the mechanical properties of the seafloor sediments, the dynamic regime they exist in and the variable sensitivity of their acoustic properties over minor sediment composition changes. Marine sediments which are predominantly saturated elastic aggregates impregnated by water, have acoustic properties largely influenced by the sediment's particulate size and porosity. One of the more important interactions between these two physical parameters is the resultant forces of attraction or repulsion between the individual sediment grains.

It is well documented by Hamilton (1961, 1970a) Blue and McLeroy (1968), and Anderson (1974) that particulate forces amongst the grains will develop according to their specific size. For example:

- i) Sand-contact friction and interlocking forces
- ii) Silt-contact friction and attractive forces
- iii) Clays (and fine silts) - either attractive forces (London Van der Waals) or repulsive electrostatic forces (the result of absorption of ions from the suspension solution).

Hamilton (1961 and 1970a) further reasons that sand aggregates under the force of gravity would settle on top of other particles (gravity dominant over the other forces) and would form a packed lattice having relatively low water content. The clay or fine silt particles on the other hand would tend to be strongly attracted to the first particles touched. A more open type of structure having a high water content would therefore occur within these finer sediments. (Hamilton, 1961 and 1970a).

As grain size decreases, porosity which can be defined as the ratio of the volume of voids to the total sample volume, increases. The relationship between grain size and porosity however is not a simple one. For instance, such factors as the uniformity of the particulates and their individual shape will affect the actual interstices between the grains. Hamilton et al, (1956); describes the interaction between sediment wet density ρ , the solid constituent or grain density ρ_s , water density ρ_w , and the porosity expressed as a fraction, n , as being:

$$\rho = (1-n)\rho_s + n \rho_w \quad (3.3)$$

From this we can see that wet density varies inversely with porosity between the extremes of no water and 100% water for any given grain density (Hamilton et al, 1956).

The dynamic shear modulus or rigidity of a sediment is also influenced by porosity. Measurements using a torsionally vibrating probe were made on sediments from various marine environments in the

Atlantic and Pacific Oceans. Figures 3.4 and 3.5 relate porosity and rigidity modulus against mean grain size (Anderson 1974). A maximum rigidity is concluded for fine sand, while the coarser sand and fine clays indicate a marked reduction.

Numerous studies have also been made to demonstrate the relationship between sound speed and porosity. In 1940, Wood developed a basic equation for sound speed to demonstrate this relationship:

$$c = \left[\frac{1}{\frac{n}{K_w} + \frac{(1-n)}{K_s} (n\rho_w + (1-n)\rho_s)} \right]^{1/2} \quad (3.4)$$

where n is the fractional porosity and ρ is the density, K is the volume elasticity or bulk modulus and subscripts w and s refer to liquid and solid fractions. Urick (1947) modified this to better fit his low porosity samples by considering rigidity. Later, White and Sengbush (1953) tackled the relationship by incorporating Poisson's ratio and Young's modulus. Others followed suit, Duffy and Mindlin (1957). A time average equation was introduced by Wyllie et al (1956) shortly followed by work done by Nafe and Drake (1957).

Combining Wyllie's time average equation for high porosities and Nafe and Drake's equation for low porosities a reasonable fit with actual data was noted. The resultant equation, suggested by Nafe and Drake (1957), substituted a pressure for a volume average. This provided a better accord across the porosity range. A rigidity term in the form of a volume fraction was supplemented in Shumway's (1958)

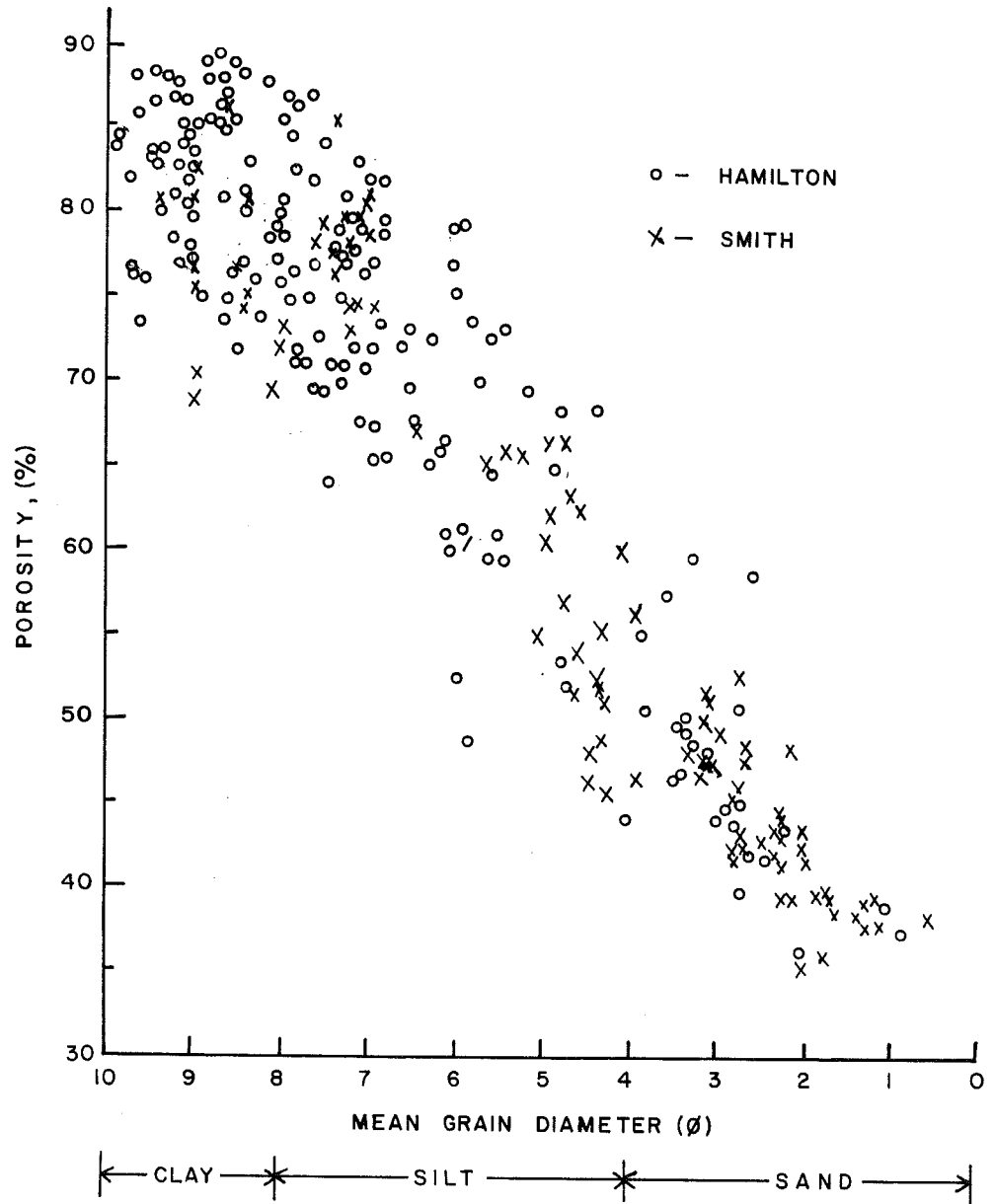


FIGURE 3.4 Porosity versus Mean Grain Size
(after Anderson, 1974)

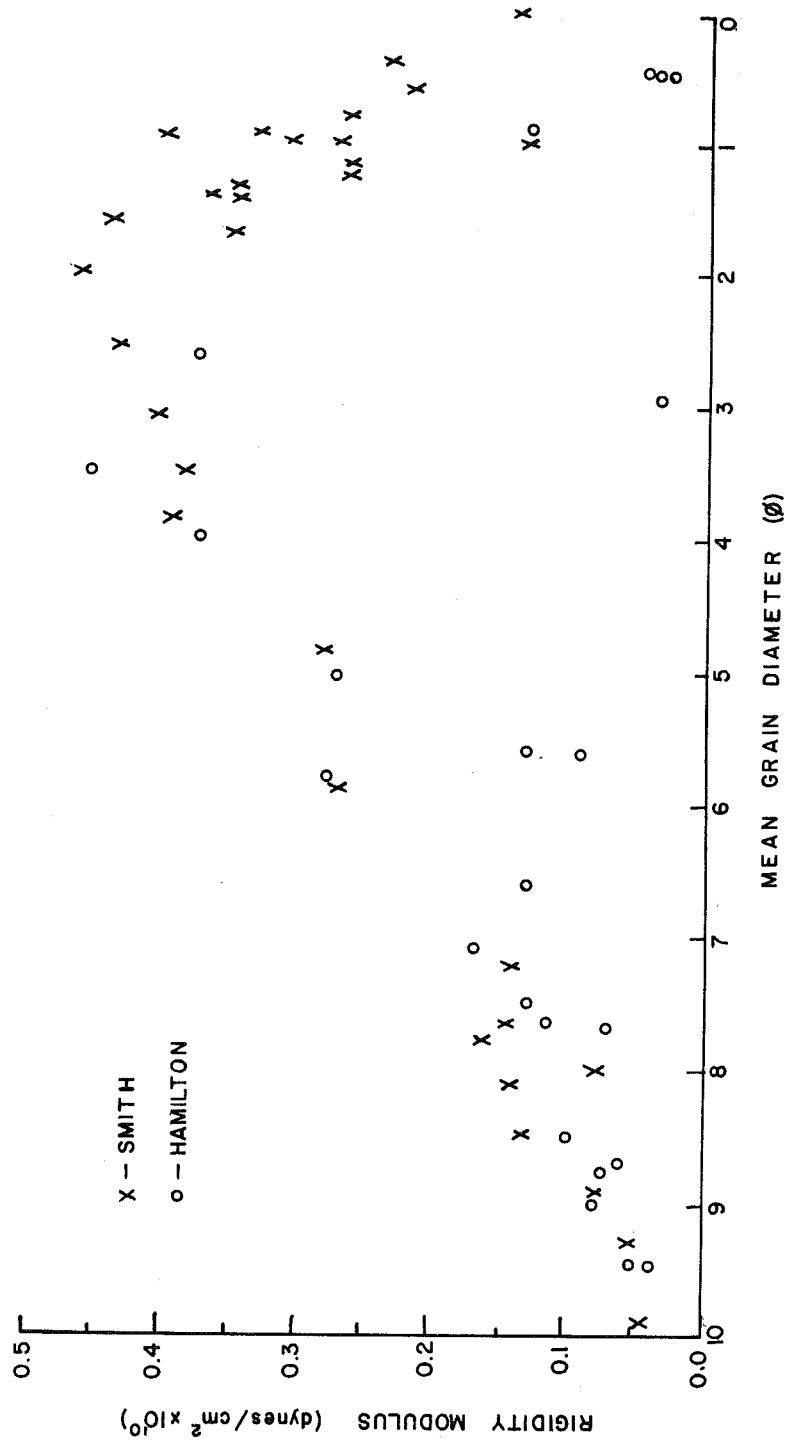


FIGURE 3.5 Rigidity Modulus versus Mean Grain Size
 (after Anderson, 1974)

investigation. The differences between each author's approach can be seen in the illustration of Sound Speed versus Porosity - by Simpkin (1975). (Figure 3.6)

Hamilton (1956) and McCann, D.M. (1968) have also observed that the relationship between sound speed and wet density is similar to that of sound speed and porosity. By comparing velocities with sediment median diameter, porosity and wet density, Hamilton et al (1956) concluded the following trends:

- i) increase in velocity with an increase in median grain size
- ii) increase in velocity as the porosity decreases
- iii) increase in velocity with an increase in density

Therefore, we can conclude that the interrelationships of porosity with median diameter and density, control the sound velocity in a given sediment. In addition, the intergrain structure and mineral composition of the sediment will also be a factor to consider. The synergetic effect of all these properties on the sediment's elastic structure will derive the final sound speed.

The transmitted energy will also undergo some form of attenuation and redistribution as the propagating sound wave encounters the seabed's water/sediment interface and enters into the sedimentary structure. A combination of absorption, of reflection and of scattering will take place.

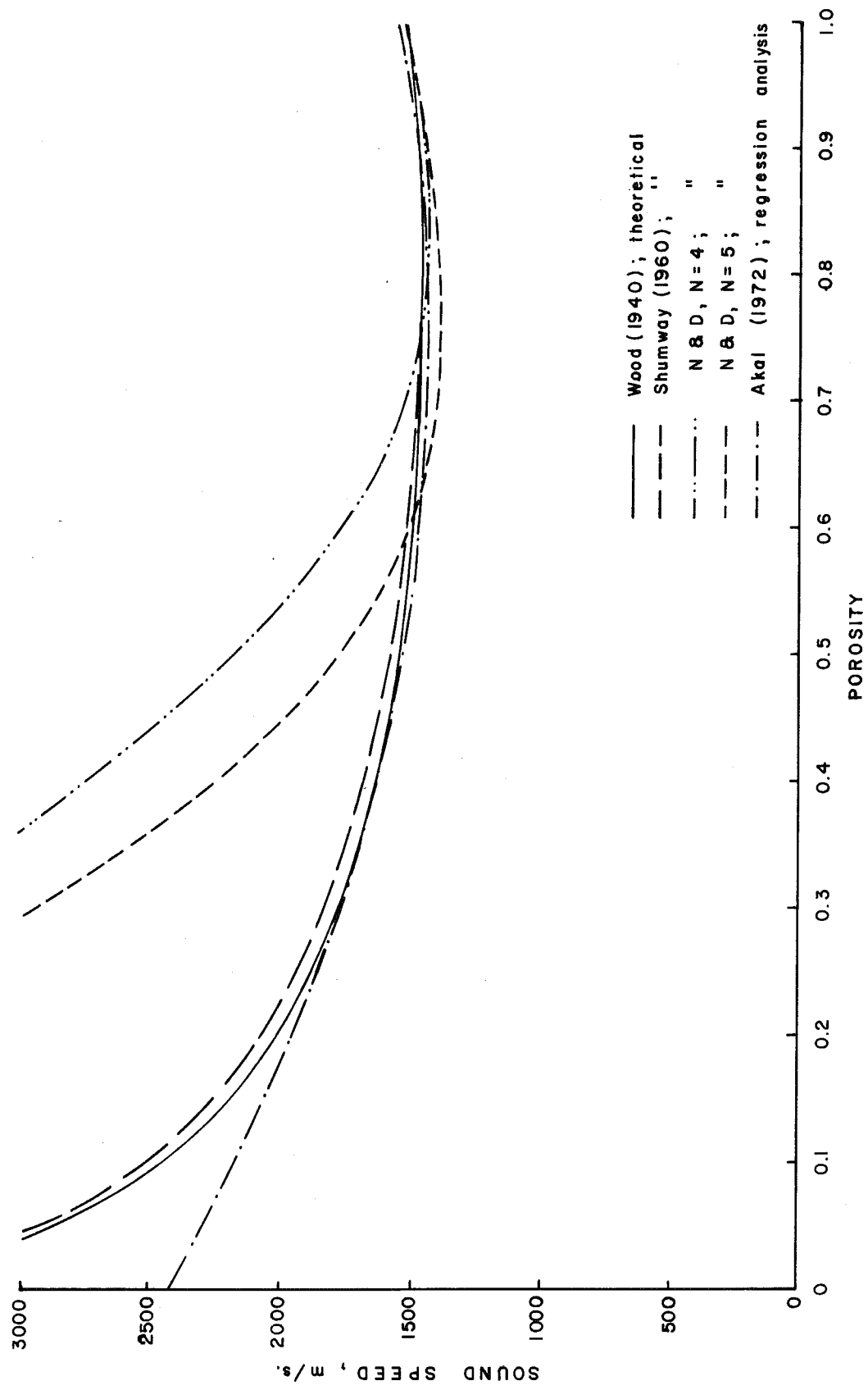


FIGURE 3.6 Sound Speed - Porosity Relationships. (after Simpkin, 1975)

3.3.1 Absorption

A small conversion of acoustic energy into heat will eventuate as an acoustic signal propagates in a medium. This process of absorption is not attributed to scattering, to refraction or to other forms of attenuation but rather to the effects of the medium's shear viscosity and ionic relaxation (Urlick 1975).

For instance we can express absorption by examining the intensity of a plane wave passing through an absorbing medium. Consider the following case: (from Urlick 1975):

$$\frac{dI}{I} = -n dx \quad (3.5)$$

where I is the intensity at some distance having a range, R_1 ; dI is the loss of intensity in travelling a small distance, dx , having a range R_2 ; n is a proportional constant with a minus sign to indicate a negative change of intensity at dI . Upon integration between the two ranges, we find the relationship between the two intensities to be:

$$I_2 = I_1 e^{-n(R_2 - R_1)} \quad (3.6)$$

Applying 10 times the logarithm to the base 10 to expression (3.6) we find:

$$10 \log I_2 - 10 \log I_1 = 10n(R_2 - R_1) \log e \quad (3.7)$$

If we substitute $\alpha = 10n \log e$, we can now obtain a change of level between R_2 and R_1 as expressed below:

$$10 \log I_2 - 10 \log I_1 = \alpha(R_2 - R_1) \quad (3.8)$$

or in other words,

$$\alpha = \frac{10 \log I_1 - 10 \log I_2}{R_2 - R_1} \quad (3.9)$$

Therefore expression (3.9) establishes the logarithmic Absorption Coefficient in decibels per metre (dB/m). For each metre travelled the intensity is diminished through absorption by α dB.

The frequency dependency of sound attenuation in water has been extensively studied and is generally supported by investigators such as Schulkin and Marsh (1962, 1963) although adjusted to best fit their data.

As the wave propagates into the sediment medium the Absorption Coefficient, α , would be affected by the physical aspects of the sediment such as porosity, particle shape and grain size. The literature contains numerous models relating to measured attenuation data and to various energy loss processes. However, it was Urick (1948) that established an attenuation relationship which would account for the viscous loss due to relative velocity between the sediment particles and the suspending fluid. His early work can be reliably used if the sediment has a high porosity and is fine enough in grain

size to be held in suspension. In the case where the grain to grain contact of larger particles is a dominant process (i.e. solid friction), Rayleigh scattering and volume resonance effects may also have to be considered. However, Nolle et al (1963) have indicated that losses due to Rayleigh scattering are very minor for sediments of mean diameter less than 0 phi (ϕ) at frequencies below 1 MHz.

Urlick's (1948) equation for the attenuation of compressional waves can be expressed as:

$$2 \alpha = C' K (\sigma-1)^2 \frac{S}{\{S^2 + (\sigma + r^2)\}} \quad (3.10)$$

where C' is the volume concentration of particles, K is the wavenumber (ω/c); σ is the density of the particles divided by the density of the suspending fluid; S is equal to

$$\left[\frac{9}{4a \sqrt{\omega/2\mu}} \cdot 1 + \left(\frac{1}{a \sqrt{\omega/2\mu}} \right) \right]; \tau \text{ is equal to } 0.5 + \frac{9}{4 a \sqrt{\omega/2\mu}} ;$$

a is the particle radius; μ is the kinematic viscosity of the fluid; ω is the angular frequency; and c is the velocity of compressional waves through the suspension. In McCann and McCann (1969 and 1970) work, Urlick's (1948) theoretical Absorption Coefficient was altered to accept relative velocities of the particles and fluid. While good agreement was found when applied to Hampton (1967) data, the Absorption Coefficients for Shumway's (1960) sands were found to be slightly lower than what had been predicted. From this they concluded that the attenuation in a given sediment is primarily due to the viscous losses

at the surface of the non-surface active particles (McCann and McCann 1969). However, the slightly lower attenuation values in Shumway's (1960) measurements infers that another process becomes involved when the concentration of surface-active particles becomes so small that they can no longer form a lattice. Therefore, solid-friction and viscous losses will have to be considered when the sediment consists of non-surface active sand and silt particles in contact with clay particles in the interstitial spaces.

Biot (1956a and b) demonstrated theoretically that the viscous loss in a fluid saturated porous solid where the elastic moduli of the solid, the matrix and the fluid are assessed, is proportional to $f^{1/2}$ for sediments with mean diameters in the range 1 phi (ϕ) to 6 phi (ϕ). McCann and McCann (1969) summed together a viscous term and a solid-friction term into the following Attenuation Coefficient with frequency predicted for sediments of mean diameter greater than 6 phi (ϕ).

$$2 \alpha = K_1 f^1 + K_2 f^N \quad (3.11)$$

(where K_1 and K_2 are constants).

Although no known relationship is available to calculate $K_1 f^1$ it was meant to account for an inter-granular loss. The value of the exponent of the frequency, N , is considered by McCann and McCann to be crucial to the expression of the processes involved in the signal losses within the sediment.

Applying this to two sets of experimental results, Nolle et al (1963) derived for sand sized sediments

$$2 \alpha = 3.7 \times 10^{-7} \left(\frac{\omega}{a}\right)^{1/2} \text{ cm}^{-1} \quad (3.12)$$

where ω is the angular frequency and a is the mean grain diameter. A further study by Nolle on the assumption that the sand matrix had no elastic strength and using an experimentally determined structure, produced

$$2 \alpha = 3.1 \times 10^{-7} \left(\frac{\omega}{a}\right)^{1/2} \text{ cm}^{-1} \quad (3.13)$$

McCann and McCann (1969) derived the same equation as (3.12) without accounting for flow resistance and structural constants by applying equation (3.11). After further comparison between measured variations of Attenuation Coefficient with frequency, with the variations calculated in expression (3.12), they concluded that solid friction is the dominant process in the attenuation of compressional waves in sediments of mean diameter greater than 6 phi (ϕ) and that the viscous component is rather small (McCann and McCann 1969).

The relationship between the geotechnical properties and the exponent of frequency, N , is not clearly explainable since the intergranular friction as applied to porous sediments is not precisely known. Consequently a very wide range of measured values have been reported in the literature for N . For instance, Shirmer (1970) gives a measured N value of 2.3 while Hampton (1967) reports an N value of 1.37

for a sediment having a 37% volume concentration of kaolinite. As referenced to earlier, Nolle (1963) indicated a N-value of .5 for his sands which tended to range in size from 0.7 phi (ϕ) to 3.2 phi (ϕ) (corresponding to a frequency range of 200 kHz to 1 MHz). There are other contradictions seen such as between the results of Stolle and Bryan (1970) and Hamilton (1972), where the first concludes that viscous loss is dominant in sand at 1 kHz while the latter contends his data for N varied close to 1.

Since marine geophysical profiling tends to involve the lower frequencies (less than 10 kHz), then Hamilton's arguments which strongly suggest that N is approximately unity for all sediments can be considered reasonable. By emphasizing the constant K in

$$\alpha = Kf^N \quad (3.14)$$

and the two key physical properties of the sediment, porosity and mean grain size; he claims the attenuation for any type of sediment can be estimated providing N is unity. (Refer to Figure 3.7).

In the context of our study, Hamilton's 1972 relationship should be valid for the wide range of sediments that are examined (refer to Figure 3.3). Nevertheless, the prediction of attenuation based on other authors' work clearly suggest that such approaches are not always effective.

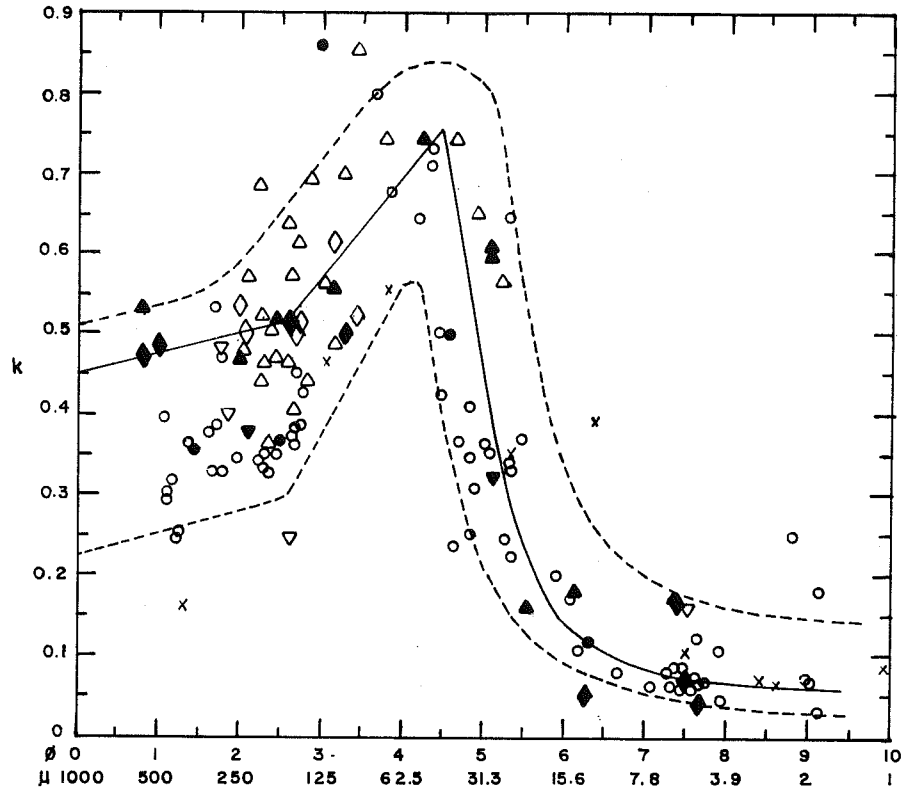


FIG. 3.7a Mean Grain Size versus k

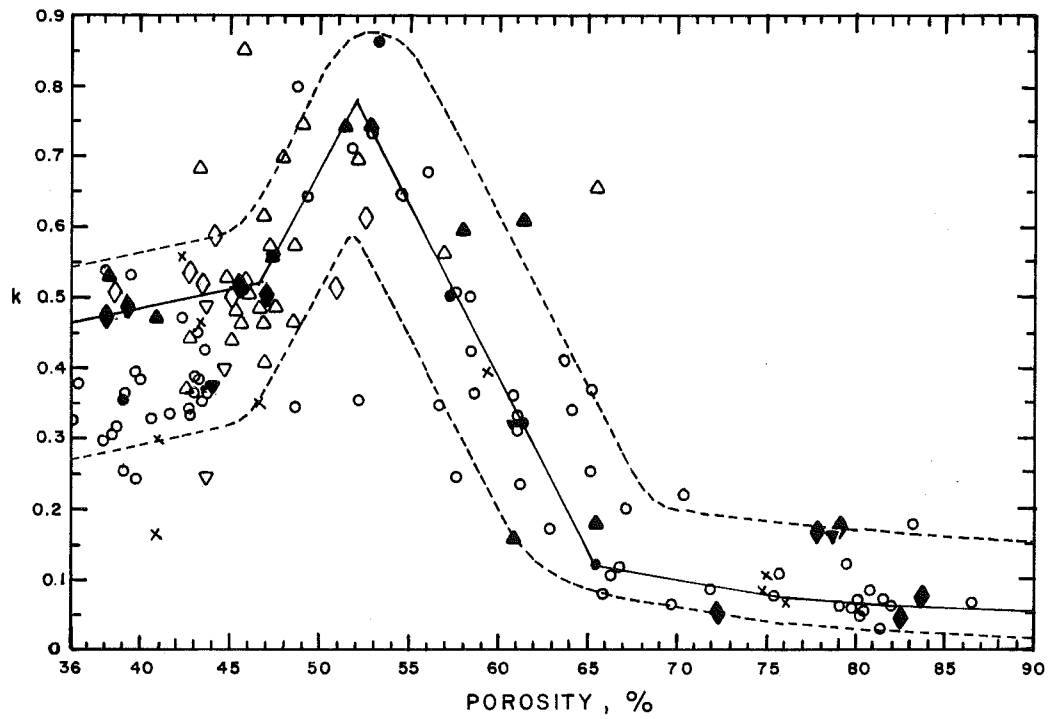


FIG. 3.7b Porosity n . versus k

FIGURE 3.7 Mean Grain Size and Porosity versus k in $\alpha = kf^1$
(after Hamilton, 1972)

3.3.2 Reflection

The amount of energy reflected when sound passes from the water medium into the upper seafloor sediment then into a second sediment type of greater impedance, is largely determined by impedance differences (Kinsler and Frey 1962). The impedance of a medium can be defined by its product of density ρ and velocity c . In seismic profiling, the strength of a reflector, which is determined by the mismatch between the two media impedance is a fundamental parameter in the interpretation. For example, Figure 3.8 illustrates two interpreted orthogonal profiles collected in the Davis Strait (Guigne 1984 in preparation). They demonstrate the terminating influence a strong impedance mismatch between two media may have on a seismic recording. Concordant with the adjacent areas in the Davis Strait, the upper layer is composed of a late Pleistocene or post-Pleistocene type of sedimentary deposit (i.e. silts/clays and fine sands). The second unit is interpreted to be Tertiary Coastal Plain Sediments. Because of the sharp impedance change between the surface sediments and Horizon "A" reflector, little penetration of the signal below this horizon can be interpreted. This high level of reflection as seen off this interface emphasizes the smoothness and hardness of the lower layer. This would suggest that this Tertiary structure is a hard consolidated cap.

Ewing et al, (1957); Officer, (1958); Kinsler and Frey, (1962) and much earlier researchers, derived reflection models for simple harmonic plane waves incident on a plane boundary between two fluids where velocities and densities changed. Examining the case of normal

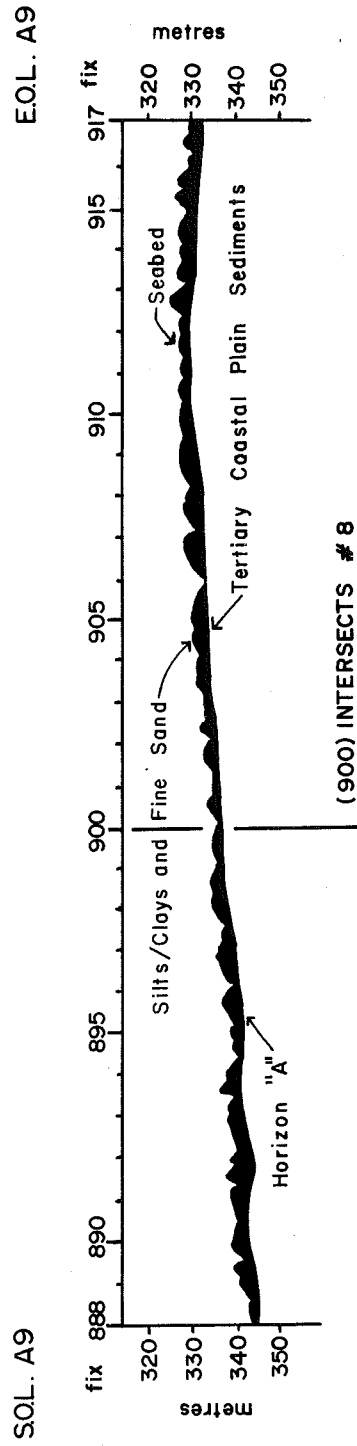
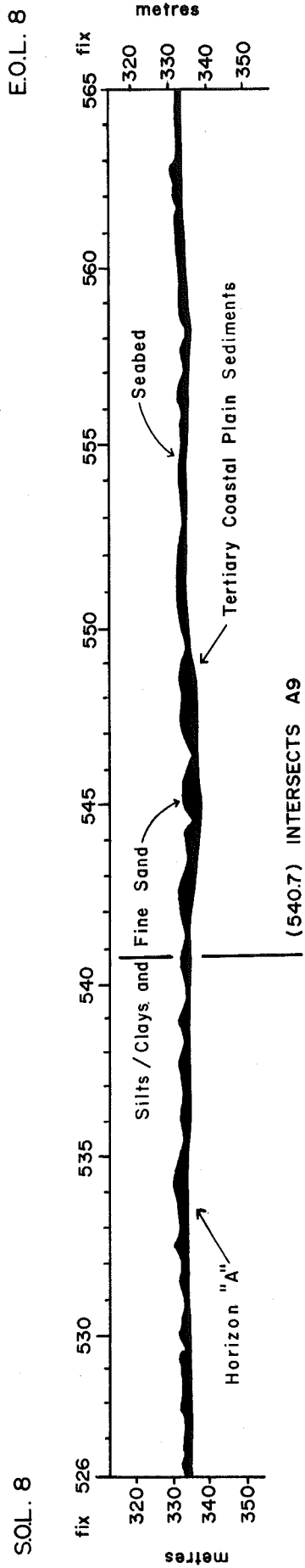


FIGURE 3.8 Interpreted Seismic Profiles, 1982 Raleigh Site, Davis Strait.
(after Guigné, 1983, in press)

incidence where the angle of incidence $i = 0$, the ratio of reflected energy in the compressional wave E_r to the incident energy E_i is:

(after Dobrin 1976)

$$\frac{E_r}{E_i} /_{i=0} = \frac{(\rho_2 c_{p2} - \rho_1 c_{p1})^2}{(\rho_2 c_{p2} + \rho_1 c_{p1})^2} \quad (3.15)$$

where c_{p1} and c_{p2} represent compressional velocities of two elastic media with respective densities of ρ_1 and ρ_2 .

Taking the square root of this ratio will express the relative amplitude of the reflected and incident waves. This ratio is referred to as the Reflection Coefficient .

$$R' = \frac{\rho_2 c_{p2} - \rho_1 c_{p1}}{\rho_2 c_{p2} + \rho_1 c_{p1}} \quad (3.16)$$

For the case where the angle of incidence is not normal ($i \neq 0$) the following expression can be used: (for all angles).

$$R' = (R'_2/R'_1 - Y) / (R'_2/R'_1 + Y) \quad (3.17)$$

where

$$Y^2 = (c_1^2/c_2^2) - \sin^2(i) (1 - \sin^2(i)) \quad (3.18)$$

and R'_1 and R'_2 are the acoustic impedances of layer 1 and layer 2.

($\rho_1 c_{p1}$ and $\rho_2 c_{p2}$).

Hamilton (1956); Buchan et al (1972); Taylor Smith (1968); illustrated the relationship between acoustic impedance and wet density, with porosity. From these relationships a Bottom Loss, BL, of a plane wave at normal incidence to the seabed could be predicted.

$$BL = 20 \log \frac{R'_2 + R'_1}{R'_2 - R'_1} \text{ (expressed in dB)} \quad (3.19)$$

Hamilton (1970 b) computed Reflection Coefficients and Bottom Losses for various sediments in relation to water impedances (refer to Figure 3.9). These Bottom Losses can be explained by considering that some energy can be lost if part of the compressional waves at the layer boundary is converted into shear waves. However, it should be noted that most of the incident wave energy does pass through natural acoustic discontinuities (Van Overeem 1977).

Examples of expected Reflection Coefficients for different sediments and rock types are reproduced below

A. Transition from water to sediment or bedrock

water →	granite	$R' = 0.7$
water →	limestone	$R' = 0.5$
water →	sand	$R' = 0.3 - 0.4$
water →	clay/silt	$R' = 0.2 - 0.1$
water →	mud	$R' = 0.05 - 0.1$

Environment sediment type	ρ^C_p		R^l		BL	
	Ave.	SE	Ave.	SE	Ave.	SE
<u>Continental Terrace (Shelf and Slope)</u>						
Sand:						
- Coarse	3.7347	-	0.4098	-	7.8	-
- Fine	3.4433	0.040	0.3749	0.005	8.6	0.12
- Very fine	3.2645	-	0.3517	-	9.1	-
Silty sand	3.0633	0.050	0.3228	0.008	9.9	0.20
Sandy silt	2.4201	-	0.2136	-	13.5	-
Sand-silt-clay	2.4939	0.059	0.2504	0.010	12.1	0.36
Clayey silt	2.1989	0.026	0.1767	0.012	15.2	0.66
Silty clay	2.1571	0.024	0.1586	0.005	16.1	0.29
<u>Abyssal Plain (Turbidite)</u>						
Sandy silt	2.6795	-	0.2627	-	16.6	-
Silt	2.6111	-	0.2208	-	12.0	-
Clayey silt	2.1154	0.048	0.1506	0.011	16.7	0.76
Silty clay	1.8919	0.014	0.0944	0.004	20.7	0.32
Clay	1.8911	-	0.0941	-	20.6	-
<u>Abyssal Hill (Pelagic)</u>						
Clayey silt	2.1615	-	0.1596	-	15.9	-
Silty clay	2.0674	0.021	0.1412	0.005	17.2	0.31
Clay	2.1118	0.035	0.1477	0.008	16.7	0.54

Notes: Laboratory values 23°C, 1 atmosphere.

ρ^C_p = sediment impedance, gm/cm² sec X 10⁴;

R^l = Rayleigh reflection coefficient;

BL = bottom loss (db);

SE = standard error of the mean

FIGURE 3.9 Sediment Impedance, Reflection Coefficient, and Bottom Loss at Normal Incidence. (after Hamilton, 1970b)

B. Transition from one soil type to another medium

mud →	clay/silt	$R' = 0.1$
clay →	sand	$R' = 0.1$
sand →	limestone	$R' = 0.2$
clay →	limestone	$R' = 0.3$
sand →	granite	$R' = 0.4$

(from Van Overeem, 1977)

Contrary to the frequency dependence attributed to absorption, the Reflection Coefficient is generally assumed to be frequency independent for plane and spherical waves.

3.3.3 Scattering

Boulders and cobbles embedded in a till matrix will reradiate a portion of the acoustic energy incident upon them. This reradiation of sound is called scattering and the sum total of the scattering contributions from all the scatterers is called reverberation (Urlick, 1975). The Total Scattering Cross Section, σ_s , which is defined by Clay and Medwin (1977) as the cross section of a body that is implied by the total power it scatters over all angles, may be larger or smaller than the Geometrical Cross-Section (depending on the frequency). Clay and Medwin (1977) suggest that the concept of Total Scattering Cross Section would be a useful parameter to establish the scatter from a distribution of omnidirectional scatterers and to

calculate Transmission Loss due to scatter. This can be stated by their equation:

$$\sigma_s = \frac{\pi_s}{I_p} = \frac{\int_{4\pi} I_s R^2 d\Omega}{I_p} = \int_{\sigma} \Gamma A d\Omega \quad (3.20)$$

- where:
- π_s is the total power scattered over all angles;
 - $d\Omega$ is the increment of solid angle;
 - I_p is the intensity of the incident sound signal at the scatterer;
 - I_s is the intensity of the signal scattered to the receiver;
 - R is the distance from the scatterer to the receiver;
 - A is the cross section of the projected area of the scatterer viewed from the source;
 - and Γ is the scattering body. This is a complex function involving angle, sound frequency and dimensions of the object. (Clay and Medwin (1977))

In the case where the intensity of the signal scattered to the receiver, I_s is independent of angle, the equation will integrate into:

$$\sigma_s = \frac{4\pi R^2 I_s}{I_p} \quad (3.21)$$

Since some absorption of energy will take place in the object, the derivation of that amount can be illustrated by computing the Absorption Cross Section; σ_a :

$$\sigma_a = \frac{\Pi_a}{I_p} \quad (3.22)$$

where Π_a would represent the sound power absorbed. The extinguished power which results is seen as:

$$\Pi_e = \Pi_s + \Pi_a \quad (3.23)$$

while the Extinction Cross Section, σ_e , of the body is:

$$\sigma_e = \sigma_s + \sigma_a \quad (3.24)$$

The scattering of sound in the direction $\theta = 180^\circ$, $\phi = 0^\circ$ is called backscattering, while the scatter that is oriented $\theta_p = 0$, $\phi_p = 180^\circ$ is referred to as forward scattering (where (θ, ϕ) and (θ_p, ϕ_p) are the spherical coordinates of the scattered sound and of the incident sound). Thus the Backscattering Cross Section, σ_{bs} , can be defined as:

$$\sigma_{bs} = \Gamma_{bs} A = \frac{I_{bs} R^2}{I_p} = \frac{(P_{bs})^2 R^2}{P_p} \quad (3.25)$$

where the subscript (bs) refers to backscattering and P_{bs} is the backscattered pressure at the receiver and P_p is the pressure at the scatterer.

Assuming the scatter to be omnidirectional, the Total Scattering Cross Section σ_s , can be defined by:

$$\sigma_s = \sigma_{bs} 4\pi \quad (3.26)$$

The use of Target Strength TS in the sonar equation is a convenient way to express the level of backscatter in decibels. Clay and Medwin (1977) combine (3.25) with (3.27)

$$TS = 10 \log_{10} \frac{A\Gamma_{bs}}{A_1} = 10 \log_{10} \frac{\sigma_{bs}}{A_1} \text{ dB re } A_1 \quad (3.27)$$

which produces an operational definition of TS:

$$TS = 10 \log_{10} \frac{I_{bs} R^2}{I_p R_1^2} = 10 \log_{10} \frac{(P_{bs} R)^2}{P_p R_1^2} \text{ (in dB)} \quad (3.28)$$

Assuming no Absorption Loss, they equated P_p in terms of the source pressure P_o at a reference range R_o ,

$$P_p^2 = \frac{P_o^2 R_o^2}{R^2} \quad (3.29)$$

therefore

$$TS = 10 \log_{10} \left(\frac{P_{bs}}{P_o} \right)^2 \frac{R^4}{R_o^2 R_1^2} \text{ (in dB)} \quad (3.30)$$

Changing the pressure into decibel notation

$$TS = SPL_{bs} - SL + 2TL \text{ (in dB)} \quad (3.31)$$

where SPL_{bs} is $20 \log_{10} (P_{bs}/P_r)$; SL is $20 \log_{10} (P_o/P_r)$; P_r is the reference pressure ($1 \mu \text{ pa}$); and TL is a one way transmission loss.

Urick (1975) describes volume reverberation as the reverberation produced by scatterers uniformly distributed over a volume (Figure 3.10 b) and surface reverberation as the reverberation produced by scatterers distributed over a nearly plane surface (Figure 3.10 a). For a volume, the equivalent plane-wave reverberation RL_v is:

$$RL_v = SL - 40 \log R + S_v + \log V \quad (3.32)$$

where V is $c\tau r^2$, SL is the projector source level, SL is $10 \log \frac{\text{intensity of source}}{\text{reference intensity}}$; R is the range, and S_v is the backscattering strength for volume reverberation.

The scattering strength for a volume is defined as $10 \log$ of the ratio of the scattered intensity produced by 1 m^3 of scattering volume respective to the incident intensity (Urick 1975). Since the scattered intensity is referred to a distance of 1 metre from the unit volume in the direction back toward the source of sound, then the Scattering Strength and the Target Strength of the target (e.g. boulders) are the same. In other words Scattering Strength is the Target Strength for scattering of a unit volume or area.

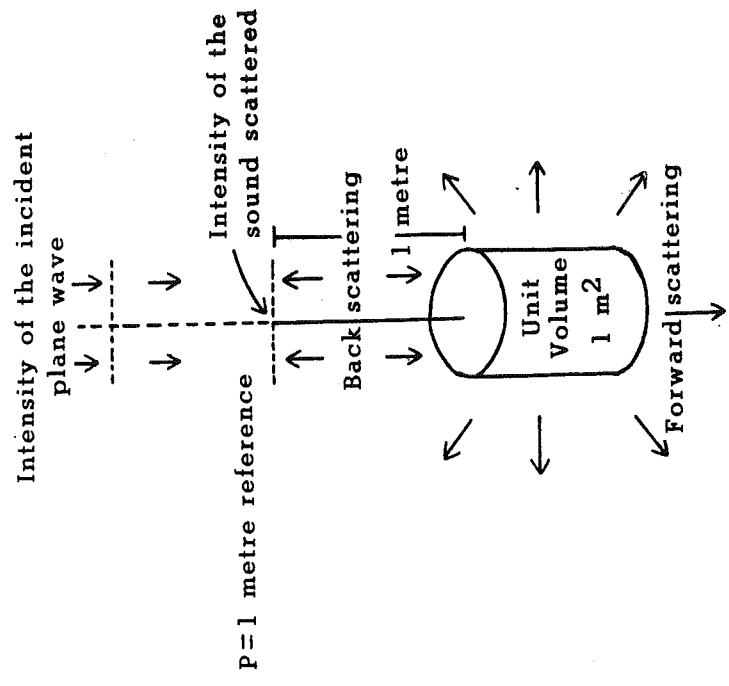


Figure 3.10a Surface Scattering

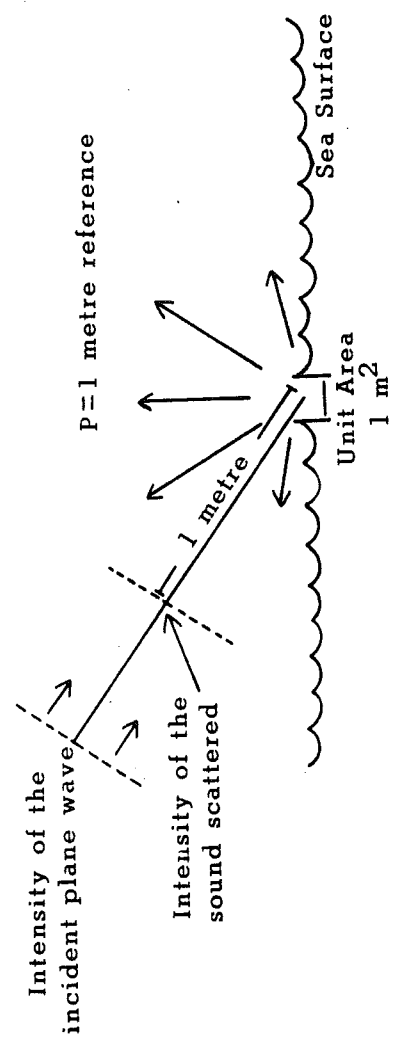


Figure 3.10b Volume Scattering

$$\text{Scattering Strength} =$$

$$10 \log \frac{\text{Intensity of the sound scattered}}{\text{Intensity of the incident plane wave}}$$

FIGURE 3.10 Conceptual Illustration of Scattering.

3.4 Analytical Appraisal of a Terminated Parametric Source in Reference to a Conventional System

A theoretical appraisal is now attempted. Design guidelines for a potential "Acoustic Sub-seabed Interrogator" prototype will develop from this study. The performance of a Parametric Array and of a Conventional Monostatic Transducer is determined in reference to the sediment model established in Section 3.2 and to the signal loss theory stated in Section 3.3.

The first evaluation, Section 3.4.1, estimates the total two-way signal loss in the sediment by quantifying the transmission loss factors that would affect the propagation of the signal. As sound is radiated into the sediment column a certain portion of its energy is lost to absorption and to spherical spreading. The second evaluation appraises the Source Level of both projector systems after optimizing their physical parameters (see Section 3.4.2). This is followed by a detailed modelling of pressure, of centre frequency and of bandwidth that would be associated with signals returning from layers at any depth in the sediment model and then received by a hydrophone near or at the seabed.

A temporal resolution evaluation is performed in Section 3.4.4 of the outgoing pulse using the findings of Section 3.4.3. The small scale fine sand/till stratigraphy noted in Layer 2 does not have boulders in its matrix but rather its composition is of a gravelly sand till (refer to Figure 3.3). Such a grain size distribution is quite

pertinent to our analysis since it is typical of the marine tills found in Conception Bay, Newfoundland. The temporal resolution at the Layer 2 depth will predict what type of signal interaction will occur within the layer's individual sand/till strata and if the detection of each thin section is possible.

In the evaluation of the Signal-to-Noise Ratio, Section 3.4.5, the radiated sound will reach the Tertiary bedrock fragment and reflect back to the transducer. The Echo Level, (EL) received at the hydrophone will mirror the very high Absorption Coefficient of the Basal Till, thus accounting for a highly rigid structure of low porosity. Scattering by the boulders/cobbles in Layer 5 is specifically addressed in the Signal-to-Reverberation Ratio computations (see Section 3.4.6). The Reverberation Target Strength (TSR) includes the incoherent addition of these reverberating elements (i.e. boulders and cobbles) within the spatial resolution confines of the glacial material as defined by the range resolution of the transmitted pulse.

The assumptions and terminology used in the following set of evaluations are summarized below by layer and are illustrated in Figure 3.11:

Water Column

- i) Height above the seabottom (z) -- 8.5 metres
- ii) Velocity of Sound (c_w) -- 1500 m/sec
- iii) Density (ρ_w) -- 1000 kg/m³

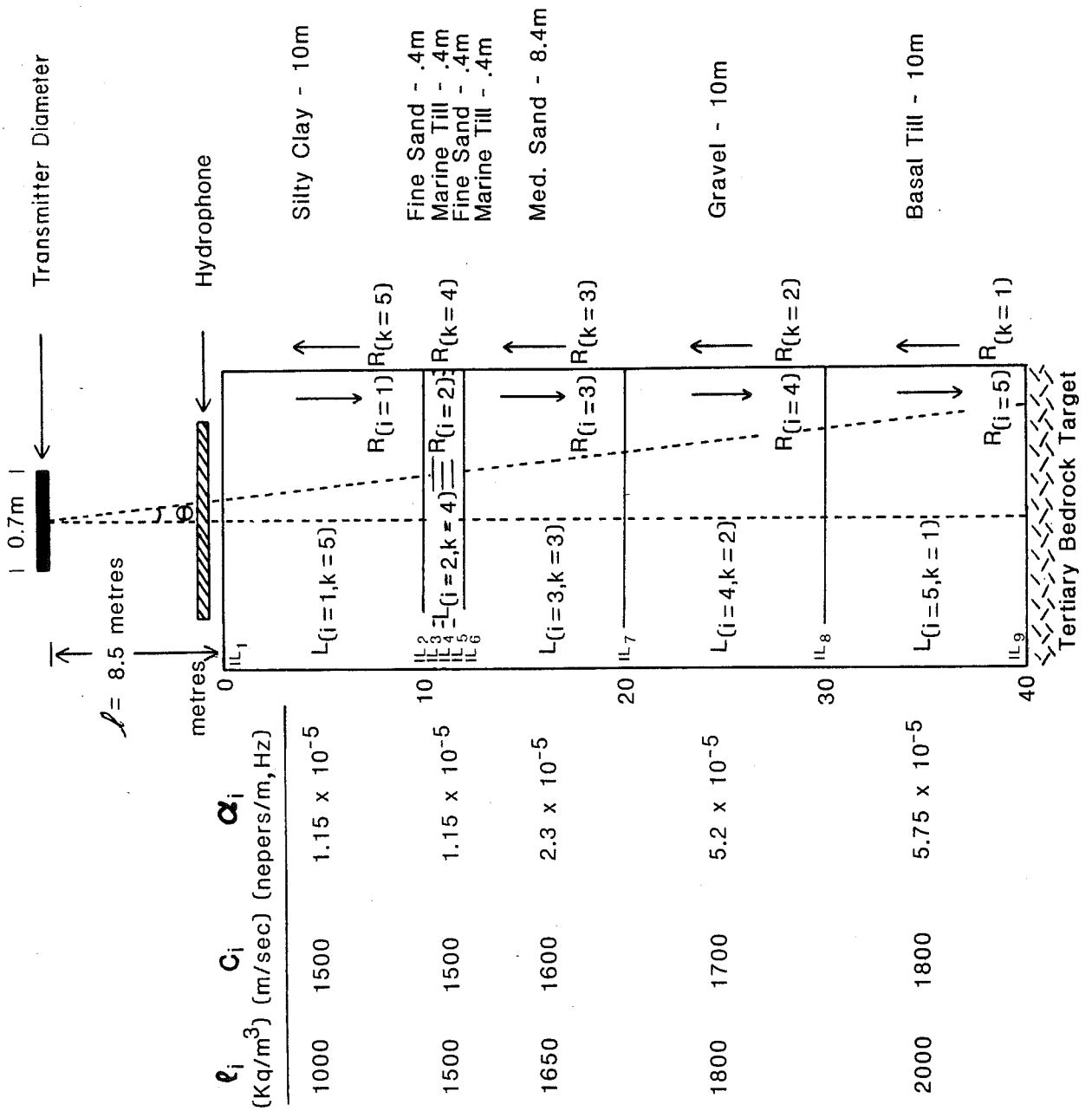


FIGURE 3.11 Stratigraphic Model Reference and Terminology.

Layer 1 - Silty Clay

i) Sediment thickness (R_1)	-- 10 metres
ii) Velocity of Sound (c_1)	-- 1500 m/sec
iii) Density (ρ_1)	-- 1500 kg/m ³
iv) Porosity (n)	-- 70%
v) Absorption Coefficient (α_1')	-- .1 (dB/m kHz)

Layer 2 - Multi-layer: Fine Sand/Till

i) Sediment Thickness (R_2)	-- 1.6 metres
ii) Velocity of Sound (c_2)	-- 1500 m/sec
iii) Density (ρ_2)	-- 1500 kg/m ³
iv) Porosity (n)	-- 70%
v) Absorption Coefficient (α_2')	-- .1 (dB/m kHz)

Layer 3 - Medium Sand

i) Sediment Thickness (R_3)	-- 8.4 metres
ii) Velocity of Sound (c_3)	-- 1600 m/sec
iii) Density (ρ_3)	-- 1650 km/m ³
iv) Porosity (n)	-- 60 - 65%
v) Absorption Coefficient (α_3')	-- .2 (dB/m kHz)

Layer 4 - Gravel

i) Sediment Thickness (R_4)	-- 10 metres
ii) Velocity of Sound (c_4)	-- 1700 m/sec
iii) Density (ρ_4)	-- 1800 kg/m ³
iv) Porosity (n)	-- 36%
v) Absorption Coefficient (α'_4)	-- .45 (dB/m kHz)

Layer 5 - Basal Till

i) Sediment Thickness (R_5)	-- 10 metres
ii) Velocity of Sound (c_5)	-- 1800 m/sec
iii) Density (ρ_5)	-- 2000 kg/m ³
iv) Porosity (n)	-- < 35%
v) Absorption Coefficient (α'_5)	-- .5 (dB/m kHz)

3.4.1 Evaluation of Signal Loss in the Sediment Model

To calculate the two way Absorption Loss ABS_{2R_i} for the Stratigraphic Model the following equation will be used:*

$$ABS_{2R_i} = 2f[\alpha'_i(R_i - R_{i-1}) + (\bar{\alpha}'_{R_{i-1}} R_{i-1})] \quad (3.33)$$

where α'_i is Hamilton's Absorption Coefficient for the i^{th} layer, R_i

* α' will be dB/m kHz while α will refer to nepers/m hz - the conversion from dB to nepers is $\frac{\alpha'}{8.686}$.

represents the thickness of the absorbing medium calculated as a depth below the seabed summed from 0 to the i^{th} layer, and f is frequency.

$\bar{\alpha}'_{R_{i-1}}$ is the average Attenuation Coefficient to a particular depth defined by R_i . (see Figure 3.11)

The rigidity of the till sediment is estimated. Since rigidity would be expected to be quite large the friction losses will also be considered high. A gradation of values for α'_i is designated to the Stratigraphic Model. These values are specifically allocated in relation to porosity and to mean grain size. For instance:

- i) An attenuation value of 0.1 (dB/m kHz) is assigned to the silt/clay layer assuming a porosity of 70%.
- ii) An attenuation value of 0.2 (dB/m kHz) is assigned to the sand to sand/silt layer assuming a porosity of 60 - 65%.
- iii) An attenuation value of 0.45 (dB/m kHz) is assigned to the coarse sand to gravel layer assuming a porosity of 36%.
- iv) An attenuation value of 0.5 (dB/m kHz) is assigned to the till matrix assuming a composition of cobbles/gravels and stiff clay.

The total 2-way Absorption Loss calculated for the five layers using their respective Absorption Coefficient and sediment thickness is 25dB (24.7 dB) for 1 kHz. (refer to expression 3.33).

The second loss which concerns this study is the geometrical Spreading Loss going down and then back up. Urlick (1975) describes this as a geometrical effect representing the regular weakening of a sound signal as it spreads outwards from the source. The farfield geometrical Spreading Loss can therefore be calculated using

expressions 3.34 and 3.35. This includes the effects of refraction at the various interfaces;

i) Spreading Loss going down:

$$TL_{D_{R_i}} = 20 \log \left[\left(\lambda + \frac{c_{i=1}}{c_w} R_{i=1} + \sum_{i=2}^n \frac{c_i}{c_{i-1}} (R_i - R_{i-1}) \right) \left(\frac{2 \bar{c}_{R_i} \bar{\rho}_{R_i}}{[\bar{c}_{R_i} \bar{\rho}_{R_i} + c_w \rho_w]} \right) \right] \quad (3.34)$$

ii) Spreading Loss going back up:

$$TL_{U_{R_i}} = 20 \log \left[\left(\lambda + \frac{c_w (R_{k=n} - R_{k=n-1})}{c_{k=n}} + \sum_{k=1}^{n-1} \frac{c_{k+1}}{c_k} (R_k - R_{k-1}) \right) \left(\frac{2 c_w \rho_w}{[c_w \rho_w + \bar{c}_{R_k} \bar{\rho}_{R_k}]} \right) \right] \quad (3.35)$$

where \bar{c}_R is the average velocity. R refers to a particular depth below the seabed from 0 to the i^{th} layer or from the base of the last layer k up to the seabed surface. $\bar{\rho}_R$ is the average density as dictated by R_i or R_k . n is the number of layers. (see Figure 3.11).

The losses that were incurred going down to the bedrock and back, due to spreading are calculated by applying expressions (3.34 and 3.35) for a range of transducer heights above the seabed:

\underline{l} (in metres)	\underline{TL}_D (dB)	\underline{TL}_U (dB)
1	34.2	28.7
3	34.6	29.1
5	35.1	29.5
7	35.4	29.9
8.5	35.8	30.2
9	35.9	30.3
10	36.0	30.5

At each χ^{th} interface there is a small loss due to the mismatch of the layer impedances which form each interface (refer to Figure 3.11 which illustrates the interfaces of χ). This loss, called the Interface Loss, IL, can be computed as a function of ρc (density and velocity);

$$IL_{\chi} = 20 \log \left[\frac{4\rho_{\chi-1} c_{\chi-1} \rho_{\chi} c_{\chi}}{(\rho_{\chi-1} c_{\chi-1} + \rho_{\chi} c_{\chi})^2} \right] \quad (3.36)$$

which corresponds to two passages across an interface. (NB: $\rho_o = \rho_w$ and $c_o = c_w$)

The calculated sum of the losses due specifically to the interfaces is very small, eg. $\ll 1$ dB. In the evaluation of Signal-to-Noise Ratio and Signal-to-Reverberation Ratio this loss will therefore not be included. However it becomes a significant loss when

applied to a permafrost type of structure because of the high impedance contrast expected between the overlying sediments and the permafrost.

Finally, a Target Strength is required for the Tertiary bedrock. It is however difficult to evaluate the true nature and strength of a returning echo by an underwater target (the Target Strength "TS"). Part of the problem is in differentiating between the process of scattering from the process of reflection. Although the nature of our sediment model is idealized towards a transmission path composed of very small spheres (e.g. fine sands to gravel where $2\pi a/\lambda \ll 1$), the assumption is made that some boulders and cobbles exist in the Basal Till. The conditions which characterize these larger spheres are:

- i) rather perfect in shape without irregularities, depressions, or protuberances
- ii) rigid or non deformable by the impinging sound beam
- iii) immovable or does not partake of the acoustic motion of the field in which it is embedded and
- iv) large compared to a wavelength, eg. $2\pi a/\lambda \gg 1$

The scattering off these large spheres establishes a Target Strength of Reverberation (TSR) (see Section 3.4.6.1). Since the Tertiary bedrock horizon is envisioned as a flat interface of infinite lateral extent rather than a sphere, then the Target Strength off this plane reflector will incorporate a Reflection Coefficient R' and a range R in its definition.

$$TS = 20 \log(R') + 20 \log(R) - 20 \log (2) \quad (3.37)$$

The component $10 \log\left(\frac{R^2}{4}\right)$ is supported by Urick (1975) for a Target Strength off a flat plane.

3.4.2 Evaluation of Source Level

i) Parametric Source

Since the Parametric Array is directed into the seabed, the seabed will cause a termination of the array. The Source Level calculations therefore will have to account for the condition where the carrier frequency wave associated with the Parametric Array is discontinuously attenuated on passing through a water/sediment interface. Adjusting the source height ℓ above the seabed to produce a termination within the nearfield of the primary, then in the farfield, the Source Level of the difference frequency (i.e. $20 \log P(\omega, l)$ or SL_d) can be stated to be:

$$SL_d = 144.88 - 60 \log c + 40 \log f_d + 20 \log W + 20 \log \ell \quad (3.38)$$

where c is in m/s, f is in Hz, W is in watts, ℓ is in metres and SL_d is in dB re $1 \mu\text{Pa}$. A detailed derivation of expression (3.38) can be found in Appendix B.

The power radiated, the transducer radius and the carrier frequency will also have to be optimized in relation to ℓ in order to attain a maximum Source Level. This means that the shock distance must coincide with the range to the termination and to the carrier

nearfield. For instance, shock is said to have formed at a range

$$R_s = \frac{\rho c^2}{k_c P \beta} \quad (3.39)$$

(or $(k\epsilon\beta)^{-1}$ which can be defined as the Acoustic Mach Number with

$\epsilon = \frac{P}{\rho c^2}$, $k = \frac{2\pi f_c}{c}$ with f_c being the primary frequency, and $\beta = 3.5$ for water)

Since P^2 must equal $\frac{2\rho c W}{\pi a^2}$ with $\frac{W}{\pi a^2} < 10^4$ watts/m² then $P^2 < 2\rho c \cdot 10^4$.

Therefore, taking the equalities

$$\lambda = R_s = \frac{\rho c^3}{2\pi f_c \beta \sqrt{2\rho c} \cdot 10^2} \quad (3.40)$$

which finally reduces to

$$\lambda = \frac{c^2 \sqrt{\rho c} \cdot 10^{-2}}{2\sqrt{2} \pi f_c \beta} \quad (3.41)$$

Assessing the carrier frequency in terms of λ derives:

$$f_c = \frac{c^2 10^{-2} \sqrt{\rho c}}{2\pi\beta\lambda \sqrt{2}} = \frac{885918}{\lambda} \quad (\text{in hertz}) \quad (3.42)$$

The radius a of the transducer can be established in terms of λ , when $\lambda \ll$ the carrier nearfield,

$$a \geq \sqrt{\lambda \lambda c} \quad \text{or} \quad \sqrt{\frac{\lambda c}{f_c}} \quad (3.43)$$

Finally, evaluating W in terms of λ , given that $W = \pi a^2 \cdot 10^4$ watts, defines W as

$$W = \frac{\pi \lambda c 10^4}{886 \cdot 10^3} = \frac{\pi \lambda^2 c 10^4}{886 \cdot 10^3} = 53.19 \lambda^2 \quad (3.44)$$

Thus the maximum Source Level at the difference frequency (f_d) in the farfield of the terminated Parametric Array will become:

$$P(\omega, 1) = \frac{W 4 \pi^2 f_d^2 \lambda \beta}{3 \sqrt{2 \pi}} = 2.765 \cdot 10^{-7} f_d^2 \lambda^3 \quad (3.45)$$

or

$$P(\omega, 1) = \lambda^3 f_d^2 2.765 \cdot 10^{-7} \quad (3.46)$$

Rewriting $P(\omega, 1)$ as SL_d the Source Level then can be expressed in dB re $1 \mu\text{Pa}$:

$$SL_d = -11.17 + 60 \log \lambda + 40 \log f_d \quad (3.47)$$

Presented in tabular form are SL_d values computed for a range of heights and frequencies;

SL_d defined by
Height Above Seabed -(λ in metres) Versus
Difference Frequency -(f_d in Hz)

f _d	λ	1	3	5	7	8.5	9	10
750		103.8	132.5	145.8	154.5	159.6	161.1	163.8
1 k		108.8	137.5	150.8	159.5	164.6	166.1	168.8
2 k		120.9	149.5	162.8	171.6	176.6	178.1	180.9
3 k		127.9	156.5	169.9	178.6	183.7	185.2	187.9
5 k		136.8	165.4	178.7	187.5	192.6	194.0	196.8
7 k		142.6	171.3	184.6	183.3	198.4	199.9	202.6
10 k		148.8	177.5	190.6	199.5	204.6	206.1	208.8
20 k		160.9	189.5	204.8	211.6	216.6	218.1	220.9

$$\text{where } SL_d = -11.17 + 60 \log \lambda + 40 \log f_d$$

(in dB re 1 μPa)

The radius, the carrier frequency and the power for the terminated Parametric Transducer as a function of height above the seabed are noted to be at optimum levels when expressions 3.42, 3.43, 3.44 are in accordance: For example;

<u>λ (in metres)</u>	<u>f_c (in khz)</u>	<u>a (in metres)</u>	<u>W (in watts)</u>
1	885.9	0.04	53.2
3	295.3	0.12	478.7
5	177.2	0.21	1,329.8
7	126.2	0.28	2,606.3
8.5	104.2	0.35	3,843.0
9	98.4	0.37	4,308.4
10	88.6	0.41	5,319.0

These interrelationships are illustrated in Figure 3.12. A height h of greater than 10 metres above the seabed is considered to be a very real practical engineering limit to the stable in-situ positioning of sonar transmitters. Therefore the 10 metre height has been set as a design boundary. A minimum carrier frequency f_c of 100 kHz establishes a second criteria since the difference frequency f_d can inherit the bandwidth of the source at the carrier frequency. For instance, a carrier frequency lower than 100 kHz at a particular Q would tend to provide a bandwidth on the low side (i.e. $\Delta f = \frac{f}{Q}$). As well, the reduced attenuation associated with a lower carrier frequency may make the discrimination of the carrier from the resulting difference frequencies received from the upper layer of the seabed, difficult.

An optimum Source Level can therefore be obtained as the source height approaches 10 metres and does not exceed the lower f_c boundary of 100 kHz. On this basis, a carrier frequency of just over 100 kHz (eq. 104 kHz) was selected for this analysis as a starting point. This designated an optimum, maximum height of 8.5 metres and a transducer radius of 0.35 metres. The matching power output is 3,483 watts (refer to Figure 3.12).

ii) Conventional Transducer

The Source Level for a Conventional Transducer is procured by the following expression:

$$SL = 170.5 + 10 \log W + DI_t \quad (3.48)$$

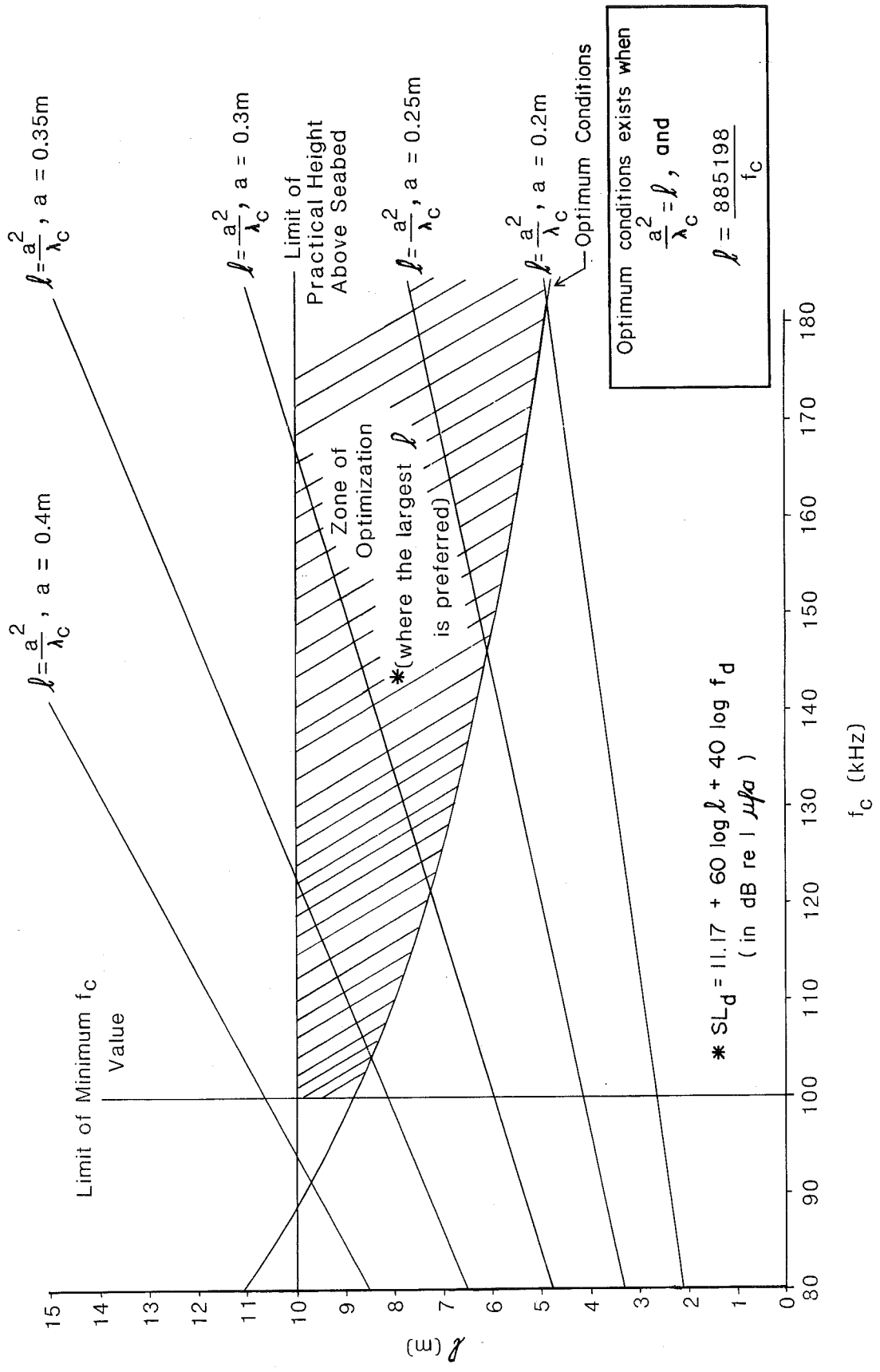


FIGURE 3.12 Optimization of a Terminated Parametric Array.

where W is the acoustic power radiated from the transducer, and DI_t is the transmission Directivity Index. DI_t is equal to $10 \log (\pi D/\lambda)^2$ for a piston of diameter D in an infinite baffle and for a wavelength λ .

Since the maximum amount of acoustic power that can be applied to a Conventional Transducer at frequencies corresponding to the difference frequencies of the Parametric Array is limited by the property of cavitation in the fluid medium, a smaller output of power will be selected for the conventional transmission than was feasible to use at the carrier frequency in the Parametric Array. Urick (1975) expresses the cavitation threshold as a peak pressure in atmospheres or as a plane-wave intensity in watts per square centimeter. When this limit is exceeded by driving the transducer harder, a number of deleterious effects will occur. For example the projector surface will start to erode. There will be a loss of acoustic power due to absorption and to scattering by the resulting cavitation bubble cloud. Likewise the beam pattern of the projector will deteriorate and a reduction in the acoustic impedance into which the projector must operate will occur (Urick 1975). To raise the cavitation threshold, a decrease in pulse duration is necessary. An increase in frequency and an increase in the sounding depth would both allow for more acoustic power to be radiated. With the Parametric Array, transducer cavitation is significantly reduced since the propagation frequencies are high (approx. 100 kHz) and pulse lengths are short. A higher cavitation threshold can therefore be applied to the transducer face. The maximum working power output in watts for the Conventional Source will be restricted by a cavitation threshold intensity of 0.3 W/cm^2 as

opposed to 1.0 W/cm^2 for a Parametric Source (based on cavitation threshold measurements from Flynn (1964) and cross checked against Rusby's studies (1970)).

To calculate the Source Level using expression (3.48) the following assumptions are considered:

- i) the transducer face will have a radius of 0.35 metres (equivalent to the Parametric)
- ii) the acoustic power level applied to the transducer will be 1155 watts (0.3 watts/cm^2 and an area of $3,848.5 \text{ cm}^2$)
- iii) the Directivity Index will be predicted for a piston transducer
- iv) the height above the seabed will be set at 8.5 metres (matching the height selected for the Parametric Array)

Assessing the Source Level (SL) for different frequencies we have:

<u>Frequency (Hz)</u>	<u>DI_t (dB)</u>	<u>SL (dB re 1 μPa @ 1 m)</u>
750	0.8	201.9
1k	3.3	204.4
2k	9.3	210.4
3k	12.9	214.0
5k	17.3	218.4
7k	20.2	221.3
10k	23.3	224.4
20k	29.3	230.4

3.4.3 Evaluation of Pressure, of Centre Frequency, and of Bandwidth beyond the Water/Seabed Interface

The truncation of the Parametric Array coincides with the termination of the water/seabed interface and the nearfield at the carrier frequency. A height above the bottom was established at 8.5 metres by applying expression (3.47) to a Parametric Source. This corresponds to a projector radius of 0.35 metres and to a carrier frequency of 104 kHz. Similarly using expression (3.48) the Source Level for a Conventional Transducer was tallied to match a similar radius and height. The pressure, associated frequencies and bandwidths, can now be rated in terms of the energy that is received at the hydrophones after a signal has propagated through the various layers to the Tertiary bedrock target and back to the surface.

i) Terminated Parametric Array

Assuming the hydrophone to be at or very near the seabed surface, we can model the pressure received as:

$$P = Bf^2 e^{-f\{2[\alpha_i(R_i - R_{i-1}) + (\bar{\alpha}_{R_{i-1}} R_{i-1})]\}} \quad (3.49)$$

where B contains all parameters which are frequency independent and where the factor f^2 comes from the parametric generation. α_i represents the individual Attenuation Coefficient for each layer of the Stratigraphic Model in nepers/m Hz. R_i is the depth below the seabed summed from 0 to the i^{th} layer and $\bar{\alpha}_{R_{i-1}}$ is the average Attenuation

Coefficient to a particular depth defined by R_i . (refer to Figure 3.11).

After substituting A for $2[\alpha_i(R_i - R_{i-1}) + (\bar{\alpha}_{R_{i-1}} R_{i-1})]$, the maximum pressure P_{max} can be calculated at a frequency f_{max} . In order to obtain P_{max} and f_{max} consider $\frac{dp}{df}$ to be set to zero. Differentiating $P = Bf^2 e^{-Af}$ with respect to f will give:

$$\frac{dp}{df} = 2Bfe^{-Af} + Bf^2 e^{-Af}(-A) = 0 \quad (3.50)$$

or

$$2Bfe^{-Af} - ABf^2 e^{-Af} = 0 \text{ which simplifies to}$$

$$Bfe^{-Af} (2-Af) = 0 \quad (3.51)$$

Therefore

$$2 - Af = 0 \quad (3.52)$$

By defining f as f_{max} , expression (3.52) can be rewritten as:

$$f_{max} = 2/A \quad (3.53)$$

Since $P = P_{max}$ when $f = f_{max}$ then substituting $f_{max} = 2/A$ into $P = Bf^2 e^{-Af}$ will define P_{max} as $Bf_{max}^2 e^{-Af_{max}}$. Therefore by substitution:

$$P_{\max} = B \cdot \left(\frac{2}{A}\right)^2 \cdot e^{(-A)} (2/A) \quad (3.54)$$

Finally, P_{\max} can be simplified into

$$P_{\max} = \frac{B4}{A^2} e^{-2} \quad (3.55)$$

If we adjust for the normalized pressure after cancelling out the frequency independent factor B then the bandwidth defined by f_1 and f_2 (at -3dB) can be reckoned with. Normalizing the pressure gives

$$\frac{P}{P_{\max}} = \frac{A^2 \cdot f^2 e^{-Af}}{4e^{-2}} \quad (3.56)$$

Rewriting expression (3.56) to equal $\frac{1}{4e^{-2}} \cdot A^2 f^2 e^{-Af}$ the expression can be reinstated as:

$$\frac{P}{P_{\max}} = 1.85A^2 f^2 e^{-Af} \quad (3.57)$$

The graph of Figure 3.13 was constructed by substituting X for Af in expression (3.57) then assigning values for X . This also established corresponding values for P/P_{\max} . By interpreting directly from the accompanying table (or from the graph, Figure 3.13), values for Af_1 , for Af_2 and for Af_{\max} were obtained (in nepers). If we let the bandwidth be set when P/P_{\max} is 0.71 (or -3 dB), then the following values can be found (in nepers) for Af :

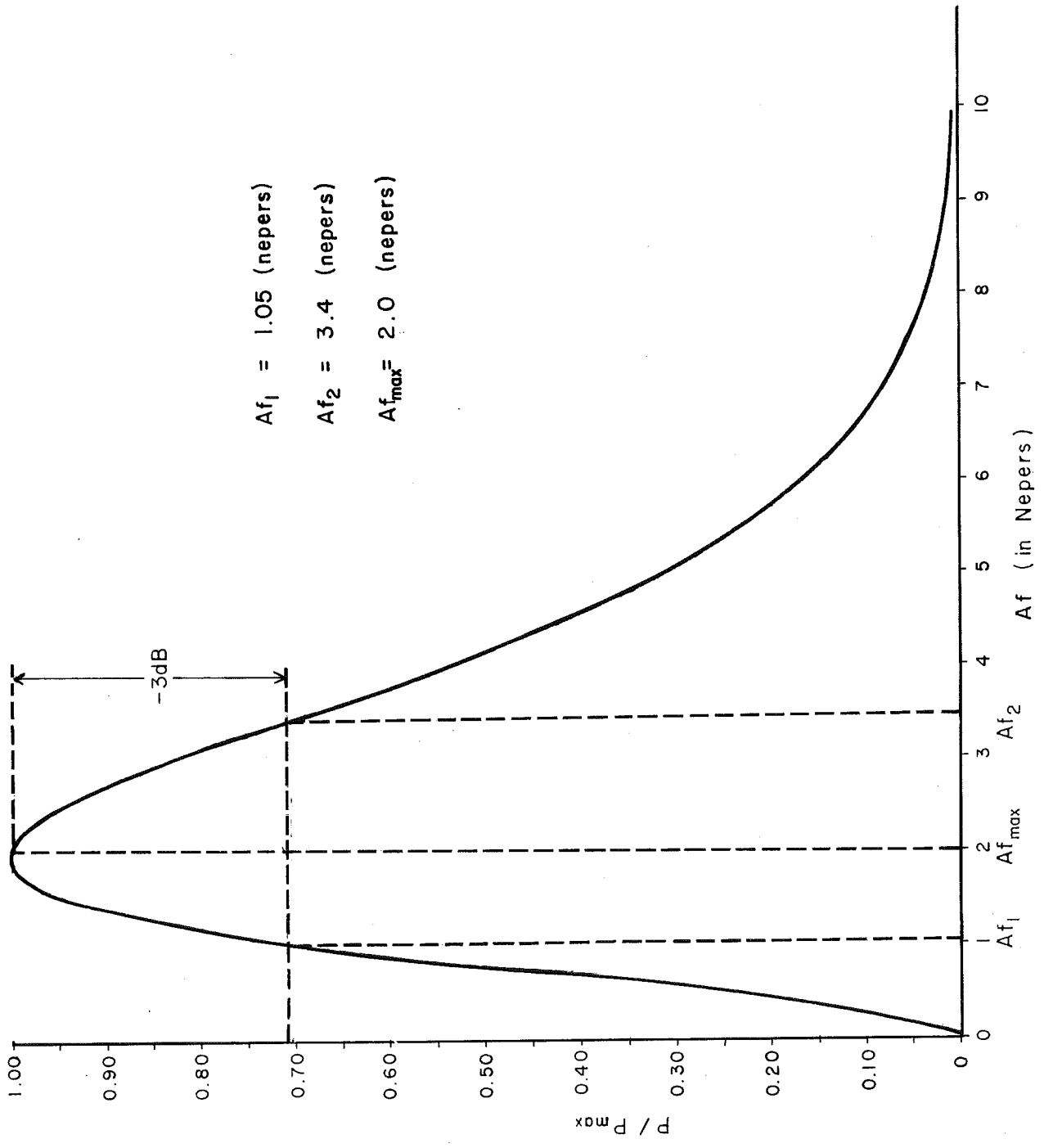


FIGURE 3.13 Values for Af_1 , Af_2 and Af_{max}

$X(Af)_1$	P/P max	$X(Af)_1$	P/P max	$X(Af)_2$	P/P max	$X(Af)_2$	P/P max
0.0	0.00	**1.05	0.71	2.1	0.999	5.6	0.21
0.1	0.02	1.2	0.80	2.2	0.99	5.7	0.20
0.2	0.06	1.3	0.85	2.3	0.98	5.8	0.19
0.3	0.12	1.4	0.89	2.4	0.97	5.9	0.18
0.4	0.20	1.5	0.93	2.5	0.95	6.0	0.17
0.5	0.28	1.6	0.96	2.6	0.93	6.1	0.16
0.6	0.37	1.7	0.98	2.7	0.91	6.2	0.14
0.7	0.45	1.8	0.99	2.8	0.88	6.3	0.13
0.8	0.53	1.9	0.999	2.9	0.86	6.4	0.13
0.9	0.61	*2.0	1.0015	3.0	0.83	6.5	0.12
1.0	0.68		(f max)	3.1	0.80	6.6	0.11
				3.2	0.77	6.7	0.10
				3.3	0.74	6.8	0.10
				***3.4	0.71	6.9	0.9
				3.5	0.68	7.0	0.08
				3.6	0.66	7.1	0.08
				3.7	0.63	7.2	0.07
				3.8	0.60	7.3	0.07
				3.9	0.57	7.4	0.06
				4.0	0.54	7.5	0.06
				4.1	0.52	7.6	0.05
				4.2	0.49	7.7	0.05
				4.3	0.46	7.8	0.05
				4.4	0.44	8.0	0.04
				4.5	0.42	8.0	0.04
				4.6	0.40	8.1	0.04
				4.7	0.37	8.2	0.03
				4.8	0.35	8.3	0.03
				4.9	0.33	8.5	0.03
				5.0	0.31	8.6	0.03
				5.1	0.29	8.7	0.02
				5.2	0.28	9.0	0.02
				5.3	0.26	9.3	0.02
				5.4	0.24	9.3	0.01
				5.5	0.23	9.7	0.01

$2 \ 2 \ -Af$
P/P max = 1.85 A f e

Let X = Af (in nepers)

* Af max

** Af (at -3 dB)
1

*** Af (at -3 dB)
2

- i) $Af_1 = 1.05$ (or 1.1)
- ii) $Af_2 = 3.4$
- iii) $Af_{max} = 2.0$

Values for A are now found by defining A in terms of the 5 layers in the Stratigraphic Model (refer to Figure 3.11) and in relation to the conditions ensconced for the terminated Parametric Source (Section 3.3.3).

R_i (meters)	A(nepers/hz)
1.0	2.3×10^{-5}
10.0	23×10^{-5}
11.6	26×10^{-5}
20.0	65×10^{-5}
30.0	169×10^{-5}
40.0	285×10^{-5}

f_{max} , f_1 and f_2 versus depth using corresponding values of A can be extracted. The resulting frequencies are:

R_1 (m)	f_1 (Hz)	f_2 (Hz)	Δf (Hz)	f_{max} (Hz)	A (nepers/hz)	Q
1.0	45,652	147,826	102,173	86,956	2.3E - 5	0.87
10.0	4783	14783	10000	8696	23E - 5	0.87
11.6	4231	13077	8846	7692	26E - 5	0.87
20.0	1692	5230	3538	3077	65E - 5	0.87
30.0	651	2012	1361	1183	169E - 5	0.87
40.0	386	1193	807	702	285E - 5	0.87

Finally, the Q-factor of the returned signal will remain constant, independent of depth. In other words, for all depths

$$Q = \frac{f_{max}}{f_2 - f_1} = 0.87 \quad (3.58)$$

ii) Conventional Source

The pressure received by the hydrophone for the Conventional Source is more difficult to model empirically than was the case for the terminated Parametric Source. As a first approximation an expression is written for pressure by incorporating a Q-factor sensitivity. Since a transducer may be approximated in terms of an RLC equivalent circuit, the frequency dependence of the power W dissipated in the resistance has the form

$$W = [1 + Q^2 \left[\left(\frac{\omega^2 - \omega_0^2}{\omega \omega_0} \right)^2 \right]^{-1}]^{-1} \quad (3.59)$$

given that ω_0 is the resonant angular frequency (for complete derivation refer to Brophy (1983)). The pressure P received at the hydrophone located very near the seabed surface is than

$$P = \frac{B_1 f e^{-Af}}{\sqrt{1 + Q^2 \left[\frac{(f^2 - f_0^2)^2}{f^2 - f_0^2} \right]}} \quad (3.60)$$

B_1 contains all parameters which are frequency independent. The factor f results from beam pattern dependence. Attenuation with depth is accounted for in A which replaces $2[\alpha_1(R_i - R_{i-1}) + (\bar{\alpha}_{R_{i-1}} R_{i-1})]$. Keeping A, B_1 and Q constant, the equation can be solved for fmax, the frequency at which the received pressure is maximum. From fmax, f_1 and f_2 (at -3dB) can be found.

This expression reliably predicts changes in pressure and in bandwidth when the attenuation levels are low. The expression does break down unfortunately as A becomes large such as observed at the 30 to 40 metre depths. The shape of the resonance curve of an RLC circuit as presented here is only an approximation which is valid when kept close to ω_0 . With high levels of attenuation such as in the real ocean seabed situation, fmax becomes too far removed from f_0 . The transitional point or inflection, where the attenuation component in the numerator dominates, lies approximately between an A of 60 to 70 E-5 nepers/metre for a Q-factor of 2.

A Gaussian Normal Distribution Curve may be of use in fostering a model that would be more sensitive to the higher levels of

attenuation. Bajpai et al (1982) state for a Gaussian Normal Distribution Curve:

$$Y = \frac{1}{\sigma\sqrt{2\pi}} e^{-1/2[(x-\mu)/\sigma]^2} \quad (3.61)$$

Applying this expression, pressure can now be written as:

$$P = \frac{B_1 f e^{-\frac{N}{2\sigma^2} (f-\mu)^2 - Af}}{\sigma} \quad (3.62)$$

To account for the asymmetrical aspect of the curve caused by the $f e^{-Af}$ component of expression (3.62), the bandwidth will have to be adjusted when A is 0 to correctly correspond to the transducer's Q-factor. σ which represents the Gaussian curve variance is directly proportional to the width of the curve. Therefore σ can be conveniently set in this model as a constant. Values for σ are initiated into the expression until σ produces a bandwidth (when A is 0) that exactly matches the required Q-factor bandwidth. For example, σ would have to be set to 1.0773 for a Q-factor of 2 which would define a Δf of 1750 Hz. Similarly a σ of 1.005 would set a Δf of 700 Hz for a Q-factor of 5.

In a Gaussian Normal Distribution Curve (expression (3.61)) the μ is assigned as the mean. Since the mean varies with changes in the distribution curve, μ would also have to alter under the effects of A. If we utilize μ to express in-situ seabed conditions a range of means

would occur with depth, reflecting the effects of attenuation. While a primary frequency of 3500 Hz would set a μ of 3500 Hz when A is 0, μ would be expected to shift to a much lower value of 1000 ± 100 (Hz) when A becomes 285×10^{-5} (nepers/metre). This is supported by seismic interpretations of complex sedimentary structures found on the East Coast Canadian Shelf (Guigne 1983).

Assuming a linear relationship between μ and A and using the two points, 3500 Hz at 0 nepers/metre and 1000 Hz at 285×10^{-5} nepers/metre a linear regression can now be engaged to define μ :

$$\mu = f_0 - 877193.1 A \quad (3.63)$$

where -877193.1 represents the slope of the two points.

N, which is related to the Q of the transducer is projected through the manipulation of

$$\frac{e}{\sigma} \frac{-\frac{N}{2\sigma^2} (f-\mu)^2}{\sigma} = .71 \text{ (-3 dB)} \quad (3.64)$$

into

$$\frac{e}{\sigma} \frac{-\frac{N}{2\sigma^2} (f_1-\mu)^2}{\sigma} = \frac{e}{\sigma} \frac{-\frac{N}{2\sigma^2} (f_2-\mu)^2}{\sigma} = .71 \quad (3.65)$$

Since $Q = \frac{f_o}{\Delta f}$ when A is 0, it would follow that $Q = \frac{\mu}{\Delta f}$ because $\mu = f_o$ when A is 0. Therefore in simplifying for N , $\frac{\mu}{\Delta f}$ will be used to entrench Q in expression (3.66);

$$N = \frac{-8\sigma^2 \ln(.71\sigma)Q^2}{(\mu)^2} \quad (3.66)$$

F_{max} can be appraised by differentiating expression (3.62)

$$\frac{dP}{df} = B_1 e^{-\left[\frac{N}{2\sigma^2}(f-\mu)^2 + Af\right]} \left(1 - f\left(\frac{N}{\sigma^2}(f-\mu) + A\right)\right) \quad (3.67)$$

For $f = f_{max}$, $\frac{dP}{df} = 0$ therefore

$$\frac{N}{\sigma^2} f_{max}^2 + \left(A - \frac{N}{\sigma^2} \mu\right) f_{max} - 1 = 0 \quad (3.68)$$

$$f_{max} = \frac{-\left(A - \frac{N}{\sigma^2} \mu\right) + \sqrt{\left(A - \frac{N}{\sigma^2} \mu\right)^2 + 4N/\sigma^2}}{\left(2N/\sigma^2\right)} \quad (3.69)$$

P_{max} can now be calculated by substituting $f = f_{max}$ into equation (3.62)

To find f_1 and f_2 at -3 dB, $P = .71 P_{max}$; hence

$$\frac{B_1}{\sigma} f e^{-\left(\frac{N}{2\sigma^2}(f-\mu)^2 + Af\right)} - 0.71 P_{max} = 0 \quad (3.70)$$

Differentiating equation (3.70)

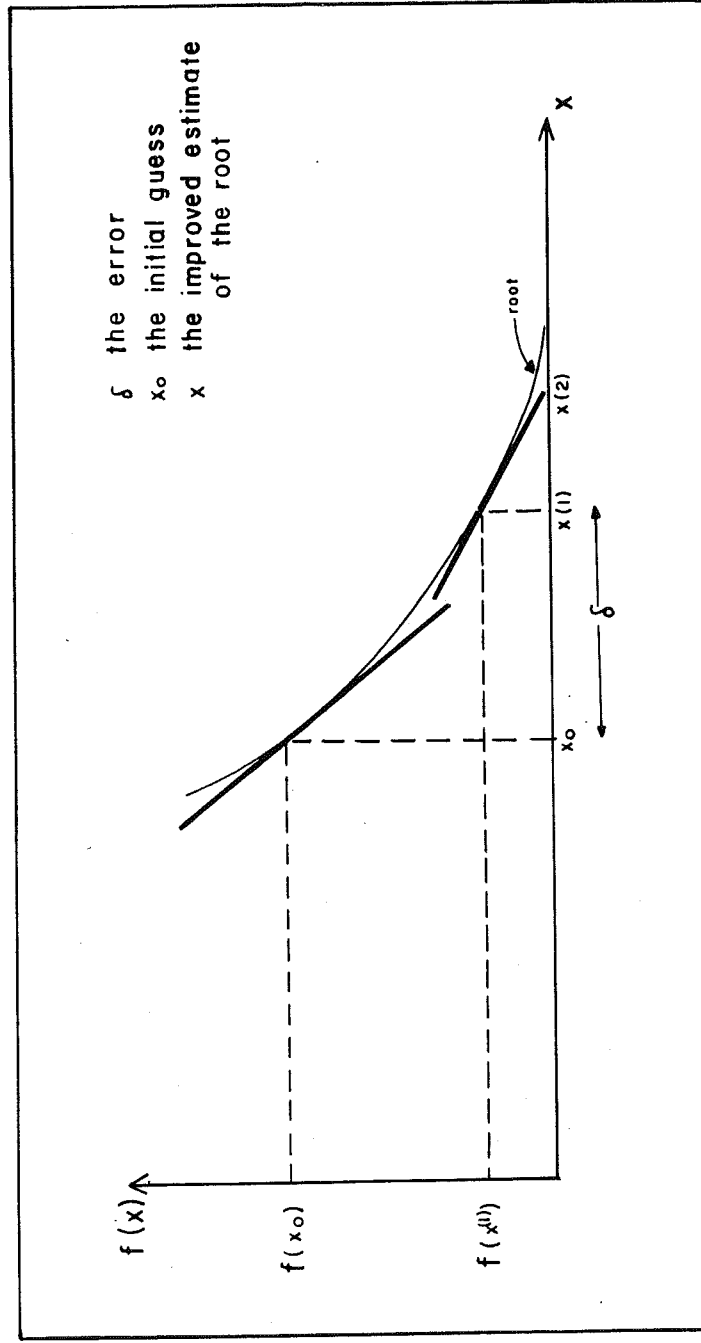
$$e^{-\left(\frac{N}{2\sigma^2}(f-\mu)^2\right) - Af} \left(1 - f\left(\frac{N}{\sigma^2}(f-\mu) + A\right)\right) = 0 \quad (3.71)$$

Finally, to solve f_1 and f_2 , Newton's Method (Newton-Raphson) as illustrated in Figure 3.14 is applied to expression (3.71). Figure 3.15 plots P/P_{\max} versus f for different values of attenuation (i.e. A in (nepers/Hz)). The results using this model are also presented in tabular form for three cases of Q :

Case I: Q of 2 and an f_0 of 3500 Hz

R_i (m)	μ (Hz)	f_2 (Hz)	f_1 (Hz)	Δf (Hz)	f_{\max} (Hz)	A (nepers/Hz)	$\mu/\Delta f$
1.0	3479.8	4645.2	2906.1	1739.1	3770.3	2.3 E-5	2.0
10.0	3298.2	4196.1	2556.1	1640.0	3370.1	23 E-5	2.0
11.6	3271.9	4134.9	2509.2	1625.7	3316.0	26 E-5	2.0
20.0	2929.8	3420.6	1979.3	1441.3	2692.9	65 E-5	2.0
30.0	2017.5	2083.6	1110.4	973.2	1589.8	169 E-5	2.1
40.0	1000.0	1082.4	596.1	486.3	836.2	285 E-5	2.1

If the root of the curve or a point reasonably close to a root is to be defined then $f(x)$ is expanded in a Taylor series about a point called x_0 such that



$$f(x) = f(x_0) + (x-x_0)f'(x_0) + \frac{(x-x_0)^2}{2} f''(x_0) + \dots + \frac{(x-x_0)^{n-1}}{(n-1)!} f^{(n-1)}(x_0)$$

FIGURE 3.14 Principles of Newton's Methods (after R.W. Hornbede, Numerical Methods)

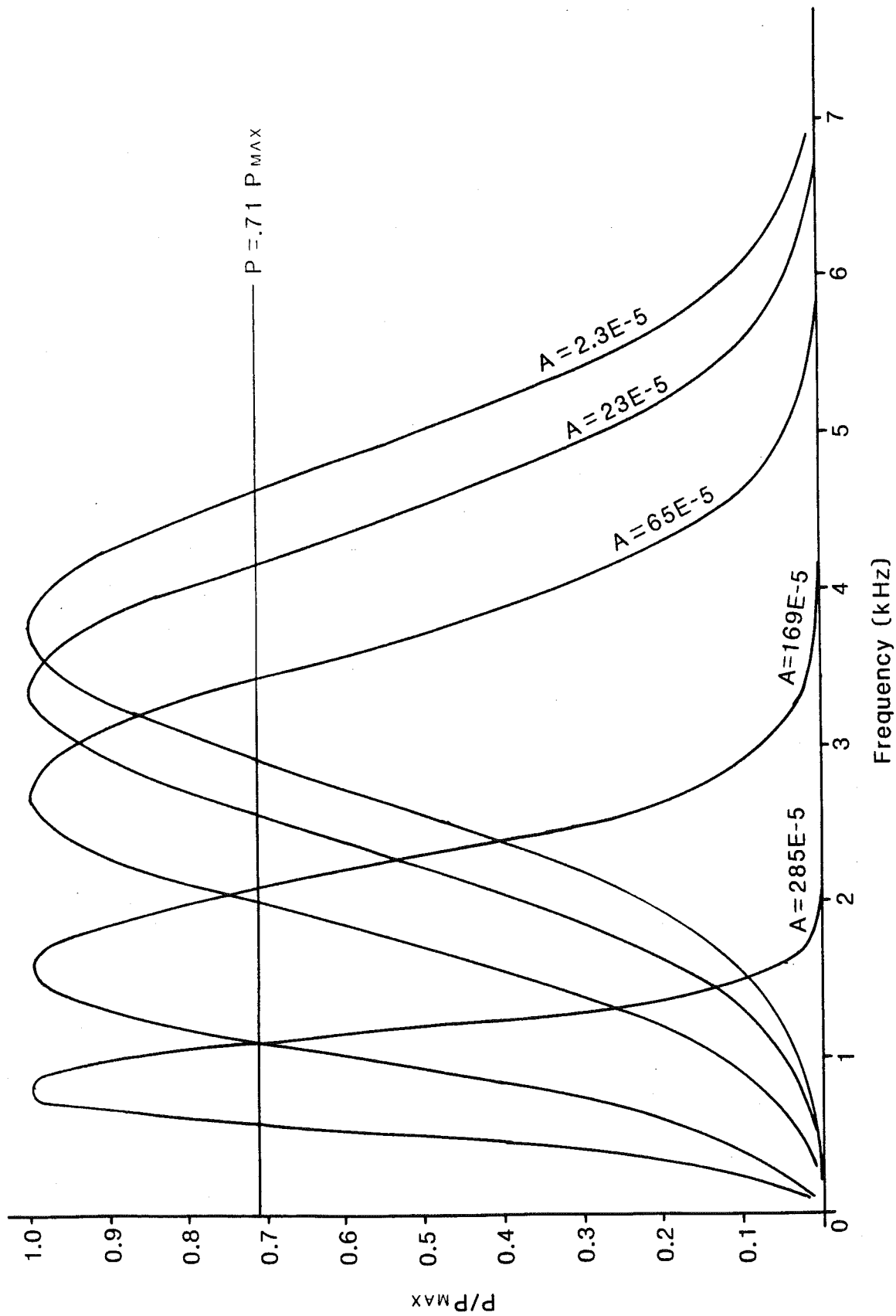


FIGURE 3.15 P/P_{MAX} Versus f at Different Values of A (nepers / Hz)

Case II: Q of 5 and an f_o of 3500 Hz

$\frac{R_{-1}}{(m)}$	$\underline{\mu}$ (Hz)	$\underline{f_2}$ (Hz)	$\underline{f_1}$ (Hz)	$\underline{\Delta f}$ (Hz)	$\underline{f_{max}}$ (Hz)	\underline{A} (nepers/Hz)	$\underline{\mu/\Delta f}$
1.0	3479.8	3874.8	3178.7	696.1	3526.6	2.3 E-5	5.0
10.0	3298.2	3639.9	2980.2	659.7	3309.9	23 E-5	5.0
11.6	3271.9	3606.4	2952.0	654.4	3279.1	26 E-5	5.0
20.0	2929.8	3184.2	2598.4	585.8	2891.2	65 E-5	5.0
30.0	2017.5	2148.4	1745.1	403.3	1946.6	169 E-5	5.0
40.0	1000.0	1073.0	873.1	199.9	973.0	285 E-5	5.0

Case III: Q of 10 and an f_o of 3500 Hz

$\frac{R_{-1}}{(m)}$	$\underline{\mu}$ (Hz)	$\underline{f_2}$ (Hz)	$\underline{f_1}$ (Hz)	$\underline{\Delta f}$ (Hz)	$\underline{f_{max}}$ (Hz)	\underline{A} (nepers/Hz)	$\underline{\mu/\Delta f}$
1.0	3479.8	3665.4	3317.6	347.8	3491.5	2.3 E-5	10.0
10.0	3298.2	3466.0	3136.3	329.7	3301.2	23 E-5	10.0
11.6	3271.9	3437.3	3110.2	327.1	3273.7	26 E-5	10.0
20.0	2929.8	3066.6	2773.7	292.9	2920.2	65 E-5	10.0
30.0	2017.5	2100.7	1899.0	201.7	1999.8	169 E-5	10.0
40.0	1000.0	1043.2	943.3	99.9	993.3	285 E-5	10.0

Finally, Figure 3.16 relates the behaviour of pressure and frequency for the Conventional and for the terminated Parametric Source by plotting the iterations of expressions (3.62) and (3.49). The resulting curves are seen to concord in sensitivity when high attenuation levels are applied. The enumerations of Section 3.4.3 will now be applied in the evaluation of temporal resolution with depth, (Section 3.4.4) and in the assessment of Echo Level with depth, (Section 3.4.5).

3.4.4 Evaluation of Temporal Resolution versus the Model's Stratigraphic Depth

The velocity of sound within the stratigraphy divided by the bandwidth must be considered when modelling the resolution as a function of depth from which the returned signal comes. Since the bandwidth Δf , is defined by the difference between f_2 and f_1 at -3dB then the resolution can be stated as:

$$\text{Resolution } (\gamma) = \frac{\bar{c}_{R_i}}{2\Delta f} \quad (3.72)$$

where \bar{c}_{R_i} is the average velocity to a particular depth defined by R_i and calculated from:

$$\bar{c}_{R_i} = \frac{[c_i(R_i - R_{i-1}) + (\bar{c}_{R_{i-1}} R_{i-1})]}{R_i} \quad (3.73)$$

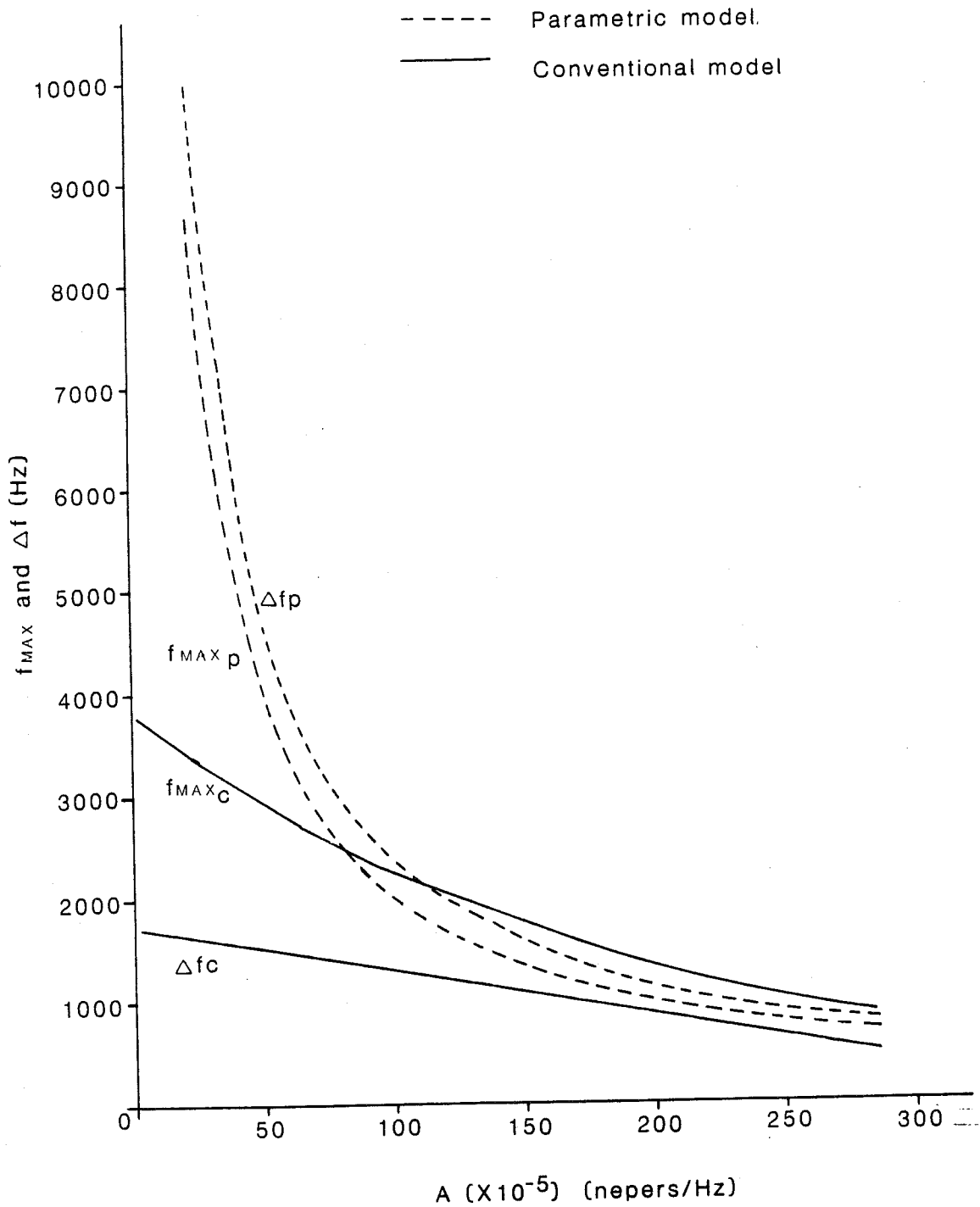


FIGURE 3.16 Comparison between the Terminated Parametric Array and the Conventional Source Models.

R_i represents the depth below the seabed summed from 0 to the i^{th} layer and c_i accounts for the speed of sound in each layer. Calculating for

\bar{c}_{R_i} ;

R_i (m)	c_i (m/sec)	$c_i(R_i - R_{(i-1)}) + (\bar{c}_{R_{(i-1)}})R_{(i-1)}$ (m ² /sec)	\bar{c}_{R_i} (m/sec)
1.0	1500	1500	1500
10.0	1500	15,000	1500
11.6	1500	17,400	1500
20.0	1600	30,840	1542
30.0	1700	47,840	1595
40.0	1800	65,840	1646

The following evaluation computes temporal resolution versus depth for both the terminated Parametric Source and the Conventional Source.

i) Terminated Parametric Source

R_i (m)	Δf (Hz)	\bar{c}_{R_i} (m/sec)	γ (m)
1.0	102,173	1500	0.01
10.0	100,000	1500	0.01
11.6	8846	1500	0.08 (0.1)
20.0	3538	1542	0.22 (0.2)
30.0	1361	1595	0.59 (0.6)
40.0	807	1646	1.02 (1.0)

ii) Conventional Source (Q of 2 and f_o of 3500)

The only Conventional Transducer which was calculated to have resolutions close to the fine resolution values assessed for the Parametric System was a transducer having a Q-factor of 2 or better. However, it should be noted that a transducer having a Q-factor of 2 or less is difficult to construct in practice because of the low efficiency that would result.

R_i m)	Δf (Hz)	\bar{c}_{R_i} (m/sec)	γ (m)
1.0	1739	1500	0.43
10.0	1640	1500	0.46
11.6	1626	1500	0.46
20.0	1441	1542	0.54
30.0	973	1595	0.82
40.0	486	1646	1.69

These iterations are illustrated in Figure 3.17. It is clear that the terminated Parametric Array has a significantly better resolution especially in the upper 30 metres.

3.4.5 Evaluation of Signal-to-Noise Ratio

In this section, a Signal-to-Noise Ratio (SNR) is established for each interface reflection of the Stratigraphic Model. The masking

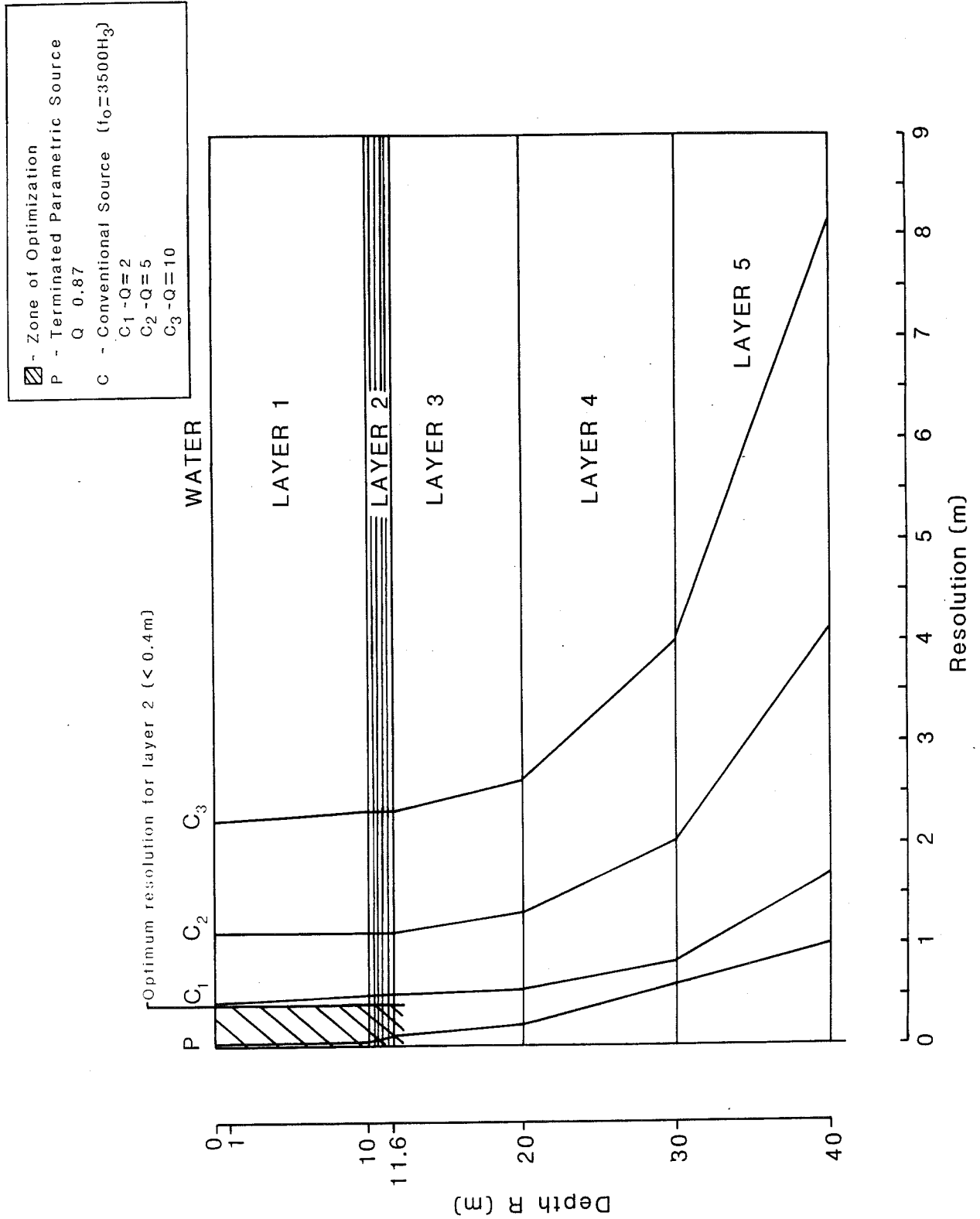


FIGURE 3.17 Temporal Resolution with Depth for a Terminated Parametric Array and for a Conventional Source.

effect of ambient noise(NL) is studied. A transmission loss value is then determined for the model that could realistically account for noise. A specific Echo Level (EL) is also derived for each layer. This is computed for a Parametric Source truncated or terminated at the water/seabed interface. As earlier defined, the nearfield of the carrier frequency corresponds to a height of 8.5 metres and the transducer radius is 0.35 metres. A similar evaluation of Echo Level is performed for a Conventional Source having the same physical transducer dimensions as that of the Parametric Source. The individual character of each source is considered while accounting for the various transmission losses in the final computations of a Signal-to-Noise Ratio.

3.4.5.1 Ambient Noise

Since the Second World War, the study of ambient noise has evolved into very detailed investigations. The characteristics and sources of ambient noise have been seen to be rather complex with different characteristics observed at various frequencies. Often times it is next to impossible to differentiate the actual source of the noise since the nature and amplitude of the noise level is a superposition effect of different sources. For instance in the Davis Strait, surface waves, sea state such as breaking whitecaps, flow noise produced by the wind blowing over the rough sea surface all contribute to the nature and amplitude of the Noise Level found there. Above all else (not including large icebreaker class ship traffic) the single most dominant

cause of noise in the Davis Strait is the breaking up of the ice pack. A conservative estimate of the extra noise level caused by the breaking ice mass is found to be 5 to 10 dB higher than in the more ice free waters of the Strait.

Wenz (1962), in an early paper which discussed the spectra and sources of ambient noise, identified the more prominent sources of noise as having one of the following origins:

- i) Biological
- ii) Water Motion
- iii) Man-made

Of the three, water motion which includes surf, hail, and tidal effects and man-made sources such as noise produced by shipping are considered in conventional seismic surveying to be detrimental to the Echo Level intensity. It is generally accepted by such authors as Stockhausen (1975), Ross and Bluy (1976), Anderson (1979), and Wagstaff (1980) that the directionality of shipping noise in deep water is near horizontal contrasting sharply with the more diffuse bias towards the vertical observed for sea surface motion. In shallower depths such as the water depths of the Scotian Shelf (< than 200 metres) most low frequency (below 1 kHz) noise appears to follow near horizontal paths. Above 1 kHz the spectrums monitored have shown a marked preference towards the vertical. This was particularly noted in the vertical noise directionality studies made in shallow water by the Canadian

Defense Research Establishment Atlantic. Informal communications with Ross, J.M. (1984) on this particular study and an internal note on the subject revealed:

"Measurements recorded in areas of the Canadian Continental Shelf have shown that in a positive velocity gradient condition and low wind speeds, distant shipping noise dominates up to at least 1 kHz. As wind speed increases, the transitional frequency at which wind generated noise dominates the noise spectrum is lowered. In negative gradient conditions, distant shipping dominates the spectrum to a lesser extent than in comparable conditions in positive gradient conditions simply because propagation conditions are less favorable". (transcribed with permission)

High frequencies within the bandwidth of 1 kHz to 20 kHz are necessary in order to differentiate shallow sedimentary strata. It would appear then from Wenz's work and from noise directionality investigations in various areas of the Canadian Continental Shelf, that surface agitation resulting from the effects of wind is the prime noise generator at these frequencies. Therefore the following values for noise are compiled from wind/surface agitation Noise Pressure Spectrum Levels (PSL), for frequencies ranging from 750 Hz to 20 kHz (refer to Figure 3.18 and the table that follow).

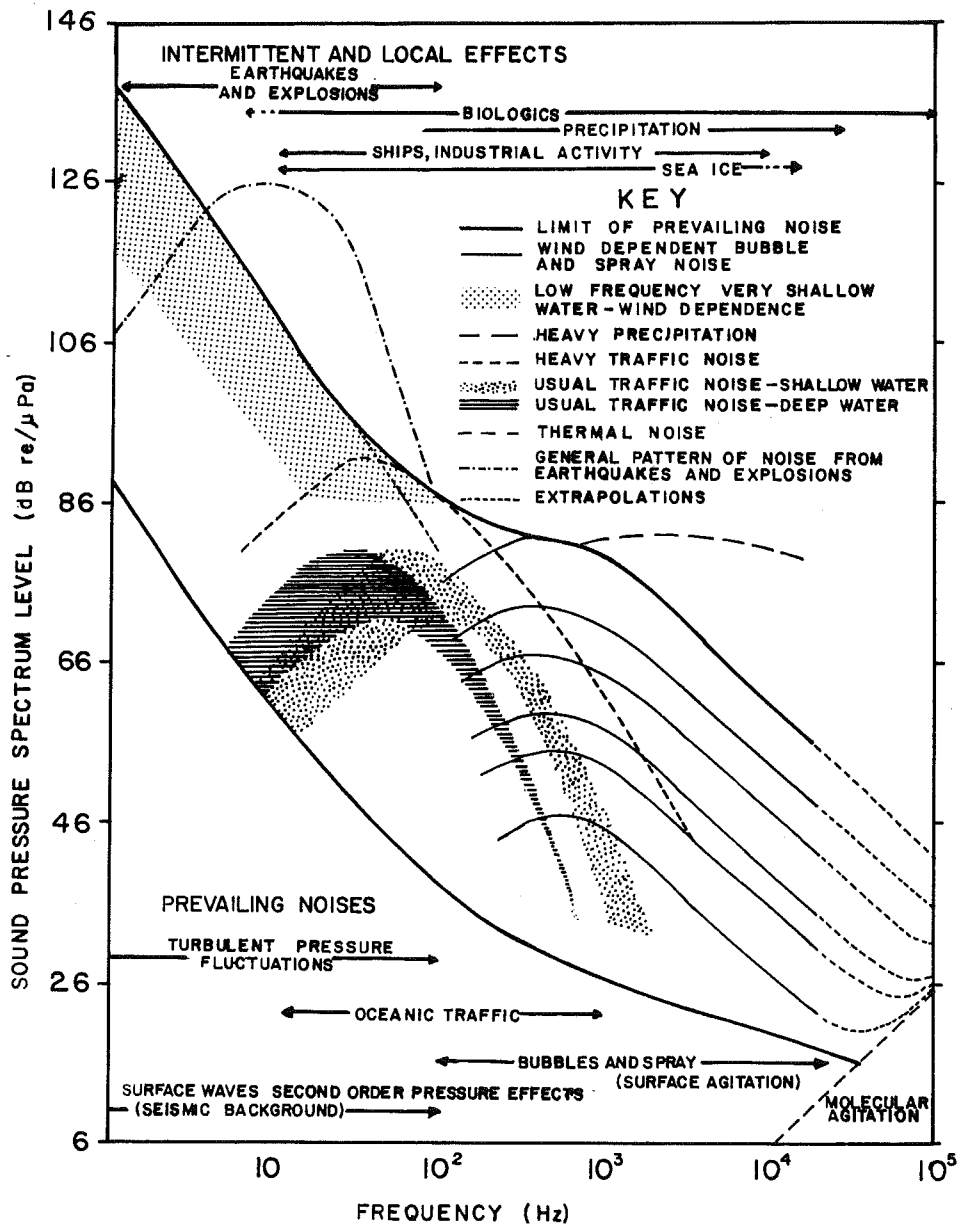


FIGURE 3.18 Composite Ambient Noise Spectrum (after Wenz 1962)

		Pressure Spectrum Level (dB re 1 μ Pa per Hz ^{1/2})								
Frequency (Hz)		750	800	1k	2k	3k	5k	7k	10k	20k
A. Wind-dependent bubble and spray noise for Beaufort Scales (1 to 8)										
1)		47.0	46.5	45.0	40.0	37.0	33.0	30.0	28.5	22.0
2)		54.5	54.0	53.5	48.5	44.0	41.0	38.0	36.0	30.0
3)		59.5	59.0	58.0	53.0	50.5	45.5	42.0	40.0	34.0
5)		66.0	65.5	65.0	61.0	57.5	52.5	50.0	48.0	42.0
8)		72.0	71.5	71.0	66.0	62.5	57.5	56.0	53.75	48.0
B. Heavy Traffic Noise										
		66.0	65.0	62.0	52.0	46.5	-	-	-	-
C. Heavy Precipitation										
		80.5	81.0	81.5	82.0	82.0	81.75	81.5	81.0	-
D. Thermal Noise										
		-	-	-	-	-	-	-	-	11.0
E. Usual traffic noise - deep water										
		-	-	-	-	-	-	-	-	-
F. Usual traffic noise - shallow water										
Lower										
		44.0	42.0	-	-	-	-	-	-	-
Upper										
		54.0	52.5	-	-	-	-	-	-	-

In this study, the Detected Noise Level (DNL) has been calculated by averaging the expected prevailing noise minimum and maximum based on Beaufort scales of 1 and 8 along with the Beaufort scale level 3. The

resultant spectrum levels are considered to be realistic of actual noise conditions encountered in typical marine geophysical surveying at frequencies above 750 Hz and up to 20 kHz. Once the bandwidth of the signal is applied, the noise effects computed are thought to be quite representative of the high in-situ levels which occur along the Canadian Atlantic offshore.

The Detected Noise Level with a bandwidth component is written as:

$$\text{DNL} = \text{PSL} + 10 \log \Delta f \quad (3.74)$$

where PSL is the Pressure Spectrum Level and Δf accounts for the bandwidth of the receiving system. The following spectrum levels are addressed in context with lower and upper limits:

	<u>Pressure Spectrum Levels (dB re 1 μPa per $\text{Hz}^{1/2}$)</u>							
Frequency (Hz):	750	1k	2k	3k	5k	7k	10k	20k
Lower Limit of prevailing noise:	28.5	27.0	25.0	24.5	22.0	20.0	20.0	12.0
Calculated average: (based on Beaufort scales 1,3,8)*	56.2	54.8	51.0	48.7	44.8	42.2	40.3	33.7
Upper limit of prevail- ing noise:	80.5	79.5	75.0	71.0	67.0	64.0	61.0	55.0

*Beaufort Scale refers to a meteorological convention that distinguishes the condition of the sea (ocean) surface. The degree of roughness is presented in terms of wind forces.

If a receiver has a 3.5 kHz bandwidth, then the bandwidth effect would add an extra 35 dB to the Pressure Spectrum Level.

3.4.5.2 Target Strength

Portions of the wavefront energy will be reflected back to the surface as the propagating signal passes through changes in the sediment medium. The calculation of a Target Strength for a flat planar interface will involve an assessment of reflectivity in conjunction with the spatial extension of the boundary. Clay and Medwin (1977) calculate Target Strength through the backscatter pressure received at the hydrophone (see expression 3.28 and 3.29) By including an appropriate Reflection Coefficient ($R'_{i,i-1}$), the backscatter pressure (P_{bs}) at the hydrophone can be stated as

$$P_{bs_i} = \frac{R'_{i,i-1} P_o R_o}{2R_i} \quad (3.75)$$

where P_o is the source pressure at a reference range R_o . The subscript o refers to a unit reference. The range element ($2R_i$) denotes the two way geometric Transmission Loss (TL). The computations also require an evaluation of Absorption Loss (ABS_{2R_i}) because of the effects of the porosity/density properties found within the five layers of the Stratigraphic Model. Hence the backscatter pressure now becomes:

$$P_{bs_i} = \frac{R'_{i,i-1} P_o R_o}{2R_i ABS_{2R_i}} \quad (3.76)$$

The Absorption Loss was specifically addressed in Section 3.4.3, expressions (3.49 and 3.53) for a terminated Parametric Array. Thus

$$ABS_{2R_i} = e^{-Af_d^{\max}} = e^{-2} = \frac{1}{e^2} \quad (3.77)$$

with A being equal to $2[\alpha_i(R_i - R_{i-1}) + (\bar{\alpha}_{R_{i-1}} R_{i-1})]$ and f_d^{\max} equated to $2/A$. The backscatter pressure can now be accounted for through the application of expression (3.78).

$$P_{bs_i} = \frac{R'_{i,i-1} P_o R_o}{2R_i e^{-2}} = \frac{R'_{i,i-1} P_o R_o e^2}{2 R_i} \quad (3.78)$$

given that pressure at the scatter (P_p) is

$$P_p^2 = \frac{P_o^2 R_o^2}{R_i^2 ABS_{R_i}^2} \quad (3.79)$$

(the subscript R_i is used to indicate a one way Attenuation Loss)

Expression (3.79) can be rewritten as

$$P_p = \frac{P_o R_o}{R_i ABS_{R_i}} = \frac{P_o R_o}{R_i e^{-1}} \quad (3.80)$$

Since the Target Strength is $20 \log \left[\frac{P_{bs} R_i}{P_p R_o} \right]$ (as seen earlier in expression (3.28)) then

$$TS = 20 \log \left[\frac{R'_{i,i-1} P_o R_o R_i R_i e}{2 R_i R_o P_o R_o} \right] \quad (3.81)$$

This simplifies into: ($R_o = 1$ metre reference)

$$TS = 20 \log \frac{R'_{i,i-1} R_i e}{2} \quad (3.82)$$

$$= 20 \log(R'_{i,i-1}) + 20 \log(R_i) - 20 \log(2) + 20 \log(e) \quad (3.83)$$

(for a terminated Parametric Array)

Urlick (1975) presented a similar expression for the Target Strength of a flat plane. Expression (3.37) denotes TS as $10 \log(R^2/4)$. By adding a Reflection Coefficient and an Absorption Loss, TS can be read as

$$TS = 20 \log(R'_{i,i-1}) + 20 \log(R_i) - 20 \log(2) + ABS_{R_i} \quad (3.84)$$

To conclude, the Target Strength calculations for the analytical model will use expression (3.84) for the Conventional Source and expression (3.83) for the terminated Parametric Array. Their differences exist only in the writing of the Absorption Loss which has peculiarities attributed specifically to each system's discrete source calculations. Both derivations of Target Strength are equivalent once the source calculations are included in the statement.

3.4.5.3 Echo Level

An Echo Level (EL) for each layer is now calculated in reference to the changes with depth of centre frequency and of bandwidth as modelled in Section 3.4.3. The sonar equation:

$$\text{Echo Level (EL)} = \text{SL} - (\text{TL}_D + \text{TL}_U) - \text{ABS} + \text{TS} \quad (3.85)$$

is the basis of the following evaluation. The SL appraisal for the truncated Parametric Array involves a calculated difference frequency at maximum pressure ($f_d \text{ max}_i$) for a specific depth (i^{th}). In applying $40 \log f_d$ of expression (3.47), $f_d \text{ max}_i$ accounts in its value for the effect of absorption since the derivation of $f_d \text{ max}_i$ was a product of attenuation (refer to expression (3.49)). However, the other two components of expression (3.47) (ie. $-11.17 + 60 \log \ell$) require an adjustment for attenuation with increasing depth. Therefore SL is resolved in two stages:

$$\text{SL}'_{R_i} = [(-11.17 + 60 \log \ell) - 17.372] + [40 \log f_d \text{ max}_i] \quad (3.86)$$

where SL_{R_i} is $\text{SL}'_{R_i} + \text{ABS}_{2R_i}$. The constant 17.372 was taken from e^{-2} as noted in $P_{\text{max}} = \frac{B^4}{A^2} e^{-2}$; expression (3.55)(see equation (3.33) for a full explanation on the ABS component).

Therefore,

i) Terminated Parametric Source

R_i (m)	$f_{d\max_i}$ (Hz)	SL'_{R_i} (dB re 1 μ pa)	$TL_{D_{R_i}}$ (dB)	$TL_{U_{R_k}}$ (dB)	TS_i (dB re 1m ²)	EL (dB re 1 μ pa)
1.0	86956	224.8	21.1	17.6	-11.0	175.1
10.0	8696	184.8	26.9	23.4	-9.5	124.9
11.6	7692	182.7	27.7	24.0	-2.6	128.4
20.0	3077	166.7	30.8	26.6	6.0	115.4
30.0	1183	150.1	33.5	28.7	10.4	98.3
40.0	702	141.1	35.8	30.2	25.6	100.7

SL'_{R_i} for a Conventional Source is also calculated in two parts similar to the derivation employed for the SL'_{R_i} of the terminated Parametric Source.

$$SL'_{R_i} = [(170.5 + 10 \log W) - \sum_{n=1}^i (ABS_{2R_n})] + [(DI_t)_i] \quad (3.87)$$

The $(DI_t)_i$ component includes in its value the effects of attenuation since f_{\max_i} is a product of attenuation. $(DI_t)_i$ is defined by 20 log

$\frac{\pi D}{\bar{\lambda}_i}$ where $\bar{\lambda}_i$ is equal to $\frac{\bar{c}_{R_i}}{f_{\max_i}}$ and D is the diameter of the transducer.

The results of the Echo Level computation for the Conventional Source are tabulized:

ii) Conventional Source

\underline{R}_i (m)	$\underline{f_{max}_i}$ (Hz)	\underline{SL}'_{R_i} (dB re 1 μ pa)	$\underline{TL}_{D_{R_i}}$ (dB)	$\underline{TL}_{U_{R_k}}$ (dB)	\underline{TS}_i (dB re 1m ²)	\underline{EL} (dB re 1 μ pa)
1.0	3770	215.2	21.1	17.6	-19.3	157.2
10.0	3370	208.1	26.9	23.4	-14.9	143.0
11.6	3316	207.0	27.7	24.0	-7.4	147.9
20.0	2693	197.4	30.8	26.6	5.0	145.0
30.0	1590	184.5	33.5	28.7	13.4	135.7
40.0	836	181.4	35.8	30.2	27.3	142.7

3.4.5.4 Signal-to-Noise Ratio

Finally, a Signal-to-Noise Ratio can be defined using:

$$SNR = EL - DNL \quad (3.88)$$

The following two tables summarize the computed SNR values for both sources in terms of reflected signals coming off of each layer and then being received by a hydrophone on or near the seabed.

i) Terminated Parametric Source

\underline{R}_i (m)	\underline{EL} (dB re 1 μ pa)	$\underline{f}_{d \max_i}$ (Hz)	$\underline{\Delta f}$ (Hz)	\underline{PSL} (dB re 1 μ pa per Hz ^{1/2})	\underline{DNL} (dB re 1 μ pa)	\underline{SNR}
1.0	175.1	86956	102,173	≈25.0	75.1	100.0
10.0	124.9	8696	100,000	41.5	91.5	33.5
11.6	128.4	7692	8846	42.0	81.5	46.9

20.0	115.4	3077	3538	48.5	84.0	31.4
30.0	98.3	1183	1361	54.0	85.3	13.0
40.0	100.7	702	807	56.5	85.6	15.1

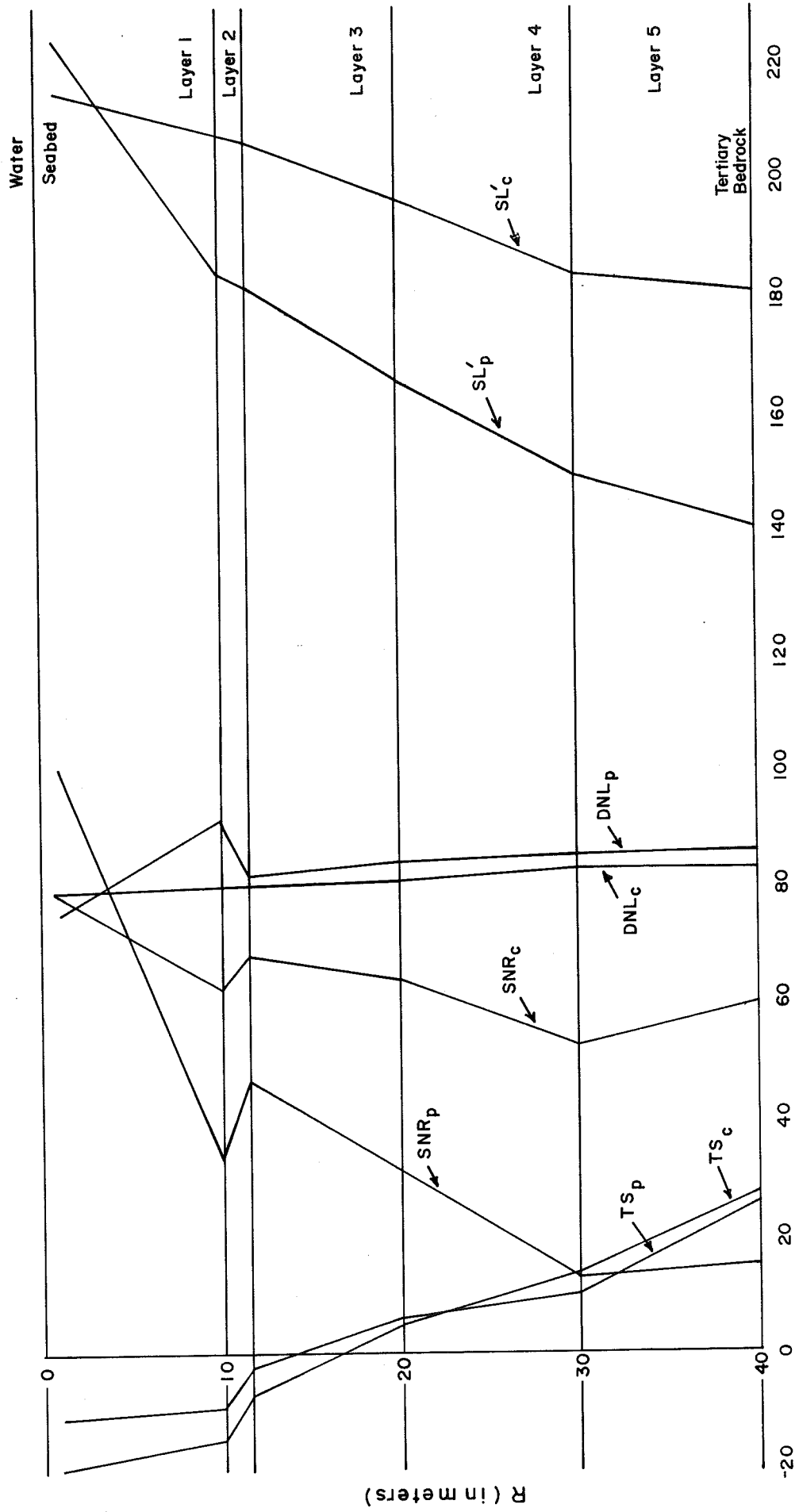
ii) Conventional Source (Q of 2 and f_o of 3500)

R_i (m)	<u>EL</u> (dB re 1 μ pa)	f_{max_i} (Hz)	Δf (Hz)	<u>PSL</u> (dB re 1 μ pa per Hz ^{1/2})	<u>DNL</u> (dB re 1 μ pa)	<u>SNR</u>
1.0	157.2	3770	1739	46.5	78.9	78.3
10.0	143.0	3370	1640	48.0	80.1	62.9
11.6	147.9	3316	1626	48.0	80.1	67.8
20.0	145.0	2693	1441	49.0	80.6	64.4
30.0	135.7	1590	973	53.0	82.9	52.8
40.0	142.7	836	486	56.0	82.9	59.8

Figure 3.19 illustrates and compares the Signal-to-Noise Ratios of the terminated Parametric Array and of the Conventional Source for descending depths R_i in reference to the model. It is clear from this graph that the Conventional Source has a stronger signal throughout the descent into the sediment column.

3.4.6 Evaluation of the Basal Till Backscatter

A fundamental objective in the development of the "Acoustic Sub-seabed Interrogator" concept is the creation of a profiling probe which would be able to scan effectively into highly scattering structures typical of glacial moraines. The intent in this section is therefore oriented towards the signal propagation performance of a terminated Parametric Array and of a Conventional Source tested



DNL, TS, SNR, SL'_c , (in dB)

FIGURE 3.19 Signal-to-Noise Ratio with Depth for a Terminated Parametric Array (SNR_p) and for a Conventional Source (SNR_c)

theoretically on a Basal Till of considerable thickness and scattering severity. The Basal Till's acoustic effects as specifically modelled in Layer 5 addresses a form of backscatter originating off a tightly packed boulder and cobble assemblage, distributed diffusely throughout the layer.

The study is presented as four interlocked parts. They are sectioned chronologically under the headings:

- i) Derivation of an Expression for Target Strength of Reverberation
- ii) Calculation of the Scattering Volume.
- iii) Modelling of a Realistic Basal Till Composition and Structure
- iv) Evaluation of each Layer's Reverberation Level.

The following sonar parameters will be used in the calculations of reverberation for the two sources tested:

- i) Reverberation (RL) = SL (or SPL) - (TL_D+TL_U) - ABS + TSR
- ii) Signal-to-Reverberation Ratio (SRR) = TS - TSR

(refer to Section 3.3 for a detailed definition of the sonar terms)

3.4.6.1 Derivation of an Expression for Target Strength of Reverberation

The Target Strength of Reverberation (TSR) has been written in this study to account for the total effects of scatter within the entire 5 layers of the stratigraphy, given the condition that $\frac{2\pi a}{\lambda} \gg 1$;

where a is the radius of the spherical elements in the scatter volume.
Hence the expression;

$$\text{TSR}_{R_k} = \text{TL}_{U_{R_k}} + 10 \log \left[\sum_{k=1}^n (\text{TSR}_k) \right]_{R_k} \quad (3.89)$$

The R_k subscript indicates a particular range from the base of the last layer (i.e. k), up to the seabed surface. (see expression (3.36) for the definition of TL_U). When $\frac{2\pi a}{\lambda}$ approaches 1 then TSR_{R_k} will not be calculated since there would not be any backscatter and therefore there would not be TL_U of the backscatter. However, TSR_k for such conditions will be considered 0 when summed to other layers.

Kinsler et al (1982) present a useful assessment of volume scatter. Their expressions of TSR form a convenient starting point to initiate the development of an expression for scatter at a particular k^{th} layer (Figure 3.11). For example: (see Kinsler et al (1982))

$$\text{TSR} = 10 \log V + S_V \quad (3.90)$$

where $V = \left(\frac{c\tau}{2}\right) A_T$. The A_T factor refers to the cross sectional area of the reverberation volume and $\frac{c\tau}{2}$ involves the speed of sound c and the pulse duration τ . The scattering strength per unit volume S_V is stated as $10 \log \left(\frac{1}{V} \sum \frac{\sigma_j}{4\pi}\right)$. This can be reexpressed as $10 \log \left(\frac{\sigma_V}{4\pi}\right)$ with σ_V accounting for $1/V \sum \sigma_j$. The σ_j factor is a simple substitute for $j\sigma$ where j refers to the number of scattering elements and σ is the backscattering cross section (per element).

Kinsler et al (1982) also introduce a geometrical transmission loss in their definition:

$$TL_{(\text{geom})} = 10 \log (A_T/\Omega) \quad (3.91)$$

The Ω is defined in terms of $\frac{4\pi}{D}$ where D accounts for the directivity of the transducer. TSR can now be restated as: (Kinsler et al (1982))

$$TSR = S_V + TL_{(\text{geom})} + 10 \log \left(\frac{\Omega c \tau}{2} \right) \quad (3.92)$$

Expression (3.92) is therefore an effective manner to derive TSR_{R_k} for the model. Applying this equation directly to a Conventional Source, an expression for TSR_k can be created assuming its Directivity Factor (D) equals $\left(\frac{2\pi}{\lambda}\right)^2 \frac{d^2}{4}$. This is a very close estimation of a circular piston's directivity where d is the diameter and λ is the wavelength.

After substituting into expression (3.89) for various terms and simplifying,

$$10 \log \left[\sum_{k=1}^n (TSR_k) \right]_{R_k} = 10 \log \left[\sum_{k=1}^n \left(\left(\frac{\sigma_v}{4\pi} \right)_k \left(\frac{2c_w^2 c_k \tau_k}{\pi d^2 f_{\max_k}} \right) \right) \right]_{R_k} \quad (3.93)$$

In this equation f_{\max_k} is the frequency of the signal at maximum pressure for a particular k^{th} layer. (refer to Section 3.3.3 for details on f_{\max}). τ_k is the average pulse duration computed within the scatter layer.

Finally TSR_k can be reduced into a working equation:

$$TSR_k = \left[\frac{\sigma_{v_k} c_w^2 c_k \tau_k}{2\pi d^2 f_{max_k}} \right] \quad (3.94)$$

Expression (3.92) can also be used to determine TSR for the terminated Parametric Source. However the Directivity Factor within Ω is more difficult to establish for the terminated Parametric Source than it was for the Conventional case. The beam patterns $B(\theta)$ for the terminated Parametric and Conventional Sources can be described in terms of $2 \frac{J_1(x_1)}{x_1} \cdot \text{Sin} \frac{(x_2)}{x_2}$ for the terminated Parametric Source and as $2 \frac{J_1(x_1)}{x_1}$ for the Conventional Source, where x_1 is equal to $(a k_d \text{Sin} \theta)$ and x_2 is equal to $(k_d a \text{Sin}^2(\frac{\theta}{2}))$ (see Appendix B). The factor k_d represents $\frac{2\pi}{\lambda_d}$ while a is the radius of the transducer and λ is the height above the seabed. The Directivity Factor D is usually defined by

$$D = 4\pi \left[\int_{4\pi} B(\theta)^2 d\Omega \right]^{-1} \quad (3.95)$$

where $d\Omega$ is the differential solid angle, (Clay and Medwin (1977)).

Since $B(\theta)$ has been stated to equal $2 \frac{J_1(x_1)}{x_1} \cdot \frac{\text{Sin}(x_2)}{x_2}$ for the terminated Parametric Source then

$$D = \frac{4\pi}{\int_0^{\pi/2} \left[\frac{2J_1(a k_d \sin\theta)}{a k_d \sin\theta} \cdot \frac{\sin(k_d \lambda \sin^2(\frac{\theta}{2}))^2}{k_d \lambda \sin^2(\frac{\theta}{2})} \right] 2\pi \sin\theta d\theta} \quad (3.96)$$

where $2\pi \sin\theta d\theta$ is the increment of the solid angle of a circular piston. Given that Ω is equal to $\frac{4\pi}{D}$ then it follows that

$$\Omega = \int_0^{\pi/2} \left[\frac{2J_1(x_1)}{x_1} \cdot \frac{\sin(x_2)^2}{x_2} \right] 2\pi \sin\theta d\theta \quad (3.97)$$

A Gauss quadrature method was used to evaluate Ω . The Gauss quadrature is a very powerful integration since it employs unequally spaced intervals in the sampling of the function to be approximated. The derivation begins along the lines used in a Chebyshev interpolation. (see Hornbeck (1975) Chapter 4 for details on Chebyshev-interpolation; Chebyshev polynomials). A polynomial is generated through this interpolation and also using the Lagrange formula. By integrating the resultant interpolating polynomial the Gauss quadrature formula is thus created. (For more details see Lanczos (1956) and Hornbeck (1975)).

A modified IMSL Mathematical Library Package within the Memorial University of Newfoundland VAXTM computer was used to apply the Gauss quadrature to expression (3.97). Sabin (1984) modified the package for ease in using the program.

Incorporating Ω into TSR_k , TSK_k can now be rewritten as:

$$TSR_k = \left[\frac{\Omega_k C_k \bar{\tau}_k \sigma_{V_k}}{2(4\pi)} \right] = \left[\frac{\Omega_k C_k \bar{\tau}_k \sigma_{V_k}}{8\pi} \right] \quad (3.98)$$

whereby $S_{V_k} = 10 \log \left(\frac{1}{V} \sum \frac{\sigma_j}{4\pi} \right)_k = 10 \log \left(\frac{\sigma_V}{4\pi} \right)_k$ (terms are from expression (3.90)).

3.4.6.2 Calculation of the Scattering Volume

To compute S_{V_k} , the scattering volume is defined as a truncated cone determined by the beamwidth (θ) of the propagating signal at a given k^{th} layer. Figure 3.20 illustrates this truncated conical volume in reference to the Stratigraphic Model. The truncated cone can be stated as having the following volume:

$$V_k = 1/3 \pi \tan^2 \Phi [(R_k + \ell)^3 - a^3] \quad (3.99)$$

with $a = R_{(k+1)} + \ell$ and $\Phi = \frac{\theta}{2}$

As a first approximation, the beamwidths (θ) for both the Conventional and terminated Parametric Sources are computed using:

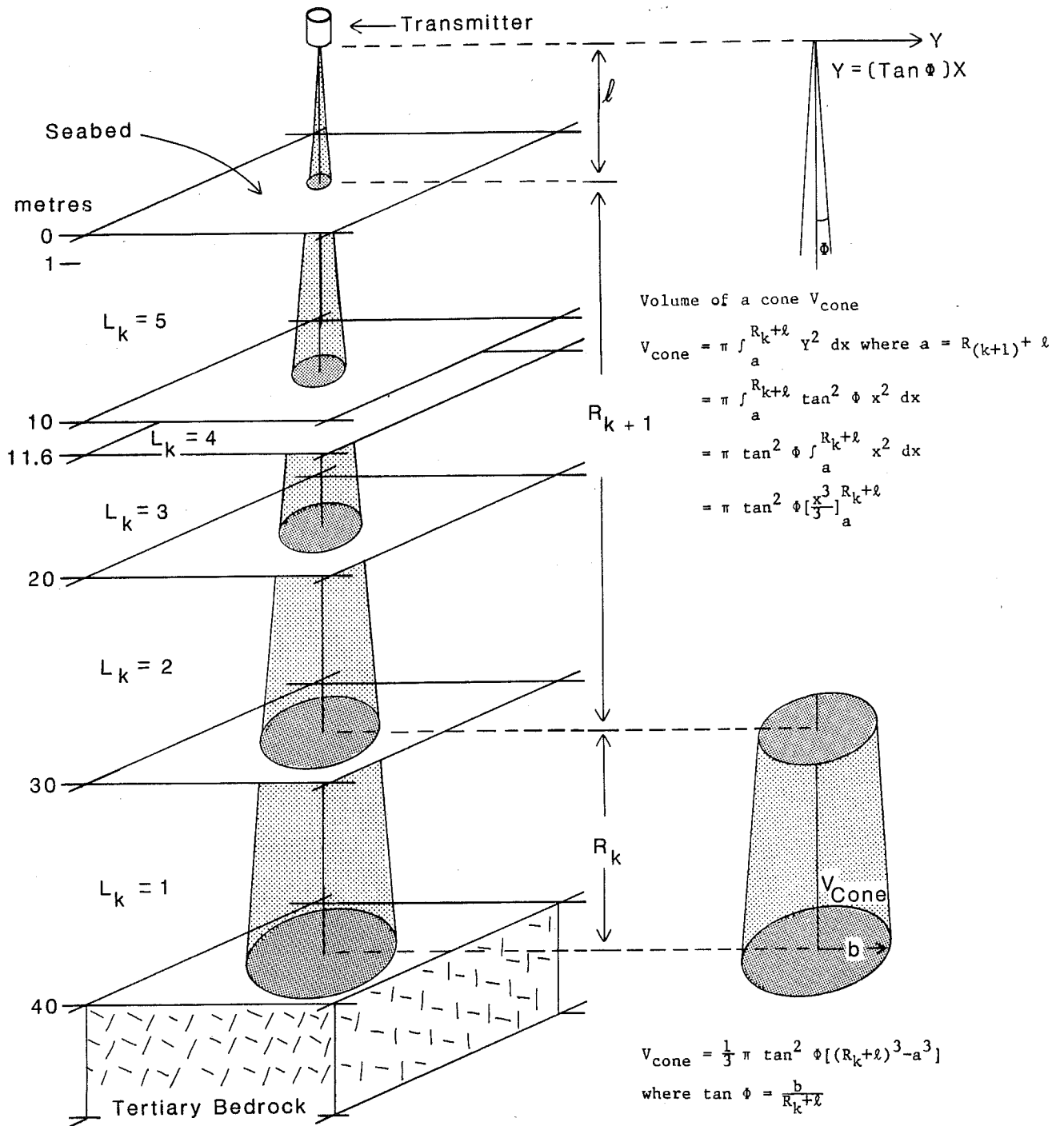


FIGURE 3.20 Truncated Conical Volume Geometry as it Applies to the Stratigraphic Model.

i) Conventional Case: (refer to Figure 3.21a)

$$\theta_c = 2 \sin^{-1} \left(\frac{1.7}{k_d a} \right) \text{ degrees} \quad (3.100)$$

and

ii) Terminated Parametric Case: (refer to Figure 3.21b)

$$\theta_p = 4 \sin^{-1} \sqrt{\frac{1.39}{k_d \ell}} \text{ degrees} \quad (3.101)$$

Figure 3.22 illustrates the approximate beam patterns of both sources versus frequency. An optimum zone has been shaded to highlight the region of interest as defined by the boundary limits:

- i) $B(\theta) \leq 30^\circ$ beampattern
- ii) $f_d \leq 4$ kHz

A better approximation of beamwidth is attained by solving the Bessel function ($J(x)$). For the Bessel function of the first kind, of order one and when $x < 2$ then the magnitude of the argument (x) is computed by

$$J_1(x) = \sum_{n=0}^{\infty} \frac{(-1)^n \left(\frac{x}{2}\right)^{2n+1}}{n! (n+1)!} \quad (3.102)$$

(n represents the number of terms in the approximation)

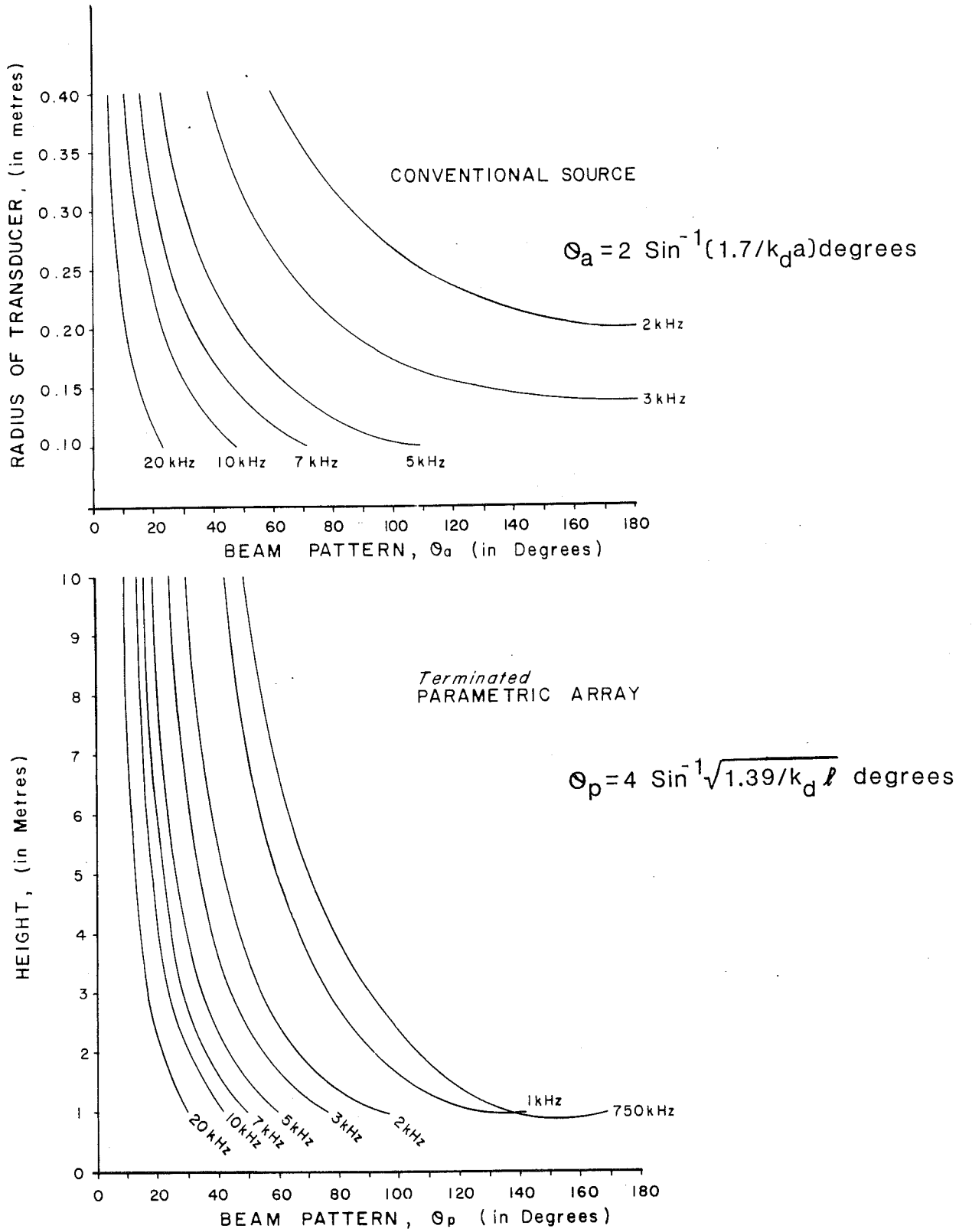


FIGURE 3.21 Approximate Beam Pattern versus Height above the Seabed and Radius of Transducer.

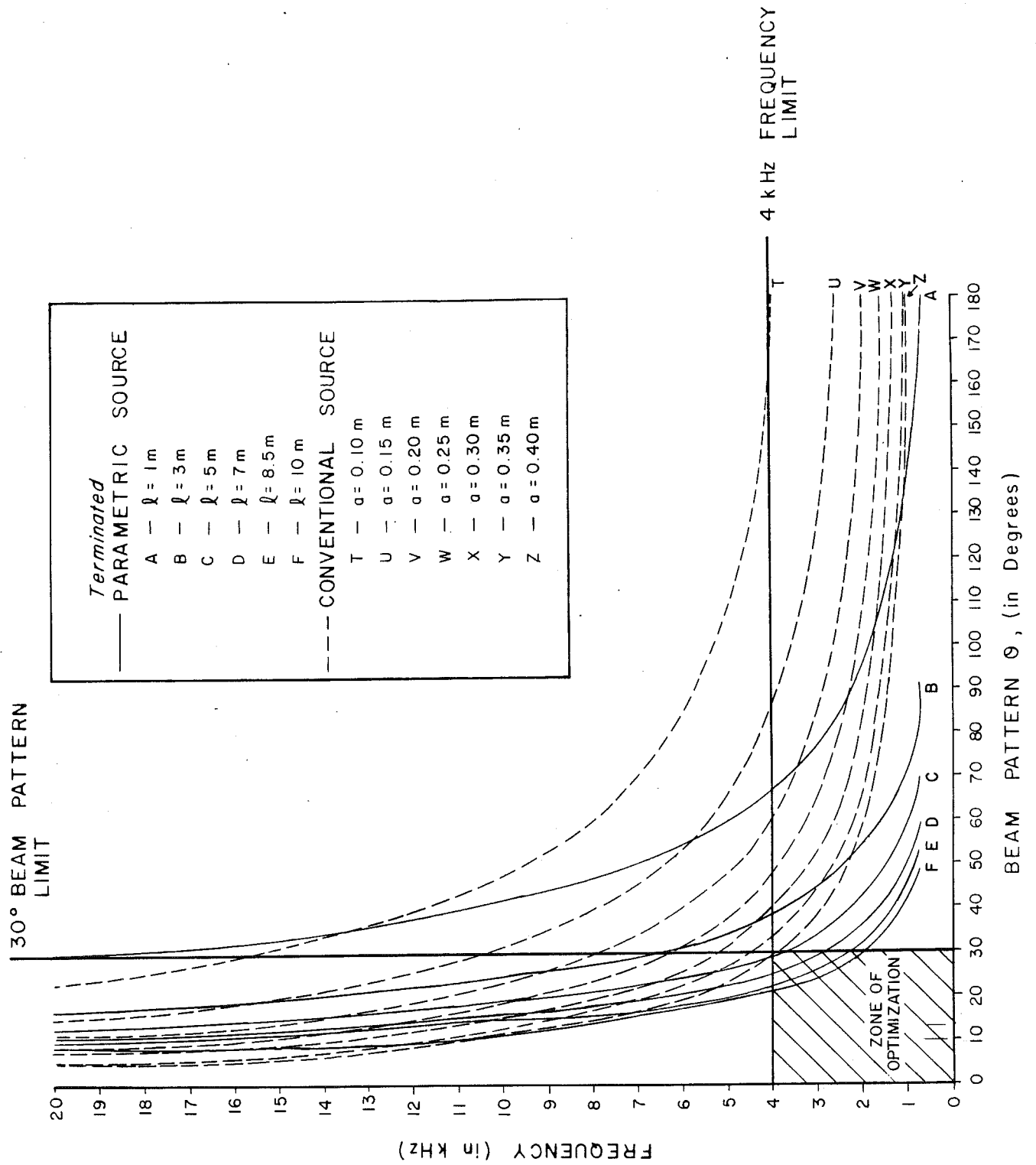


FIGURE 3.22 Approximate Beam Pattern versus Frequency

This provides a very close estimate of $J_1(x)$.

According to Kinsler and Frey (1982) a good approximation for large values of $x > 2\pi$ would be

$$J_1(x) \approx \frac{\sqrt{2}}{\pi x} \cos\left(x - \frac{3}{4}\pi\right) \quad (3.103)$$

In our evaluation of $J_1(x)$ for an argument of (x) greater than 2, expression (3.103) was found to be satisfactory.

Functional behaviour curves were drawn for both the Conventional and terminated Parametric Sources (refer to Figure 3.23(a and b)). While the curves for different frequencies fall on the same behaviour curve for the Conventional case, different behaviour curves occur for different frequencies and heights for the terminated Parametric source.

Figure 3.24(a and b) utilized polar plots to illustrate and to compare beam patterns for both sources at different frequencies using the formula $\text{dB} = 20 \log_{10} B(\theta)$ to convert $B(\theta)$ into dB. A volume for the truncated cone at the k^{th} layer can now be resolved since the beamwidth establishes the shape of the volume cone.

The primary concern in the model is to define a realistic composition of boulder/cobble sizes which would reflect the highly erratic character of a glacial till. S_{V_k} is therefore computed given

Conventional Source

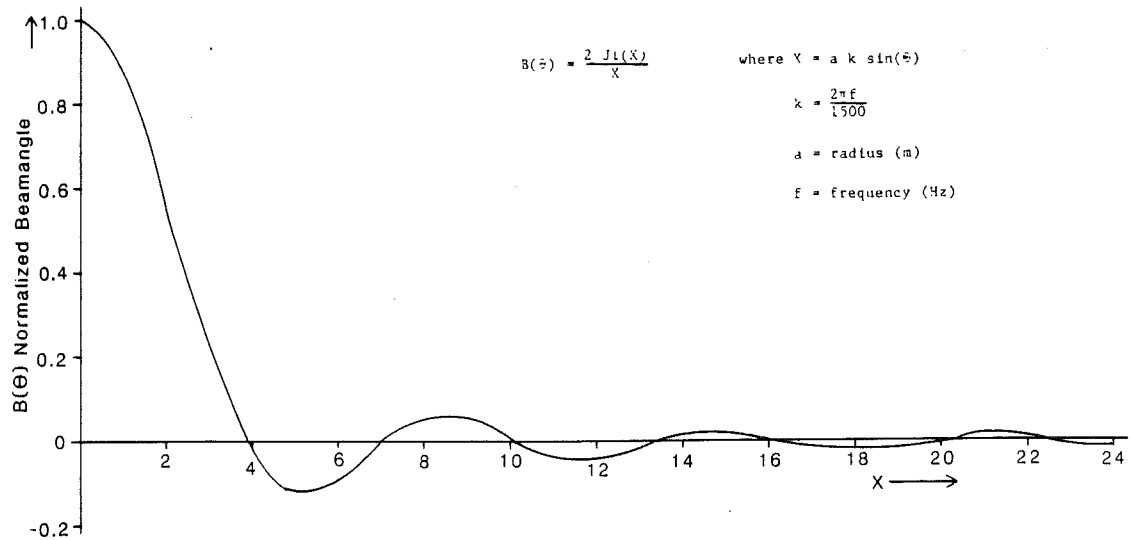


Figure 3.27a For all cases of f_0 and Q

Terminated Parametric Array

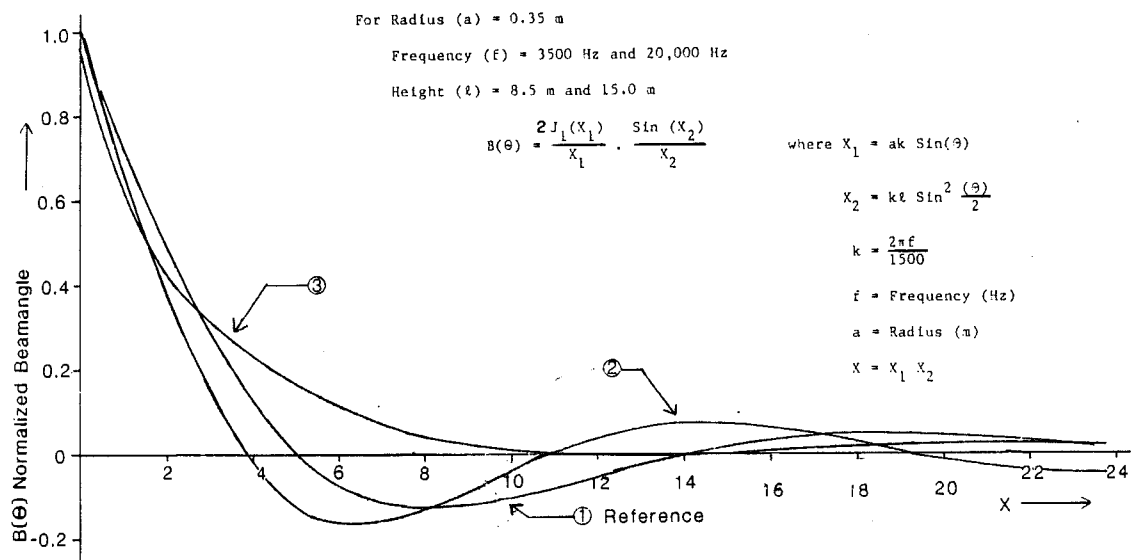
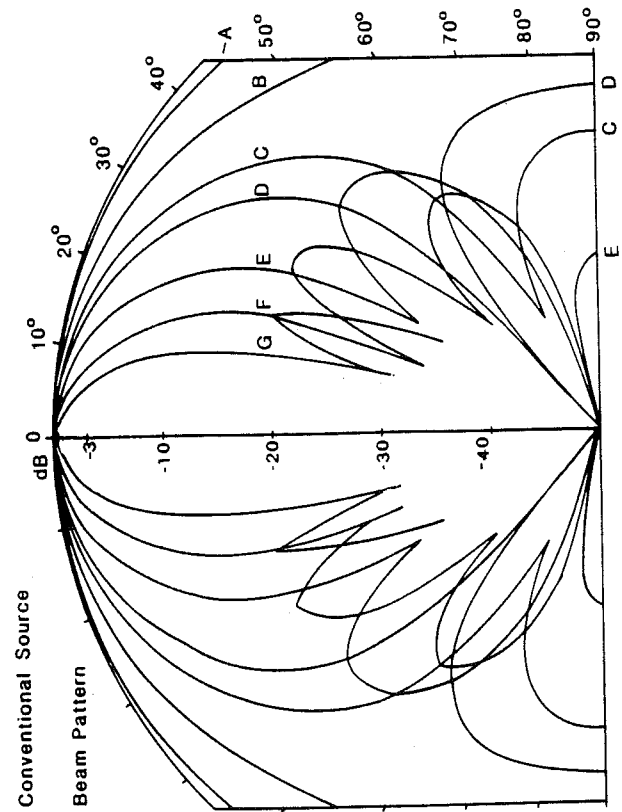


Table of comparison

NQ	Radius (m)	Frequency (Hz)	Height (m)
①	0.35	3500	8.5
②	0.35	3500	15.0
③	0.35	20000	8.5

Figure 3.27b At Different Frequencies and Heights

FIGURE 3.23 Functional Behaviour Curves for a Conventional Source and for a Terminated Parametric Array.



A = 0.35m

Frequency (Hz)	Beamangle(°)	
	-3dB	-10dB
1000	A	*∞
2000	B	130
3000	C	78
3500	D	35
5000	E	24.5
7000	F	16.5
10000	G	12

$$B(\theta) = 2 \frac{J(X)}{X}$$

where: $X > 2$;

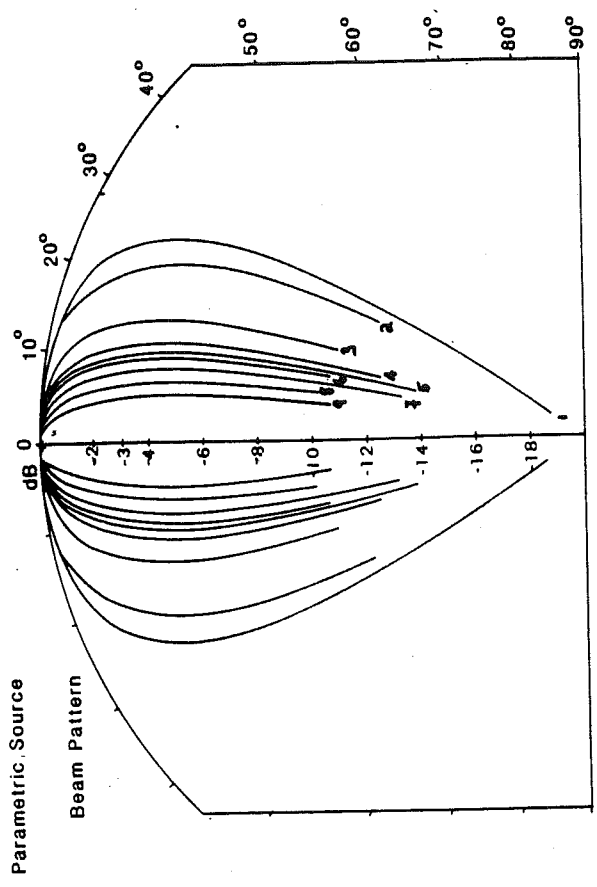
$$2 \frac{J(X)}{X} = \sqrt{\frac{2}{\pi X}} \cos(X - \frac{3}{4}\pi)$$

and

$$2 \frac{J(X)}{X} = \sum_{s=0}^{\infty} \frac{(-1)^s X^{2s+1}}{(2s+1)!} / (s!(s+1)!)$$

*∞ = Omni directional

Figure 3.28a Conventional Source



f = 8.5m A = 0.35m

Frequency (Hz)	Beamangle B(θ) (°)	
	-3dB	-10dB
1	52	65
2	44	59
3	30	40
4	24	32
5	22	30
6	20	28
7	17	24
8	14	20
9	11	16

$$B(\theta) = \frac{2J(X)}{X} \cdot \frac{\sin(X/2)}{X/2}$$

where: $X > 2$;

$$2 \frac{J(X)}{X} = \sqrt{\frac{2}{\pi X}} \cos(X - \frac{3}{4}\pi)$$

and

$$2 \frac{J(X)}{X} = \sum_{s=0}^{\infty} \frac{(-1)^s X^{2s+1}}{(2s+1)!} / (s!(s+1)!)$$

dB = 20log₁₀ (B(θ))

Figure 3.28b Terminated Parametric Array

FIGURE 3.24 Calculated Beam Patterns for a Conventional Source and for a Terminated Parametric Array.

the permutations of the sizes and saturation percents presented below since it is addressed through the number and the scatter cross section of the elements within a kth volume:

- i) Sizes (diameter in metres) {0.1, 0.25, 0.5 and 1.0}.
- ii) Numbers (%) {1, 50 and 100}.

The following table transforms these permutations into values for S_V :

<u>Size</u> (diameter in metres)	<u>j</u> (in %)	Φ_p (radian)	j_p (number)	Φ_c (radian)	j_c (number)	σ_v (per metre)	S_V (dB)
.1	1	0.19	4.3 E 4	0.31	1.1 E 5	0.3	-16.2
	50	0.19	2.2 E 6	0.31	5.7 E 6	15.0	0.8
	100	0.19	4.3 E 6	0.31	1.1 E 7	30.0	3.8
0.25	1	0.19	2.8 E 3	0.31	7.3 E 3	0.1	-20.2
	50	0.19	1.4 E 5	0.31	3.6 E 5	6.0	-3.2
	100	0.19	2.8 E 5	0.31	7.3 E 5	12.0	-0.2
0.50	1	0.19	3.4 E 2	0.31	9.1 E 2	0.06	-23.2
	50	0.19	1.7 E 4	0.31	4.5 E 4	3.0	-6.2
	100	0.19	3.4 E 4	0.31	9.1 E 4	6.0	-3.2
1.0	1	0.19	4.3 E 1	0.31	1.1 E 2	0.03	-26.2
	50	0.19	2.2 E 3	0.31	5.7 E 3	1.5	-9.2
	100	0.19	4.3 E 3	0.31	1.1 E 4	3.0	-6.2

The stated terms ϕ and j were calculated for a terminated Parametric Array (subscript p) and a Conventional Source (subscript c) having an f_d and f_o of 3500 Hz.

3.4.6.3 Modelling of a Realistic Basal Till Composition and Structure

A glacial till accumulation is rarely sorted or composed of one clast size. Therefore an agglomeration of particle sizes must be considered in the final structure of Layer 5. To accommodate the wide range of potential compositions of a till deposit, four cases are specifically developed. The first case emphasizes the presence of cobbles in a fine matrix while the third case highlights the predominance of a bouldery composition embedded into a matrix of fine sediment. The second case is a mixture of cobbles, boulders and very fine particulates. The last case represents a more typical Basal Till composition as observed in specific moraines found offshore. Its composition ranges over a wide particulate size domain covering boulders, cobbles and coarse gravel imbedded in a very fine stiff clay/silt base. The four cases described are illustrated below:

Basal Till Composition Proposed for the Stratigraphic Model

<u>Case</u>	<u>Volume (in %)</u>	<u>Size (diameter in metres)</u>	<u>Description</u>
I	5	0.5	- Diffuse scatter off a dominance of cobbles
	10	0.25	
	40	0.1	
	45	VFM	
II	10	1.0	- Scatter off a mixture of boulders and cobbles
	15	0.5	
	15	0.25	
	15	0.1	
	45	VFM	

III	35	1.0	- Point source scatter off boulders
	15	0.5	
	5	0.25	
	45	VFM	
IV	2	0.5	- Typical glacial till particulate distribution and composition
	2	0.25	
	16	0.2	
	10	0.1	
	70	VFM	

(where VFM is a very fine stiff matrix such as a clay base)

Calculating σ_v and S_v for the four cases gives:

Case	Size (dia.m)	Φ_p (radian)	j_p (number)	Φ_c (radian)	j_c (number)	σ_v (per metre)	S_v (dB)
I	0.5	0.19	1723	0.31	4534	13.5	0.3
	0.25		27575		72554		
	0.1		1723465		4534640		
	VFM		-		-		
II	1.0	0.19	430	0.31	1133	7.5	-2.2
	0.5		5170		13603		
	0.25		41363		108831		
	0.10		646299		1700490		
	VFM		-		-		
III	1.0	0.19	1508	0.31	3967	2.5	-6.9
	0.5		5170		13603		
	0.25		13787		36277		
	VFM		-		-		
IV	0.5	0.19	689	0.31	1813	5.8	-3.4
	0.25		5515		14510		
	0.2		86173		226732		
	0.1		430866		1133660		
	VFM		-		-		

where Φ and j are stated for a terminated Parametric Array and for a Conventional Source having an f_d and f_o of 3500 Hz. σ_v and S_v are controlled by particulate size and by number in a specific volume, hence no specific subscripts.

3.4.6.4 Evaluation of each Layer's Reverberation Level

Finally the Reverberation Levels (RL) for the three cases can be calculated in reference to the modelling of Section 3.3.3. Recapping:

i) Terminated Parametric Source

R_i	$f_{d\max R_k}$	Φ_{R_k}	$\bar{\tau}_k$	Ω_{R_k}	SL'_{R_k}	$TL_{D R_i}$	$TL_{U R_k}$
(m)	(Hz)	(radians)	(ms)		(dB re 1 μ pa)	(dB)	(dB)
			- 0.05 -				
1.0	86956	0.01		0.8 E-3	224.8	21.1	17.6
			- 0.01 -				
10.0	8696	0.1		4.0 E-2	184.8	26.9	23.4
			- 0.20 -				
11.6	7692	0.1		4.4 E-2	182.7	27.7	24.0
			- 0.38 -				
20.0	3077	0.2		1.6 E-1	166.7	30.8	26.6
			- 0.51 -				
30.0	1183	0.3		0.4	150.1	33.5	28.7
			- 1.00 -				
40.0	702	0.5		0.8	141.1	35.8	30.2

where SL'_{R_k} was derived in accordance with expression (3.86). The four

cases of TSR_{R_k} , RL and SRR are presented in Figure 3.25. These were

calculated on the understanding that $\Omega_{R_k} = 0.1$, $c_k = 1800$ m/sec,

$$\bar{\tau}_k = 1.0 \times 10^{-3} \text{ sec, } k=1, \text{ SRR} = \text{TS} - \text{TSR}_{R_k}, \Gamma = 10 \log \left[\sum_{k=1}^n (\text{TSR}_{R_k}) \right]_{R_k}$$

and $TSR_{R_k} = \Gamma - TL_U$. Similarly, recapping for a Conventional Source:

i) Terminated Parametric Source

R_i (m)	<u>Case I</u>		<u>Case II</u>		<u>Case III</u>		<u>Case IV</u>	
	Γ	$\frac{TSR_{R_k}}{k}$ (dB)	Γ	$\frac{TSR_{R_k}}{k}$ (dB)	Γ	$\frac{TSR_{R_k}}{k}$ (dB)	Γ	$\frac{TSR_{R_k}}{k}$ (dB)
1.0	-	-	-	-	-	-	-	-
10.0	-	-	-	-	-	-	-	-
11.6	-	-	-	-	-	-	-	-
20.0	-	-	-	-	-	-	-	-
30.0	-	-	-	-	-	-	-	-
40.0	-4.2	26.0	-6.7	23.4	-11.5	18.7	-7.9	22.3
		101.1		98.2		93.8		97.1
		(dB re 1 μ pa)		(dB re 1 μ pa)		(dB re 1 μ pa)		(dB re 1 μ pa)

$SRR_1 = -0.4$ $SRR_2 = 2.2$ $SRR_3 = 6.9$ $SRR_4 = 3.3$

Note: The bar (-) in place of a value denotes a null effect.

ii) Conventional Source

R_i (m)	<u>Case I</u>		<u>Case II</u>		<u>Case III</u>		<u>Case IV</u>	
	Γ	$\frac{TSR_{R_k}}{k}$ (dB)	Γ	$\frac{TSR_{R_k}}{k}$ (dB)	Γ	$\frac{TSR_{R_k}}{k}$ (dB)	Γ	$\frac{TSR_{R_k}}{k}$ (dB)
1.0	-	-	-	-	-	-	-	-
10.0	-	-	-	-	-	-	-	-
11.6	-	-	-	-	-	-	-	-
20.0	-	-	-	-	-	-	-	-
30.0	-	-	-	-	-	-	-	-
40.0	5.4	35.6	2.8	33.0	-1.9	28.2	1.6	31.9
		151.1		148.5		143.7		147.4
		(dB re 1 μ pa)		(dB re 1 μ pa)		(dB re 1 μ pa)		(dB re 1 μ pa)

$SRR_1 = -10.6$ $SRR_2 = -8.0$ $SRR_3 = -3.2$ $SRR_4 = -6.9$

FIGURE 3.25 RL for the Four Case Histories

ii) Conventional Source

R_i	$f_{\max R_k}$	Φ_{R_k}	$\bar{\tau}_k$	SL'_{R_k}	$TL_{D R_i}$	$TL_{U R_k}$
(m)	(Hz)	(radians)	(ms)	(dB re 1 μ pa)	(dB)	(dB)
			- 0.57	-		
1.0	3770	0.3		215.2	21.1	17.6
			- 0.59	-		
10.0	3370	0.3		208.1	26.9	23.4
			- 0.61	-		
11.6	3316	0.3		207.0	27.7	24.0
			- 0.65	-		
20.0	2693	0.4		297.4	30.8	26.6
			- 0.86	-		
30.0	1590	0.7		184.5	33.5	28.7
			- 1.50	-		
40.0	836	$\pi/2$		181.4	35.8	30.2

Where SL'_{R_k} is stated in accordance with expression (3.87).

The four Basal Till cases are evaluated from this data set. Their results are also shown in Figure 3.25 . It should be noted that the following was used for the calculations: $f_{\max R_k} = 1590$ Hz, $\bar{\tau}_k = 1.5 \times 10^{-3}$ sec, $c_k = 1800$ m/sec, $k=1$, $SRR = TS - TSR_{R_k}$, $\Gamma = 10$

$$\log \left[\sum_{k=1}^n (TSR_k) \right]_{R_k} \text{ and } TSR_{R_k} = \Gamma - TL_U.$$

3.5 Synopsis

The results of the analysis pertaining to the Echo Level, Detected Noise Level and Reverberation Level with depth as seen by a hydrophone at or near the seabed are brought together in Figure 3.26. This presentation does highlight in a concise manner, the limits of the terminated Parametric Source and those of a Conventional System.

It is seen from this figure that although the Echo Level for the Conventional Source is much stronger than for the terminated Parametric Array their differences in terms of Reverberation Level clearly favours the Parametric approach. While the Conventional Source is reverberation limited the Parametric approach is noise limited. The Signal-to-Reverberation Ratios calculated for the four Basal Till cases are significantly better for the Parametric Source. Overall this type of transmission demonstrates a distinct advantage in conditions of reverberation. Ambient noise however becomes a primary concern because of the lower Source Level akin to Parametric Arrays.

The question at the start of Chapter 3.0 "Is it possible to get a signal back" is answered with a qualified "yes". The terminated Parametric Array's wider bandwidth, narrower beamwidth, and short transient pulse are distinctly noted in these evaluations as being important to the coherent scanning of a morainic seabed. The lower level of signal makes it more susceptible to being limited by noise. Therefore its receiving array requires careful planning in a manner that would reduce the effect of noise. Coherent signal averaging is also a first necessity to ensure a suitable Echo Level exists.

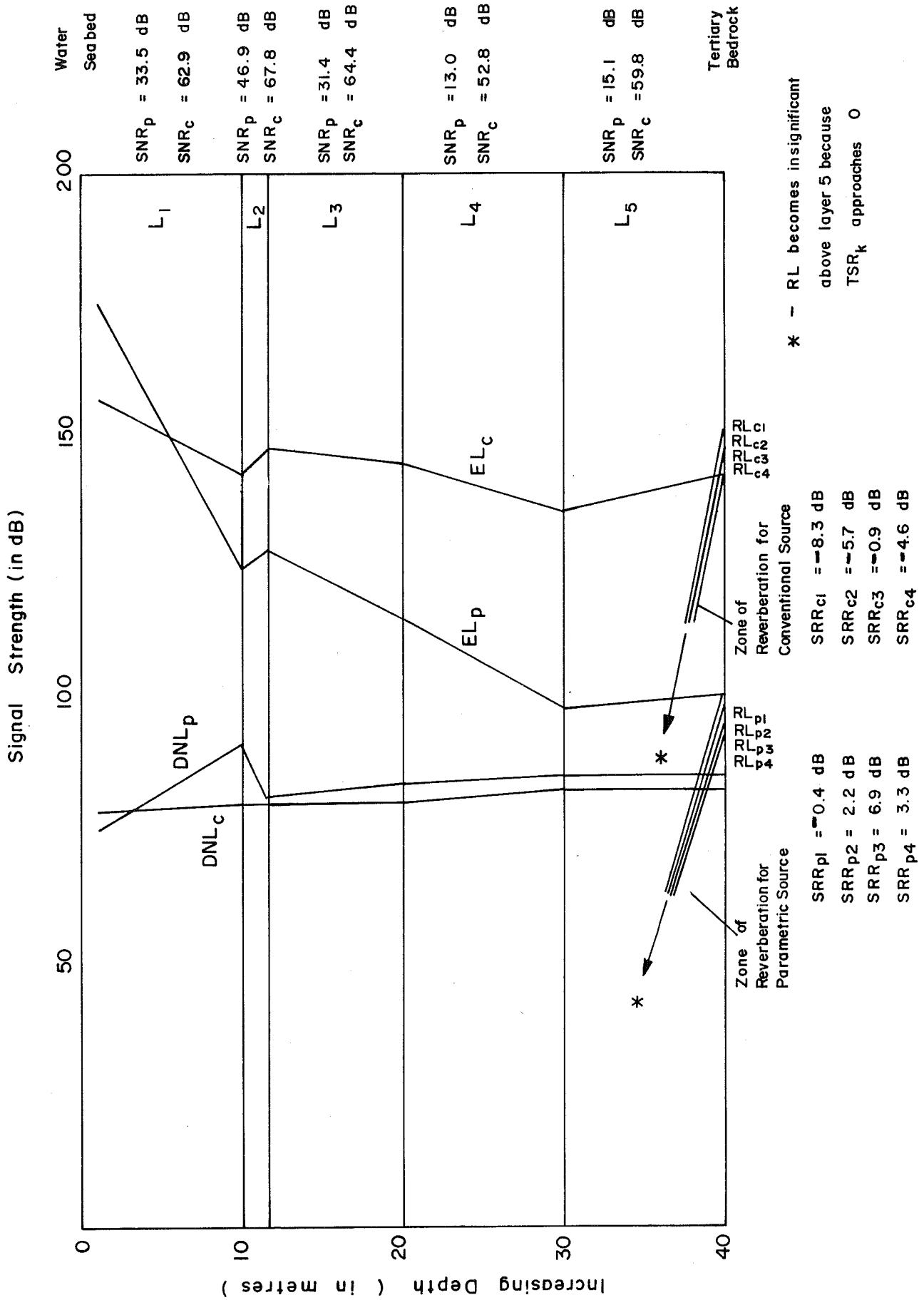


FIGURE 3.26 EL, DNL and RL Evaluations Versus Depth.

4.0 EXTRACTION OF SUB-SEABED INFORMATION FROM THE RETURNED SIGNALS

4.1 Foreword

It was established in the analysis of Chapter 3.0, that it is feasible to get a signal back from a complex layered sedimentary column of high attenuation and of high scatter using a terminated Parametric Array. The stationary position provided by the ASI's operational mode would help raise the low Signal-to-Noise Ratio by supporting coherent signal averaging. Once a signal is received and is identified as a primary echo then the next step is to extract from it, information relating to sub-seabed structure and composition. From Vetter (1984):

"Seismic probing involves the generation of some energetic disturbance in a medium, which in its simplest form consists of the displacement of some medium particles from their equilibrium positions. The disturbance imparts energy to the medium in the form of kinetic energy (particle motions) and potential energy (local deformations, or compressional energy in the case of liquids and gases) in the vicinity of the source; that energy is then propagated through the medium in the form of wave motions, through the mechanism of continuous conversion of the energy between its kinetic and potential states. Details of the propagation phenomenon depend on the nature of the disturbance and on the spatial distribution of the medium parameters which are involved in the energy interactions."

Waves propagating into a seabed may encounter variations in the sedimentary composition of the medium. If a significantly different gradient occurs, a reversal in the wave's propagation will result with a portion of the wavefront energy returning to the surface. Information pertaining to the seabed's geomorphology and geotechnical

properties can be interpreted from the character of the reflected energy and from the arrival time of the returned wave to a set of sensors. Along with the arrival of this primary reflection, other energy will also follow in the form of diffraction, reflected refraction and multiple reflections. Section 4.2 examines a variation of Normal Moveout which has been modified to precisely discriminate between true primary returns from multi-echo paths. In this approach the use of a spatial coherency network is exploited to enhance the acquisition of angular information, time and spatial position. An estimate of velocity is obtained for each layer by employing this technique (see Section 4.2.3). Complementing this Normal Moveout application is the capability of the receiving array to focus. Focussing is meant to improve or sharpen the lateral resolution aspect of the ASI (refer to Section 4.3).

The time history data are manipulated using the Hilbert Transform. Through this method the peak positions of the magnitude or envelope of the signals can be determined. This forms a unique and precise time reference for each echo return. The theoretical treatment of the Hilbert Transform is briefly introduced in Section 4.4. An "Acoustic Core" is then created. This is highlighted in Section 4.5. The central design of the ASI's interrogation pivots on the development of the "Acoustic Core" product.

4.2 Detection of Primary Reflections using a Moveout Technique

A very powerful approach to separate reflections, diffractions, reflected refractions and multiples is to apply dynamic moveout corrections (Sheriff (1982)). Moveout refers to a systematic difference from trace to trace in the arrival time of an event in reference to a hydrophone position. These arrival time differences are well documented in the marine geophysical literature and can be explained by: (see Sheriff (1978), Keary and Brooks (1984) and Robinson (1980)).

- i) the variations in transmitter to receiver distance along the reflection paths (referred to as Normal Moveout)
- ii) the effect of a reflector dip (called the Dip Moveout)
- iii) the elevation and weathering variations (usually considered as Static Moveout)

By removing the Normal Moveout, primary reflections appear as straight lines. Diffractions and multiples on the other hand will show some curvature since their Normal Moveout are greater than that of the first order reflections. Refractions which generally are aligned in a straight fashion before moveout, demonstrate an inverse curvature after the correction is applied.

In exploration seismics, the travel distance to the hydrophone is gradually increased for successive traces of a collection to ensure that the reflected energy will arrive later in time. This provides for a calculated time delay (i.e. Normal Moveout). To apply the technique of Normal Moveout the transmission path requires some form of lateral

distance and time variation. Unfortunately, the magnitude in time of a Normal Moveout is only significant when the propagation distances are great. The time differences are found to be too small in relation to pulse length to be effective when Normal Moveout is applied to shallow overburden depths such as for sediment thicknesses of less than 100 metres, typical of Quaternary sediments.

4.2.1 Establishing an Interrelationship between θ , t , and z

A dynamic variation on Normal Moveout can however be manipulated through the introduction and the application of precise angular information. If the transmission angle is accurately known then the time of arrival can be predicted for a given geometry. Since the horizontal position of the arrivals can be established along the extent of a receiving array, a triangular relationship develops between

- i) angle (θ) and time (t)
- ii) time (t) and horizontal position (z)
- iii) angle (θ) and horizontal position (z)

A discriminant results from the simultaneous application of all three relationships. A predictive time and horizontal position argument can be computed for all cases of θ after the arrival time is initially recorded when θ is 0° . (see Figure 4.1). For example:

When $\theta = 0^\circ$

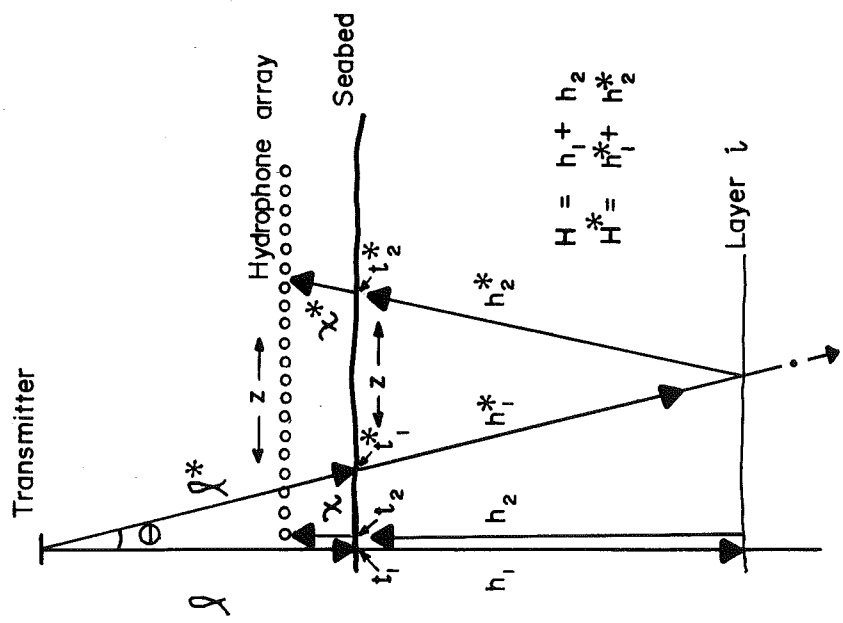


FIGURE 4.1a Transmission and Reception Geometry for the ASI

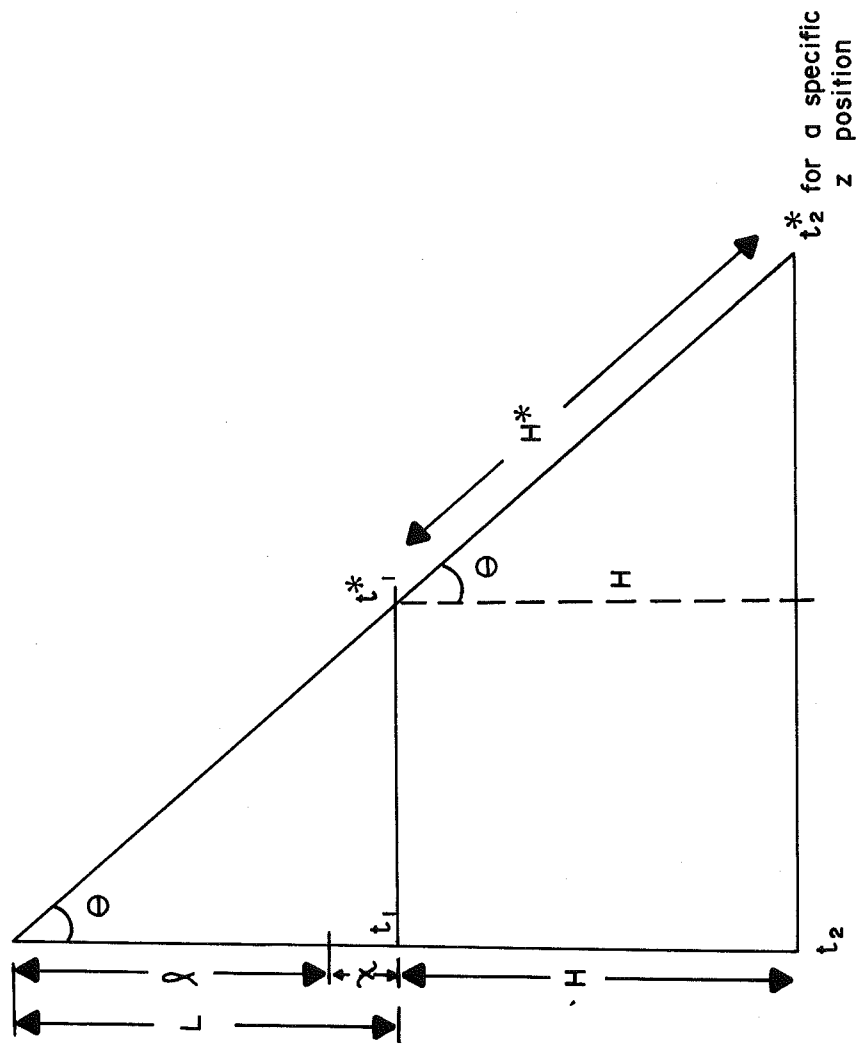


FIGURE 4.1b Geometry for the Normal Moveout Time and Angle Calculations based on Figure 4.1a

FIGURE 4.1 Geometry Used in the Normal Moveout Calculations

$$H = c\Delta t = c(t_2 - t_1) \quad (\text{for a specific } z) \quad (4.1)$$

given that;

- i) ℓ is the height from the transmitter to the seabed
- ii) χ is the height from the hydrophone array to the seabed
- iii) subscripts refer to the interface separating the layers as well as the layer itself
- iv) c is the velocity of the medium
- v) H is a two way travel distance
- vi) t is an arrival time
- vii) θ refers to a specific transmission angle
- viii) z identifies an exact position on the hydrophone array

If $\theta \neq 0^\circ$ then

$$H^* = \frac{H}{\cos \theta} = \frac{c\Delta t}{\cos \theta} \quad (\text{for a specific } z) \quad (4.2)$$

The asterisk * refers to a slant range path dictated by θ (when $\theta \neq 0$).

Δt^* can therefore be defined as;

$$\Delta t^* = \frac{H^*}{c} = \frac{c\Delta t}{c \cos \theta} = \frac{\Delta t}{\cos \theta} = \frac{t_2 - t_1}{\cos \theta} \quad (4.3)$$

and as;

$$\Delta t^* = t_2^* - t_1^* \quad (4.4)$$

Hence by substitution

$$t_2^* = \frac{t_2 - t_1}{\cos \theta} + t_1^* \quad (\text{for a specific } z) \quad (4.5)$$

Finally, it follows that for all cases:

$$t_n^* = \frac{t_n - t_{n-1}}{\cos \theta} + t_{n-1}^* \quad (\text{for a specific } z) \quad (4.6)$$

Thus, the arrival time of any primary reflection can be easily predicted for any angle using the time/angle relationship stated in expression (4.6). The arrival of the signal at a particular position along the horizontal axis sets the value of z .

The identification of a multiple path return from a primary echo coincident in time, uses as a discriminant the differences in position along z for a particular angle θ . In other words, a multiple would not arrive at the same position z , given a complimentary arrival time for a set angle θ .

4.2.2 Developing a Procedure to Systematically Identify True Echoes from Multiples

A procedure can now be installed to identify true echoes from multiples by applying a logical process of cross referencing and of elimination. The two steps that form this procedure are described below. Figure 4.2 graphically presents the terminology used and

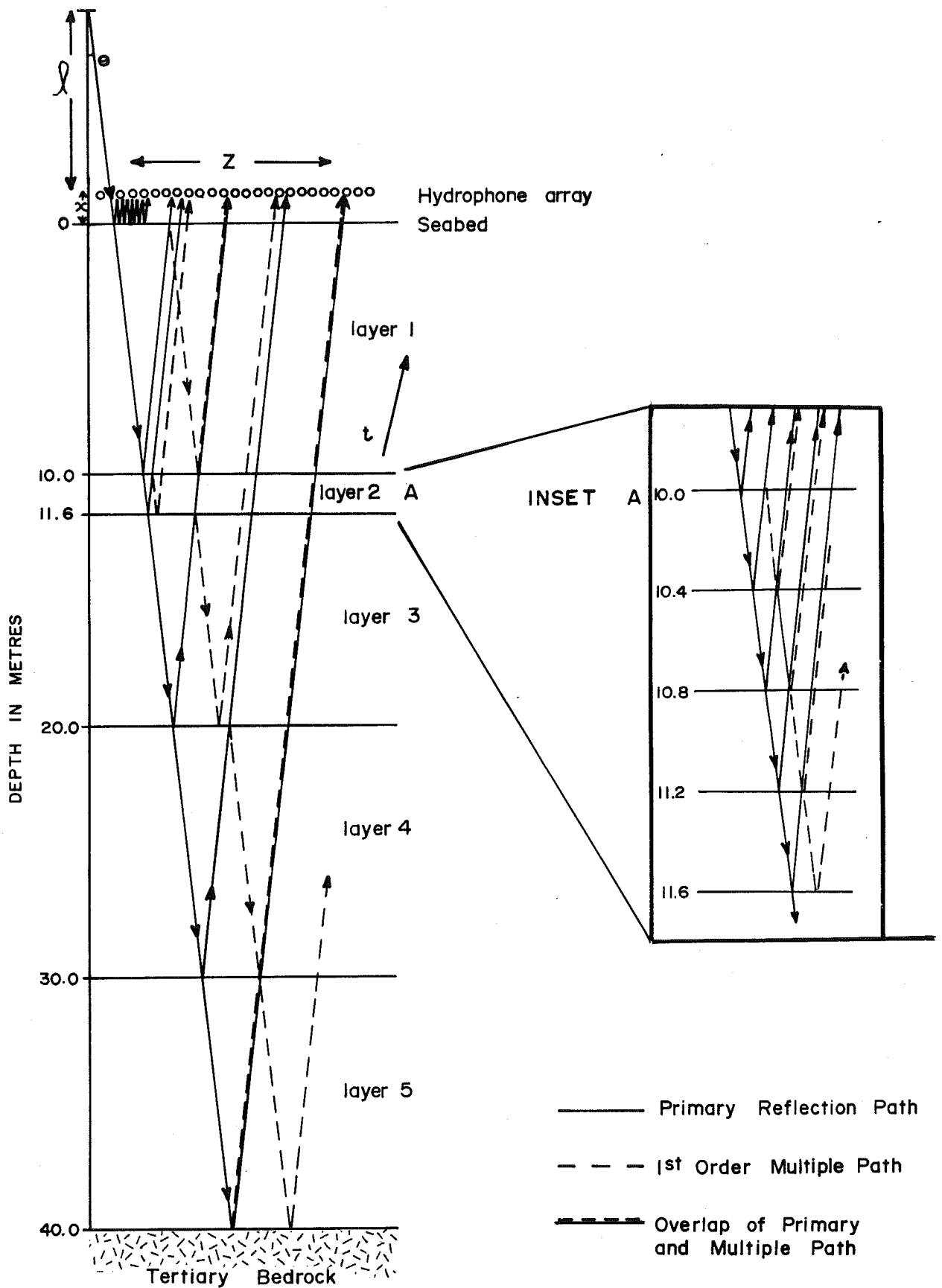


FIGURE 4.2 Primary Reflection and 1st Order Multiple Ray Geometry as Applied to the Stratigraphic Model

therefore should be closely referred to. The prime notation (') will consistently refer to a multiple path return.

i) Step 1

To initiate the approach, the arrival time (T) and position (z) of the seabed return are captured. The multiples that may be associated with the seabed/water boundary are accounted for or identified by their frequency content and therefore are discounted immediately. The next echo that could follow the seabed reflection (and its multiples) is a signal coming off the first sub-seabed layer. This can be easily corroborated.

Using the information corresponding to the seabed echo and to the first layer reflection, the first order multiple off Layer 1 is then predicted for a selected transmission angle θ . For instance, by applying the seabed echo's time of arrival and its position z the following computations develop:

$$z_o = \lambda \tan(\theta) + \chi \tan(\theta) \quad (4.7)$$

$$= (\lambda + \chi) \tan(\theta) \quad (4.8)$$

This will set for Layer 1

$$d_1 = (z_1 - z_o)/2 \quad (4.9)$$

The travel time of the first order multiple ($t'_1(\theta)$) reflected within the upper and lower boundaries of Layer 1 is expressed in terms of a two-way travel (slant) time ($t_1(\theta)$).

$$t'_1(\theta) = 2t_1(\theta) \quad (4.10)$$

Likewise, the total time (T'_1) is written to include the travel time from the transmitter into the layer plus the time for a multiple reflection to take place in addition to the departure time out of the layer until the signal is captured at a position z .

$$T'_1(\theta) = T_1(\theta) + (t'_1(\theta)/2) \quad (4.11)$$

$$= T_1(\theta) + t_1(\theta) \quad (4.12)$$

Finally, the position z is predicted for the first layer multiple by applying

$$z'_1 = z_1 + 2d_1 = 2z_1 - z_0 \quad (4.13)$$

ii) Step 2

The received signal following the Layer 1 echo return is correlated with the predicted multiple path time $T'_1(\theta)$ and position z'_1 . If the echo time and position correspond, it is then identified as the multipath return associated with Layer 1. If they do not accord within

an established error range, then the signal is interpreted to belong to a true primary reflection coming off Layer 2. Hence the Layer 2 primary echo is identified. Following this, the predictive iterations are applied again for the multiples that might result within the physical confines of Layer 2. A correlation is made with the actual reflection arrival times and positions. An identification of either a true echo or of a multiple results. The procedure is then repeated for the next set of signals.

The position and time for multiples of any layer n can be found by employing

$$T'_n(\theta) = T_n(\theta) + t_n(\theta) \quad (4.14)$$

and

$$z'_n = z_n + 2d_n = 2z_n - z_{n-1} \quad (4.15)$$

given that $d_n = (z_n - z_{n-1})/2$.

As an example, the following primary echo's and associated first order multiple's time and position are calculated for the five layers of the Stratigraphic Model (see Chapter 3.0) for a θ of 3° . The results are also graphically exhibited on Figure 4.3 along with simulations for 6° and 9° angles.

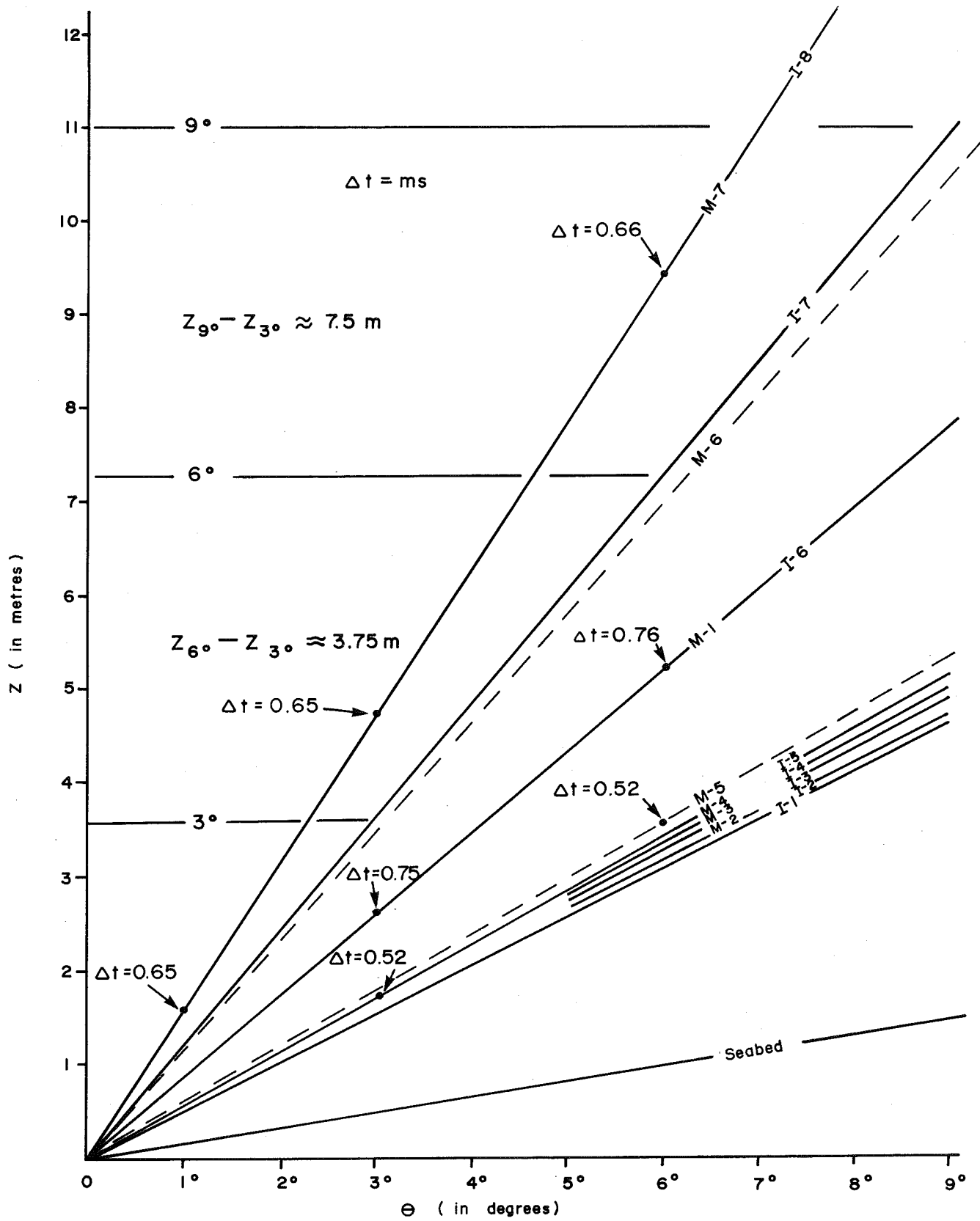


FIGURE 4.3 Results of the Analytical Model Simulation

<u>n</u>	<u>Layer</u>	$\frac{h}{n}$ (m)	[Primary Echoes]		[1st Order Multiples]	
			$\frac{T}{10^{-4}}$ (s)	$\frac{z}{}$ (cm)	$\frac{T'}{10^{-4}}$ (s)	$\frac{z'}{}$ (cm)
1	1	10	196.94	154.61	330.46	259.43
2		0.4	202.19	158.87	207.44	163.13
3		0.4	207.36	163.20	212.53	167.53
4	2	0.4	212.61	167.46	265.14	171.72
5		0.4	217.78	171.80	222.95	176.14
6	3	8.4	322.94	265.72	428.10	359.64
7	4	10	440.80	384.55	441.98	503.38
8	5	10	552.13	510.38	663.46	636.21

Although the closely spaced stratified sequence of Layer 2 does not allow for large discriminant separations to occur in time and horizontal distance they can nevertheless be differentiated as discrete layers.

4.2.3 Deriving a Velocity Value for each Layer

A velocity measurement can now be attempted for each layer given that their z position and time are known. Snell's Law is applied to account for the raypath bending that a propagation will encounter in passing through different densities. Using the transmission angle θ , the resultant propagation angle β can be obtained from:

$$\frac{\sin\theta}{c_0} = \frac{\sin\beta}{c_1} \quad (4.16)$$

and for all cases that follow:

$$\frac{\sin(\beta_n)}{c_n} = \frac{\sin(\beta_{n-1})}{c_{n-1}} \quad (4.17)$$

where $\beta_0 = \theta$

By rewriting expression (4.17), c_n is defined as

$$c_n = \frac{c_{n-1} \sin(\beta_n)}{\sin(\beta_{n-1})} \quad (4.18)$$

Since $\sin(\beta_n) = \frac{d_n}{H_{s_n}}$ then c_n can be stated as

$$c_n = \frac{c_{n-1} d_n}{H_{s_n} \sin(\beta_{n-1})} \quad (4.19)$$

where H_{s_n} refers to the slant height of the ray path in the n^{th} layer

(refer to Figure 4.2). Likewise, c_n can also be denoted by

$$c_n = \frac{2H_{s_n}}{t_n(\theta)} \quad (4.20)$$

Combining expressions (4.19 and 4.20) enacts this relationship:

$$\frac{c_{n-1} d_n}{H_{s_n} \sin(\beta_{n-1})} = \frac{2H_{s_n}}{t_n(\theta)} \quad (4.21)$$

While H_{s_n} is established through

$$H_{s_n}^2 = h_n^2 + d_n^2 \quad (4.22)$$

h_n can be written as

$$h_n = \sqrt{\frac{c_{n-1} d_n t_n(\theta)}{2 \sin(\beta_{n-1})} - d_n^2} \quad (4.23)$$

It therefore follows that

$$c_n = \frac{(2\sqrt{\frac{c_{n-1} d_n t_n(\theta)}{2 \sin(\beta_{n-1})} - d_n^2})}{t_n(0)} \quad (4.24)$$

where $t_n(0)$ is equal to the normal incident arrival time and/or to

$$\frac{h_n t_n(\theta)}{\sqrt{h_n^2 + d_n^2}}, \quad c_o \text{ is the velocity of water, } \beta_o \text{ is the transmission angle}$$

and d_n is equal to $(z_n - z_{n-1})/2$.

This procedure for determining h and c requires iterations that start at the first layer and then follow in a sequential manner. The velocity measurements must also follow suit.

4.3 Horizontal Location of Arriving Echos Using a Spatial Coherency Approach and a Focussing Application

The horizontal location of the returned signals is the most difficult measurement to make of the three components in the dynamic moveout approach suggested in Section 4.2. The technique designed to acquire a more precise position for z uses the highest amplitude over a group (group being a horizontal cluster of receiving elements) to isolate an echo. In practice, the spatial resolution that results is not always of the order required for a precise identification to take place. The echo location in a group can however be sharpened by processing the coherency of the returns over a spatial net. This therefore necessitates some form of scanning offset.

4.3.1 Assembling a Spatial Offset Network

Since the "Acoustic Sub-seabed Interrogator" is a stationary profiler this offset can be established through the physical geometry of the transmitters and of the receptors. On this basis, Figure 4.4 presents an array configuration which allows for four primary scanning offsets to occur called A, B, C and D as well as n number of intermediate secondary offsets (eg: A_1 to A_n). The coherency between each of the four primary and corresponding secondary positions is evoked by signal averaging each receiving element. The averaged group of each position is then averaged together. The peak of the resultant averaged amplitude processed over the four primary sets and if available secondary sets would thus indicate a sharp echo position z , for a particular t and θ .

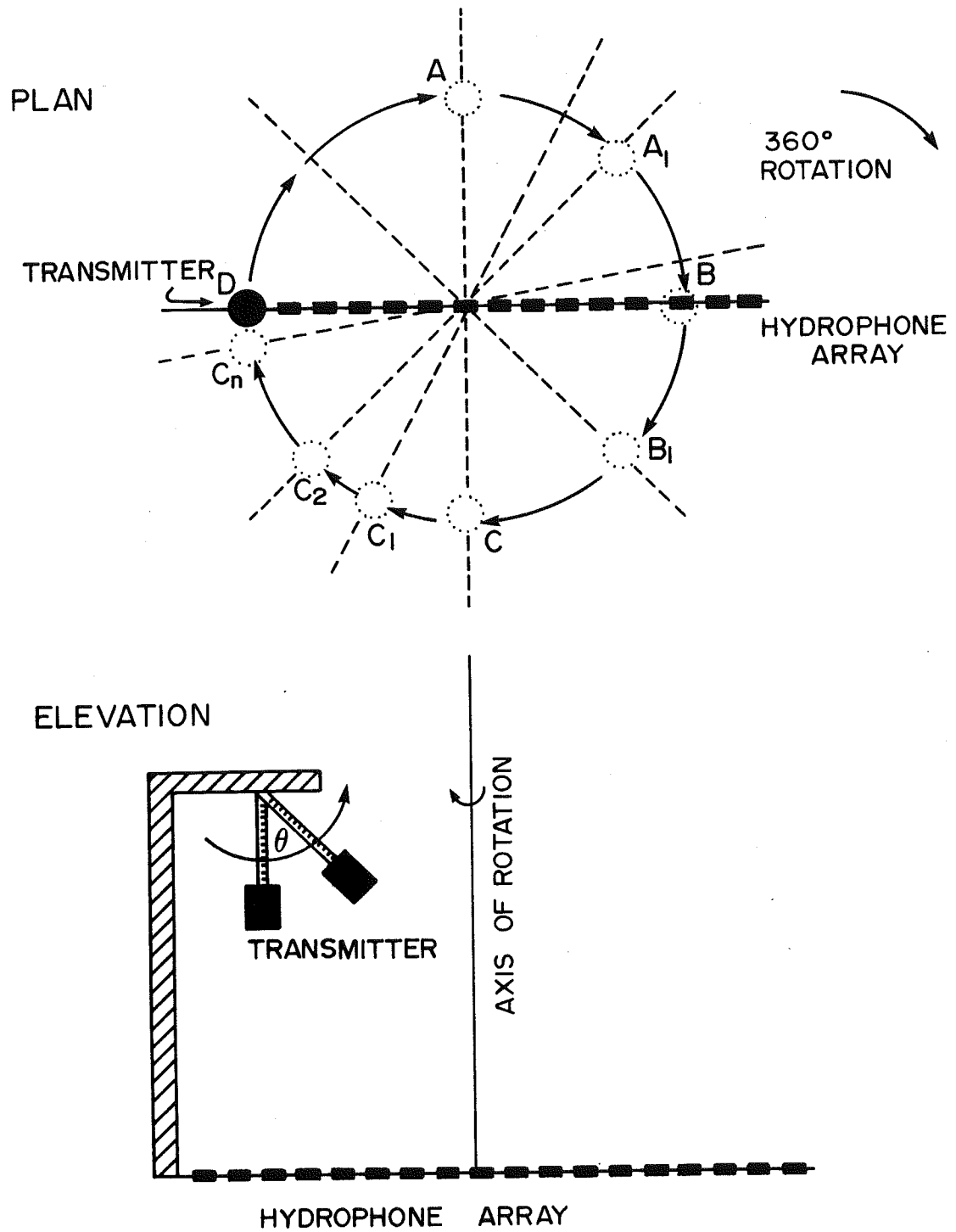


FIGURE 4.4 Configuration of the Spatial Offset Network.

4.3.2 Engaging a Focussing Approach

If the lateral resolution of z is deficient after spatial coherency averaging has taken place for a particular boundary interrogation then the anomaly is further investigated by engaging the receiving array in a focussed mode of operation. This is easily accomplished by applying delays to the digitised output of the individual hydrophone elements along the z -axis then summing all outputs. Adjusting the inter-element phase shifts in this way will cause the signals of the array to converge along the desired interface.

Phase array technology is developed in the literature by such authors as Havlice et al (1974), Yuen et al (1982), and Ong (1978 and 1979). However, focussing down through a medium has not been tried. It is proposed that the phase array be focussed at a particular focal depth where the beam can be made to scan or be steered. Figure 4.5a illustrates the principle of constructive interference between wavefronts arriving at the receiving array. Figure 4.5.b demonstrates the effects of simultaneously focussing and deflecting the sound beam.

In practice, the focus can be swung sideways (as presented in Figure 4.6) and at any depth where a high order of lateral resolution is required. For example, if a bouldery matrix is encountered during the primary interrogation then the returning signals could initially record it as a potential interface. The receiving array is focussed

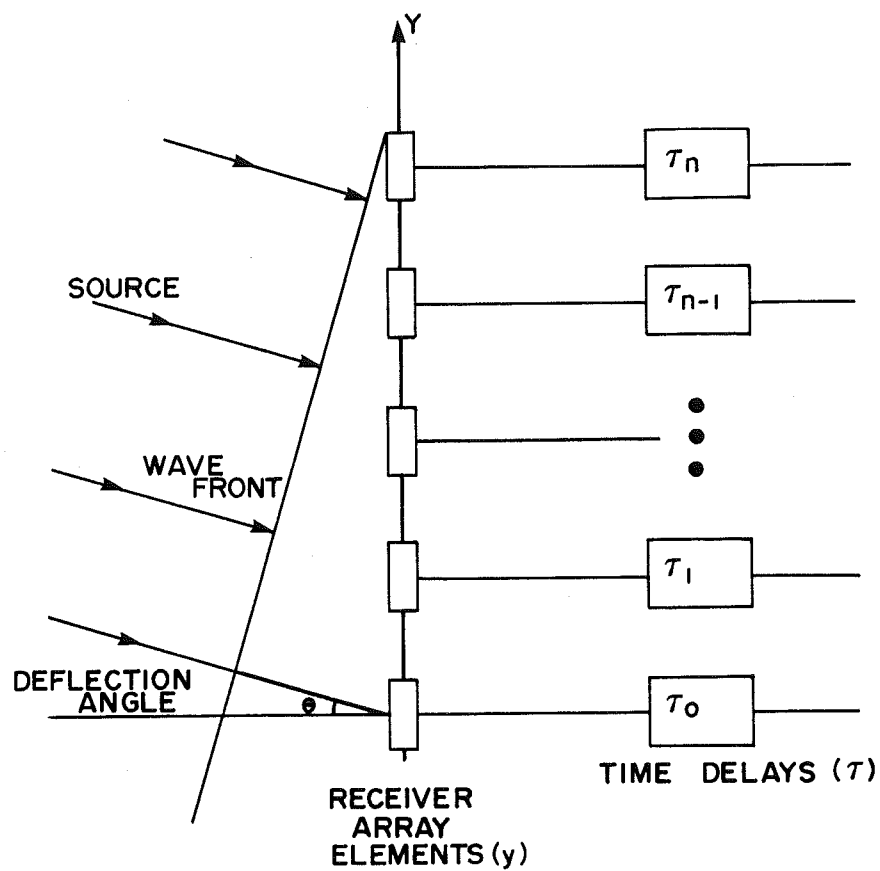


FIGURE 4.5a Constructive Interference Between Wavefronts (modified from Yuen 1982)

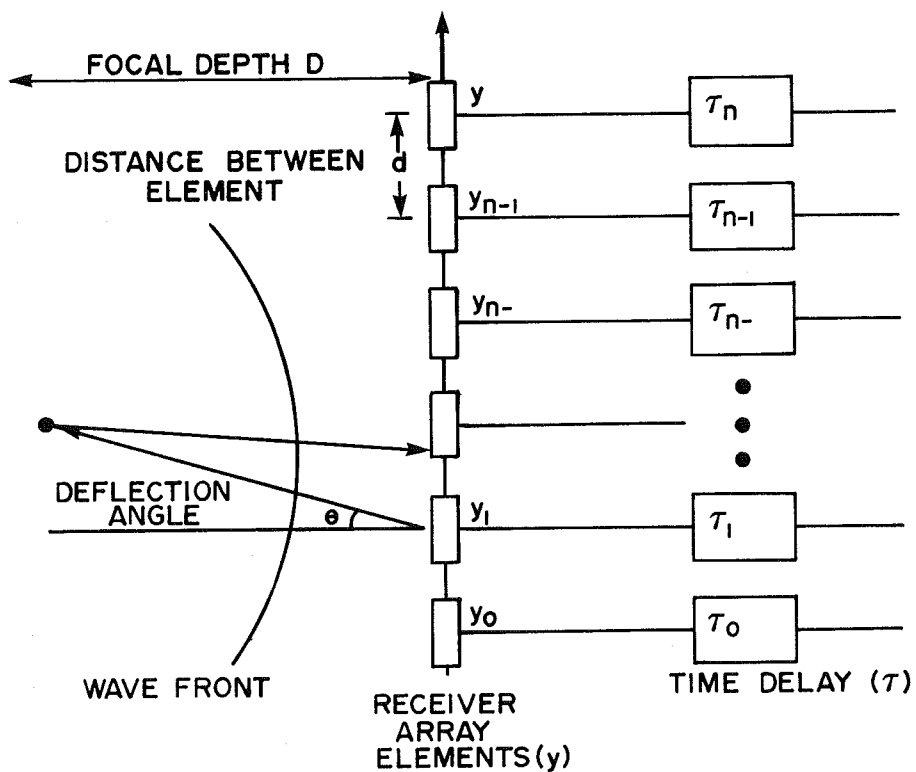


FIGURE 4.5b Effects of Simultaneous Focussing and Deflecting (modified from Yuen 1982)

FIGURE 4.5 Engaging a Focussing Approach

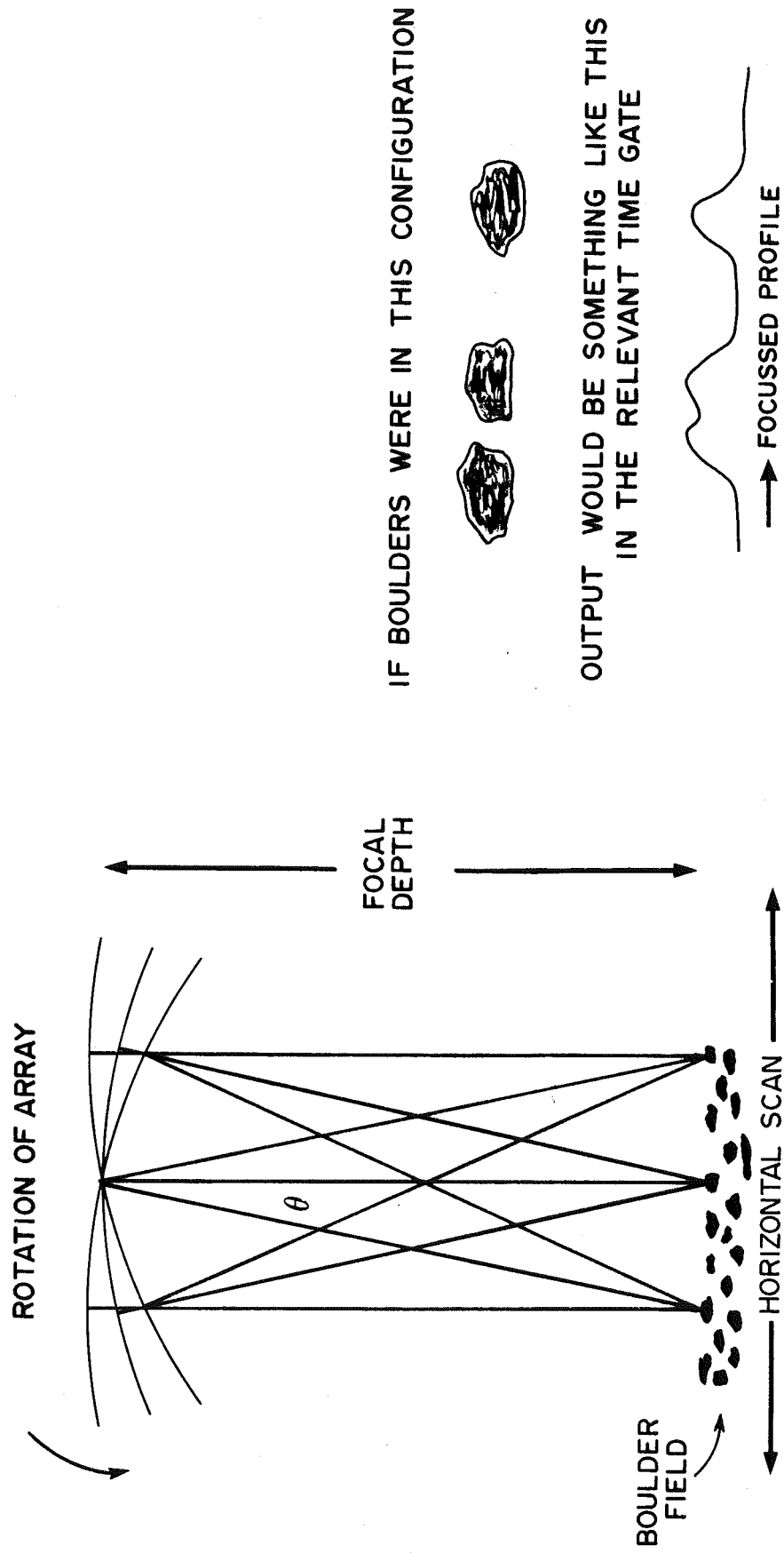


FIGURE 4.6 Qualitative Sketch of a Focused Profile over a Boulderly Structure

at this depth. Scanning along this depth's horizontal perspective may provide new information which would help discount the first interpretation of a sedimentary boundary. This use of focussing is a tentative suggestion yet to be proven.

4.4 Specific Application of the Hilbert Transform

There are many ways to express seismic data. One of the more promising techniques is in the application of "complex trace analysis" Taner et al (1979). In conventional seismic data, signals can be transformed from the time domain to the frequency domain by employing the Fourier Transform. This derives averaged properties over a wide sample. Applying "complex trace analysis" can compliment the Fourier Transform in that it maintains or retains better the local character of the signal in the rearrangement. This is an important consideration since the ASI is primarily directed towards the calibration of all sub-seabed information extracted and the establishment of confidence in the acquired values.

4.4.1 Describing the Hilbert Transform

The data are treated as analytic signals. This separates in a natural way amplitude and phase information or attributes. The phase attribute is the basis of acquiring an Instantaneous Frequency measurement. Farnbach (1975) and Taner and Sheriff (1977) discuss at

length the theoretical background of this type of analysis. Particular treatment is given by Taner et al (1979) to the seismic signal application and therefore should be referred to for details, derivations and definitions.

An accurate time reference is developed in the ASI concept using the Hilbert Transform of the real part to acquire the imaginary part. In this manner, the normal real valued time domain functions are made complex. From the transformation an envelope function is attained and can be displayed similar to functions in the frequency domain. The Hilbert Transform shifts each time component by $1/4$ wavelength while it gives all frequency components a -90° phase shift; much like an integration of the signal.

An approach to calculate the Hilbert Transform of a time signal is to use the Fourier transform to rearrange the trace into the frequency domain then change the phase of each of the frequency components by $\pm 90^\circ$, depending on the polarity of the frequency. From this stage the time domain is returned via an inverse Fourier transform. As a result the magnitude of the signal can be shown.

It is the resulting peak amplitude of the magnitude envelope which makes for an attractive time marker. The time measurements which were discussed in Section 4.2 are successfully manipulated in the experiments (see Chapter 6.0) using the Hilbert Transform as an integral part of the data processing.

4.4.2 Identifying Sub-seabed Lithologies

Since the envelope represents a reflection strength that is independent of phase then the maximum of the energy-time curve (ie. magnitude) may lie at phase points other than the high and/or lows of the real trace. Taner et al (1979) emphasize this point, stating that the maximum amplitude or reflection strength associated with a reflection event may be different from the amplitude of the largest real trace peak or trough especially where an event is the composite of several reflections. The ASI therefore incorporates in its interrogation the reflection strength character as a discrete property.

Identification of sub-seabed lithologies should be enhanced by highlighting the variability in reflective strength within a spot profile. The boundaries associated with sea level fluctuations and with changes in the depositional environment could be made more lucid given that the magnitude curve is sensitive to small scale variations. The mapping of such formations is generally difficult under standard seismic practise. Hence, this handling of reflective strength may prove to be of great benefit. Anomalies such as faults, hydro-carbon accumulations (ie. gas) could be specifically focussed on once the overall background lithology is established. The minor imagery changes associated with the anomalies would be sharpened or emphasized.

Finally, Instantaneous Frequency is calculated as another product of the Hilbert Transformation. Complimenting the use of magnitude in the ASI, the Instantaneous Frequency holds equal strength in importance. Interrogating the seabed in terms of frequency content revolves around a point in time and space. The Instantaneous Frequency provides values for a particular moment.

Superpositioning individual reflections will formulate a distinct frequency pattern when applied to a structural boundary. The frequency pattern along with the time domain magnitude can codify composite reflections into indicators of a complex lithology. Certain sedimentological conditions would alter the change in Instantaneous Frequency more readily or dynamically than what would normally be observed.

It should become possible to coherently map the edges of hydro-carbon water interfaces, reflectors belonging to small scale shallow oil reservoirs, condensates, gas sand boundaries and pinchouts by applying this frequency analysis in a correlation mode within the ASI's spatial offset network (see Section 4.3.1). All of these situations would record frequency shifts to lower levels. A more indepth understanding could potentially ensue. This would help to explain better the processes that formed these structures and answer why they engender such discrete drops in frequency.

An attempt is made in the experiments to use Instantaneous Frequency to compute an Attenuation Coefficient for the inhomogeneous, pseudo glacial till model. (see Chapter 6.0)

4.5 Development of an "Acoustic Core" Product

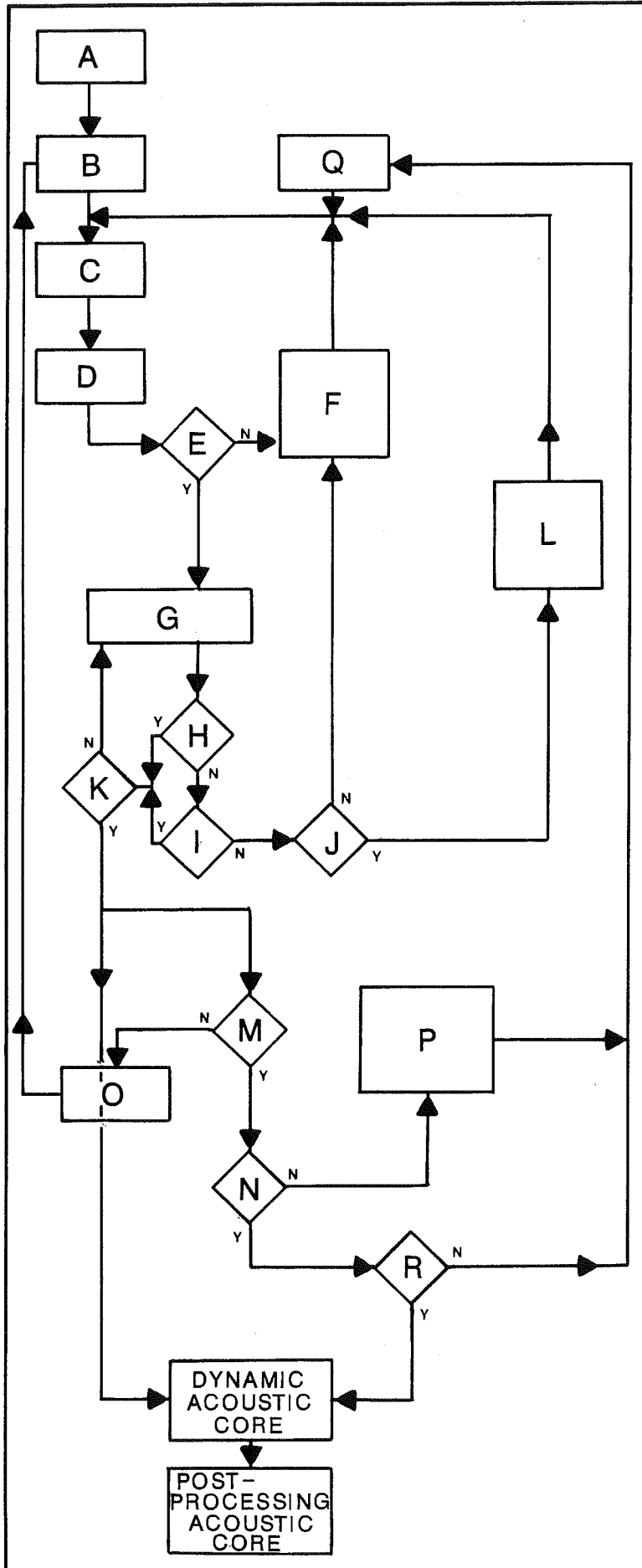
The concept of the ASI revolves essentially around an underwater probe which has the ability to intelligently interrogate signal and noise responses in situations where there are severe sound propagation constraints. The basis of the interrogation entails a family of echo discrimination routines and an active use of coherency/correlation techniques. The logic involved in creating the interrogation is epitomized into the flow chart of Figure 4.7.

The results of the analytical interrogation, echo discrimination, focussing and sediment property identification - classification are synthesized into a display called the "Acoustic Core". The "Acoustic Core" has a dynamic and a post-processing character. This is noted in Figure 4.7.

4.5.1 Designing the Three Dimensional Logic of the Dynamic "Acoustic Core"

The dynamic "Acoustic Core" which simulates a pseudo sediment core, interacts dynamically with the echos that are captured by the hydrophone array. Mathematical manipulations and transformations are used in the 3-D matrix design (for an indepth discussion on 3-D

FLOW DIAGRAM ILLUSTRATING THE INTERROGATION PROCESSES



LEGEND

- A. Height of the Transmitter above the seabed is confirmed for scanning position A of the Outer Circle.
- B. Transmission starts with position A out of the set of primary Outer Scanning Circle positions A, B, C, D and primary Inner Scanning Circle positions a, b, c, d
- C. Signals are received by the hydrophone and sent to a Real Time Signal Analyser.
- D. At the Signal Analyser the signals are:
 - i) Digitized
 - ii) Averaged (e.g. 200)
 - iii) Hilbert Transformed
- E. Is the transmission angle $\theta \neq 0$? Yes? No?
- F. A dynamic Normal Movement Routine is activated:
 - i) A specific transmission angle is set $\theta = 0^\circ$
 - ii) A time of arrival and position along the hydrophone array is predicted for a selected transmission angle and using the time of arrival noted when $\theta = 0$.
- G. The predicted time of arrival and positions along the hydrophone array for the selected transmission angle are compared against the measured arrival times and positions in a descending manner.
- H. Do the predicted and measured values concord and fall within a predetermined error range for the true primary echo identification? Yes? No?
- I. Do the predicted and measured values fall well outside the limits set for a true primary echo? i.e. is it a multiple? Yes? No?
- J. Operator decision to activate focussing.
- K. Is the identification of primary echos complete (in a descending manner)? Yes? No?
- L. Focussing of the hydrophone array is considered;
 - i) A focal depth is decided on using the information available
 - ii) The beam is made to steer along the horizontal extent of the focal depth
- M. Are the two primary scanning sets completed? Yes? No?
- N. Is the statistical derivation of the secondary scanning sets in place? Yes? No?
- O. Next primary position
- P. A statistical evaluation of the deviations between the primary scanning positions is performed. A secondary scanning set for both scanning circles is derived e.g. A ...n.
- Q. Parameters for the secondary transmission are established and programmed. Transmission starts with position A ...n.
- R. Are the two secondary scanning sets completed? Yes? No?

FIGURE 4.7

designing see Newman and Sproull (1979), Foley and Dam (1982), and Rogers and Adams (1976)). The echos that come back from a sub-seabed structure are assigned Y time-values within the matrix which correspond to a specific column of the core in accordance to the spatial positions of the ASI propagation. For instance, the four primary spatial positions A, B, C, D and their complimentary secondary positions (eg. A_1 to A_n) coincide exactly to the columns that formulate the "Acoustic Core" configuration, see Figure 4.7. The X and Z components of the matrix are the distances between the legs shaping the core.

As signals are sent to the core the data is assigned into a multi-column array called the Master-Cube*. The Master-Cube which manipulates the elemental X, Y and Z components of the "Acoustic Core" involves the following set of elements:

* The 3-D programming is based on the HP 9000 SERIES 200 - BASIC 3.0 Graphics Techniques: Chapter 6.0 "Data Display and Transformations." The multi-column array of the Master-Cube is unique to the "Acoustic Core".

$$\text{Master-Cube} = \left\{ \begin{array}{cccc}
 X_A & Y_{A(1 \text{ to } k)} & Z_A & 1 \\
 X_{A1} & Y_{A1(1 \text{ to } k)} & Z_{A1} & 1 \\
 X_{A2} & Y_{A2(1 \text{ to } k)} & Z_{A2} & 1 \\
 \vdots & \vdots & \vdots & \vdots \\
 \vdots & \vdots & \vdots & \vdots \\
 X_{Aj} & Y_{Aj(1 \text{ to } k)} & Z_{Aj} & 1 \\
 X_B & Y_{B(1 \text{ to } k)} & Z_B & 1 \\
 \vdots & \vdots & \vdots & \vdots \\
 \vdots & \vdots & \vdots & \vdots \\
 \vdots & \vdots & \vdots & \vdots \\
 X_{Bj} & Y_{Bj(1 \text{ to } k)} & Z_j & 1 \\
 X_C & Y_{C(1 \text{ to } k)} & Z_C & 1 \\
 \vdots & \vdots & \vdots & \vdots \\
 \vdots & \vdots & \vdots & \vdots \\
 \vdots & \vdots & \vdots & \vdots \\
 X_{Cj} & Y_{Cj(1 \text{ to } k)} & Z_{Cj} & 1 \\
 X_D & Y_{D(1 \text{ to } k)} & Z_D & 1 \\
 \vdots & \vdots & \vdots & \vdots \\
 \vdots & \vdots & \vdots & \vdots \\
 \vdots & \vdots & \vdots & \vdots \\
 X_{Dj} & Y_{Dj(1 \text{ to } k)} & Z_{Dj} & 1
 \end{array} \right\} \quad (4.25)$$

where A, B, C, and D are the four primary positions. Their subscript j refers to the secondary scanning locations. Subscript k indicates the signals recorded in time along the Y-axis. The Master Cube uses this set (4.25) to manipulate discrete scale and translation matrices.

A 3-D rotation transformation can be performed on the Master-Cube about the X and Y axes (i.e.; the horizontal and vertical axes). A rotation about the X-axis at an angle θ_1 adjusts the core to slant forward by θ_1 in reference to the vertical. Similarly, a rotation about the Y-axis at an angle θ_2 enables the core to be viewed at an angle which concords with θ_2 . The rotation about the X-axis is

$$\Psi = \begin{bmatrix} 1 & 0 & 0 & 0 \\ 0 & \cos\theta_1 & -\sin\theta_1 & 0 \\ 0 & \sin\theta_1 & \cos\theta_1 & 0 \\ 0 & 0 & 0 & 1 \end{bmatrix} \quad (4.26)$$

while the rotation about the Y-axis is

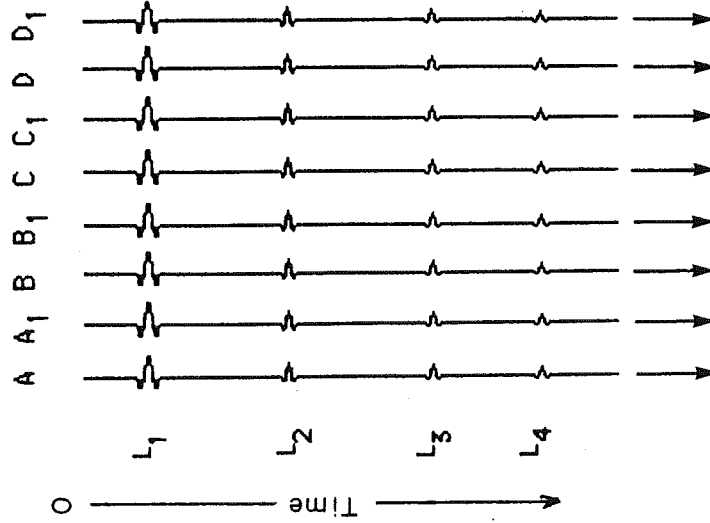
$$T = \begin{bmatrix} \cos\theta_2 & 0 & \sin\theta_2 & 0 \\ 0 & 1 & 0 & 0 \\ -\sin\theta_2 & 0 & \cos\theta_2 & 0 \\ 0 & 0 & 0 & 1 \end{bmatrix} \quad (4.27)$$

Ψ and T are the square matrices of the rotational transformation about the X and Y axis respectively. The Transformation-Matrix is the matrix product of Ψ and T . A further matrix evolves out of this called the Core-Matrix-1. This Core-Matrix-1 is the direct result of imposing the Transformation-Matrix onto the Master-Cube. The Core-Matrix-1 is the foundation of the visual "Acoustic Core" product (see Figure 4.8).

The Core-Matrix-1 can be rearranged into a sliced or halved core by recreating the Master-Cube into an Auxillary-Master-Cube then executing from this a new Core-Matrix. In other words:

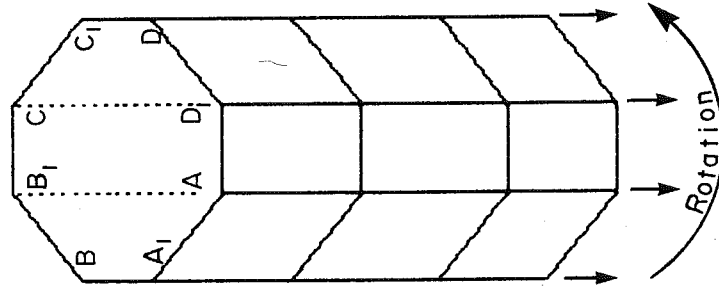
$$\text{Core-Matrix-2} = \text{Auxillary-Master-Cube} \times \text{Transformation-Matrix} \quad (4.28)$$

Digitizing and Categorizing
the Time Signals



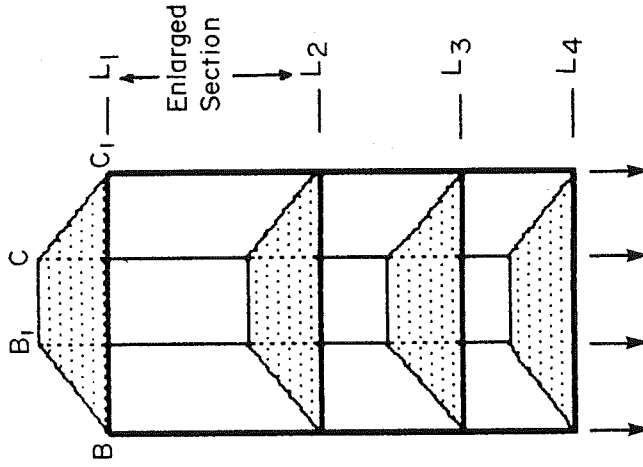
Time History Data

Forming the Initial
Core Structure



Core - Matrix - 1

Splitting of the Core



Core - Matrix - 2

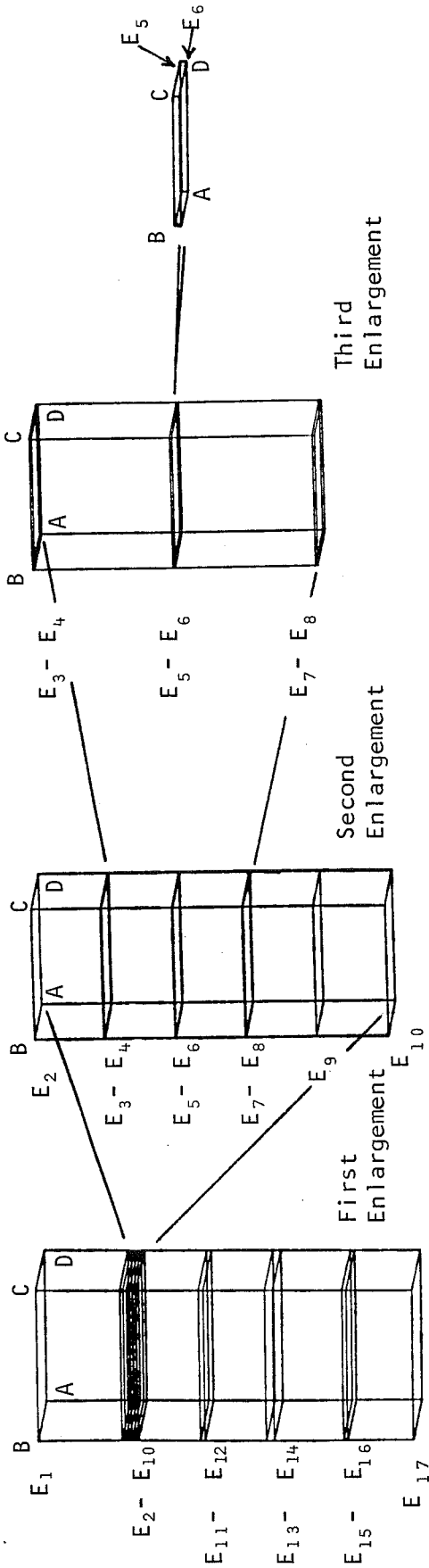
Figure 4.8 "ACOUSTIC CORE" Product

4.5.2 Applying the "Acoustic Core" Product to the Stratigraphic Model

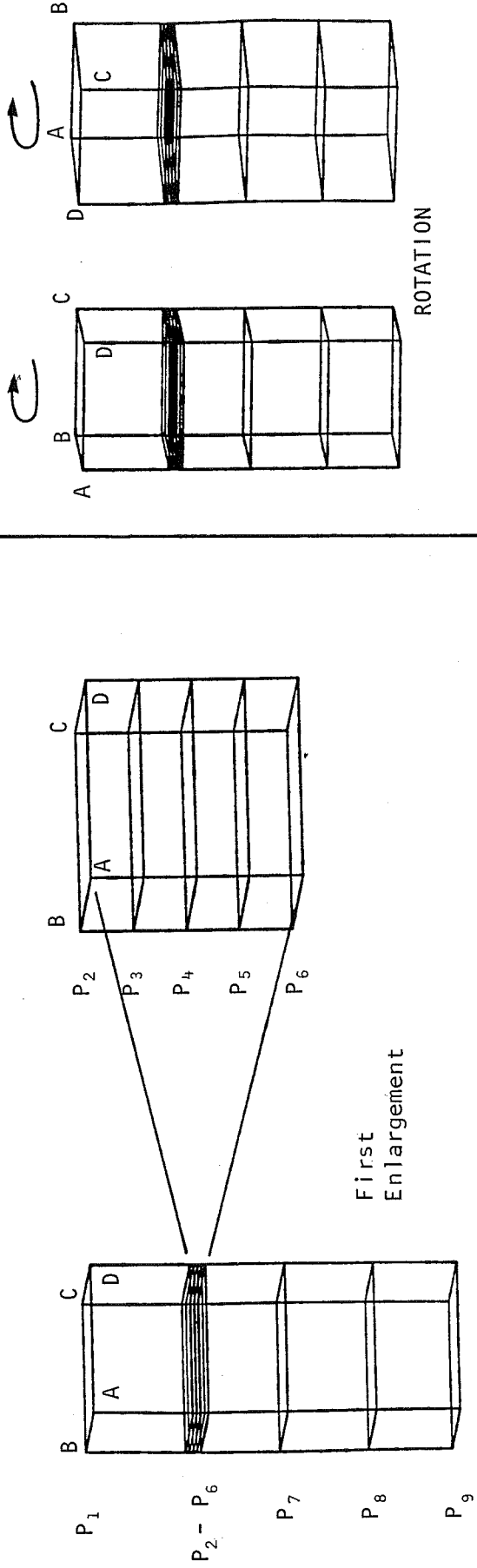
The "Acoustic Core" logic can now be computer simulated using the set of data established earlier in Section 4.2.2 for the Stratigraphic Model. The model's arrival times, transmission angle and z positions are pre-programmed into a data file. Since the Stratigraphic Model is a theoretically derived model, the assumption is made that all the columns of the "Acoustic Core" are equal (i.e. ABCD are assigned the same data). The methodology delineated in Section 4.2.2 is activated to identify the true echoes from multiple path returns. The multiple paths were created through a simple algorithm.

The theoretical primary signals and 1st order multiples were first sent to a Master-Cube. The Master-Cube then assigned the X, Y and Z values of the core. Figure 4.9 pictorially depicts the steps and phases involved in the transformation of the Master-Cube based on the data supplied theoretically into a four column "Acoustic Core" product. The normal moveout routine of Section 4.2.2 is summoned. The multiples are identified and removed (see Figure 4.9d).

The resulting core can now be expanded and magnified. By specifying the layers to be expanded the data base is readdressed, with only pertinent values directed back to the Master-Cube. The size of the screen window is adjusted such that the core elucidates over a selected percent of the vertical screen. The horizontal dimensions



a) PRIMARY AND MULTIPLE ECHOES (E).
 b) ENLARGEMENT OF ECHO #2 TO 10.
 c) ENLARGEMENT OF ECHO #3 TO 8 AND ENHANCEMENT OF ECHO #5 AND 6.



d) PRIMARY ECHOES AFTER MULTIPLE DIFFERENTIATION (P).
 e) ENLARGEMENT OF PRIMARY #2 TO 6.
 f) $\theta = 15^\circ$ $\theta = 30^\circ$

NB: θ IS THE ANGLE OF ROTATION ABOUT THE VERTICAL AXIS THROUGH THE CENTRE OF THE 'CORE'

FIGURE 4.9 Computer Simulation of the "Acoustic Core"

remain the same. This is a useful routine to use when fine layered structures are present such as those noted in Layer 2 of the model (see Figure 4.9c). The final product of the computer simulations substantiates the graphic value of the "Acoustic Core".

The flow logic of the programming and the interfacing of the transmitters, receivers, primary stage analysers, secondary stage processor and "Acoustic Core" controller are development steps that belong to a prototype study. This phase is outside of the present project scope, however an attempt is made to experimentally establish certain aspects of the logic in the laboratory trials of the "Acoustic Sub-seabed Interrogator". The laboratory modelling and simulation of the ASI concept are dealt with in Chapters 5.0 and 6.0.

5.0 PREPARATIONS FOR THE ACOUSTIC EXPERIMENTS

5.1 Pre-amble

An appreciation of the practical aspects of the model's acoustic theory is required to properly gauge the behaviour of the "Acoustic Sub-seabed Interrogator" before a full scale prototype is entered into. Unfortunately, the simulation of the concepts in a sea environment and the interpretation of the different sediment types encountered are difficult to measure unless very stringent controls are enforced. An alternative is to initiate the testing through scaled experiments in a laboratory environment. Such investigations can command high levels of exactness using precision positioning and geometric control within the confines of a water tank. The wave shape changes recorded can be studied in a scaled format with great detail and perspicacity since specific experimental criteria are enhanced and/or are singled out. Therefore the testing of the acoustic concepts explicated in the first four chapters, will be investigated primarily under scaled experimental conditions.

5.2 Experimental Objectives

The foremost objective of the experimental modelling is to scrutinize the validity of the acoustic concepts that were articulated in the analytical evaluations. A Parametric Array will be used. The "Acoustic Sub-seabed Interrogator" concepts are simulated to test the overall transmission and reception behaviour of the probe with the end

goal to optimize a system that can effectively interrogate a complex seabed. In particular, the precise modelling of a glacial till layer is considered a priority in the experimentation. A structure of this nature provides for a unique forum to better understand the way propagating energy is redistributed in an inhomogeneous sedimentary matrix.

Since the correlations between geotechnical measurements, the geoacoustic record and sub-seabed geology have not been well established, an attempt is made to ensure that sufficient calibrated controls are in the experimental laboratory setting to allow for a closer correlation to occur. A sediment/acoustic classification program can evolve if the correlations are significant and reliable. Ultimately, the long term objective is to address specific geotechnical properties directly from an acoustic impulse response.

5.3 Scaling Factor

In most well designed experiments, the analyses are usually simplified if the experiments are orthogonal in nature.

"Orthogonality is that property of the design which ensures that the different classes of effects to which the experimental material is subjected to shall be capable of direct and separate estimation without any entanglement."
Yates (1970)

If the aspects within the experiments are orthogonal then the processes which are executed will cause true scientific results regardless of scale. Lack of orthogonality is a disadvantage affecting

both the complexity of the analysis required and the overall efficiency encountered. This is especially important in reference to the varying quantities which exist in our glacial till model and in our sound source. Each of these different quantities will therefore command an individual scaling appraisal to maintain truth in representation and in behaviour.

A scaling factor of 17.5 is used in the physical and acoustical model experiments. This was derived by considering the physical constraints of the acoustic water tank and optimizing the best scale for overall efficiency in the handling of a large complex sedimentary structure while still maintaining a very close physical resemblance to an actual seabed. For instance a scaling limit of 20 was initially assigned after assessing the problems in representing geotechnical properties at a higher scale level. The cut off point in scaling fine particulate size classes is in the vicinity of 20:1.

The scale factor of 20 was then adjusted down to 17.5 through the optimization of the transducer crystal. The crystal's resonant frequency of 2.0 MHz corresponded closely to the 1:20 scaling, however the frequency dropped to 1.82 MHz once the backing material and transformer were attached to it. Hence a 17.5 scale factor evolved, which matched the 1.82 MHz frequency of the transducer to the full scale 104 kHz carrier frequency (see Chapter 3.0 - optimization of f_c).

The following key source parameters and sediment model properties are highlighted for discussion given that the full scale prototype is

to operate under the criteria defined in the previous two chapters:

- i) Power - (W)
- ii) Carrier Frequency - (f_c)
- iii) Difference Frequency - (f_d)
- iv) Transducer Radius - (a)
- v) Transducer Height - (λ)
- vi) Beam Angle - (θ_p)
- vii) Sediment Particulate Size - (K_1 and K_2)

5.3.1 Discussion

If we let k be the scaling factor 17.5 then the height above the seabed λ will have to be scaled down in context to the scaling of a unit of length.

$$\lambda \rightarrow \lambda/k \quad (5.1)$$

Likewise the transducer radius will also reduce down linearly in terms of length.

$$a \rightarrow a/k \quad (5.2)$$

If we examine the expressions which defined Power and Carrier Frequency for a terminated Parametric Array then the following factors are ratified:

$$W = \frac{\pi c 10^4 \lambda^2}{886 \times 10^3} = 53.187 \lambda^2 \rightarrow W/k^2 \quad (5.3)$$

and

$$f_c = \frac{886 \times 10^3}{\lambda} \rightarrow f_c \times k \quad (5.4)$$

To define the scaled difference frequency (f_d), attenuation and range must be deliberated as seen in the derivation of P in relation to the 5 layers of the Stratigraphic Model

$$P = 2.8 \times 10^{-7} \lambda^3 f_d^2 e^{-f \{2[\alpha_i(R_i - R_{i-1}) + (\bar{\alpha}_{R_{i-1}} R_{i-1})]\}} \quad (5.5)$$

After differentiating f_d from P and equating $\frac{dP}{df_d} = 0$

$$f_{d \max} = \frac{1}{2[\alpha_i(R_i - R_{i-1}) + (\bar{\alpha}_{R_{i-1}} R_{i-1})]} \quad (5.6)$$

Since R is a measure of length it will scale down by

$$R \rightarrow R/k \quad (5.7)$$

Therefore, using the last two expressions (5.6, 5.7)

$$f_d \rightarrow f_d \times k \quad (5.8)$$

given that the product $f_d \max\{2[\alpha_i(R_i - R_{i-1}) + (\bar{\alpha}_{R_{i-1}} R_{i-1})]\}$ is a constant.

Expression 3.101 calculated the beam angle for the terminated Parametric Array. From this $f_d \times \lambda$ will remain constant along with the velocity of sound c . For example, using an approximation for the derivation of a terminating parametric beam angle, θ_p will not change in the scaling.

$$\theta_p = 4 \sin^{-1} \sqrt{\frac{1.39}{2\pi f_d \lambda}} \quad (5.9)$$

Finally, the sedimentary material is scaled in terms of its particulate sizes. Applying this condition to the model the following is found: (K_1 will range from sand to gravel/cobbles)

$$K_1 \rightarrow K_1/k \quad (5.10)$$

When boulders are introduced into the model, they will have to be defined in terms of a specific Target Strength for a specific particulate size. The scaling factor k however does still apply.

$$K_2 \rightarrow K_2/k \quad (5.11)$$

5.3.2 Summary

The scaled results of the discussion are summarized as follows:
(for a terminated Parametric Array and for $k = 17.5$)

<u>Full Scale Prototype</u>	<u>Conversion</u>	<u>Scaled System</u>
f_d (difference frequencies) 1 to 10 kHz	$f_d \times k$	17.5 to 175 kHz
a (radius of transducer face) 35 cm	a/k	2.0 cm
f_c (primary frequency) 104 kHz	$f_c \times k$	1.8 MHz
W (power) \approx 3800 Watts	W/k^2	\approx 12.4 Watts
λ (height above seabed) 8.5 metres	λ/k	48.6 cm
R (design distance for the penetration in the glacial till layer) 10 metres	R/k	57.1 cm
θ_p (parametric beam angle) $\pm 11^\circ$ (for an f_d of 3.5 kHz)	$\theta_p \times 1$	$\pm 11^\circ$
K_1 (gravel/cobbles size)	K_1/k	* coarse sand
K_2 (boulder size)	K_2/k	*medium gravel

*Refer to Section 5.4.4.2 for a more detailed breakdown of the soil types scaled and simulated for the till layer.

5.4 Experimental Details

The experimental setting used to test the "ASI" concepts are categorized into the following four components:

- i) Acoustic Tank and Positioning System
- ii) Transmitting Instrumentation
- iii) Receiving Instrumentation
- iv) Sediment and Acoustic Propagation Modelling

5.4.1 Acoustic Tank and Positioning System

The task of scaling an ocean sound field in a laboratory environment presents certain problems. These relate to a multitude of tank wall interferences. The signals generated are not only affected by the media they are meant to propagate through, but they are also affected by the walls of the tank. In experimental situations where continuous waves are transmitted, the tank must be anechoic capable of totally absorbing the wall and bottom reflections. Expensive sound absorbing liners can be used when high frequencies are generated, however this becomes impractical with the propagation of the low frequencies. It is difficult to produce liners thick enough to meet the longer pulse lengths of the lower frequencies. Employing pulsing wave techniques does allow for low frequency signals to be received without interference as long as the arrival times of the various reflections are correctly managed and can be separated from the desired signal by time gating. The suitability of a water tank can be

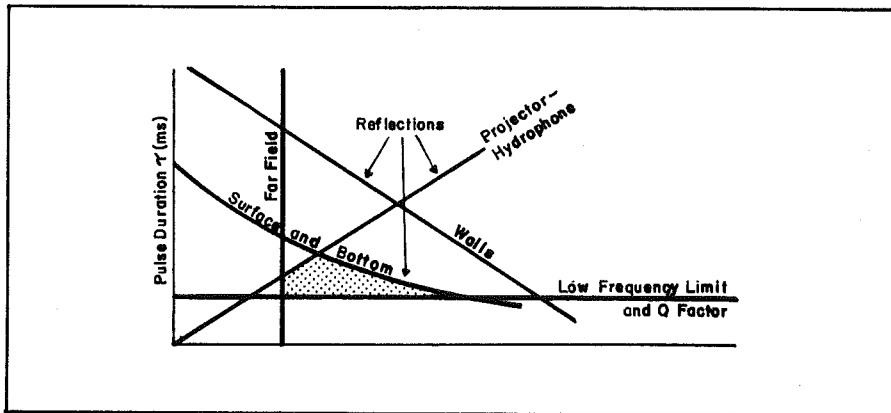
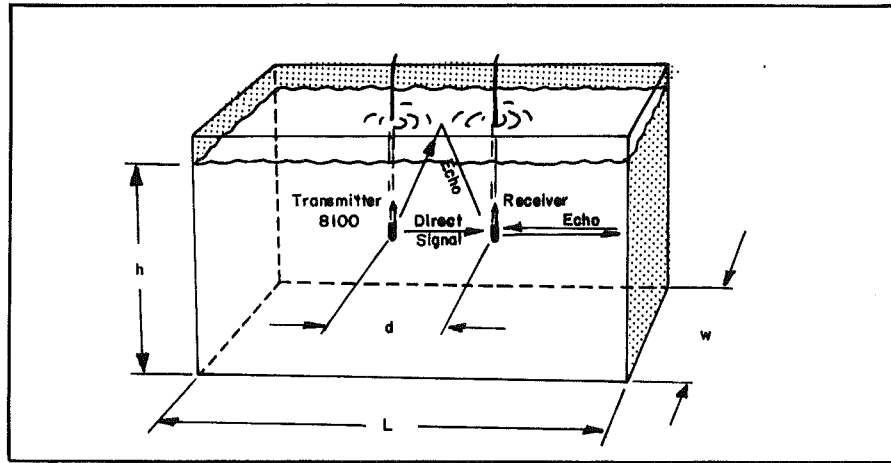
evaluated by assessing the pulse duration, the repetition rate and the geometrical travel distances between the transmitter and hydrophones. For example, Figure 5.1 illustrates the dimensions and limitations to pulse duration and to transducer spacing for a water tank of given dimensions.

5.4.1.1 Description of Setup

The tank selected for this acoustic study is in the Hydraulic Laboratory facilities of Memorial University of Newfoundland (Newfoundland, Canada). The tank dimensions: 4 metres deep, 4 metres wide and 4 metres long, provide exceptionally good free field conditions in relation to the high frequencies used. Since a high order of precision is required in the transmission and in the reception, an accurately machined positioning system was designed and built. The complete system comprises of the following parts:

- i) Carriage Tracks
- ii) Transmitter Carriage
- iii) Fixed Positioning Bracket
- iv) ASI Simulator
- v) Transmitter Rotation Apparatus
- vi) Hydrophone Carriage
- vii) Transmitter and Hydrophone Support Probes

Figure 5.2 illustrates the laboratory setting, particularly the ASI Simulator.



limitations to Pulse Duration (τ):

$$\tau \leq \frac{2d}{c}$$

(reflection between transducers)

$$\tau \leq \frac{L-d}{c}$$

(reflection from wall)

$$\tau \leq \frac{\sqrt{h^2 + d^2} - d}{c}$$

(reflection from upper or bottom surface)

FIGURE 5.1 Water Tank Geometry and Limitations (from Brüel and Kjaer Application Notes : Introduction to Underwater Acoustics.)

Experimental Layout of the ASI SIMULATOR and SEDIMENT MODEL

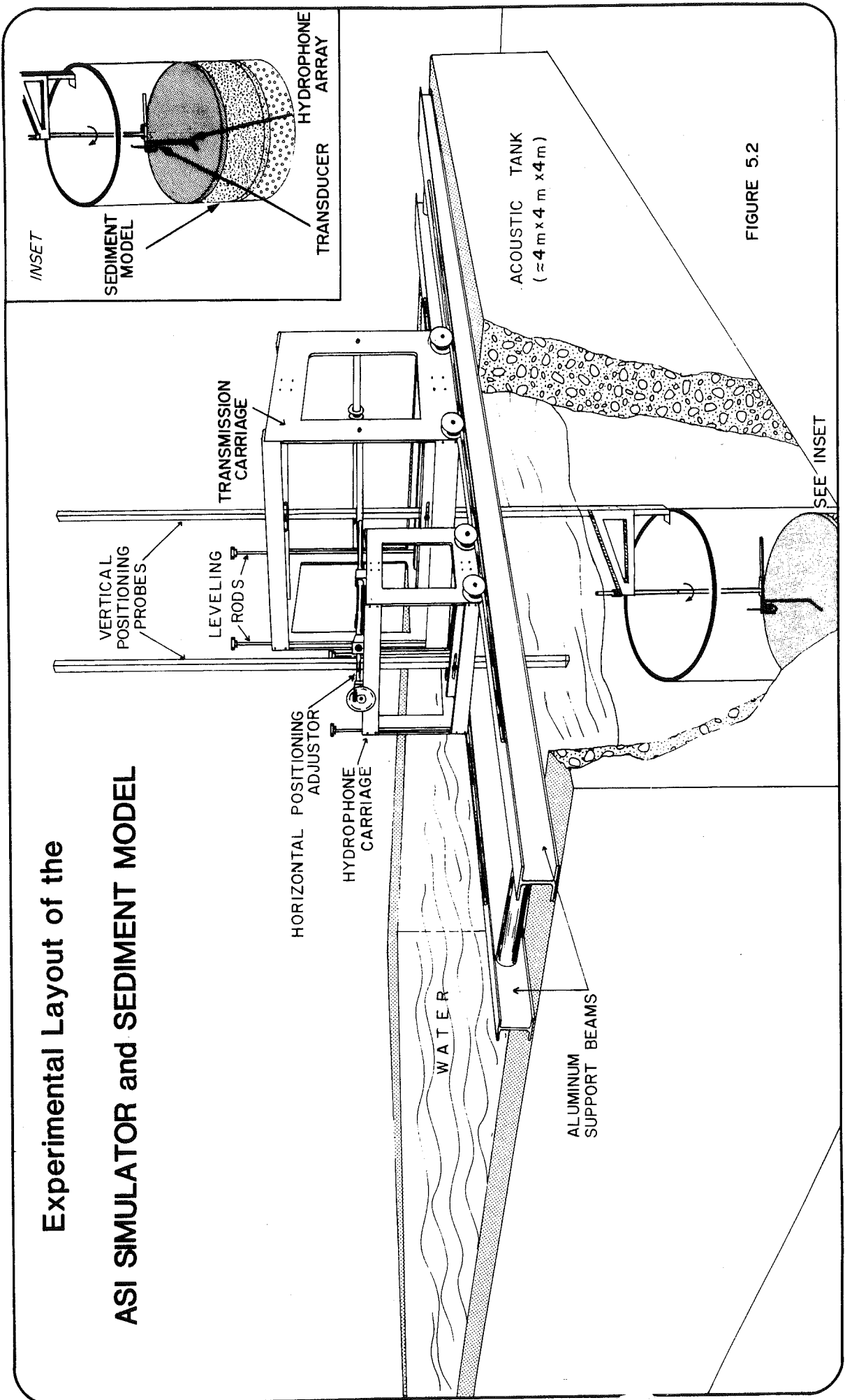


FIGURE 5.2

5.4.1.2 Carriage Tracks

Carriage Tracks made of stainless steel round stock were machined to very high tolerances to provide an accurate reference plane and horizontal linear motion guide for the transmitter and receiver carriages. These tracks are secured over aluminum support beams and can be adjusted throughout their length by small power screws. These small screws raise or lower the tracks within a one centimetre range. Along the length of the support beams, machinist scales are secured for manual distance control. The overall deflection calculated for the traversing beams is in the order of < 1 mm.

5.4.1.3 Transmitter Carriage

A square aluminum carriage, 500 mm by 500 mm, with a special set of DelrinTM wheels were built to hold the transmitter apparatus. The shape of the wheels was machined after careful consideration was placed on its design such that the contact is made between the outer sides of the track and the tapered inner portion of the wheel. This ensures a smooth and stable roll over the tracks with minimal play in the carriage.

5.4.1.4 Fixed Positioning Bracket

The majority of the experiments require the transmitter and the receiver to be in a fixed central position with variability in their azimuth direction. To ensure maximum stability, reproducibility and

security, a complex bracket support and sliding shoe apparatus were incorporated into the underframe of the Transmitter Carriage and on the lip of the Sediment Tank. A stainless steel vertical axle secured onto the lip of the Sediment Tank provides the shoe with an effective riding surface between the carriage and the tank.

In preparation to an experiment, the ASI Simulator (see Section 5.4.1.5) would be attached to the extended bracket. The ASI Simulator holds the transmitter and receiver in position. Once secured, the whole bracket assembly can then be lowered by sliding along the constraining axle until the shoe locks onto the lip of the Sediment Tank.

5.4.1.5 ASI Simulator

The ASI Simulator manipulates precisely the transmission angle and the hydrophone position along the z-axis. It also sets the distance between the hydrophone and the transmitter at 45.0 cm. The apparatus can best be described through the inset of Figure 5.2 and by the illustration in Figure 5.10.

The right angled bracket which supports the transmitter and hydrophone array can be rotated along its transverse axis by 360° thus providing the basis of the spatial moveout required in the coherency measurements. To reproduce the hydrophone array a Bruel and Kjaer hydrophone (see Section 5.4.3) is incrementally moved by millimetres using a manually turned threaded rod axle.

The transmitter angle adjustment is fixed at intervals of 0° , 3° , 6° and 9° through a machined "peg and slot" constraint plate. In other words the change of angle is performed by simply removing a peg and reinserting it in the appropriate angle slot. This does allow the transducer to rotate and then to maintain an exact angle during transmissions.

Finally a desired transmission radius is accommodated for along the right angled bracket. This is bolted in place once it is secured in the selected scanning circle.

5.4.1.6 Transmitter Rotation Apparatus

The purpose of the rotation apparatus is to provide a direct means of rotating the transmitter by one degree steps for calibration purposes. The rotation (0.2 degree accuracy) consists of a powerful DC motor with a high efficiency gear train. To ensure proper position control, two closed loop feedback systems are designed into the controlling circuitry. Two potentiometers are meshed into the gear train, matching the feedback potentiometers within the control unit. A waterproof rotation housing was also constructed out of aluminum and is fitted with O-ring seals. The rotator axle made of stainless steel protrudes outwards through the top flange. Bushings of brass provide good bearing surfaces. An O-ring fitted into the flange bushing ensures water tightness. The main body of the rotator is bolted onto a 3 metre long square tube assembly which will enable vertical motion of the rotator within the confines of the Transmission Carriage. Vertical

depth adjustments can be made through rollers mounted in the center of the carriage. The output from the rotator is digitally read off a LCD display in degrees and in turn unloaded onto a controller.

5.4.1.7 Hydrophone Carriage

A matching carriage to the Transmission Carriage was built but with a half scaled height and breadth. Since the movement of the Hydrophone Carriage is meant to simulate the spacing of a receiving array, this carriage is directly attached to the transmission frame via an adjustable threaded rod link up and a stabilizing bar assembly. Horizontal changes can therefore be executed precisely. A second hydrophone to the one attached in the Fixed Positioning Bracket is mounted onto a vertical probe. This square tube probe can be raised or lowered to any depth in the tank.

A thin wall (0.3 mm) stainless steel tube houses the hydrophone. The hydrophone sits inside a DelrinTM sleeve which is press-fitted into the end of the tube. The last two centimetres of the tube where the hydrophone enters were specifically machined down to a final wall thickness of 0.1 mm. This is to eliminate the potential for longitudinal vibrations in the tube from reaching the hydrophone.

5.4.2 Transmitting Instrumentation

The instrumentation involved in the transmission can be discussed as three complementary parts.

- i) General Application Transducers
- ii) Primary Transducers
- iii) Electronic Circuitry

5.4.2.1 General Application Transducers

Five piezoelectric transducers were built for general experimental application using a variety of materials in their housing and in their backing. Such mixtures as MICROBALLOONSTM mixed with ARALDITETM were experimented with and then applied to simulate an air back condition. In addition to MICROBALLOONSTM, another material, PLASTIC CELLTM was found and tested. PLASTIC CELLTM's composition best matches the reflective property of air and therefore was preferred over the MICROBALLOONSTM, achieving a relatively high Q or high efficiency transducer.

Three types of crystals were investigated, PZT4, PZT5A and Quartz. The overall dimensions of the transducers are:

- i) Crystal Size: 20 mm diameter, 1 mm thickness
- ii) Frequency: resonant at 2 MHz
- iii) Housing: PLASTIC CELLTM and also MICROBALLOONSTM
- iv) (approx) Impedance: 30 to 40 ohms at 2 MHz

Since two of these general purpose transducers are to be used as backup sensors or possibly receivers, their coax cables were double

shielded and coated in TeflonTM. This helps to reduce the effects of noise.

5.4.2.2. Primary Transducer

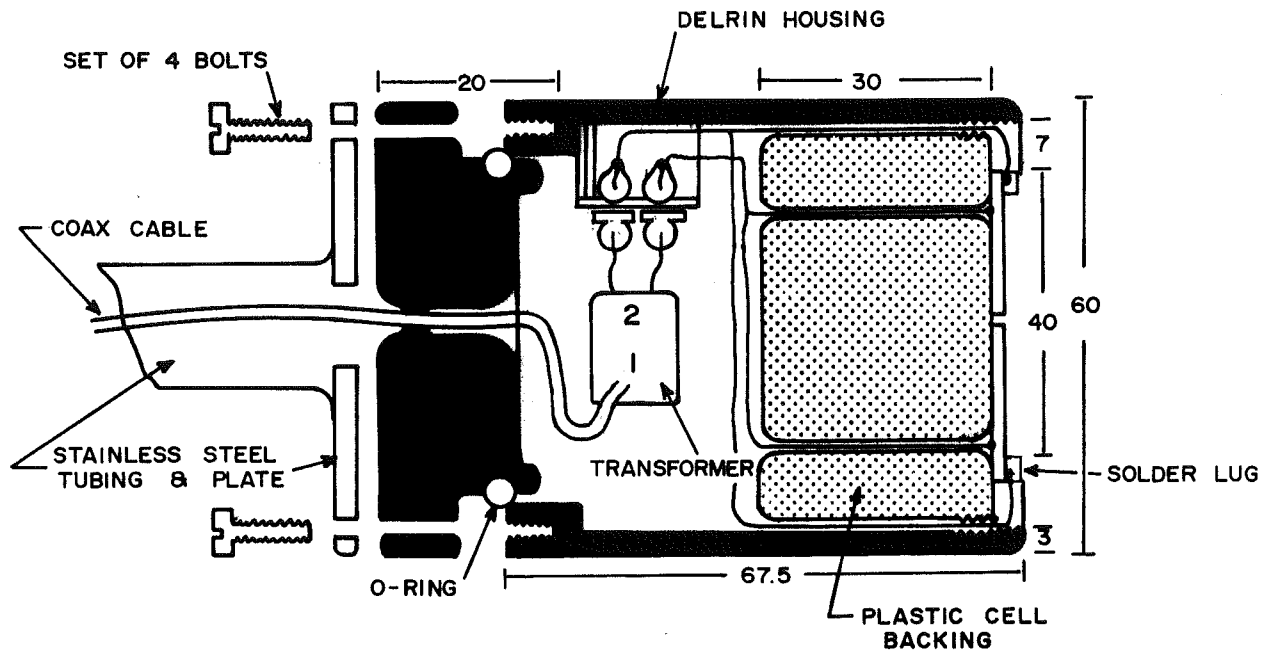
A transmitter was designed and built to operate in a parametric mode over a difference frequency (f_d) range of ≈ 10 kHz to 175 kHz. This is concordant with the criteria outlined in the analytical modelling and with the scaling factor of 17.5 set in Section 5.3. A specific crystal thickness was selected so resonance could occur near 2MHz (1.8MHz). The composition of the crystal is PZT5a.

Since the efficiency of the transduction is very low when operated in the parametric mode, the transducer was constructed in a manner that would attain an optimum level of efficiency with a suitable bandwidth. A simulated air-backed transducer was finally decided on. It uses PLASTIC CELLTM material to back the crystal.

The transducer dimensions are illustrated in Figure 5.3. The crystal surface has an overtone gold finish polish. The crystal was also quartered to prevent shear wave or flexing from occurring within the crystal. Otherwise, the thinnest related to a 4 cm crystal at such a frequency could potentially induce shear-waves. Each of its segments was parallel wired. The ARALDITETM resin finish of the face seals the crystal. This was machined to a $\lambda/4$ thickness for maximum efficiency.

ELEVATION VIEW

ALL DIMENSIONS IN MILLIMETRES



PLAN VIEW

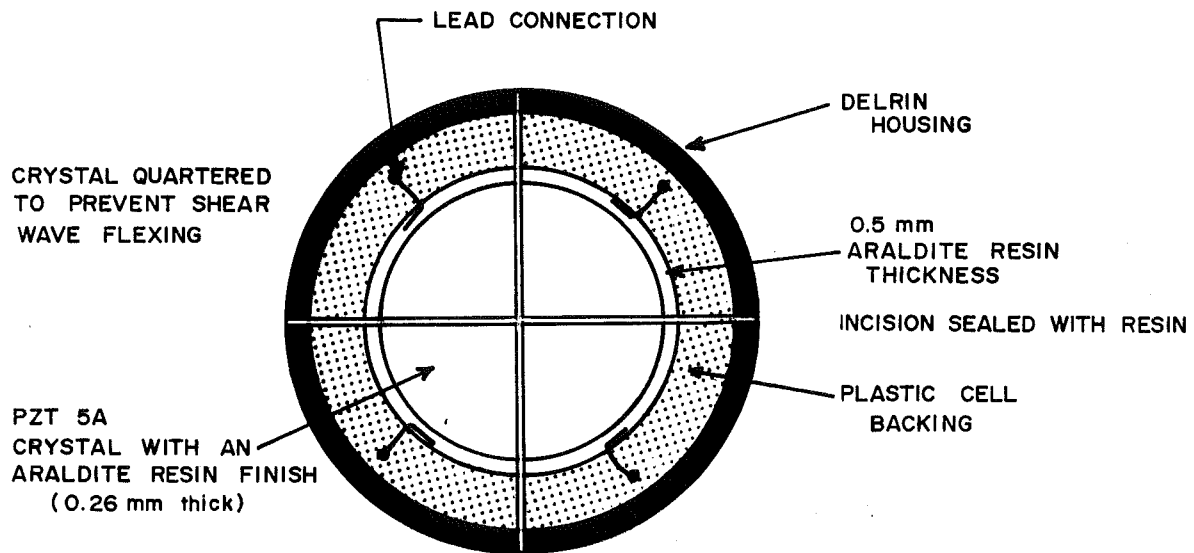


FIGURE 5.3 Primary Transducer Dimensions.

A Torroid transformer was also incorporated into the design to match the low impedance of the crystal. The crystal's 5 ohm impedance at 1.8 MHz was raised to a higher impedance level of 25 ohms. With this transformer in place, a 3 metre cable was attached. A second transformer, a pot core type, was then matched to the resultant complex impedance of the crystal, Torroid and cable. This brought the impedance into the vicinity of 60 ohms at 1.8 MHz (in air). An alternative was devised whereby an extra 1 metre cable was attached bypassing the second transformer. This provided extra length. When the transducer was operated under two metres of water the impedance was measured to be near 50 ohms for this setup. A third approach was also attempted using a three metre length of extra cable. The measured impedance was however recorded to be quite high under the load of the water, exceeding 80 ohms at 1.8 MHz.

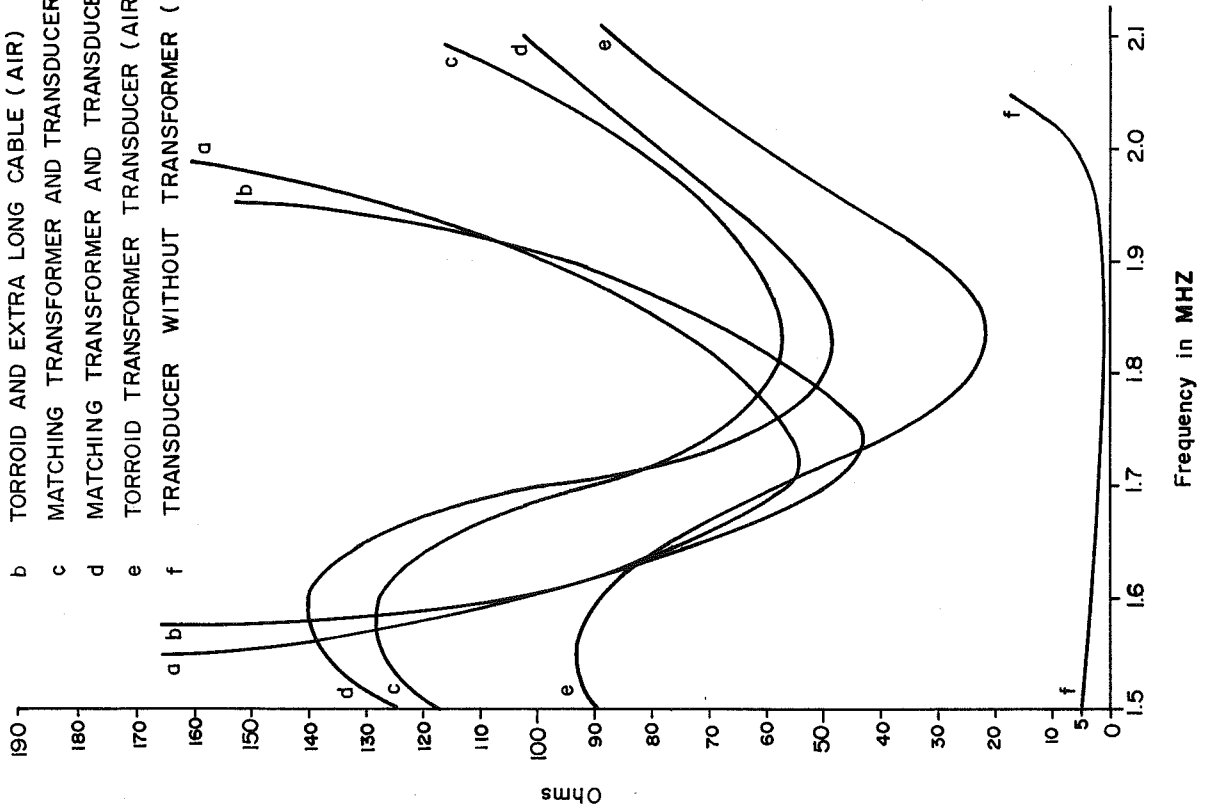
Figure 5.4 plots the complex impedances measured for the crystal and for combinations of transformers, cable, and crystal. The amplitude and the phase are shown for circuits tested under 0.5 metres of water and tested in air. Finally, the electronic circuitry excluding the transducer indicated a 50 ohm impedance at 1.8 MHz. The assembly inside the transducer was constructed in a modular plug in format for ease in testing and in trouble shooting.

5.4.2.3. Electronic Circuitry

As first mentioned in Chapter 2.0, two collinear acoustic beams are formed when a transducer is energized with two slightly different high frequencies. A parametric beam at a secondary difference

AMPLITUDE

- a TORROID AND EXTRA LONG CABLE (H₂O)
- b TORROID AND EXTRA LONG CABLE (AIR)
- c MATCHING TRANSFORMER AND TRANSDUCER (H₂O)
- d MATCHING TRANSFORMER AND TRANSDUCER (AIR)
- e TORROID TRANSFORMER AND TRANSDUCER (AIR)
- f TRANSDUCER WITHOUT TRANSFORMER (AIR)



PHASE

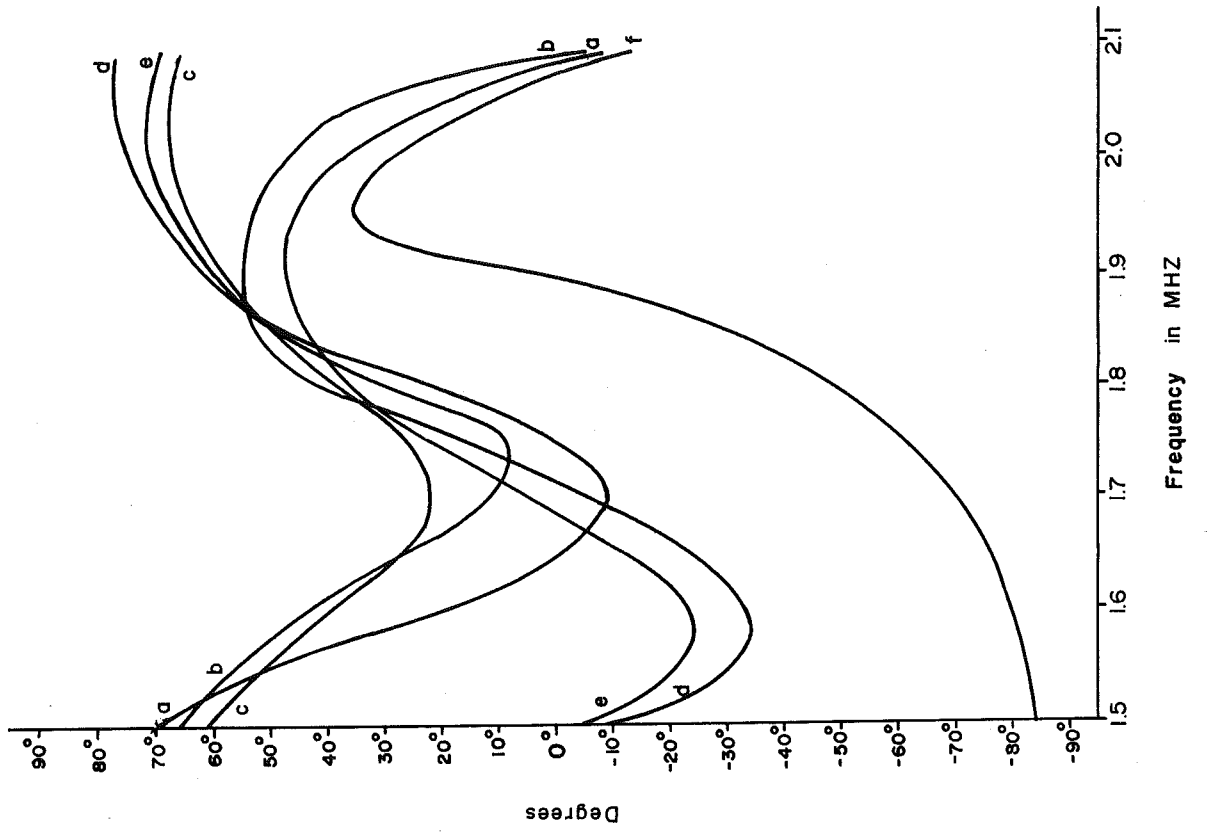


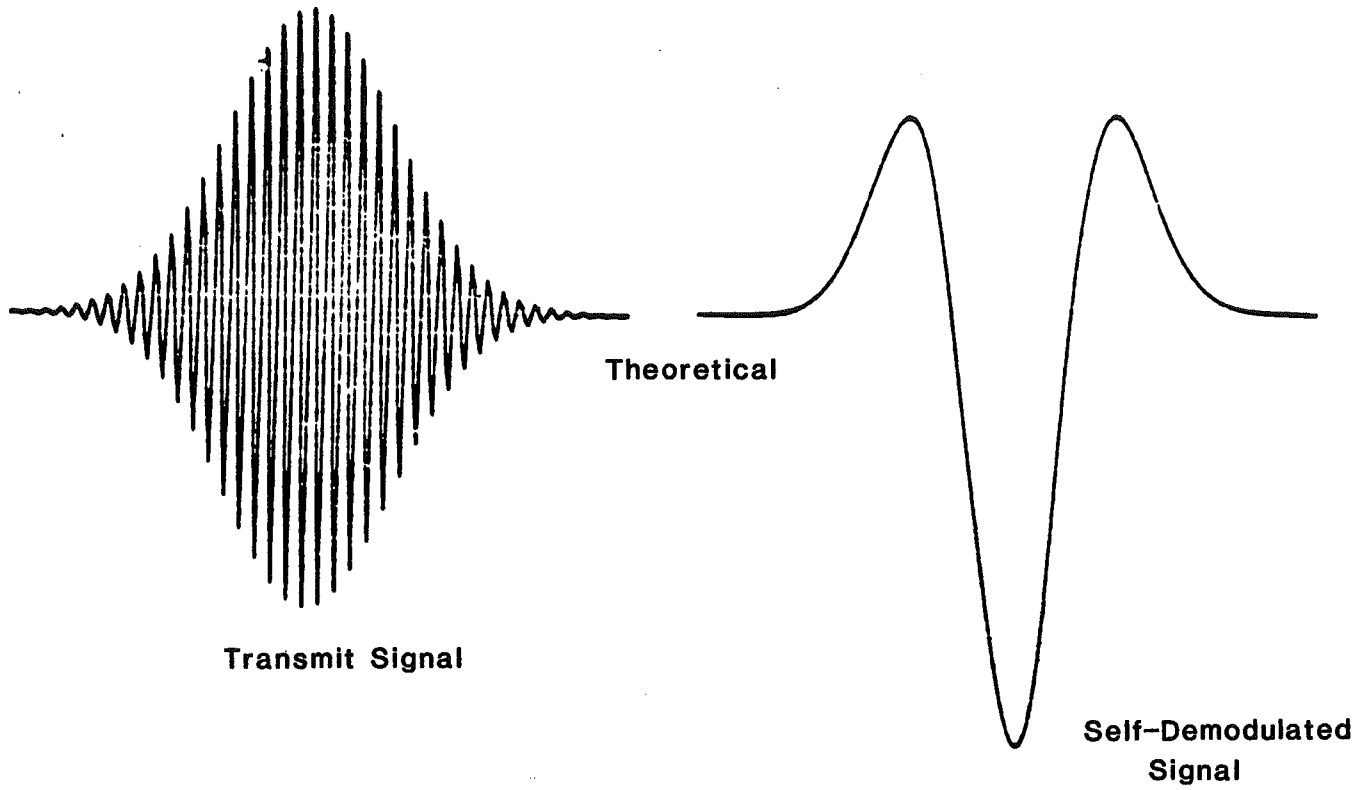
FIGURE 5.4 Complex Impedance Measurements

frequency is then produced from the interaction of the beams in the water column. The resultant secondary beam has the characteristics of an exponentially tapered end fire array, the exponential taper being caused by the water attenuation at the primary frequency and the end fire array is formed in the narrow water column below the transducer.

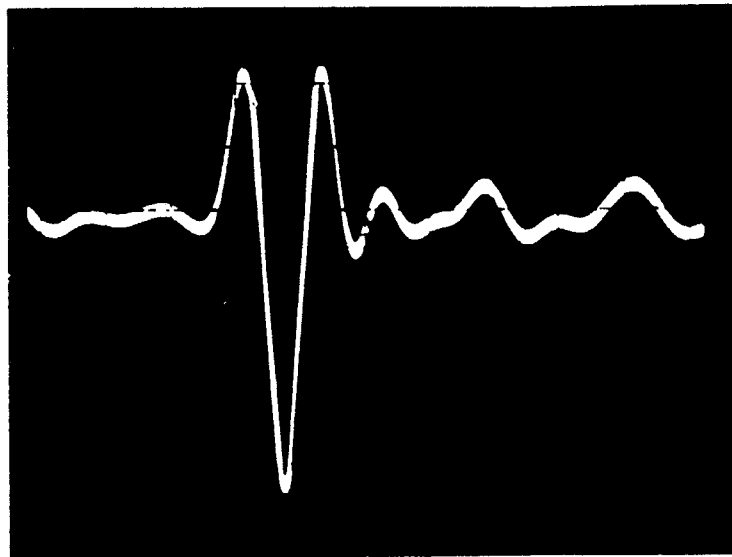
A slightly different approach is selected for the "Acoustic Sub-seabed Interrogator". Instead of two high frequencies, a carrier wave modulated by a Gaussian envelope is sent to the transducer. As this Gaussian modulated acoustic pulse travels through the water it self demodulates. (see Figure 5.5 for a qualitative look at the resultant inverse Ricker wavelet generated through self-demodulation). This effect generates the low frequency pulse required.

The self demodulation in water of a sound waveform in the form of a pulsed carrier was first predicted by Berktaf (1965) and investigated experimentally by Moffett, Westervelt and Beyer (1971), Muir (1969), Merklinger (1971), and Pace (1979,1981). For a Gaussian modulated carrier the process produces an acoustic pulse of similar time duration to that of the carrier pulse (Pace (1981)). This provides for a means to create a pulse with a bandwidth as large as that of the carrier pulse but of a mode frequency dependant upon pulse length.

The transmission electronics employed in the experiment are described in schematic form in Figure 5.6a. Briefly the carrier frequency is generated through an HP Generator/Sweeper and mixed in a Hatfield Double Balance Mixer with a Haversine (or "Raised Cosine



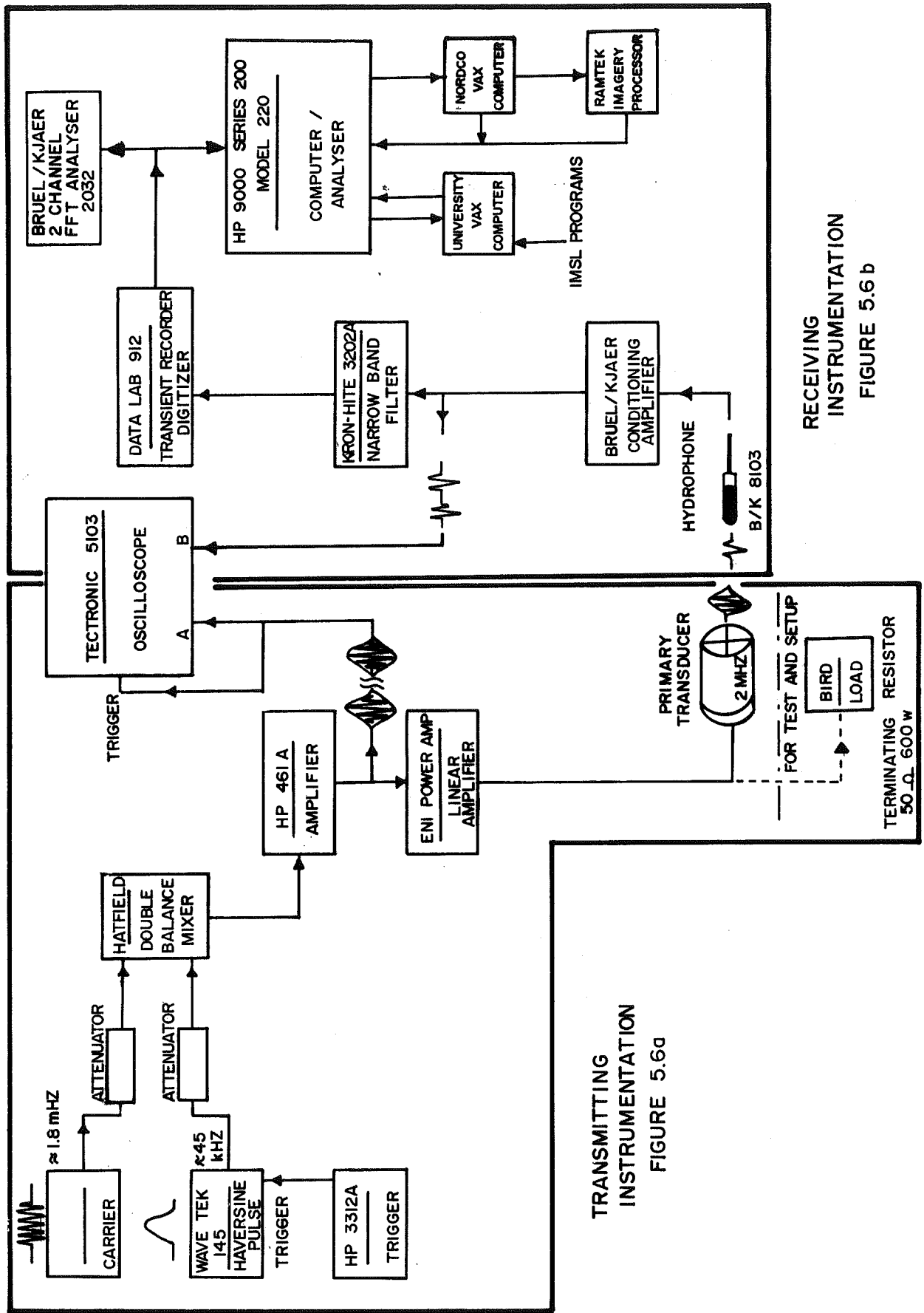
Experimental Tank Test



April 2, 1984 Vertical 50mV/DIV Horizontal 10μs/DIV

Self-Demodulated Signal

FIGURE 5.5 Inverse Ricker Wavelet



RECEIVING INSTRUMENTATION
FIGURE 5.6 b

TRANSMITTING INSTRUMENTATION
FIGURE 5.6a

FIGURE 5.6 Transmitting and Receiving Instrumentation Schematic

Bell") envelope created from a Wavetek Function Generator. The modulation is then amplified by an HP Buffer Amplifier before being sent through an ENI Power Amplifier. From the Power Amplifier the waveform enters the transducer.

To modify the envelope of the transmitted pulse the modulating function was adjusted by manipulating the starting phase and d.c. offset of a single cycle of the sinusoidal wave as obtained from the function generator. Using this technique, the duration of the demodulated pulse was set through the frequency of the Haversine selected.

5.4.3 Receiving Instrumentation

The receiving instrumentation employs conventional measuring devices and comprehensive signal processing support. This is illustrated in Figure 5.6b. Once transmitted, the signals are picked up by a miniature hydrophone (Bruel and Kjaer) then passed on through a conditioning amplifier (Bruel and Kjaer) and a band pass filter (KHROHITE) before being digitized by a transient recorder (Data Lab 912). The buffers of the transient recorder are controlled by a powerful desk top computer (HP 9000 model 220-series 200) which also stores the signals during the initial stages of data reduction and of data processing.

The system for the HP 9000 computer can be booted in two languages:

i) BASIC 3.0 (HP)

and

ii) PASCAL 3.0 (HP)

An emulation package is also incorporated in this unit to directly integrate the system with the Memorial University of Newfoundland Vax Computer and with NORDCO Ltd.'s RAMTEX Imagery Processor. In addition a dedicated Bruel and Kjaer Dual Channel Signal Analyzer (Type 2032) is employed in the post processing stage of the testing. The manipulation of the Hilbert Transform is performed by this analyzer to procure an energy envelope of the time signals on a log scale and to make Instantaneous Frequency measurements.

5.4.4 Sediment and Acoustic Propagation Modelling

The sediment model ensconced for the experimental testing of the ASI concepts simulates only the Basal Till - Case IV of Section 3.4.6.3 (refer to the Stratigraphic Model developed in Chapter 3.0 - Layer 5 for details). The boulders and cobbles of the layer are accounted for by hand sieved beach gravel passing a sieve size of 32 mm and retained at 16 mm. The fine matrix is formed by using Asphalt Plant Dust with a very small fraction of Montmorillonite clay. A dense (5 cm) StyrofoamTM S100 base reproduces the high reflectivity character of a Tertiary bedrock interface. The foam surface is thinly coated with ARALDITETM resin for added hardness. The acoustic propagation is scaled according to the discussions of Section 5.3.1.

The following three subsections elaborate the simulation aspects of the model in terms of the acoustic theory applied and of the sediment composition used in the scaled till structure.

5.4.4.1 Acoustic Simulation Parameters

i) Establishing the Single Layered Character of the Pseudo Till Model:

Four Reverberation Levels were calculated in Section 3.4.6.4. A correction or adjustment is now required in the modelling to represent the unique character of a single till layer and not of a multi-layered structure. The effects of the layers above the till in the Stratigraphic Model are reexamined then eliminated appropriately.

If the transmitter is stationary at 8.5 metres (or 48.6 cm in the scaled case) above the till layer then the following size distribution, number, σ_v , S_v and description can be articulated for three till cases:

Case I: A single layered revised till model based on Section 3.4.6.3 (Case IV) is assumed. The four overburden layers of the Stratigraphic Model are eliminated leaving only the till layer.

<u>Volume</u> (in %)	<u>Size</u> (dia. in metres)	j_p (number)	<u>Synopsis</u>
2	0.5	160	Total Elements: 121843
2	0.25	1284	σ_v (per metre): 5.8
16	0.20	20066	S_v (dB): -3.4
10	0.10	100333	
70	VFM	—————	

Case II: A laboratory model (17.5 scale factor), based on the conditions set in Case I is calculated.

<u>Volume</u> (in %)	<u>Size</u> (dia. in mm)	$\frac{j}{p}$ (number)	<u>Synopsis</u>
1.2	25.4	43	Total Elements: 318492
1.3	19.1	111	σ_v (per metre) : 192.9
1.3	12.7	377	S_v (dB): 11.9
0.1	11.1	43	
2.4	7.9	2886	
8.4	5.5	29566	
11.3	4.1	100505	
3.1	2.9	78877	
0.3	2.2	17236	
0.6	1.6	88848	
70.0	Aquagel and Asphalt Plant Dust		

Case III: A full scale equivalence of the Case II laboratory model is now stated.

<u>Volume</u> (in %)	<u>Size</u> (dia. in metres)	$\frac{j}{p}$ (number)	<u>Synopsis</u>
1.2	0.44	141	Total Elements: 944293
1.3	0.33	362	σ_v (per metre): 11.0
1.3	0.22	1224	S_v (dB): -0.6
0.1	0.19	146	
2.4	0.14	8775	
8.4	0.10	84280	
11.3	0.07	330544	
3.1	0.05	248827	
0.3	0.04	47031	
0.6	0.03	222963	
70.0	-	-	

Figure 5.7 presents the Cumulative Distribution Curve for the actual physical sediment model (Case II) and its corresponding full scale model curve (Case III). Curves for the theoretical Case I are also shown as a control for both scales. Figure 5.8 categorizes in a condensed format the volume fractions used for each averaged grain size diameter.

ii) Setting an Optimum f_d :

The optimum f_d (f_d max) for the experiments is found by applying the derivation of P: (from expression 5.5)

$$P = 2.8 \times 10^{-7} \lambda^3 f_d^2 e^{-f_d} \{2[\alpha_i(R_i - R_{i-1}) + (\bar{\alpha}_{R_{i-1}} R_{i-1})]\}$$

which after differentiating, becomes: (from expression 5.6)

$$\frac{dP}{df_d} = 0; f_d^{\max} = \frac{2}{2[\alpha_i(R_i - R_{i-1}) + (\bar{\alpha}_{R_{i-1}} R_{i-1})]}$$

Applying this to a single till layer:

$$f_d^{\max} = \frac{1}{\alpha R} = \frac{8.686}{\alpha' R} \quad (5.12)$$

where α is equal to $\frac{\alpha'}{8.686}$ in nepers/m Hz and α' is expressed in dB/m Hz. R is a one way travel depth associated with the layer. A value for R was calculated to be 0.57 metres which corresponds to a full scale value of 10 metres.

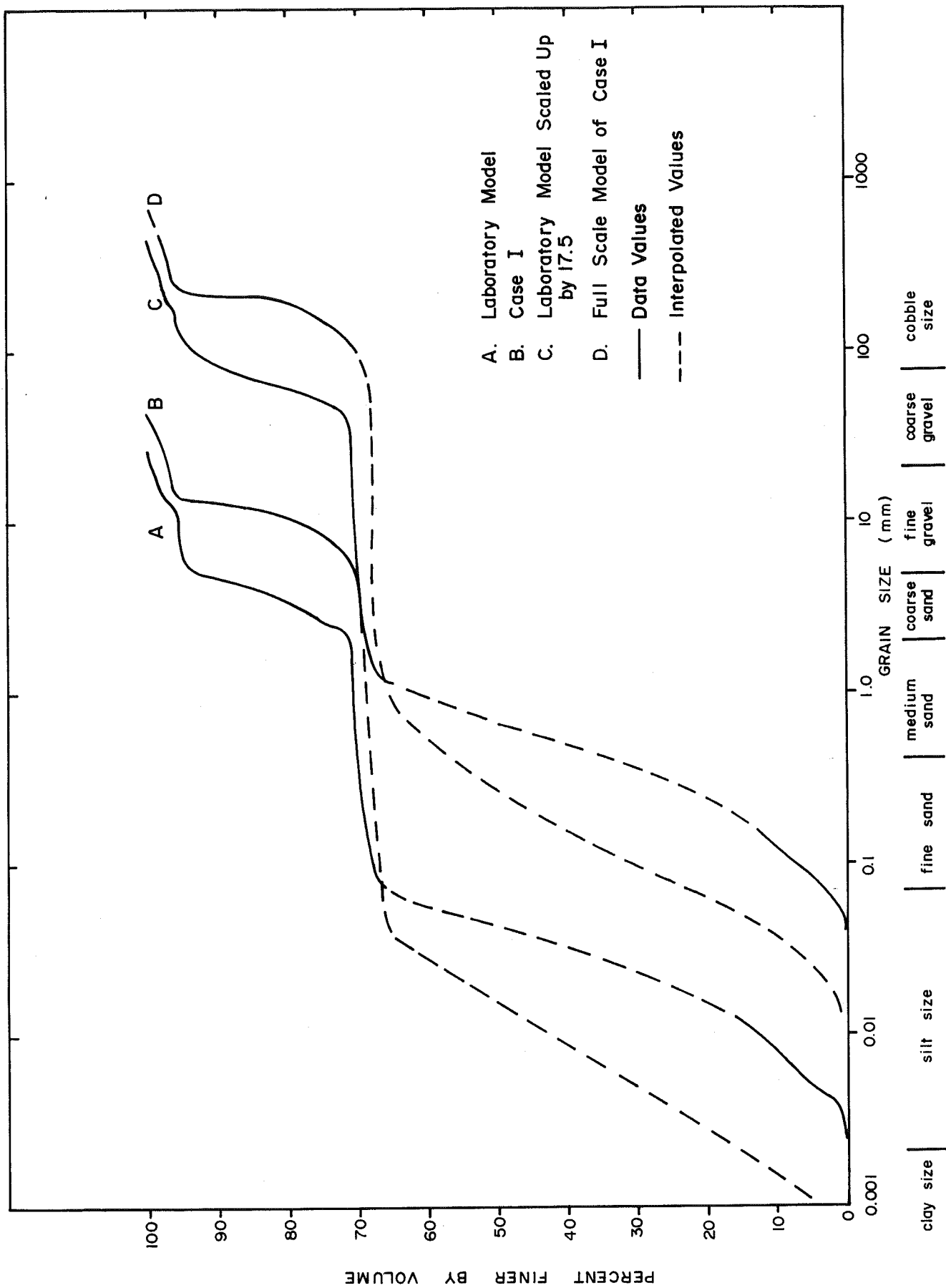


FIGURE 5.7 Cumulative Distribution Curves for the Physical Sediment Model and its Corresponding Scaled Up Case.

Volume (m ³)	Laboratory Model		Full Scale Model		Percentage finer by volume %
	grain size (mm) (in diameter)	averaged grain size (mm) (in diameter)	grain size (cm) (in diameter)	averaged grain size (cm) (in diameter)	
0.7005	Aquagel & Asphalt	-	-	-	70.0
6.12 x 10 ⁻³	plant dust	1.59	2.07 - 3.50	2.79	70.6
3.40 x 10 ⁻³	1.18 - 2.00	2.18	3.50 - 4.13	3.82	70.9
3.10 x 10 ⁻²	2.00 - 2.36	2.86	4.13 - 5.88	5.00	74.0
1.14 x 10 ⁻¹	2.36 - 3.36	4.06	5.88 - 8.33	7.11	85.3
8.50 x 10 ⁻²	3.36 - 4.76	5.53	8.33 - 11.03	9.68	93.7
2.40 x 10 ⁻²	4.76 - 6.30	7.91	11.03 - 16.43	13.73	96.1
6.80 x 10 ⁻⁴	6.30 - 9.51	11.11	16.43 - 22.22	19.33	96.2
1.31 x 10 ⁻²	9.51 - 12.7	12.7	22.22	22.22	97.5
1.31 x 10 ⁻²	12.7	19.1	33.43	33.43	98.8
1.31 x 10 ⁻²	19.1	25.4	44.45	44.45	100
1.21 x 10 ⁻²	25.4				

FIGURE 5.8 Comparing the Grain Size Distribution for the Laboratory Model and for the Full Scale Model.

The differences in density between the sea model and the scaled tank model are not very large because the fine matrix of both are similar in particular size and character. Only the larger sediment fraction is scaled. Therefore a density of 2300 kg/m^3 is expected in the tank model layer. The velocity of sound in the medium should theoretically be in the vicinity of 2000 ms. Both the density and the velocity concord well with measured values taken off North Atlantic Cores (Taylor Smith 1974). A minimum value of $2.0 \times 10^{-4} \text{ dB/m Hz}$ is hypothesized for the sediments' Attenuation Coefficient based on the density and the mean grain size distribution. While the height λ above the sediment bed is 0.486 metres, the optimum f_d was found to be approximately 76 kHz.

The following table illustrates the correlation between the seabed and the scaled physical model in terms of the signal's frequency content.

\underline{R} (m)	$\underline{\lambda}$ (m)	$\underline{f_1}$ (Hz)	$\underline{f_2}$ (Hz)	$\underline{\Delta f}$ (Hz)	$\underline{f_d \text{ max}}$ (Hz)	$\underline{\alpha'}$ (dB/m Hz)
(Seabed)						
10	8.5	912.0	2953.2	2041.2	1737.2	5.0×10^{-4}
(Scaled Sediment Model)						
0.57	0.486	40001.3	129528.1	89526.8	76,193.0	2.0×10^{-4}

iii) Predicting a Source Level:

The Source Level can be predicted for a two way transmission into the one layer model providing that,

$$P = 2.8 \times 10^{-7} \lambda^3 f_d^2 e^{-f_d^2(\alpha R)} \quad (5.13)$$

This can be rewritten in dB re 1 μ Pa:

$$SL'_d = -11.17 + 60 \log \lambda + 40 \log f_d - 40 f_d \alpha R \log e \quad (5.14)$$

where $40 f_d \alpha R \log e = 40 \log e$ since $f_d = \frac{1}{\alpha R}$ as seen in expression 5.12. λ is in metres, f is in hertz, R is in metres, $\log e$ is equal to 0.434294 and the prime ' indicates that an absorption component is present in the expression.

In the case of the full scale seabed model, $SL_d = 156.8$ dB re 1μ Pa while for the physical model, $SL_d = 147.9$ dB re 1μ Pa. The Source Level SL_d at the model-bed/water interface is 165.3 dB re 1μ Pa. Therefore the intensity difference expected, between the level at the model-bed and after a two way propagation path in the till layer is in the vicinity of 20 dB re 1μ Pa. This value is meant to represent a minimum attenuation level anticipated for the experimental propagation.

iv) Calculating a Reverberation Level

TSR_R , EL, RL and SRR are deliberated for the three cases as first approximations. The results are indexed as follows:

<u>Case</u>	<u>λ</u>	<u>R_1</u>	<u>TS</u>	<u>Γ</u>	<u>TSR_{R_k}</u>	<u>EL</u>	<u>RL</u>	<u>SRR</u>
	(m)	(m)	(dB)		(dB)	(dB re 1 μ Pa)		
I	8.5	10	9.3	-12.5	7.4	117.0	115.1	1.8
II	0.49	0.57	-19.8	-17.9	-24.9	129.6	124.5	5.1
III	8.5	10	9.3	-9.7	10.2	117.0	117.9	-0.9

(Note: $SRR = TS - TSR_{R_k}$ and $\Gamma = 10 \log \left[\sum_{k=1}^n (TSR_k) \right]_{R_k}$)

5.4.4.2 Sediment Preparation

A critical step in the preparation of the sediment is the complete removal of the air held by the attractive forces between the sediment particulates. Without this manoeuver the entrapped air would cause unwanted scattering and reflections.

A 30 gallon tank made of 1/8" mild steel plate was acquired and modified to accept a high speed vacuum pump. A 4" dia. PVC ball valve was attached to release the sediment after an evacuation. Vacuum shut-off, water intake valves and various gauges provide an ease in controlling the overall operation. After two hours of air evacuation water is sent into the vacuum chamber. A water saturated sediment is then released through a water filled hose into the semi-submerged Sediment Model Tank.

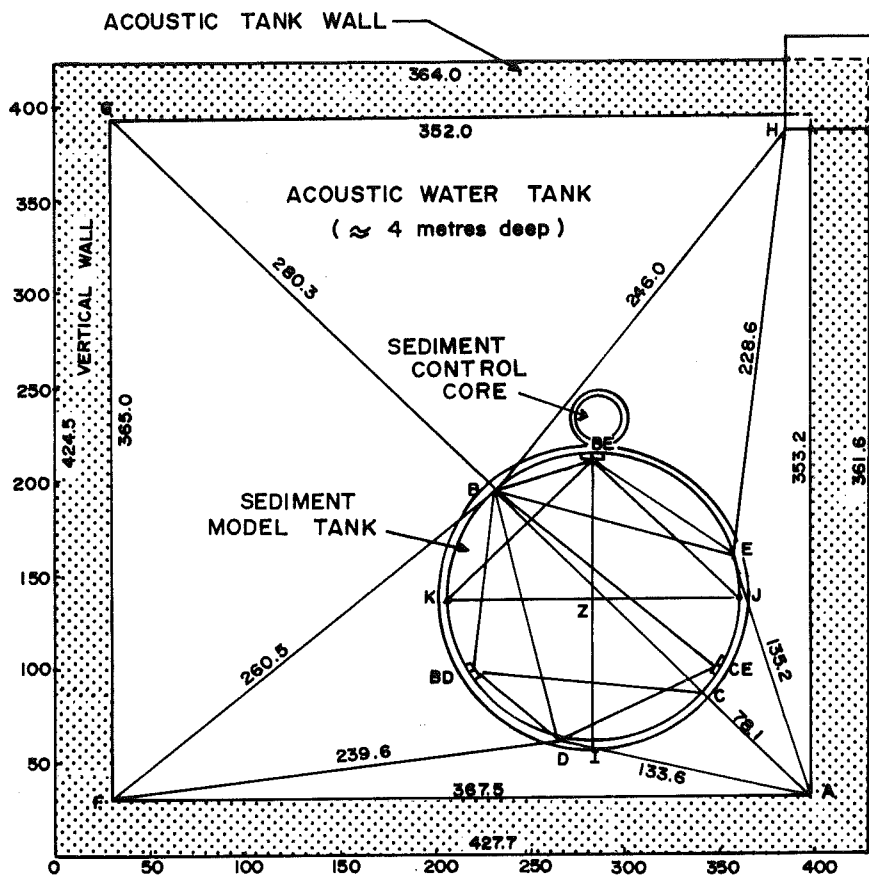
5.4.4.3 Supporting Containers

A mild steel cylindrical tank was built then placed inside the Acoustic Tank in order to support the simulated glacial till layer. Its dimensions are illustrated in Figure 5.9 and are briefly summarized below:

- i) Height = 244.8 cm
- ii) Outer diameter = 150 cm
- iii) Wall Thickness = 1.2 cm

The transmitting transducer and the receiving hydrophone are positioned in the central region of the Sediment Model. The top rim of the Sediment Model Tank (S.M.T.) provides a useful horizontal datum plane for the experiments. This tank rim was surveyed using as reference markers, the four corners of the deep Acoustic Tank. (Refer to Figure 5.9 for details on the measurements made).

In addition to the Sediment Model Tank, a smaller tank called a Sediment Control Core (S.C.C.) was designed and placed adjacent to it. This tank which is made of polyethylene, is used to simulate an in-situ undisturbed core. As the sedimentary layer is placed in the larger tank an identical layer is formed in the smaller one. To facilitate the pouring of the sediments a long narrow plexiglass window was installed into the control core wall. Potential layer thickness shrinkage due to the settling of the fine matrix can thus be monitored by viewing the overall structure through this window. The physical dimensions of the tube are (refer to Figure 5.9):



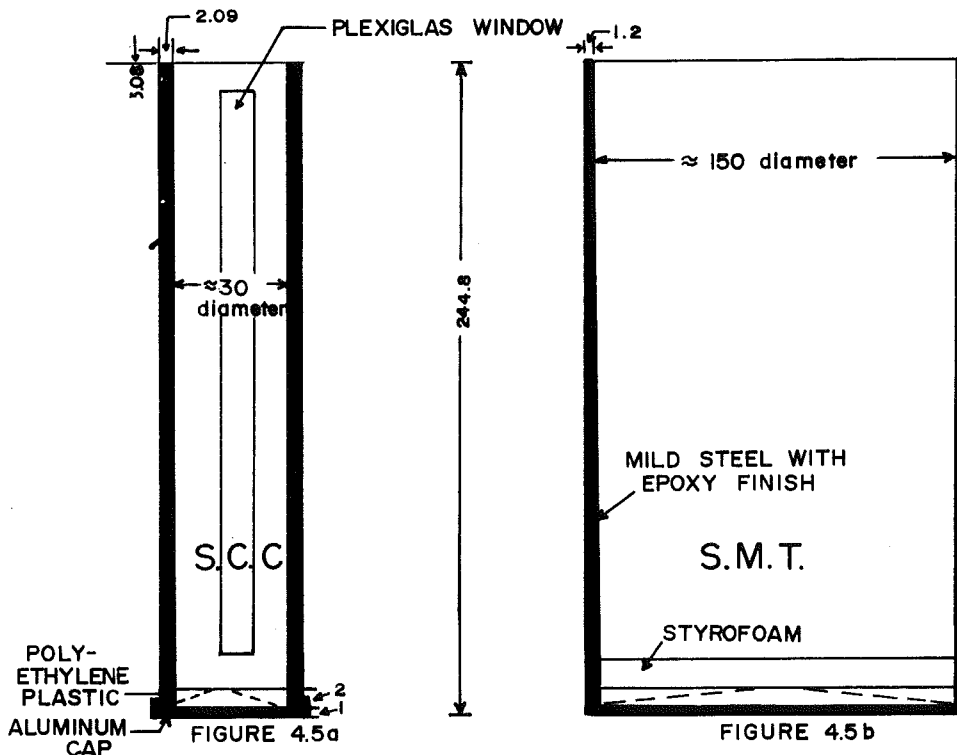
SURVEYED LENGTH

- BC = 154.9
- BD = 138.2
- BE = 129.6
- CE = 78.5
- DE = 132.8
- DI = 23.9
- EI = 125.5
- IK = 108.1
- JK = 155.0
- JI = 110.0
- BBD = 96.5
- BBE = 52.9
- BCE = 148.7
- CBD = 122.4
- DBD = 60.3
- DCE = 88.3
- EBE = 89.2
- IBE = 149.8
- JBE = 106.6
- KBE = 106.1
- ZBE = 73.0
- ZI = 77.0
- ZJ = 78.0
- ZK = 76.8

APPROX SCALE
1:25

PLAN VIEW

ALL VERTICAL COLUMNS / WALLS
ARE ASSUMED UNIFORM AND
VERTICAL.



DEVIATION FROM IDEAL

DISTANCE	I IDEAL TANK	II IDEAL TANK	$\Delta = I - II$
IJ	109.96	110.0	0.0
IK	109.96	108.1	1.9
JK	155.5	155.5	0.5
IBE	154.3	149.8	4.5
JBE	109.11	106.6	2.5
KBE	109.11	106.1	3.0
ZBE	76.55	73.0	3.6
ZI	77.75	77.0	0.8
ZJ	77.75	78.0	-0.2
ZK	77.75	76.8	1.0

ALL DIMENSIONS ARE IN
CENTIMETRES

ELEVATION VIEW

FIGURE 5.9 Acoustic Water Tank, Sediment Model Tank and Control Core Dimensions.

- i) Height = 245 cm
- ii) Inner diameter = ~ 30 cm
- iii) Wall thickness = ~ 2.1 cm

5.5 Experimental Compendium

One of the aims of the tests is to map the spatial inhomogeneity and character of the pseudo glacial till. In order to accomplish this, two spatial scanning circumferences are executed. Each ring represents eight spatial positions. This corresponds to the "Acoustic Core" spatial columns discussed in Chapter 4.0, Section 4.3.

The first circular scan has an outer diameter of 23.5 cm. Its eight locations are coded:

$$\text{1st Ring Positions} = \{A, A_1, B, B_1, C, C_1, D, D_1\} \quad (5.15)$$

The second ring is an inner ring. Its diameter is 8.5 cm and the elemental locations on this ring are coded:

$$\text{2nd Ring Positions} = \{a, a_1, b, b_1, c, c_1, d, d_1\} \quad (5.16)$$

At each of these positions the transducer can be set at angles 0° , 3° , 6° and 9° . Complementing the transmission angle is the hydrophone array settings. This is executed in an incremental linear fashion along the z axis.

A synopsis of the project's experimental approach and setting is put forward in Figure 5.10.

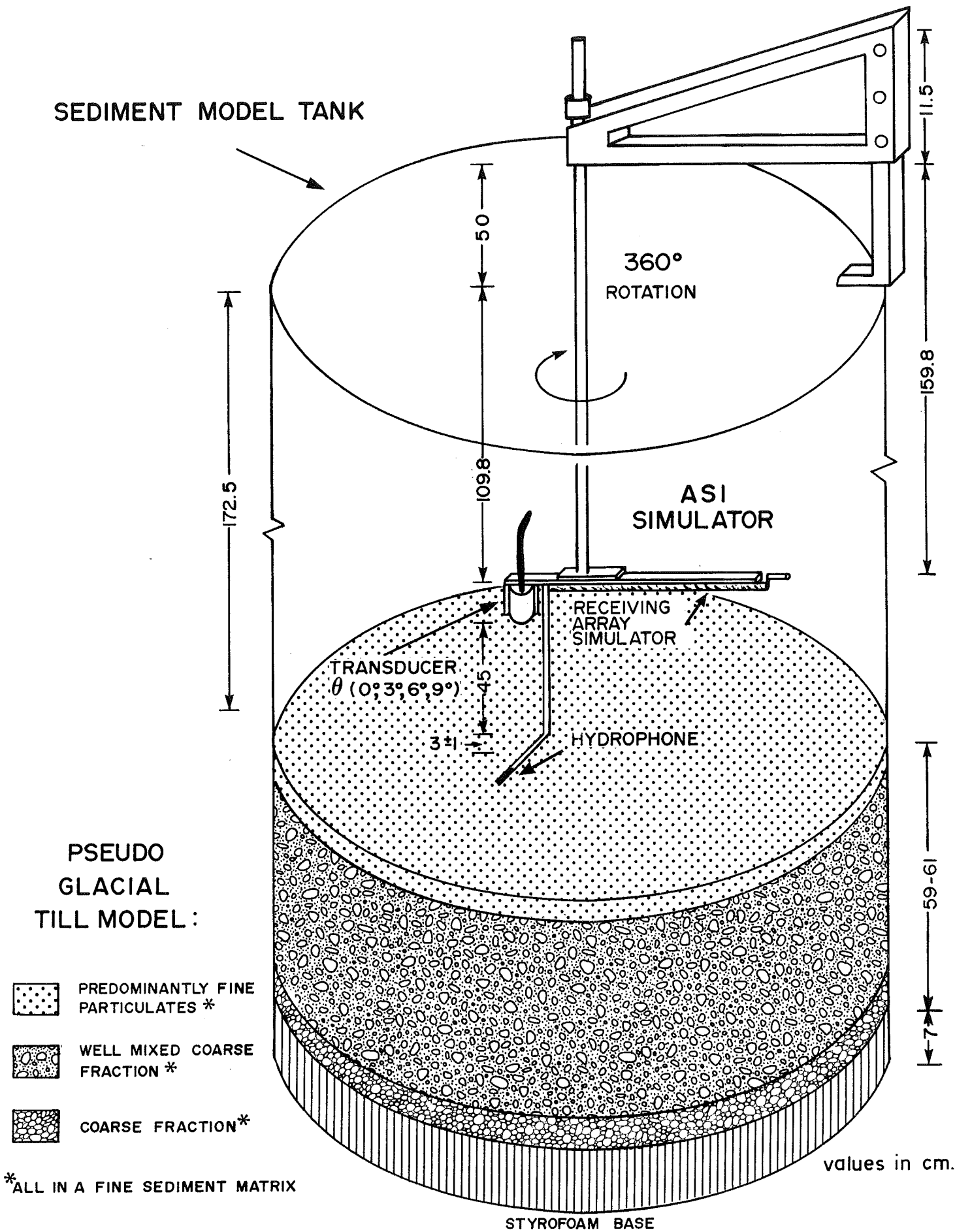


FIGURE 5.10 Overview of the Experimental Setting.

6.0 LABORATORY SIMULATION EXPERIMENTS

6.1 Scope

This chapter presents the results of an experimental simulation of the "Acoustic Sea-bed Interrogator" concept as prescribed by the analytical modelling of Chapters 3.0 and 4.0. Preparations for the experiments are discussed in detail in Chapter 5.0. The primary objective of the laboratory simulations is to test the acoustical behaviour of the spot profiler concept over a complex sediment layer that would represent one of the worst structures to seismically scan.

The ability of the ASI to interrogate the physical model in terms of velocity and of attenuation is fundamentally important. A meaningful velocity value for an inhomogeneous layer (e.g. glacial till) is very difficult if not in most cases impossible to make. The evaluation of the model's inhomogeneity through the properties of velocity and of attenuation as expressed by the spatial simulations of the laboratory ASI, highlights the potential of this new approach to generate geotechnical related information.

Apart from providing a unique insight into the character of glacial tills, the statistical analysis of the results also constitutes a foundation for an acoustic sediment classification.

6.2 Hypotheses to be Tested

The first set of experiments are designed to help corroborate the analytical evaluations of Chapter 3.0. Recapping, a theoretical study was undertaken to appraise the feasibility of getting a signal back from a complex sedimentary column involving a glacial till matrix. The computations of the theoretical study indicated that non-linear acoustics can successfully be used. It follows then that the first questions to be posed in the experiments relate to this.

- i) Will a signal return after having propagated into an inhomogeneous structure of high attenuation and scatter? Is it feasible to use a Parametric Array, optimized to be truncated at the water/sediment interface?

The second supposition refers to the methodology developed to discriminate returning echoes (see Chapter 4.0). The interrogation procedures which were designed to extract sub-seabed information are specifically tested in the laboratory investigation. The acquisition of a meaningful velocity and attenuation value is of particular significance. The use of the Hilbert Transform is stressed; allowing for envelopes of all the time functions to be registered. The following interrogative statements examines the efficacy of the techniques hypothesized:

- ii) What type of sub-layer information can be extracted, once a signal is captured? Is it feasible to measure velocity and attenuation

using the technique described in Section 4.2? What type of values can be obtained for an inhomogeneous structure? How effective is the Hilbert transform approach?

The results of the echo discrimination and of the analytical interrogation are manipulated through the "Acoustic Core" product. The returning signals once captured are exhibited in a three dimensional dynamically responding graphic display (see Chapter 4.0, Section 4.5). Hence, the post-processing evolves around this exposition; the next set of inquiries will relate to the role the "Acoustic Core" product plays:

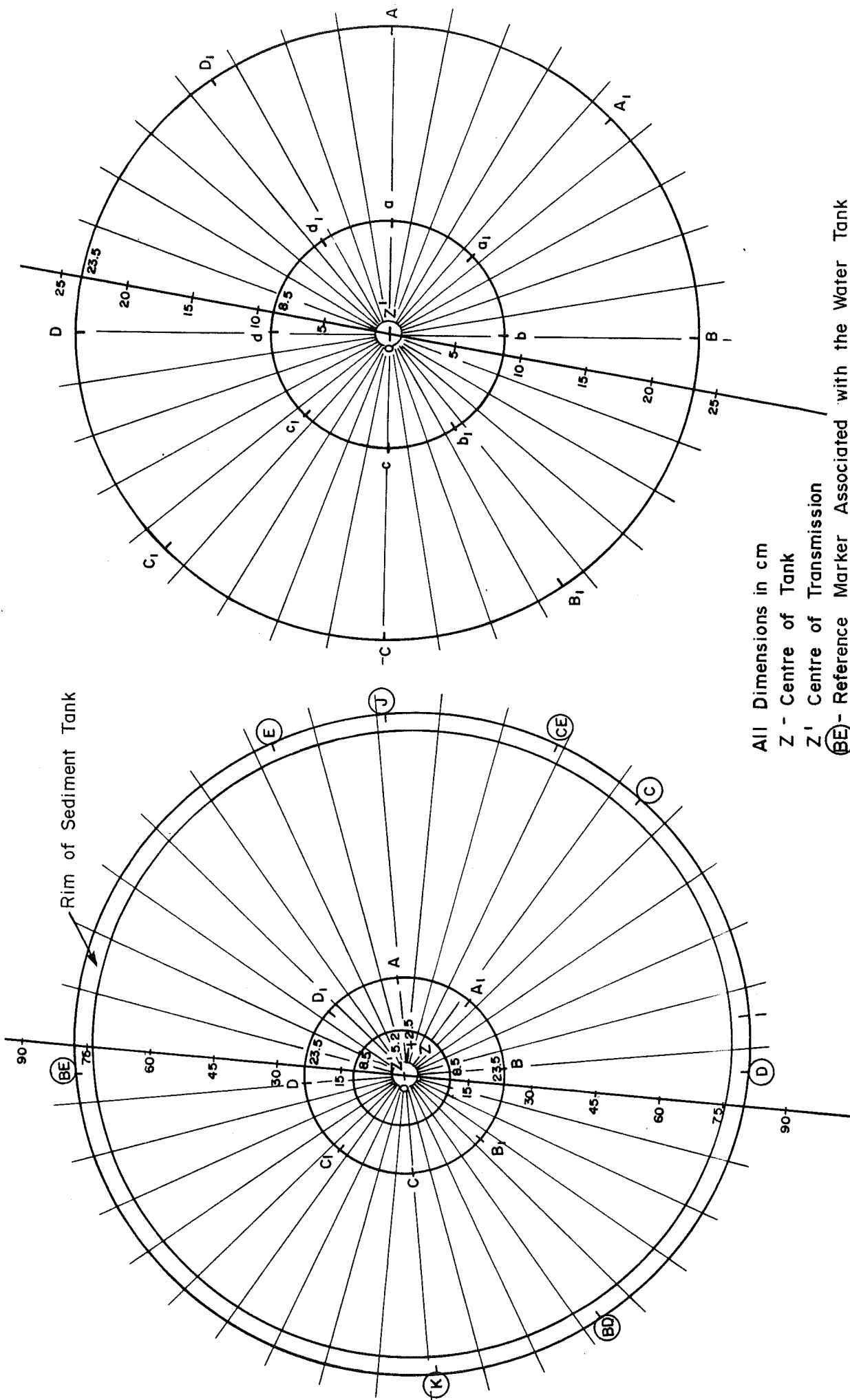
iii) What is the most cogent approach to display the information that is released out of the interrogation routines that merge in the "Acoustic Core" product?

6.3 Nomenclature and Setting Used

The nomenclature used in the experimental procedures, processing and results is illustrated and defined in Figures 6.1 and 6.2.

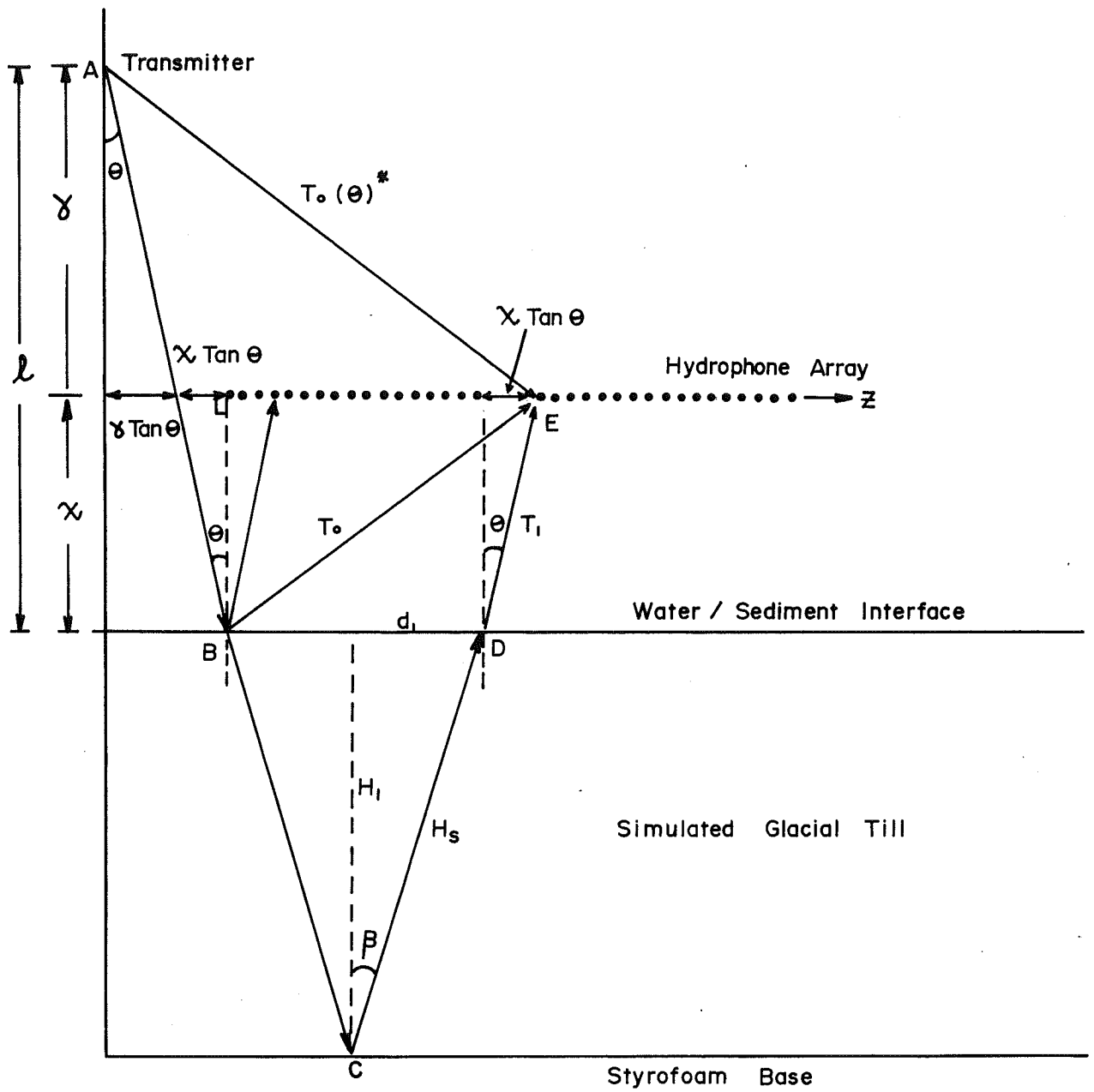
6.4 Simulation Results

The ASI interrogation ordains discrete information on each layer in a descending order. Therefore the tasks which are closely associated with the logic of the interrogation will be distinguished in the text by explicit steps. The two main layers investigated are:



All Dimensions in cm
 Z - Centre of Tank
 Z' - Centre of Transmission
 BE - Reference Marker Associated with the Water Tank
 A - Spot Position on the Outer Scanning Ring
 a - Spot Position on the Inner Scanning Ring

FIGURE 6.1 Spot Profiling Positions in Context to the Sediment Tank and to the Inner and Outer Scanning Rings.



$T_o =$ Time travelled between AE
 $T_o =$ Time travelled between ABE
 T_o or $T_i =$ Time travelled between ABCDE

FIGURE 6.2 Terminology and Ray Path Geometry used in the Experimental Simulation Trials.

- i) the water/boundary layer
- ii) the pseudo-glacial till layer

6.4.1 Establishing the Initial Character of the Water/Sediment Interface

Step 1 Manipulating the Time History Data and the Hilbert Transform

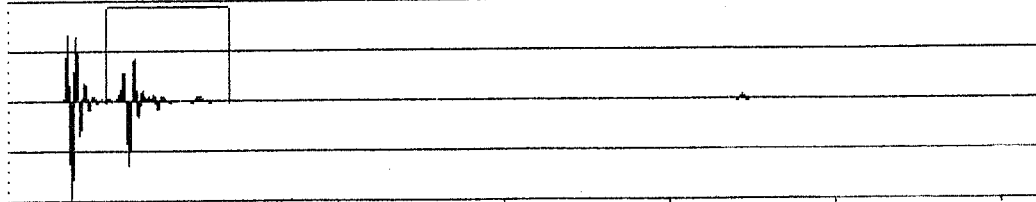
The time history data for each of the sixteen scanning positions is captured, digitized then unloaded onto an FFT Analyser for processing. PLATE 1 exhibits the premeasurement settings used and displays the digitized time signals captured at Position A. (For all other positions see PLATES 1A to 1d₁, Appendix C, Volume II). An external transient recorder (DL 912) was necessary because of the high sampling rate called for by the approximate 80 kHz centre frequency of the transmit signals. The Bruel and Kjaer Dual Channel Signal Analyser was restricted to an upper digitizing limit of 25.6 kHz.

Once the signals were digitized they were reformatted from their 8 bit resolution character into 13 bit data; their difference in resolution pre-empted by a blank buffer. The data was also duplicated before being sent to the analyser. By duplicating the data, the two channels of the analyser received the data as if the data were instantaneously coming from two separate measurement sources.

Both the time and the frequency domain analysis carries a correction factor C to account for the external sampling rate. This

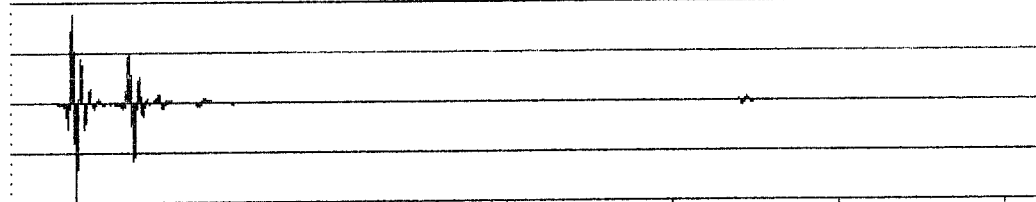
PLATE 1A - OUTER SCANNING CIRCLE
PRE-MEASUREMENT SETTINGS

W1 TIME CH.A REAL DELT Y: 18.6E-9U - REAL PART
Y: 10.6U X: 0.000ms/C
X: 0.000ms/C + 31.3ms/C OVERLOAD FLEX: 0.00000000



SETUP 1
MEASUREMENT: DUAL SPECTRUM AVERAGING - SETTINGS
TRIGGER: FREE RUN
DELAY: CH.A+B: 0.000ms/C
AVERAGING: EXP 10 OVERLAP: 0%
FREQ SPAN: 25.6kHz*0 ΔF: 32Hz*0 T: 31.3ms/C ΔT: 15.3μs/C
CENTER FREQ: BASEBAND C = EXT SAMPL FREQ/65536Hz
WEIGHT CH.A: TRANSIENT SHIFT: 2.944ms/C LENGTH: 3.738ms/C
WEIGHT CH.B: TRANSIENT SHIFT: 21.469ms/C LENGTH: 1.129ms/C
CH.A: 10V + 3Hz DIR FILT: 25.6kHz 250mV/PA
CH.B: 10V + 3Hz DIR FILT: 25.6kHz 250mV/PA
GENERATOR: DISABLED
SPECIAL PARAMETER #100: ZOOM KEY 0 DEC VALUE: 1

W1 TIME CH.A IMAG DELT Y: 34.2mU - IMAGINARY PART
Y: 10.6U X: 0.000ms/C
X: 0.000ms/C + 31.3ms/C OVERLOAD FLEX: 0.00000000



SETUP 1 OVERLOAD
PHASE
INPUT DELT Y: 90.0DEG
X: 0.000ms/C
ΔX: 0.000ms/C
FLEX: 0.00000000
0

W1 TIME CH.A PHASE
Y: -200 TO +200 DEG
X: 0.000ms/C + 31.3ms/C OVERLOAD
SETUP 1 OVERLOAD

C=30.52 (0.5μs external sampling rate)

factor C is noted throughout the post processed results as a reminder that an adjustment is prescribed. The value of C is 30.52. This corresponds to a 0.5 μ s external sampling rate.

All the normal real valued time domain functions were made complex through the use of the Hilbert Transform incorporated in the analyser. By applying this transform, two discrete properties emerged:

i) the Envelope

and

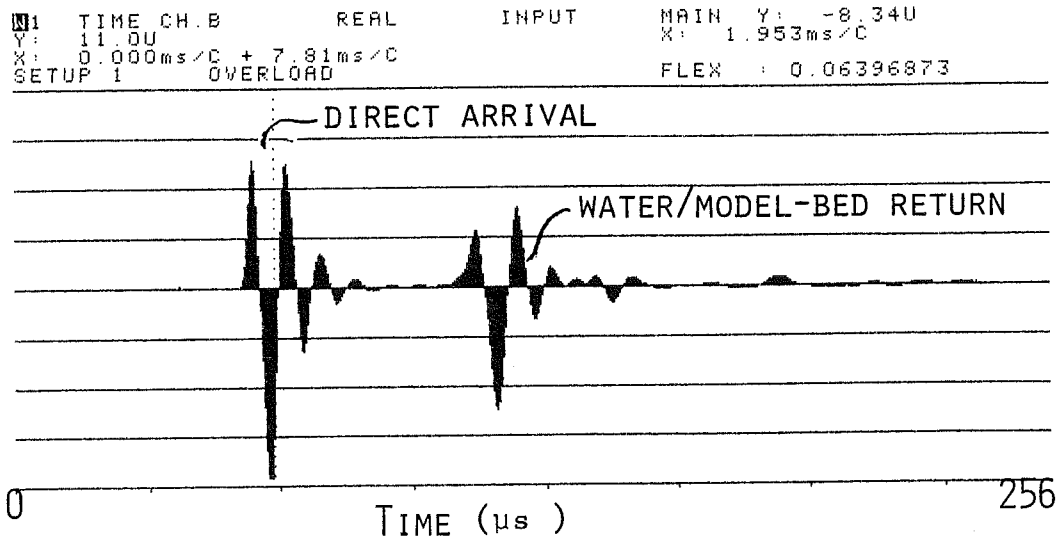
ii) the Instantaneous Frequency

(refer to Section 4.4)

PLATE 2 - Part I is a traditional presentation of the time signals showing the real part on a linear amplitude scale. By contrast the envelope or magnitude of the time signals can be computed then executed on a 40 dB logarithmic scale as seen on PLATE 2 - Part II.

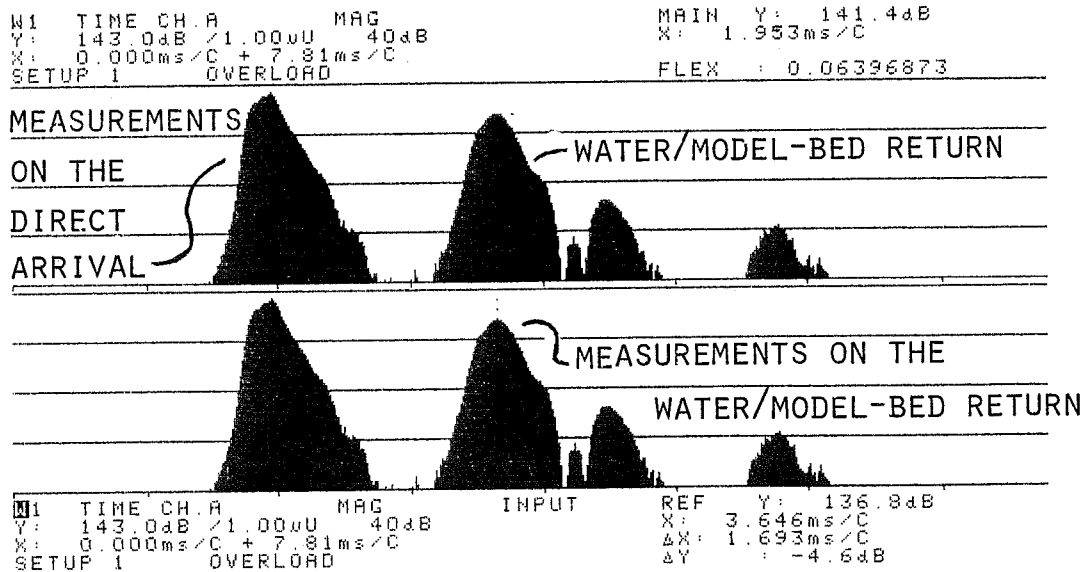
The peak position of the magnitude forms a unique and a more detailed reference position. This is significant to the interrogation routines entrenched in the ASI concept and is considered an innovative technique. A more lucid and exact time difference can be constituted using the Hilbert Transform procedure than if the conventional real

TWO PRESENTATIONS OF THE SAME TIME HISTORY DATA



TRADITIONAL TIME HISTORY TRACE

C=30.52 (0.5 μ s external sampling rate)



ENVELOPE CALCULATED USING THE HILBERT TRANSFORM

part of the signal was employed. (refer to the time measurements shown on PLATE 2).

Step 2 - Acquiring a Value for c_o and χ_p

The geometric distances between transmitter/hydrophone in relation to Position (A) are precisely known when $\theta = 0$. This provides a reference to which all other positions and conditions can be correlated to. Considering that

$$\chi_p = \left(\frac{\Delta t}{2}(o,p)\right)c_o \quad (6.1)$$

where subscript p refers to the position of the transmitter, then c_o can be readily found. χ_A is 0.041 m between hydrophone and sediment surface. The two way travel distance from the hydrophone to the seabed then back to the hydrophone corresponds to an experimentally measured $\Delta t_{(o,A)}$ time of 55.5×10^{-6} seconds. Therefore it follows that c_o is 1474 m/s which concords well with the theoretical derivation of velocity using the temperature of water as an input (see Kinsler and Frey 1982).

$$c(P_g, t_*) = 1402.7 + 488t_* - 482t_*^2 + 135t_*^3 + (15.9 + 2.8t_* + 2.4t_*^2)(P_g/100) \quad (6.2)$$

where P_g is the gauge pressure in bars and t_* is equal to $T_*/100$ with T_* in degrees Celcius. This equation is a close approximation to within

0.05 percent assuming the conditions; $0 \leq T_* \leq 100^\circ\text{C}$ and $0 \leq P_g \leq 200$ bar (1 bar = 10^5 Pa) are met.

The temperature of the water was measured to be 17.5°C while the pressure was measured at 989.3 m bars. This simplifies into a velocity of water value of 1474.22 m/s.

A close assessment of χ_p is performed for all transmitter positions using 1474 m/s as a constant. ℓ_p is determined by $\chi_p + \gamma$. γ is a constant set at 0.45 m. The values for $\Delta t_{(o,p)}$ were computed through the peak position of the analytical envelopes. Refer to PLATES 2 and 3, A to d_1 ; Appendix C of Volume II. From this diagnosis:

<u>Outer Scanning Ring</u>				<u>Inner Scanning Ring</u>			
<u>Position</u>	ℓ_p	$\Delta t_{(o,p)}$	χ_p	<u>Position</u>	ℓ_p	$\Delta t_{(o,p)}$	χ_p
	(cm)	(μs)	(cm)		(cm)	(μs)	(cm)
A	49.1	55.5	4.1	a	48.6	49.0	3.6
A ₁	48.6	48.5	3.6	a ₁	48.4	45.5	3.4
B	47.2	29.5	2.2	b	48.0	41.0	3.0
B ₁	47.1	28.5	2.1	b ₁	47.7	36.5	2.7
C	47.9	38.5	2.8	c	47.9	39.5	2.9
C ₁	47.8	38.0	2.8	c ₁	48.0	41.0	3.0
D	47.9	39.0	2.9	d	48.6	49.0	3.6
D ₁	48.8	51.0	3.8	d ₁	48.7	50.0	3.7
Average :	48.1	41.2	3.1	Average:	48.2	43.9	3.2
$\pm\sigma$:	0.7	9.8	0.7	$\pm\sigma$:	0.4	5.1	0.4

where the Standard Deviation was calculated using : (from Chatfield (1976))

$$\sigma = \left(\frac{[\sum_{p=1}^n X_p^2] - n \bar{X}^2}{(n-1)} \right)^{1/2} \quad (6.3)$$

X is the value of the variate and n is the number of observations.

Step 3 - Predicting and Comparing $T_{(o,p)}$ when $\theta \neq 0$

Predicting the total time of travel in the water $T_{(o,A)}(\theta \neq 0)$ (see Figure 6.2 - travel path ABE) using the parameters established when $\theta = 0$ does allow for a second evaluation of the water boundary measurements. The comparison between the predicted time of arrival and the actual measured time of arrival should be essentially the same since the water medium for all intensive purpose can be considered homogeneous. The difference in values may provide a first look at how the propagation is affected by the micro-topography character of the sediment surface.

The prediction of $T_{(o,p)}$ is executed through

$$T_{(o,p)} \text{ (predicted)} = \frac{(\gamma + \chi_p)/\cos\theta + (\chi_p/\cos\theta)}{c_o} \quad (6.4)$$

where $T_{(o,p)}$ (predicted) corresponds to a specific $z_{(o,p)}$ position which is determined by;

$$z_{(o,p)} \text{ (predicted)} = \gamma \tan\theta + (2\chi_p \tan\theta) \quad (6.5)$$

$z_{(o,p)}$ (predicted) is crosschecked against the z position of the highest amplitude water/sediment return. γ is equal to 0.45 metres and χ_p is procured through expression (6.1).

<u>Position</u>	<u>θ</u> (degree)	<u>$z_{(o,p)}$</u> (cm)	<u>$T_{(o,p)}$ (predicted)</u> (μs)	<u>$T_{(o,p)}$ (measured)</u> (μs)	<u>$\Delta T_{(o,p)}$</u> (μs)
A	3°	2.8	361.4	**	**
A ₁	3°	2.7	354.6	**	**
B	3°	2.6	335.6	**	**
B ₁	3°	2.6	334.2	**	**
C	3°	2.7	345.1	346.5	1.4
C ₁	3°	2.7	343.8	350.4	6.6
D	3°	2.8	345.1	348.9	3.8
D ₁	3°	2.7	357.3	361.3	4.0
I.	average:		347.1	351.8 [4.7]	4.0
	$\pm\sigma$:		9.9	6.6 [3.3]	2.1
	$\pm\bar{\xi}$:		-	i) 0.014 (1.4%)	ii) 0.011 (1.1%)
a	3°	2.7	354.6	354.3	0.3
a ₁	3°	2.7	351.9	352.0	0.1
b	3°	2.7	346.5	346.5	0.0
b ₁	3°	2.7	342.4	344.9	2.5
c	3°	2.7	345.1	343.4	1.7
c ₁	3°	2.7	346.5	345.7	0.8
d	3°	2.7	354.6	351.2	3.4
d ₁	3°	2.7	356.0	355.1	0.9

(continued)		$T_{(o,p)}$ (predicted) (μs)	$T_{(o,p)}$ (measured) (μs)	$\frac{\Delta T}{T}$ (o,p) (μs)
II.	Average:	349.7	349.1 [0.6]	1.2
	$\pm\sigma$:	5.2	4.5 [0.7]	1.2
	$\pm\bar{\xi}$:	-	- i) 0.002 (0.2%)	ii) 0.003 (0.3%)
I. and II.	$\pm\bar{\sigma}$:	-	- [2.0]	-
	$\pm\bar{\xi}_{max}$:	-	- 0.014 (1.4%)	-

** no data

I. Outer Scanning Ring

II. Inner Scanning Ring

Given that:

[n] - The quantity n is the absolute value for the difference between the average predicted and the average measured T.

$$\pm\bar{\xi} - \text{Error} \quad \begin{aligned} \text{i)} &= \left| \frac{\text{Average Predicted T} - \text{Average Measured T}}{\text{Average Predicted T}} \right| \\ \text{ii)} &= \left| \frac{\text{Average } \Delta T}{\text{Mean Between Average Predicted And Average Measured T}} \right| \end{aligned}$$

$\pm\bar{\xi}_{max}$ - The maximum value of ξ between the Inner and Outer Rings.

$\pm\bar{\sigma}$ - The average value of $[\sigma]$ between the Inner and Outer Rings.

6.4.2 Appraising the Internal Dimensions of the Pseudo-Glacial Till Structure

Step 4 - Measuring $\Delta t_{(1,p)}$ and Establishing the First Velocity Estimate for the Layer when $\theta = 0$.

$\Delta t_{(1,A)}$ is experimentally measured. This derives a value of 608×10^{-6} seconds which refers to the two-way time interval within

the layer. The layer thickness is $0.59 \pm .01$ metres at A. This was set as a laboratory control for position A. Therefore it follows that the velocity of the till layer at A is 1941 m/s. Velocity is computed using the simple relationship

$$c_{(1,A)} = \frac{2H_{(1,A)}}{\Delta t_{(1,A)}} \quad (6.6)$$

From A, λ^* is determined by summing λ_A and $H_{(1,A)}$. Since λ^* is a constant for all transmitter positions and has a value of 107.7 cm; then $H_{(1,p)}$ can be redefined as

$$H_{(1,p)} = \lambda^* - \lambda_p \quad (6.7)$$

The table below presents the first estimate of velocity for all transmitter positions p using the constant λ^* to compute $H_{(1,p)}$.

<u>Outer Scanning Ring</u>				<u>Inner Scanning Ring</u>			
<u>Position</u>	$\Delta t_{(1,p)}$	$H_{(1,p)}$	$C_{(1,p)}$	<u>Position</u>	$\Delta t_{(1,p)}$	$H_{(1,p)}$	$C_{(1,p)}$
	(μs)	(cm)	(m/s)		(μs)	(cm)	(m/s)
A	608	59	1941	a	606	59	1947
A ₁	604	59	1954	a ₁	606	59	1947
B	604	61	2020	b	604	60	1987
B ₁	604	61	2020	b ₁	604	60	1987
C	606	60	1980	c	602	60	1993
C ₁	602	60	1993	c ₁	608	60	1974
D	599	60	2003	d	604	59	1954
D ₁	606	59	1947	d ₁	606	59	1947
Average:	604	59.9	1982	Average:	605	59.9	1967
$\pm \sigma$:	2.7	0.8	13.9	$\pm \sigma$:	1.9	0.5	20.3

PLATE 3 - Part II graphically illustrates the real part of the signal received off the pseudo glacial till base. The envelope or magnitude of the signals are also shown. $\Delta t_{(1,p)}$ values were established using the peak of the envelopes as a reference. The computations for all positions can be seen in PLATES 2 and 3, A to d₁; Appendix C of Volume II.

Step 5 - Predicting and Comparing $T_{(1,p)}$ and $c_{(1,p)}$ when $\theta \neq 0^\circ$

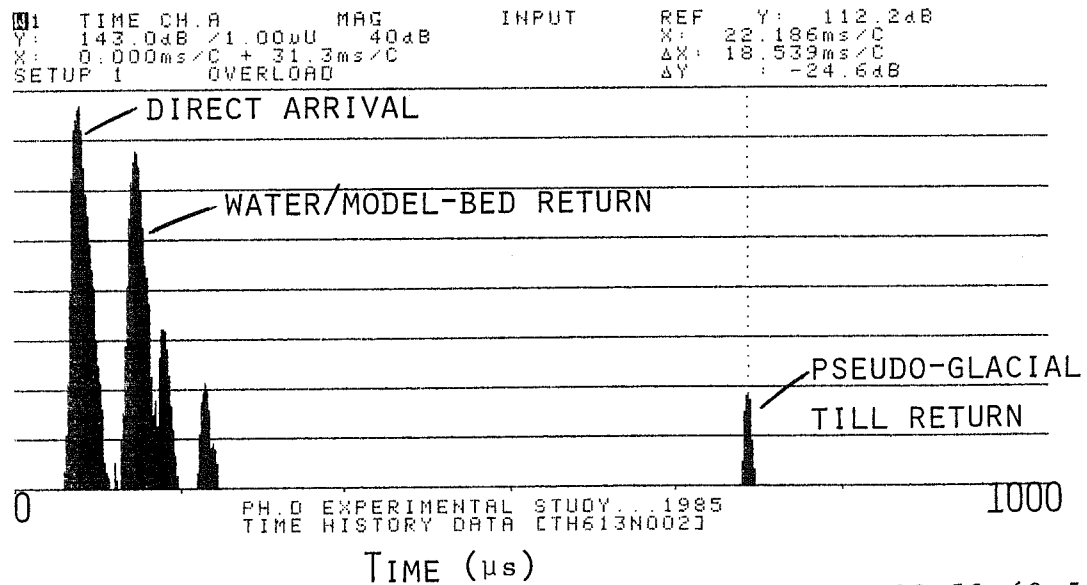
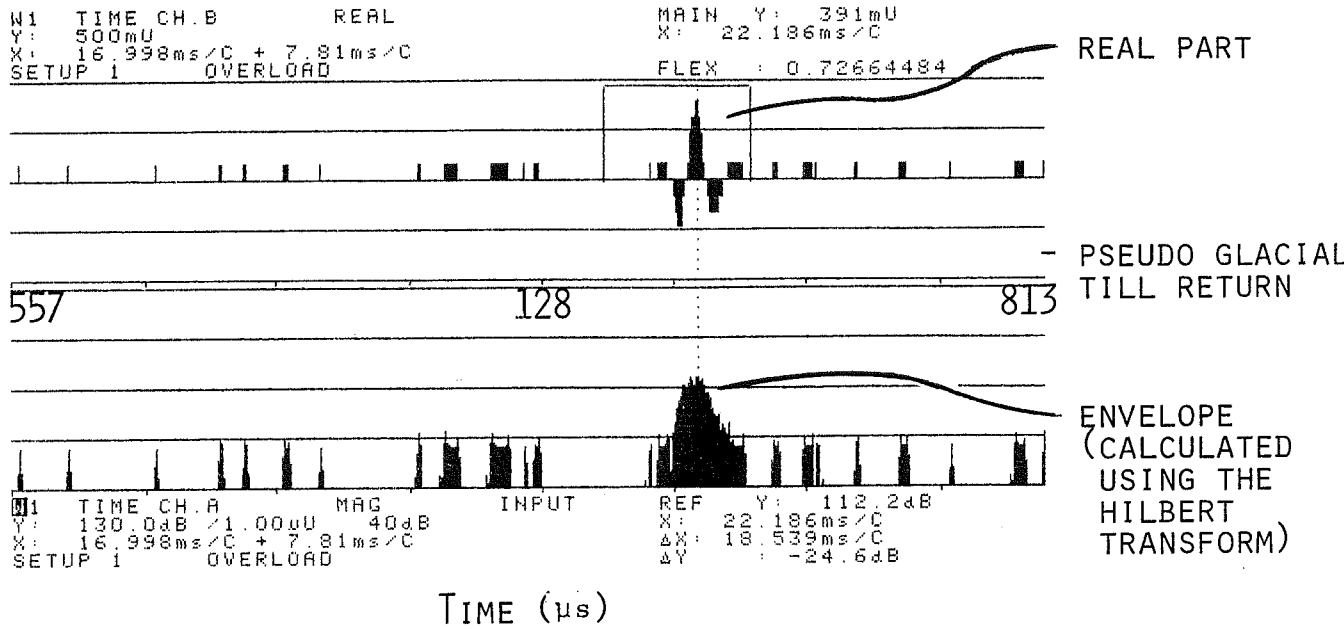
In the ocean environment, velocity cannot be measured using λ^* since λ^* is an experimentally set control. However, the methodology discussed in Chapter 4.0, Section 4.2 can be employed as long as the transmission angle θ is manipulated accurately. In this approach $T_{(1,p)}$ is predicted then compared to the actual returning time through the application of: (for a specific θ)

$$T_{(1,p)}(\text{predicted}) = \frac{(2\chi_p + \gamma)}{c_o \cos\theta} + \frac{2 H_{(1,p)}}{c_{(1,p)} \cos\beta_{(1,p)}} \quad (6.8)$$

where $\beta_{(1,p)} = \sin^{-1} \left[\frac{c_{(1,p)} \sin\theta}{c_o} \right]$. Snell's Law is used in expression (6.8) to account for a raypath bending caused by the differing densities of the water and of the sediment. χ_p and $H_{(1,p)}$ were obtained through expressions (6.1 and 6.7). γ was earlier stated as a constant having a value of 0.45 metres.

$T_o^*(\theta)$ is the direct arrival from the transmitter to the hydrophone at z. It is used as a convenient time mark in the digitizing of

PSEUDO-GLACIAL TILL RETURN
(REAL PART AND ENVELOPE)



C=30.52 (0.5μs external sampling rate)

$T_{(1,p)}(\theta)$. $T_o^*(\theta)$ is computed through expression (6.9) (refer to Figure 6.1 for a description of its travel path);

$$T_o^*(\theta) = \frac{[(\lambda_p - \chi_p^2) (z_p)^2]^{1/2}}{c_o} \quad (6.9)$$

The time measurements that are made for $T_{(1,p)}(\theta)$ represent a true path from the transmitter to the reflector base to the hydrophone. The predicted time path follows the same route. $c_{(1,p)}$ is derived by using the measured values of $T_{(1,p)}$ for a specific angle. The iterations are performed by employing expression (6.10),

$$c_{(1,p)} = \frac{2 H_{(1,p)}}{\cos\beta_{(1,p)} [T_{(1,p)} - (\frac{2\chi_p + \gamma}{c_o \cos\theta})]} \quad (6.10)$$

which involves

$$H_{(1,p)} = d_{(1,p)} / \tan\beta_{(1,p)} \quad (6.11)$$

where

$$d_{(1,p)} = [z_{(1,p)} - (\gamma \tan\theta + 2\chi_p \tan\theta)] / 2 \quad (6.12)$$

The element z manifests itself experimentally. That is to say the occupancy at a particular point on z corresponds to a received signal

of highest amplitude. To cross-check this, z measured is then compared against a calculated z using:

$$z_{(1,p)} = 2 d_{(1,p)} + (\gamma \tan\theta + 2\chi \tan\theta) \quad (6.13)$$

where

$$d_{(1,p)} = H_{(1,p)} \tan \theta \quad (6.14)$$

The predictions and the experimental measurements for $T_{(1,p)}$ and $c_{(1,p)}$ are synthesized into the following data table:

<u>Position</u>	<u>Predicted</u>	<u>Measured</u>		<u>Measured</u>	<u>Measured</u>	
				($\theta = 0$)	($\theta = 3$)	
\underline{P} $\underline{z}_{(1,p)}$	$\underline{T}_{(1,p)}$	$\underline{T}_{(1,p)}$	$\underline{\Delta T}_{(1,p)}$	$\underline{c}_{(1,p)}$	$\underline{c}_{(1,p)}$	$\underline{\Delta c}_{(1,p)}$
(cm)	(μs)	(μs)	(μs)	(m/s)	(m/s)	(m/s)
A 10.9	971	983*	12	1941	1903	38
A ₁ 10.9	960	979*	19	1954	1894	60
B 11.4	941	**	**	2020	**	**
B ₁ 11.4	940	**	**	2020	**	**
C 11.1	953	956	3	1980	1969	11
C ₁ 11.2	947	949	2	1993	1988	5
D 11.2	946	953	7	2003	1979	24
D ₁ 10.9	965	964	1	1947	1950	3

(continued)

<u>Position</u>		<u>Predicted</u>	<u>Measured</u>		<u>Measured</u>	<u>Measured</u>	
		($\theta = 3$)	($\theta = 3$)		($\theta = 0$)	($\theta = 3$)	
\underline{p}	\underline{z} (1,p) (cm)	\underline{T} (1,p) (μ s)	\underline{T} (1,p) (μ s)	$\frac{\Delta T}{\underline{T}}$ (1,p) (μ s)	\underline{c} (1,p) (m/s)	\underline{c} (1,p) (m/s)	$\frac{\Delta c}{\underline{c}}$ (1,p) (m/s)
I.	Average:	953	964 [11]	7	1982	1947 [35]	24
	$\pm\sigma$:	11	14 [3]	7	32	40 [8]	22
	$\pm\bar{\xi}$:	-	- i) 0.012 ii) 0.007 (1.2%) (0.7%)		-	-	-
a	10.9	962	964	2	1947	1941	6
a ₁	10.9	959	956	3	1947	1958	11
b	11.2	952	957	5	1987	1970	17
b ₁	11.1	948	948	0	1987	1987	0
c	11.2	949	949	0	1993	1993	0
c ₁	11.1	956	956	0	1974	1974	0
d	10.9	960	960	0	1954	1954	0
d ₁	10.9	964	964	0	1947	1947	0
II.	Average:	956	957 [1]	1	1967	1966 [1]	4
	$\pm\sigma$:	6	6 [0]	2	20	19 [1]	7
	$\pm\bar{\xi}$:	-	- i) 0.001 ii) 0.001 (0.1%) (0.1%)		-	-	-
I.	$\pm\bar{\sigma}$:	-	- [1.5]	-	-	- [4.5]	-
and II.	$\pm\bar{\xi}_{\max}$:	-	- 0.012 (1.2%)	-	-	-	-

* Poor Record Trace

** No Data

I. Outer Scanning Ring

II. Inner Scanning Ring

Given that:

[n] - The quantity n is the absolute value of the difference between the average predicted and the average measured T.

$$\pm \bar{\xi} \quad - \quad \text{Error} \quad \begin{array}{l} \text{i) } \left| \frac{\text{Average Predicted T} - \text{Average Measured T}}{\text{Average Predicted T}} \right| \\ \text{ii) } \left| \frac{\text{Average } \Delta T}{\text{Mean Between Average Predicted and Average Measured T}} \right| \end{array}$$

$\pm \bar{\xi}_{\max}$ - The maximum value of ξ between the Inner and Outer Rings.

$\pm \bar{\sigma}$ - The average value of $[\sigma]$ between the Inner and Outer Rings.

Step 6 Extracting an Absorption Coefficient for the Model

The next phase in the interrogation involves the characterization and distribution of the attenuation losses in the till model. This is accomplished through the Instantaneous Frequency property defined while using the Hilbert Transform (refer to Chapter 4.0, Section 4.4). The peak frequency position of the energy/frequency curve of the returned signal from the water/sediment interface, establishes an f_{\max} . The Power or Source Level at this particular frequency is recorded and then used as a reference. The energy/frequency curve of the echo belonging to the glacial till/basement interface is read at this reference frequency. The difference in the level of power between the reference reading and the till-base interface value derives the attenuation loss.

The attenuation loss can be rewritten into an Absorption Coefficient after considering the thickness of the layer at a specific position and after accounting for the reference frequency used in

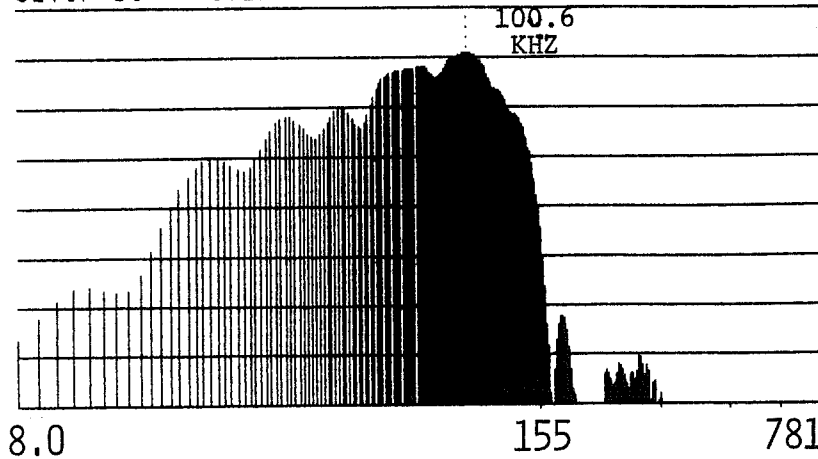
making the measurements. PLATE 4 illustrates the Instantaneous Frequency property. This is expressed on a logarithmic scale for both magnitude and frequency at scanning position A. A complete set of plates are included in Appendix C, Volume II for all positions of the scanning network (see PLATES 4, A to d_1). The attenuation losses can be read directly off these plates as a value of ΔY .

A synopsis of the attenuation analysis is collated onto the following table:

<u>Position</u>	<u>$f_{\max}(o,p)$</u> (kHz)	<u>Mean Square Spectrum</u> <u>(o,p)</u> (dB re $1\mu\text{Pa}^2$)	<u>Mean Square Spectrum</u> <u>$(1,p)$</u> (dB re $1\mu\text{Pa}^2$)	<u>Δ Mean Square Spectrum</u> (dB re $1\mu\text{Pa}^2$)
A	100.6	113.1	87.3	25.8
A_1	121.1	112.0	85.8	26.2
B	107.4	117.7	86.7	31.0
B_1	105.5	120.8	92.6	28.2
C	122.1	111.5	80.1	31.4
C_1	123.0	121.1	90.4	30.7
D	85.0	113.9	81.6	32.3
D_1	109.4	116.5	87.7	28.8
I. Average:	109.3	115.8	86.5	29.3
$\pm\sigma$:	13.0	3.8	4.1	2.4
a	99.6	117.1	83.6	33.5
a_1	108.4	114.7	89.2	25.5
b	108.4	118.1	89.7	28.4
b_1	111.3	114.7	86.3	28.4
c	103.5	120.6	87.1	33.5
c_1	121.1	117.7	85.0	32.7
d	119.1	113.1	81.2	31.9
d_1	95.7	116.9	82.4	34.5

PLATE 4A - OUTER SCANNING CIRCLE
 INSTANTANEOUS FREQUENCY
 (USING THE HILBERT TRANSFORM)

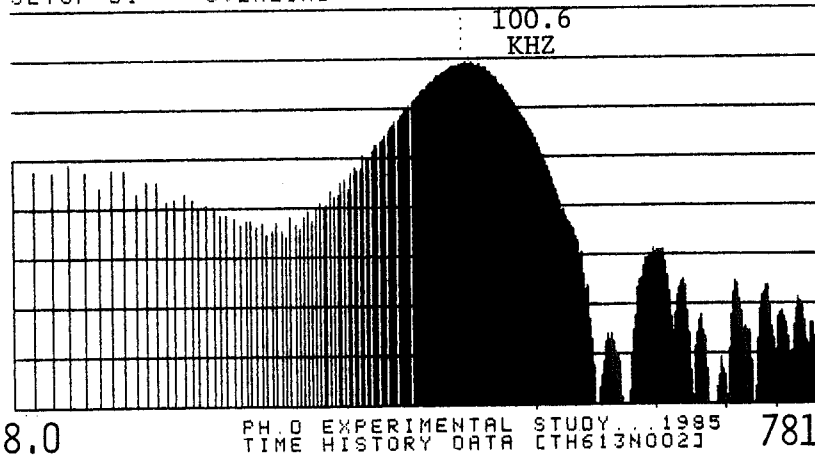
01 INST SPEC CH A MAG INPUT MAIN Y: 95.5dB
 Y: 100.0dB / 1.00E-12U² PWR 40dB X: 3296Hz*C
 X: 256Hz*C TO 25.6kHz*C LOG TOTAL : 113.1dB/YREF
 SETUP D1 OVERLOAD



WATER/MODEL-BED
 RETURN

FREQUENCY (IN KHZ)

01 INST SPEC CH B MAG INPUT MAIN Y: 69.4dB
 Y: 75.0dB / 1.00E-12U² PWR 40dB X: 3296Hz*C
 X: 256Hz*C TO 25.6kHz*C LOG TOTAL : 87.3dB/YREF
 SETUP D1 OVERLOAD



BOTTOM REFLECTION
 PSEUDO-GLACIAL TILL

PH.D EXPERIMENTAL STUDY... 1985
 TIME HISTORY DATA [TH613N002] 781
 FREQUENCY (IN KHZ)

C=30.52 (0.5μs EXTERNAL SAMPLING RATE)

(continued)	$f_{\max}(o,p)$ (kHz)	Mean Square Spectrum (o,p) (dB re $1\mu\text{Pa}^2$)	Mean Square Spectrum $(1,p)$ (dB re $1\mu\text{Pa}^2$)	Δ Mean Square Spectrum (dB re $1\mu\text{Pa}^2$)
II. Average:	108.4	116.6	85.6	31.1
$\pm\sigma$:	8.8	2.4	3.1	3.2

I. Outer Scanning Ring
 II. Inner Scanning Ring

From this table, an Absorption Coefficient can be calculated for each position:

<u>Outer Scanning Ring</u>			<u>Inner Scanning Ring</u>		
<u>Position</u>	α' (dB/m kHz)	$\pm\xi_{\alpha'}$	<u>Position</u>	α' (dB/m kHz)	$\pm\xi_{\alpha'}$
A	0.22	0.003	a	0.30	0.004
A ₁	0.18	0.003	a ₁	0.20	0.003
B	0.25	0.004	b	0.22	0.003
B ₁	0.22	0.003	b ₁	0.22	0.003
C	0.22	0.003	c	0.28	0.004
C ₁	0.21	0.003	c ₁	0.26	0.004
D	0.42	0.006	d	0.23	0.003
D ₁	0.23	0.003	d ₁	0.30	0.004
Average:	0.24		Average:	0.25	
$\pm\sigma$:	0.074		$\pm\sigma$:	0.039	

Note: $\pm\xi_{\alpha'}$ is calculated by assuming the maximum error (from ξ_{\max} in T) to be 1.4% of α' .

6.4.3 Quantifying and Illustrating the Coherency between the two Spatial Scanning Rings

Step 7 Statistically Evaluating the Homogeneity Character of the Water and of the Sediment Model

The "Acoustic Sub-seabed Interrogator" utilizes an Outer and an Inner Scanning Ring to create a statistical base to quantify the incoherency of the medium in a coherent manner. The spatial movement within the rings allows for a comparison and appraisal to occur between individual positions along each circumference as well as between circumferences. The result of such an audit is the property of homogeneity.

While a Standard Deviation (σ) is a first indicator of variance, it doesn't directly highlight the significance of the variation. Therefore a Coefficient of Variation is introduced. This is modified from Chatfield (1976);

$$T = \frac{100 \sigma}{\bar{n}} \quad (6.15)$$

where σ is the Standard Deviation and \bar{n} is the averaged property (ie: velocity or attenuation).

The maximum averaged measurement error ($\xi_{\bar{n}}$) was stated in Section 6.4.1 to be 1.4% for \bar{n} . This error is now incorporated into the deviation computations in the form of a compounded maximum measurement error (ξ_T);

$$\xi_T = \frac{100\sigma}{(\bar{n})^2} \xi_{\frac{-}{n}} = \frac{T\xi_{\frac{-}{n}}}{\bar{n}} \quad (6.16)$$

The Coefficient of Variation is accentuated non-linearly to emphasize the differences in the deviation values. A coherency scale (γ) can be set once the measurement error is accounted for in the value differences.

i) γ_a - Attenuation Classifier

$$\gamma_a = T_i^x \quad (\text{where } i \text{ refers to a specific layer}) \quad (6.17)$$

given that x is equal to $\log [\gamma_{a(\max)}] / \log [T_{(\max)}]$. $\gamma_{a(\max)}$ is a value that corresponds to the coherency scale. This can be experimentally assigned. For the pseudo glacial till, a value of 10 was allocated as a first estimate in developing the scale. The compounded maximum measurement error in γ_a is now introduced into the Coefficient of Variation:

$$\xi_{\gamma_a} = x \xi_T T^{x-1} \quad (6.18)$$

ii) γ_c - Velocity Classifier

$$\gamma_c = 45 T_i^x \quad (\text{where } i \text{ refers to a specific layer}) \quad (6.19)$$

providing x is equal to $\log[\frac{\gamma_{c(\max)}}{45}] / \log[T_{(\max)}]$. $\frac{\gamma_{c(\max)}}{45}$ is a velocity component of the classification scale. $\gamma_{c(\max)}$ divided by

45 (which is a first estimate of slope) allows $\gamma_{c(\max)}$ to be represented by a high value while $\gamma_{c(\min)}$ is maintained correctly as a low value. It should be remembered that once sufficient field data is available for a calibration of the classifiers then a reference standard can evolve.

The compounded maximum measurement error in γ_c is expressed by

$$\xi_{\gamma_c} = 45x\xi_T T^{x-1} \quad * \quad (6.20)$$

Figure 6.3 assembles and displays the data for the pseudo glacial till and for the water column. T , γ and ξ are included in the statistical digest given that;

- i) when γ_a is equal to 100, the value corresponds to 1 dB/m kHz
- ii) when γ_c is equal to 75, the value corresponds to T of 1.6
- iii) $\overset{\circ\circ}{\sigma}_{\text{INNER}}$ is the σ normalized with respect to the σ of the Inner Ring, multiplied by 100.
- iv) $\pm \xi_{\overset{\circ\circ}{\sigma}_{\text{INNER}}}$ is the compounded maximum measurement error in

$\overset{\circ\circ}{\sigma}_{\text{INNER}}$. For example;

$$\xi_{\overset{\circ\circ}{\sigma}_{\text{INNER}}} = 100 \frac{\xi_{\sigma_I}}{\sigma_{II}} + 100 \frac{\xi_{\sigma_{II}} \sigma_I}{\sigma_{II}^2} \quad **$$

where I is the Inner Circle and II is the Outer Circle.

*Expressions 6.18 and 6.20 are developed along standards set for handling maximum probable error. For example:

$$\gamma = \gamma^x; \quad \xi_{\gamma} = \frac{x \xi_{\gamma} \gamma}{\gamma} = x \xi_{\gamma} \gamma^{x-1}$$

**Likewise, the $\xi_{\overset{\circ\circ}{\sigma}_{\text{INNER}}}$ definition is based on the following model:

$$\overset{\circ\circ}{\sigma}_{\text{INNER}} = 100 \frac{\sigma_I}{\sigma_{II}}; \quad \xi_{\overset{\circ\circ}{\sigma}_{\text{INNER}}} = \left(\frac{\xi_{\sigma_I}}{\sigma_I} + \frac{\xi_{\sigma_{II}}}{\sigma_{II}} \right) \overset{\circ\circ}{\sigma}_{\text{INNER}} = \frac{100 \xi_{\sigma_I}}{\sigma_{II}} + \frac{100 \xi_{\sigma_{II}} \sigma_I}{\sigma_{II}^2}$$

Property	Outer Circle		Inner Circle		Difference Between Inner & Outer Circle		All 16 Positions	
	Water Column	Pseudo-Glacial Till	Water Column	Pseudo-Glacial Till	Water Column	Pseudo-Glacial Till	Water Column	Pseudo-Glacial Till
Average Velocity (in m/s)	1474	1982	1474	1967	0.0	15.0	1474	1975
$\pm\sigma$ (in m/s)	1.0	31.9	1.0	20.3	0.0	11.6	1.0	27.0
$\pm\xi_{\sigma}$ (in m/s)	0.0	0.4	0.0	0.2	0.0	0.2	0.0	0.3
$\sigma_{\text{INNER}}^{**}$	100.0	63.6	100.0	100.0	0.0	36.4	-	-
$\pm\xi_{\sigma_{\text{INNER}}}^{**}$	0.0	3.5	0.0	2.0	0.0	1.5	-	-
T	0.1	1.6	0.1	1.0	0.0	0.6	0.1	1.4
γ_c	2.5	75.0	2.5	46.6	0.0	28.4	2.5	63.0
$\pm\xi_{\gamma_c}$	0.0	1.1	0.0	0.7	0.0	0.4	0.0	0.9
Attenuation Coefficient								
Average Absorption Coefficient (in dB/m kHz)	0.01	0.24	0.01	0.25	0.00	0.1	0.01	0.25
$\pm\sigma$ (in dB/m kHz)	0:0001	0.074	0.0001	0.039	0.0000	0.035	0.0001	0.057
$\pm\xi_{\sigma}$ (in dB/m kHz)	0.000	0.000	0.000	0.000	0.000	0.000	0.000	0.000
$\sigma_{\text{INNER}}^{**}$	100.0	52.7	100.0	100.0	0.0	47.3	-	-
$\pm\xi_{\sigma_{\text{INNER}}}^{**}$	0.0	0.0	0.0	0.0	0.0	0.0	-	-
T	1.0	30.3	1.0	15.6	0.0	14.7	1.0	23.1
γ_a	1.0	10.0	1.0	6.4	0.0	3.6	1.0	8.3
$\pm\xi_{\gamma_a}$	0.00	0.09	0.00	0.06	0.00	0.03	0.00	0.08

FIGURE 6.3 Statistical Data Digest

An important aspect of the statistics is the emphasis on the differences between the Inner and Outer Circle. There were two assessments performed in exhibiting these differences:

- i) A primary evaluation which examined the coherency or homogeneity along the scanning circumferences;
- ii) and a secondary evaluation that addressed the homogeneity along a radial path between the Inner Circle (acting as an origin) and the Outer Circle.

These two approaches quantify and help to illustrate the significance of the deviations in a spatial dimension. For example, if both scanning circles have very high deviation levels along their circumferences but hold a low or negligible difference in their radial deviation then this would suggest the presence of a well mixed medium. If the difference in deviation between the circles is very high then the existence of a sedimentary matrix composed of distinct anomalies could be interpreted such as boulders and cobbles scattered in a more uniform base.

Normalized deviation values are shown in Figure 6.3. The deviation differences are normalized with respect to the Inner Circle and multiplied by 100. The Inner Circle represents a statistical origin from which the radial homogeneity was measured from. The normalized results for both the velocity and the Absorption Coefficients implies that the pseudo glacial till model has wide changes in its internal physical properties.

Step 8 Merging the Processed Data into an "Acoustic Core" Product

The data base which was collected through the interrogations can now be displayed as isolines. This presents the visual distribution of the values. The contours outline the variations statistically calculated. The internal structure of the pseudo glacial till model is revealed through the patterning of the contours.

Software called "Surface II"* by Sampson (1978) was modified to accept the experimental data. An algorithm was written into the software to configure the isoline information within a circumference which corresponded to the boundaries of the outer scanning circle. The grid matrix values were generated by the irregularly spaced X, Y, Z sample data points and by calculating grid values beyond the range of the same data. From Sampson (1978):

"At each sample data point, a first-order trend surface is fit to the nearby sample data points found by the specified search routine. The trend surface is constrained so it passes through the control point being evaluated, and so is a least squares estimate of the dip of the surface at that point. Coefficients of this trend surface are then evaluated for the X, Y location of the grid node being estimated, in effect projecting the dip of the surface from the sample data point to that grid intersection. A distance-weighted average is then made of the projected dips from the sample data points found in the specified search around the grid point."

*"Surface II" or "Surface II Graphics System" is a graphic software package which is supplied by Computer Services Section, Kansas Geological Survey, Lawrence, Kansas. Modifications to the program were made by Mr. Eugene Guy of C-Core, Memorial University of Newfoundland.

The data sent to "Surface II" was weighted during the estimations to control their influence away from the points being estimated. For example, a weighting function which declines slowly with distance will produce heavily averaged estimates. The result is a surface with slowly changing gradients. Conversely, a rapidly declining weighting function places great emphasis on the values of nearest points in the estimation procedure. This will yield a rapidly changing surface (Sampson (1978)).

A constrained distance-squared weighting function was selected to best reproduce the surfaces defined by the experimental simulations over the pseudo till structure. The function used is

$$\omega^1 = \left(1 - \frac{D}{1.1 \times D_{\max}}\right)^2 \div \left(\frac{D}{1.1 \times D_{\max}}\right)^2 \quad (6.21)$$

where ω^1 is the weight attached to a sample data point at a distance D from the grid intersection being estimated. D_{\max} is the distance from the grid intersection to the most distant sample point in the set being used in the estimation.

The isolines generated using the weighting function (expression (6.18)) closely simulate the physical model's surface. This was verified experimentally through a series of test scans. Since the actual scanning circles are small and the data is close in value then the isolines formed by "Surface II" conform closely to spot values and checks. The following four figures spatially present the distribution of the results:

- i) Figure 6.4 - Bathymetry (in cm)
- ii) Figure 6.5 - Thickness (in cm)
- iii) Figure 6.6 - Velocity of Sound (in m/s)
- iv) Figure 6.7 - Absorption Coefficient (in dB/m kHz)

Complimenting the last three figures is a set of three 3-dimensional projections of the data (see Figures 6.8 to 6.10). They are meant to be viewed only as qualitative illustrations though they correctly reproduce the data contours. Any measurements to be lifted should be made in connection with Figure 6.11.

The 3-dimensional projections were determined by establishing a percent of range in the X- or Y-direction (whichever was greater) into which the range Z was scaled. The percent selected was 35%. The function which transformed the isolines into a 3-dimensional plot is called "TRAN'SECT". This is an integral part of the "Surface II" program.

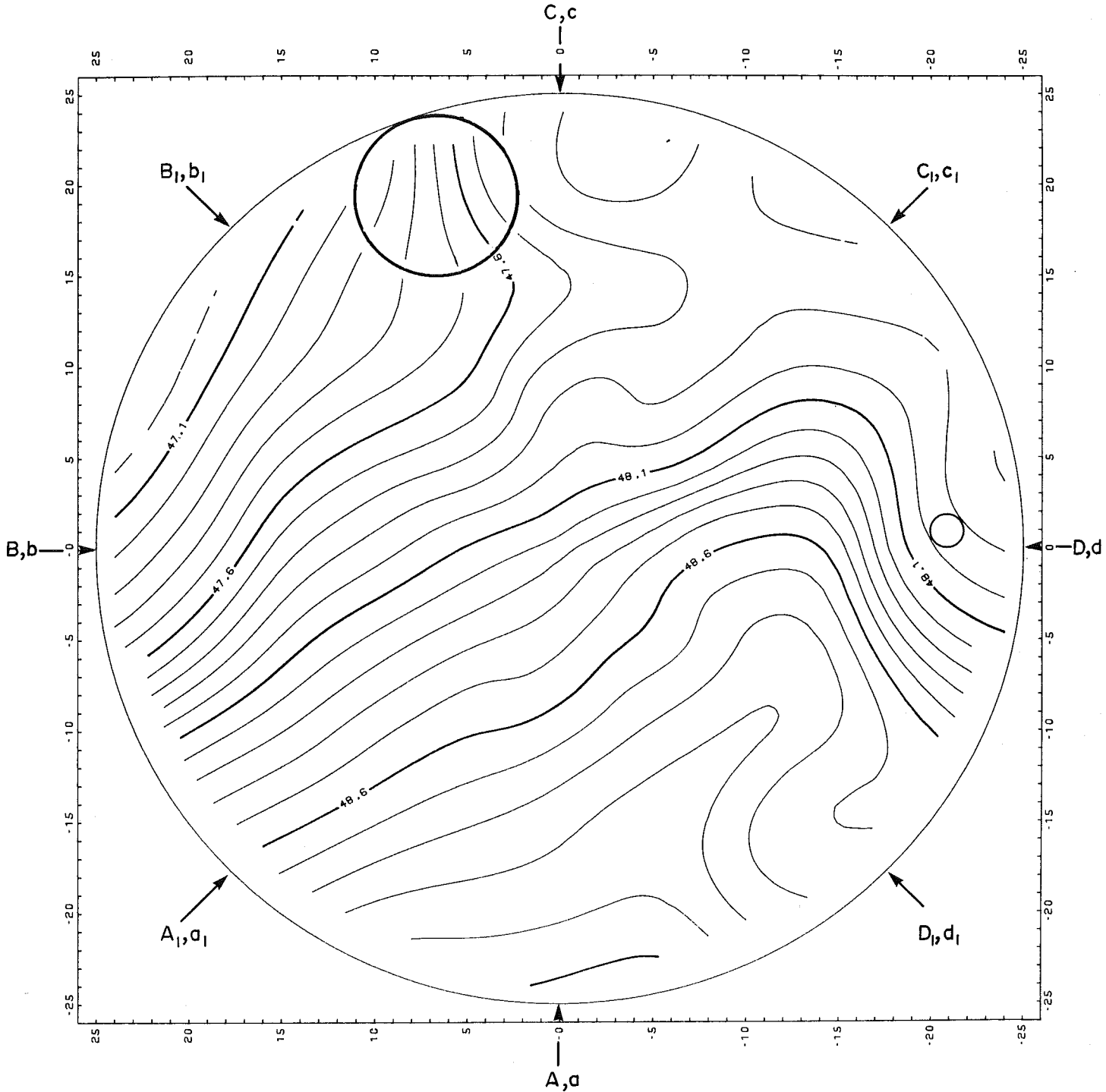
6.5 Final Interpretation

6.5.1 Appraising the Bathymetric and Thickness Contours

The bathymetry and thickness isolines concord in form and value (refer to Figure 6.4 and 6.5). The physical floor of the model gently slopes from a topographic high of 47.1 cm in the vicinity of $B_1 \rightarrow C$ to a low of 49.0 cm around A. The averaged slope is $\approx 7\%$. The thickness values agree with those of the bathymetry; the thickest region being in $B_1 \rightarrow C$ and the thinnest sector existing around A. The isopachyte

NOTE: i) X,x refers to the axis of two specific scanning positions
 (see Figures 6.1 and 6.3 for exact locations)

ii) grid divisions are in centimetres



all the sediment was poured onto this spot during the construction of the layer.
 raking of the sediment occurred from this position.

FIGURE 6.4 Bathymetry Isolines (in cm)

NOTE: i) X,x refers to the axis of two specific scanning positions
 (see Figures 6.1 and 6.3 for exact locations)

ii) grid divisions are in centimetres

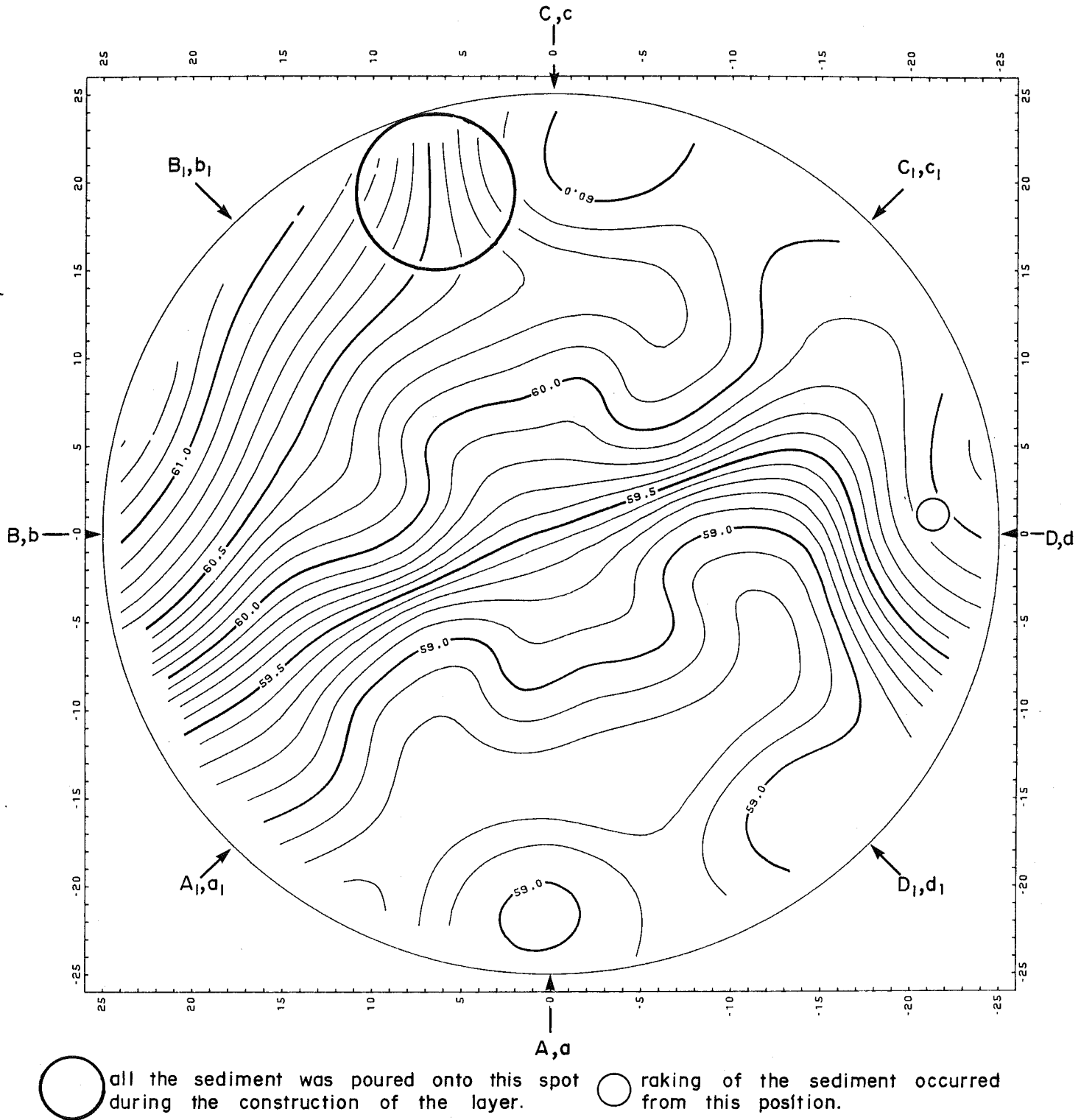


FIGURE 6.5 Thickness Isolines (in cm)

NOTE: i) X,x refers to the axis of two specific scanning positions.
 (see Figures 6.1 and 6.3 for exact locations)
 ii) grid divisions are in centimetres

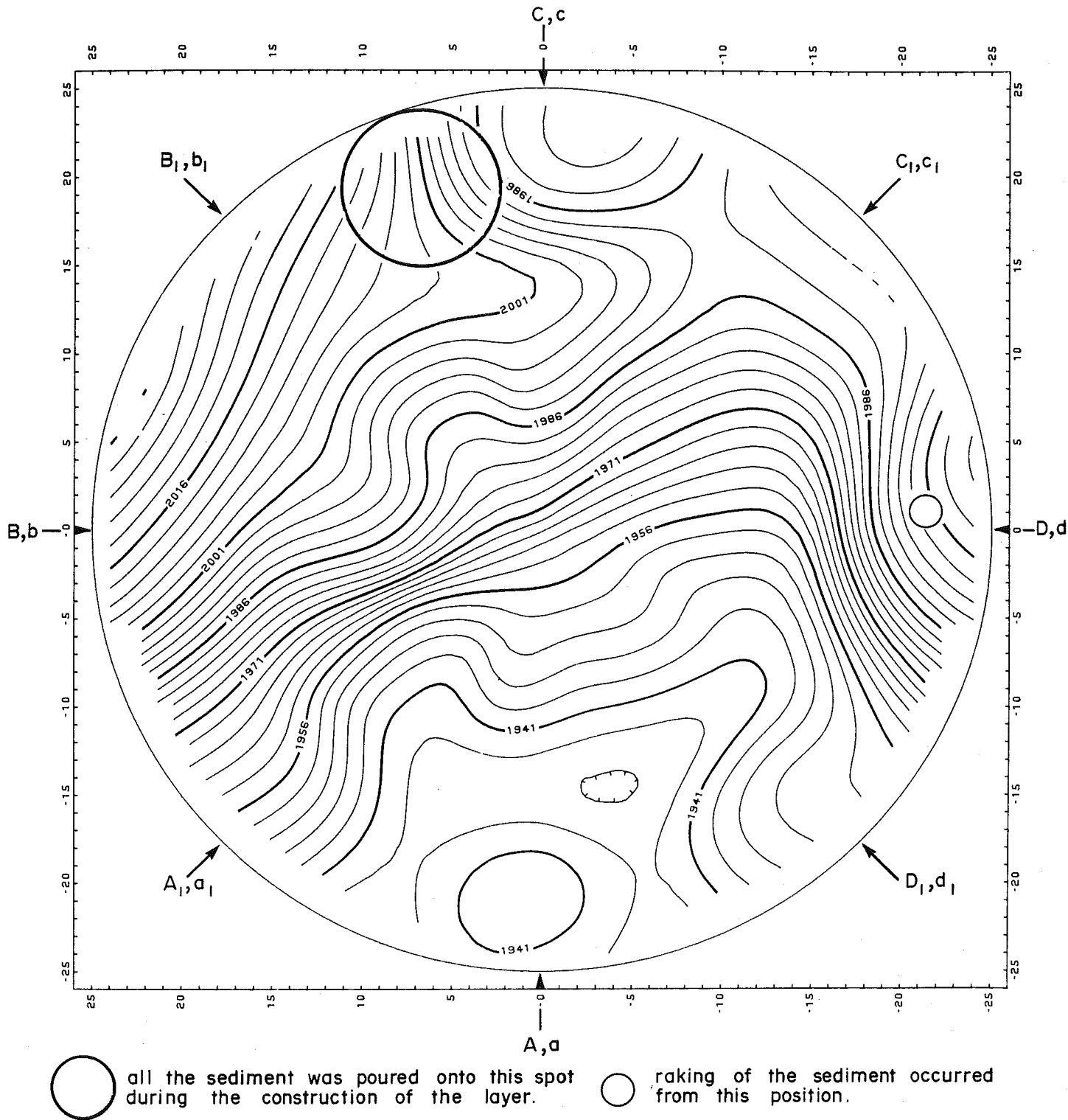


FIGURE 6.6 Velocity of Sound Isolines (in m/s)

NOTE: i) X,x refers to the axis of two specific scanning positions.
 (see Figures 6.1 and 6.3 for exact locations)
 ii) grid divisions are in centimetres

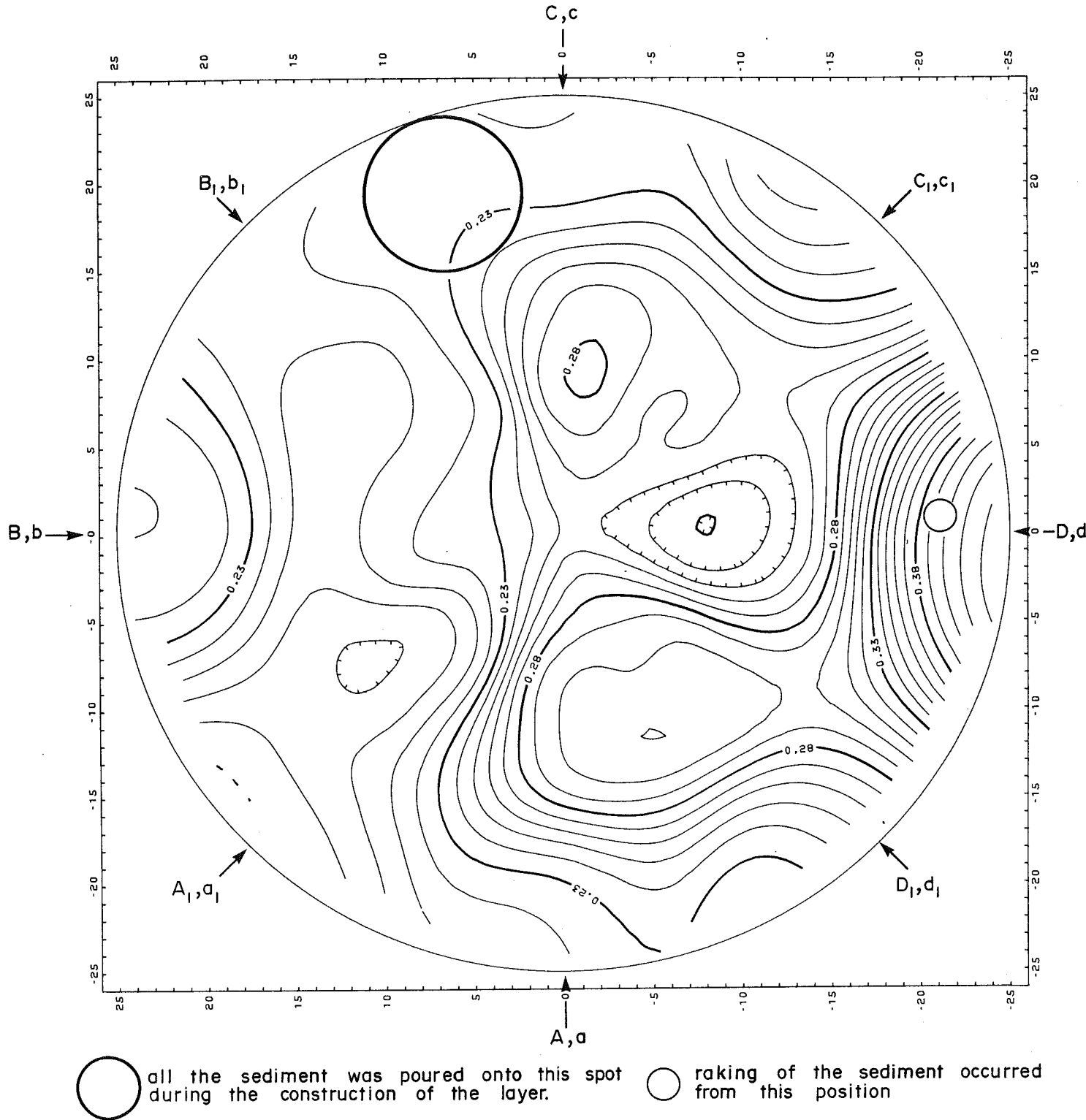


FIGURE 6.7 Attenuation Coefficient Isolines (in dB/mkHHz)

NOTE: i.) Vertical Ranges were normalized at 35% of the X-values.
 ii.) X,x refers to the axis of two specific scanning positions
 (see Figure 6.1 and 6.3 for exact locations)

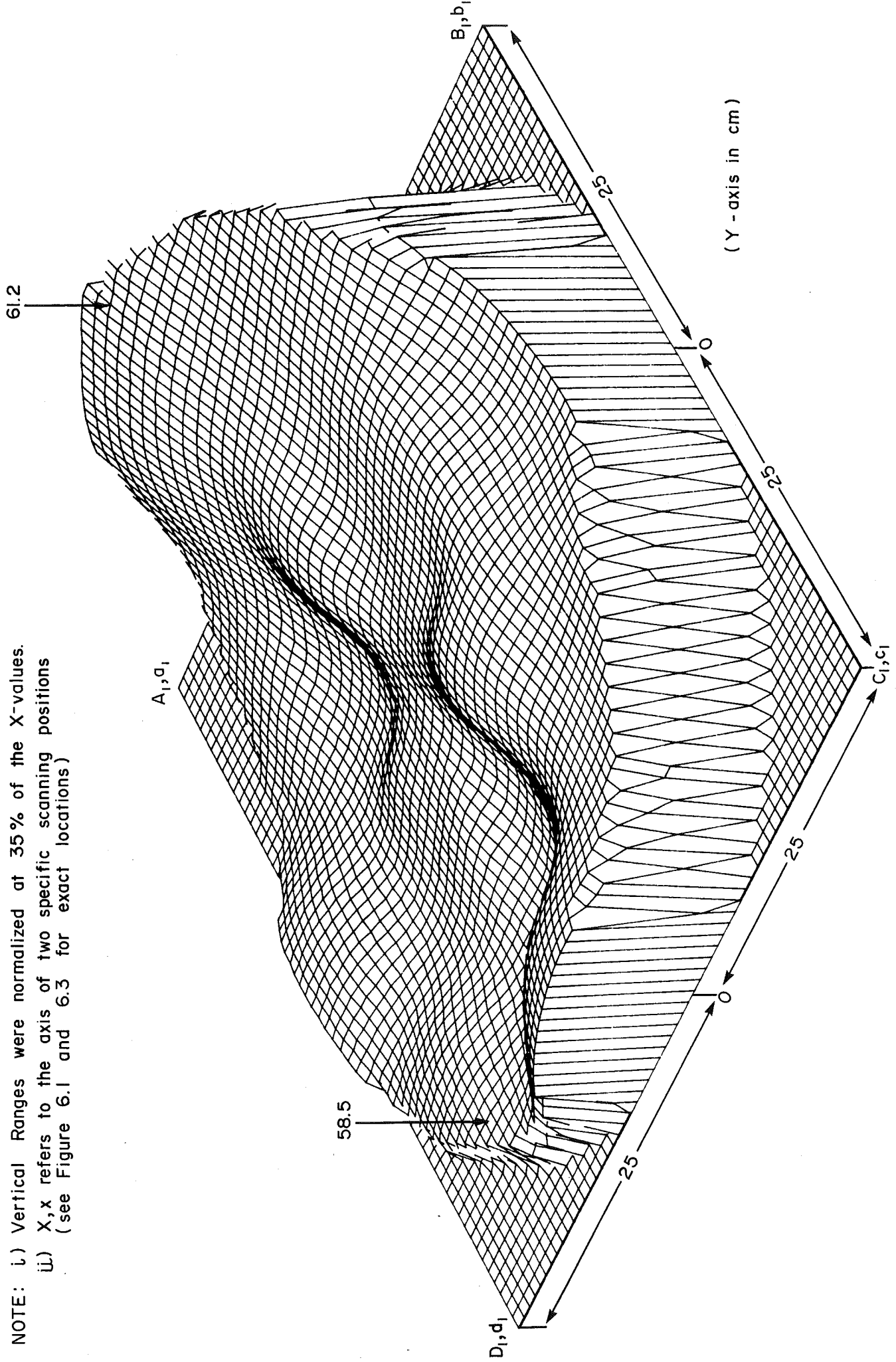


FIGURE 6.8 Qualitative 3-Dimensional Distribution of Thickness (in cm)

NOTE: i.) Vertical Ranges were normalized at 35% of the X-values.

ii.) X,x refers to the axis of two specific scanning positions.
(see Figures 6.1 and 6.3 for exact locations)

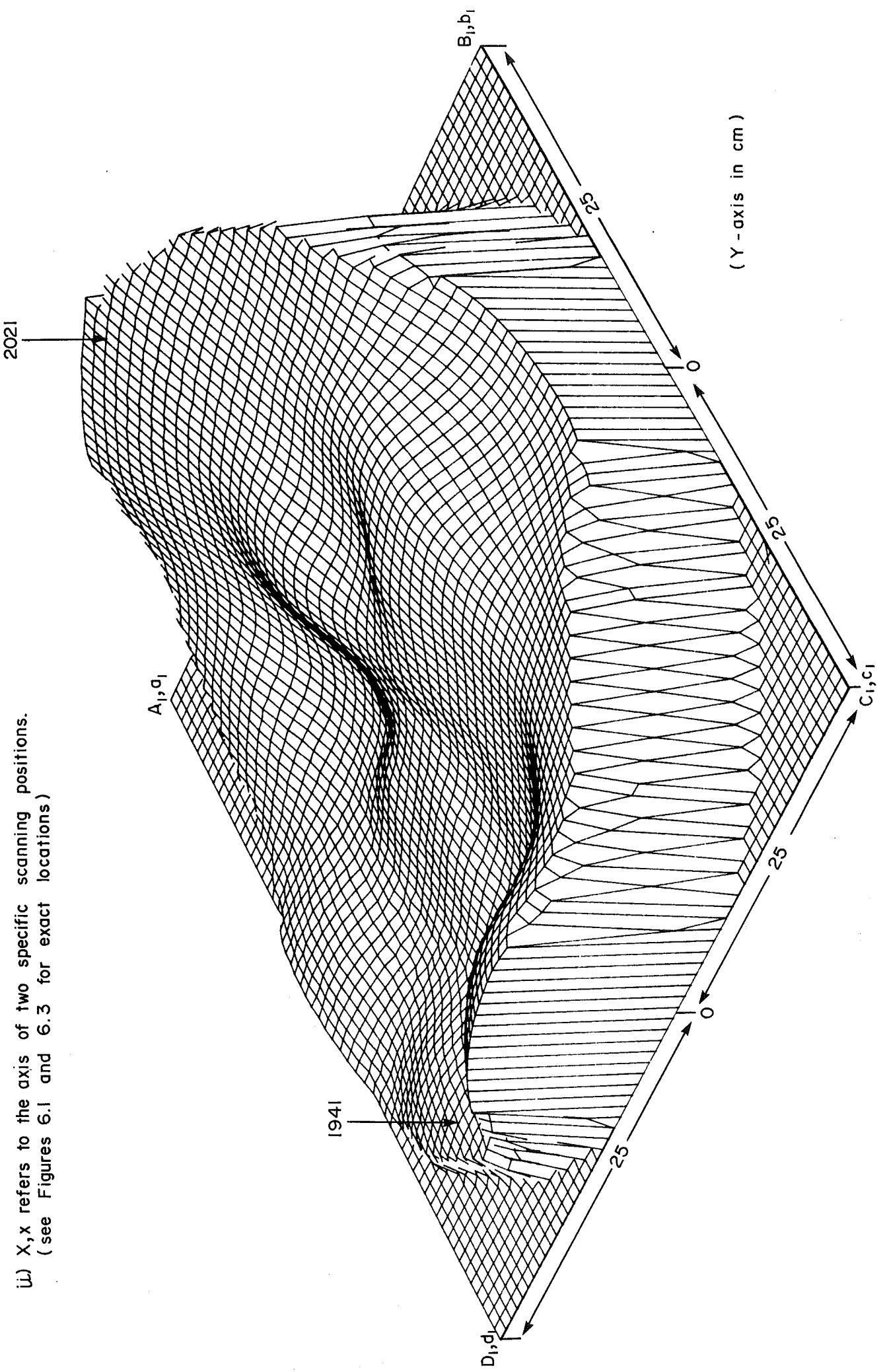


FIGURE 6.9 Qualitative 3-Dimensional Distribution of Velocity (in m/s)

NOTE: i) Vertical Ranges were normalized at 35 %
of the X-values

ii) X,x refers to the axis of the two specific scanning positions.
(see Figures 6.1 and 6.3 for exact locations)

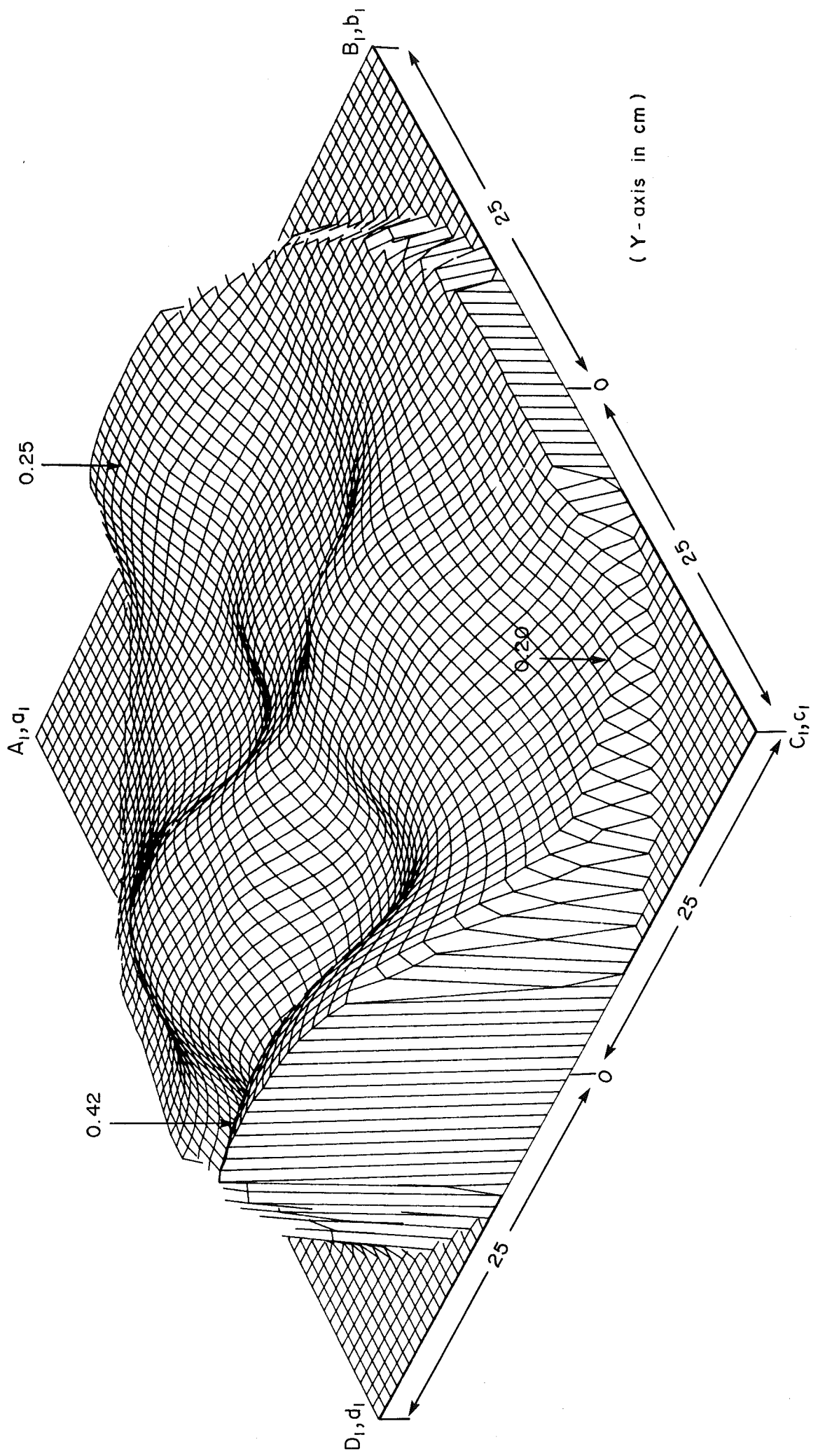


FIGURE 6.10 Qualitative 3-Dimensional Distribution of Attenuation Coefficients (in dB/mk/Hz)

DATA POSITIONS AND VALUES

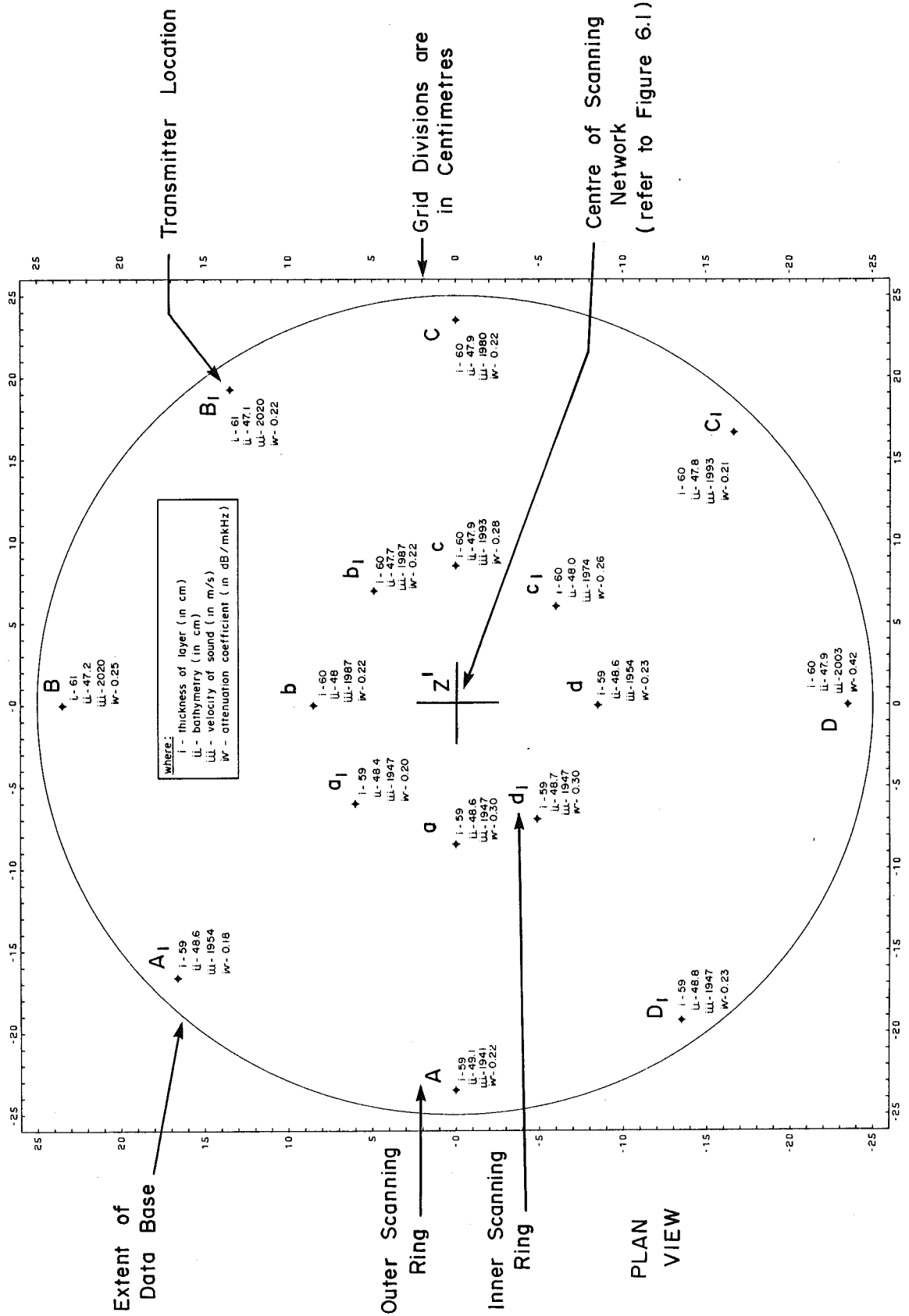


FIGURE 6.11 Reference Chart

ranges from approximately 61.0 to 58.0 cm. There are a few minor anomalies; the most prominent is situated near D.

The topographic distribution reflects the construction technique employed in the building of the layer. The site of the pourings was confined to the region of $B_1 \rightarrow C$ because of the fixed 5-TON overhead gantry crane used as a platform to the sediment/air evacuation process. All of the model's sediments were dumped directly onto a spot in the sediment container. This area is noted on the figures.

A raking method was employed to spread the material over to D_1 , A, A_1 and B. The anomaly at D coincides exactly with the zone where the raking was manipulated from. Standing directly onto the sediments of the model was tightly restricted to D during the construction and mixing.

6.5.2 Appraising the Velocity and Attenuation Contours

The most striking feature observed on Figure 6.6 is the flow pattern exhibited around $B_1 \rightarrow C$. The shape of the velocity isolines conform to density/porosity values that are expected or predicted for the model given the manner the material was laid in the tank. It is significant that the flow patterns mapped show such clarity in direction. This is indicative of the high order of measurement sensitivity inherent in the ASI interrogation.

The gentler nature of D_1 , A, A_1 and B stands in sharp contrast to the high velocity values profiled in D and in $B_1 \rightarrow C$. The lower more

consistent velocities around the A region would suggest a decrease in density for the sediments of this sector. The high velocities at D also tie in well with the higher levels of density expected to have occurred because of the physical stomping of the sediment that took place during the construction of the model.

Similarly, the distribution of the Absorption Coefficients is revealing. While absorption is sensitive to density and porosity changes, mean grain size also has a prominent effect. The absorption contours delineate a gentle slope in the overall distribution of values in accordance to certain trends:

Case I - Coarse Material (eg. Sands)

i) increase in density	}	decrease in attenuation
ii) decrease in porosity		
iii) increase in velocity		

Case II - Finer Sediment (eg. Clays)

i) decrease in density	}	decrease in attenuation
ii) increase in porosity		
iii) decrease in velocity		

These trends complement velocity versus density/porosity and mean grain size curves taken or derived off North Atlantic Cores (Taylor Smith (1974)). They also are in accordance with Hamilton's (1972) Attenuation Coefficient versus Porosity data.

However, there is one distinct anomaly observed on the Absorption Coefficient plot. (see Figure 6.7). The D-zone reveals an area of high absorption and at the same time of high velocity/density. This anomaly is a direct result of the raking technique used. The raking of the

sediment mixed the material and then pushed it into the outer regions of A and A₁. In the process of moving the sediment, a differentiation of the very large particulates representing the boulder fraction, accumulated around D. It can therefore be inferred that the high Absorption Coefficients noted in this spot reflect the presence of a cluster of large particulates.

6.5.3 Summary

The suppositions introduced at the onset of the experiments have been answered. The incorporation of an optimized truncated Parametric Array for the ASI transmission is feasible and does provide versatility in bandwidth, in pulse length, and in the formation of a narrower beamwidth. The Hilbert Transform rendered a significant contribution to the handling of time history data. Envelopes of all time functions were easily formed, along with the procurement of Instantaneous Frequency.

The inhomogeneous character of the model was exposed through the extraction of sub-layer information in the shape of velocity and attenuation. The display of the results exhibits the potential of the "Acoustic Core" as a "hands on" product. A real time "Acoustic Core" could dynamically control the operation of the ASI by directing attention on anomalies. Transmission positions could be manipulated or established as a function of these preliminary iterations of the core. The interrogations can thus be directed in a very effective manner for in-situ work.

7.0 TRANSFORMING ACOUSTIC RESPONSES INTO DISCRETE PHYSICAL AND ELASTIC PROPERTIES

The morphology of glacial deposits and the processes of forming these deposits in a marine environment can only be defined if geophysical/geotechnical techniques are able to probe and map the internal variability of these features. At present, reflection seismic techniques are limited because they emphasize the coherency of seismic traces and for the most part discard the incoherent component. Unfortunately, the inhomogeneous character of a structure is essentially revealed within this incoherency aspect. The experimental simulations of the ASI concept demonstrated the potential and the principle of quantifying the homogeneous nature of a sedimentary layer. The final results testify to the precision with which changes in the physical properties of the layer were mapped and the degree to which these changes could be related to the formation processes of the layer.

Understanding morainal features on land comes primarily from direct measurements employing a variety of geotechnical probes which result in detailed cross sections. The processes involved in their deposition are recreated by precisely noting the distribution and orientation of the sediments along with the variations in their physical properties such as density and packing. However attempts at physically coring a morainal bed at sea have been met by poor sediment recovery, disturbed cores and high costs. This is due to the over consolidation of the material and to the near impenetrable matrix

of large particulate fractions such as cobbles and boulders. These limitations in ground truthing, reinforce the value of using remote sensing tools for probing spatial variations in the unconsolidated sediments of the sub-seabed.

In Chapter 1.0 it was stated that a pressing geophysical requirement in the development of offshore oil is for the clear structural definition of potential drilling hazards. The efficiency and safety in drilling an exploratory well is seriously affected if prior knowledge of lithological anomalies are not known or defined. Likewise, the safety of a gravity base production platform becomes questionable if engineering site surveys result in inadequate or insufficient geotechnical detail on the seafloor material beneath the foundations. Realistic models are presently in place to predict the effects of wave loading or action on offshore structures. However, the soil - structure interaction in a heavy sea is poorly understood and yet is of importance as a design criteria. There is a need for a technology to obtain in-situ measurements that relate directly to the dynamic modelling of the sedimentary processes.

Recent work by Dawe (1984) and studies initiated by Clark (1985) involve the liquefaction of the seabed by wave induced pore pressure changes. Using physical modelling, Dawe (1984) demonstrated that a hydrodynamic lag exists; the maximum pore pressure generated in some soils may not necessarily coincide with the wave peak. Clark further argues that in the case of a bottom founded structure it is possible to have a situation whereby for certain soil types the maximum wave

induced pore pressure may become in phase with the trough of the wave as it passes the installation. The maximum foundation load and load induced pore pressure may be in phase with a maximum wave induced pore pressure, resulting in a bearing capacity failure.

Soil types and conditions must be well understood in advance of a bottom platform placement if catastrophic failures are to be prevented. At present the determination of the dynamic properties of seabed soils remains a difficult task and often the properties measured are unreliable. The "Acoustic Sub-seabed Interrogator" may provide a means of defining geotechnical data using its calibrated acoustic response.

In its simplistic form, the transformation from an acoustic response into discrete dynamic or elastic properties is manipulated using the elastic equations involving compressional wave velocity (c_p), bulk modulus (K) and material density (ρ). The most important parameter, shear modulus (μ) can be found through velocity if K is known

$$c_p = \frac{(K + \frac{4\mu}{3})^{1/2}}{\rho} \quad (7.1)$$

Poisson ratio (σ) can also be defined employing velocity. For instance,

$$\sigma = \frac{3K - \rho c_p^2}{3K + \rho c_p^2} \quad (7.2)$$

Unfortunately, the derivation of shear modulus using estimations for bulk modulus is not very accurate since the bulk modulus is very much larger than the shear modulus. A more accurate assessment of shear modulus is directly obtainable through equation (7.3):

$$c_s = \left(\frac{\mu}{\rho}\right)^{1/2} \quad (7.3)$$

where c_s is the shear-wave velocity. However the measurement of shear-wave velocity is impractical to execute in an ocean - seabed condition using currently available techniques. (Lee and Baecher (1983)).

The correlation of attenuation data with rigidity may provide an indirect mensuration of shear-wave velocity. Thomas and Pace (1980) experimented with the attenuation of sound propagating through water saturated sands as a continuous function of frequency over a range of two octaves centred on 160 kHz. The results of this study in conjunction with other sound velocity, grain size and porosity measurements indicated that increases in the particle-particle contact area resulted in decreases in both the sound attenuation (solid friction losses) and the dynamic rigidity.

The implication of the solid friction losses, centers on the existence of a matrix formed by the sediment particles in contact. From the matrix a frame bulk modulus K_F can be introduced as a component of the total bulk modulus of the saturated sediment. The frame bulk modulus indicates the degree to which the sediment can

support shear stress. The total bulk modulus K is expressed by Hamilton (1971) through

$$K = K_s(K_F + Q)/(K_s + Q) \quad (7.4)$$

$$= \rho c_p^2 - \frac{4}{3} c_s^2 \quad (7.5)$$

where

$$Q = K_F(K_s - K_F)/(N(K_s - K_w)) \quad (7.6)$$

K_s is the bulk modulus of the individual sediment particles and K_w corresponds to the bulk modulus of the water. The parameter N is a porosity percentage.

Hamilton (1971) also produced regression equations for K_F of the form

$$\log K_F = B - AN \quad (7.7)$$

using simultaneous measurement of ρ , c_p , c_s and N . Hamilton (1971) stated that for pure quartz sands K_F is equal to K_s when N is 0.

Concordantly, 10^B is given the value of $377.3 \times 10^9 N_m^{-2}$ and the mean value of A is set at 4.28.

In Figure 7.1b, Thomas and Pace (1980) illustrates the bulk modulus K , defined by expression (7.5) as a function of porosity. K_F

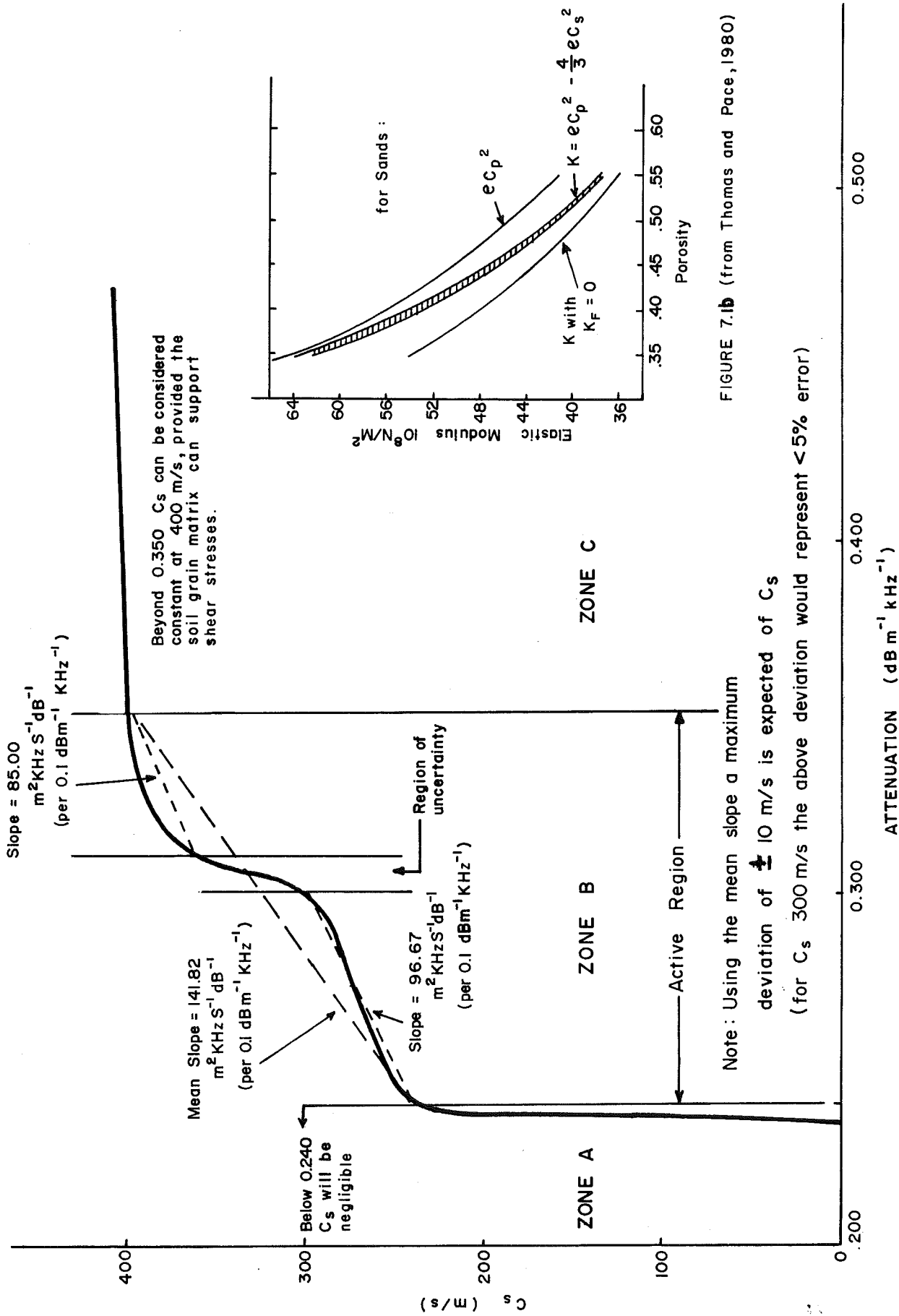


FIGURE 7.1b (from Thomas and Pace, 1980)

(attenuation loss data from Thomas and Pace, 1980)

FIGURE 7.1 Attenuation Loss versus Shear Wave Velocity Hypothesis

is equal to 0 in one case and K_F is calculated by expression (7.7) in a second case. The limiting condition of a suspension without any particle-particle contacts is represented when K_F is equal to 0. The errors in the estimate of K using expression (7.7) is noted to be $\pm 2\%$ (Thomas and Pace (1980)). This reflects a small uncertainty in the constant A .

Experimentally determined values of compressional velocity and density (ρc_p^2) were also plotted against porosity (refer to the upper most curve in Figure 7.1b). The results show that when the porosity dropped below 35%, the dynamic rigidity ($\frac{4}{3} \rho c_s^2$) of the sedimentary matrix becomes insignificant in the total bulk modulus (K) (see equation 7.5).*

As the porosity values increased, the reverse situation developed with rigidity becoming a more important factor. This change is at the expense of the contribution to the total bulk modulus by the intergranular contact. Therefore when the porosity is less than 35%, the shear-wave velocity is seen as a negligible factor in the total bulk modulus. Under such conditions the direct usage of the compressional velocity for bulk modulus calculations can be reliably employed. When porosity is around 40%, the rigidity of the matrix becomes an important if not a crucial component to consider.

*This statement should be taken in the context that we are dealing with and are only concerned about an adiabatic moduli and not the static moduli case.

The use of attenuation to define a shear-wave velocity may therefore be possible given that changes in particle-particle contact have been noted to produce similar effects on attenuation. Figure 7.1 attempts to develop this relationship by reexpressing data for sands, found in the Thomas and Pace (1980) study (see Figure 7.1b). The resulting curve denotes three key zones:

- i) below an attenuation of 0.24 dB/m kHz, the shear-wave velocity is seen to be negligible (ie. approaching 0 m/s).
- ii) between an attenuation of 0.23 and 0.35 dB/mkHz, the curve undulates with three discrete inflections.
- iii) beyond an attenuation of 0.35 dB/m kHz, the shear-wave velocity appears to have peaked and the curve flattens at ≈ 400 m/s. The shear-wave velocity remains constant until the value of the frame bulk modulus becomes so small that the sediment can no longer support shear stresses. When the sediment property approaches 60%, the shear-wave velocity would drop rapidly to 0 m/s.

The curve of the middle zone can be reexpressed by a mean slope. A maximum deviation of ± 10 m/s is determined using the calculated mean slope as a datum line. This deviation translates into an error of less than 5% for a shear-wave velocity of approximately 300 m/s. Whilst this curve is plotted for sands, it is believed to be representative of a family of curves for other soil types and therefore suggests a plausible correlation approach to measure shear-wave velocity in-situ.

8.0 FINAL DISCUSSION AND CONCLUSION

This research project is centered around the design and experimental development of a unique subbottom stationary probe concept called an "Acoustic Sub-seabed Interrogator". The objectives behind the concept deal with the creation of a remote sensing tool that is capable of interrogating complex lithologies of a seabed. The results obtained in the experimental simulations support the philosophy of the ASI and of its complementary "Acoustic Core" product. The principal ideas and conclusions of the study are condensed under the following sections:

- i) Acoustic Criteria for the Concept
- ii) ASI Model Development
- iii) Extracting Sub-seabed Information
- iv) Results of the Experimental Simulations over a Pseudo-Glacial Till
- v) Attenuation Loss Approach to Measure and Monitor Changes in Shear-Wave Velocity.
- vi) Future Directions

8.1 Acoustic Criteria for the Concept

The investigation started with a review of the acoustic theory associated with seabed profiling. This phase highlighted the differences and importance of the lateral and temporal factors involved in the resolution criterion. The study concluded that:

8.1.1 Lateral Resolution

i) Although the use of combined instruments with overlapping spectrum performances, such as recommended in the Gerth 1976 study, does significantly improve the interpretive quality of the combined records, it will not provide a comprehensive nor detailed sub-seabed picture in a hard morainic bottom.

ii) The continuity of interface reflectors are often non-existent in areas characterized by high levels of volume and/or surface scatter. This means that conventional seismic profilers which map the coherent portion of the returning signals become severely restricted or limited when the traces become discontinuous.

iii) To obtain maximum information on sediment properties the transducer should be placed as low as possible to the seafloor. The Fresnel area establishes a horizontal resolution cell which in turn dictates the objects that can be detected or discriminated.

iv) The spatial coherency and/or continuity of a profile is governed by the proximity of the horizontal resolution cells recorded. A very low tow speed over the seabed is necessary if a target echo is to be extracted or accentuated from a scattering background.

v) Synthetic aperture sonar techniques could potentially enhance the horizontal discrimination of reflecting interfaces. This is at a cost of large amounts of processing and of preprocessing. The trajectory control must also be of a quality compatible with the resolution to be achieved.

8.1.2 Temporal Resolution

i) The length of the acoustic pulse determines the vertical discrimination ability of the sound source. If the pulse length is too long in relation to a sequence of true horizons, a masking effect will occur.

ii) The length of the outgoing signal is a function of the pulse bandwidth. The pulse bandwidth determines the sharpness of the amplitude change with frequency near resonance or Q of the system. As the bandwidth is increased the pulse length will shorten and the Q of the system will lower.

iii) A decrease in Signal-to-Noise power ratio will also occur proportionally to the shortening of the pulse length; efficiency being a function of Q .

iv) A wide bandwidth at low frequencies with a narrow beam pattern can be attained by employing non-linear acoustics. The application of a Parametric Source does appear to have favourable subbottom profiling attributes. A high order of resolution and potential for penetration depth seems feasible using the wide bandwidth inherent in the source at a low difference frequency.

v) The limitation of the technique is in its very low power efficiency and in its requirement for stability.

The final concept of the "Acoustic Sub-seabed Interrogator" revolves around these two resolution parameters. The ASI concept amalgamates fully the benefits of a Parametric Source while operating in a stationary mode. A high temporal resolution capability is attained with a high degree of lateral resolution. The parametric design provides an ease in manipulating a wide band of frequencies, while the stationary base allows for geometrical manipulations of the transmitters and receiving arrays. Effective signal recovery and enhancement is thus achievable.

8.2 ASI Model Development

The acoustic propagation of a signal travelling within a structurally complex sediment model was theoretically appraised in

terms of Signal-to-Noise Ratio and Signal-to-Reverberation Ratio. This set the acoustic design foundation to test analytically the behaviour of a proposed truncated Parametric Array against an optimized Conventional Source. The results of the evaluations are summarized by the following points:

8.2.1 The Project Model

i) Understanding the geomorphological processes which have taken place along the Eastern Canadian Shelf has been limited and confined by the scarcity of data collected and above all else by the difficulties encountered in interpreting the seismic profiles.

ii) A realistic five layer, 40 metre thick stratigraphy was modelled on a Pleistocene drift sequence. The bottom layer emphasizes the boulder and cobble complex of a till such as seen on land moraines. The laboratory experimentation focussed on this particular layer structure.

8.2.2 Signal-to-Noise and Signal-to-Reverberation Evaluation

i) The Source Level calculations for the Parametric Array accounted for the condition where the carrier frequency wave is discontinuously attenuated on passing through a water sediment interface. The power radiated, the transducer radius and the carrier frequency were all optimized in relation to the height of the transmitter above the bottom in order to obtain a maximum Source Level.

ii) An optimum design was found to have a radius of 0.35 metres, a power output of 3,500 watts, a carrier frequency of just over 100 kHz for a height above the seabed of 8.5 metres.

iii) An order of magnitude better was noted for the temporal resolution of the terminated Parametric Array than for the Conventional Case. This was particularly striking in the upper 30 metres. The

terminated Parametric Array differentiated the thin sedimentary bands without any distortion. The Conventional Source's longer pulse however does introduce interference and masking of the sedimentary bands. Hence, in a real situation the Conventional Source would not have been able to reproduce an undistorted profile of Layer 2's multiple strata.

iv) The modelling of Ambient Noise at the 1 to 10 kHz frequency range indicated that the noise component has a vertical directionality in its character.

v) It is clear from the Signal-to-Noise evaluations that the terminated Parametric Array is noise limited in comparison with the Conventional Source. This is not surprising since the efficiency is poor during the non-linear conversion. Even with optimum settings the Echo Level of the terminated Parametric Array is unable to match the strength of the Conventional Source.

vi) The Conventional Source by contrast was found to be reverberation limited. This explains why the seismic horizons underlying a morainal seabed tend to be mapped by discontinuous reflections and with poor spatial resolution quality. A small but distinct reverberation advantage was noted for the terminated Parametric Array.

To summarize, the terminated Parametric Array does possess better temporal and spatial resolution attributes. This attested advantage is deemed essential in the definition of Layer 2's fine stratigraphy. The lower reverberation level measured analytically implies that a better Signal-to-Reverberation Ratio would occur using an optimized terminated Parametric Array over morainic seabeds. However, the noise level limitation could be a problem if this is not appropriately addressed through coherent signal averaging techniques. The ease in manipulating the Parametric Array pulse waveform, its bandwidth and centre frequency is reckoned to be a very important asset for an ASI transmission.

8.3 Extracting Sub-seabed Information

Once a signal is received it must be identified as a primary echo or as a multiple. If the echo is a primary return then information relating sub-seabed structure and composition is extracted using innovative geometric signal processing techniques involving the Hilbert Transform. The post-processing was designed to be the framework of the envisioned "Acoustic Core". The approach and methodologies developed to attain an "Acoustic Core" product are recapitulated below in the three subsections that follow:

8.3.1 Detection of Primary Reflections using a Moveout Technique

i) A dynamic variation on Normal Moveout can be manipulated through the application of precise angular information. If the transmission angle is accurately known then the time of arrival can be predicted for a given geometry. A triangular relationship develops between the transmission angle and arrival times, the arrival times and horizontal receiver position, and the transmission angle and horizontal receiver position.

ii) A discriminant results from the simultaneous application of all three relationships. For example, the identification of a multiple path return from a primary echo coincident in time, uses the differences in position along the receiver array for a particular transmission angle. A multiple can not arrive at the same receiver position given a specific transmission angle and complimenting arrival time.

iii) A velocity of sound for each layer scanned is a byproduct of the primary echo/multiple differentiation. Once the time of arrival is confirmed at a specific receiver position given a particular transmission angle, then a geometric raypath is forged which allows a layer thickness and velocity of sound to be calculated.

8.3.2 The Spatial Offset Network

i) The horizontal location of the returned signal is difficult to identify with precision. The highest amplitude over a cluster of receiving elements is used to improve the detection resolution along the axis. The isolation of an echo in such a group is further sharpened by processing the coherency of the signals over a spatial net.

ii) The spatial net configuration utilizes two sets of four primary offsets along an inner and outer scanning circle. Accompanying these spot measurements are (n) number of intermediate secondary offsets.

iii) The coherency between each set of four primaries and corresponding secondary positions is evoked by signal averaging each receiving element. The averaged group of each position is then averaged together. The peak of the resultant averaged amplitude processed over the primary and secondary sets would indicate a sharp echo position for a particular time and transmission angle.

iv) If the lateral resolution is deficient after spatial coherency averaging has taken place for a particular boundary interrogation then the anomaly is singled out and further refined by engaging the receiving array in a focussed mode of operation.

v) Phase array technology is presently well developed. It is proposed that the phase array be focussed at a particular focal depth where the beam can be made to scan or be steered.

vi) Focussing down through a medium which scatters has not been tried. Therefore this use of focussing is a tentative suggestion for the ASI and is yet to be validated experimentally.

8.3.3 The Hilbert Transform Approach

i) A time reference is advanced in the ASI concept using the Hilbert Transform of the real part to acquire the imaginary part. The

normal real valued time domain functions are hence made complex. From the transformation an envelope function is attained and can be displayed similar to functions in the frequency domain.

ii) The two key properties that are prominent in the ASI signal analysis are the Envelope and the Instantaneous Frequency.

In summing up, the ASI concept involves an underwater probe which can intelligently interrogate signal and noise responses in situations where there are severe sound propagation constraints. The echo discrimination routine is first performed to identify a primary from a multiple. The horizontal location of the returned signals is then isolated by processing the coherency of the reflection over an established or known hydrophone network and transmitter geometry. The coherency between each of the four scanning offsets is signal averaged. The resultant deviation is measured. Velocity of sound in the layers are found. If anomalies occur, focussing down through the medium is executed at a particular focal depth. The beam is then steered. The referencing of time is controlled by the Hilbert Transform's energy envelope.

As these techniques take place a real time "Acoustic Core" exhibits each operational result. The graphic display responds and synthesizes the signals in two and three dimensions during the post processing.

The final output is in the form of statistical data on the sediment properties of each descending layer along with isoline spatial representation of the data values. A more qualitative picture is also

mapped in 3-D for a rapid on-ship interpretation of a site. An essential asset of the "Acoustic Core" is its statistical coherency, deviation and measurement error.

8.4 Results of the Experimental Simulations Over a Pseudo-Glacial Till

The ultimate objective of the laboratory simulations was to test the acoustical behaviour of the ASI concept over a complex sediment layer which would represent one of the worst structures to seismically scan. The results of the experimentation impressed three main points:

8.4.1 Time History Data Using the Hilbert Transform

i) The energy envelope or magnitude of the time signals was computed and then executed on a 40 dB logarithmic scale. The peak position of the magnitude formed a discrete reference location for all time measurements to be made from. A more lucid and exact time difference was constituted using the Hilbert Transform procedure then if the conventional real part of the signal was employed.

ii) The differences between the averaged measured arrival times for the water column and the averaged predicted arrival times were very small ($\pm\sigma = 2.1 \mu\text{s}$ for the outer ring; $\pm\sigma = 1.2 \mu\text{s}$ for the inner ring). This translated into a maximum averaged measurement error of 1.4%.

iii) Similarly, the differences between the averaged measured times of arrival for the pseudo glacial till and the averaged predicted values were also minor ($\pm\sigma = 7 \mu\text{s}$ for the outer ring; $\pm\sigma = 2 \mu\text{s}$ for the inner ring). This defined a maximum averaged measurement error of 1.2%.

8.4.2 Statistical Evaluation of the Pseudo Glacial Till's Homogeneity Character

i) The variation in velocity over the two scanning circles produced a deviation of:

- Outer Circle: $\pm\sigma = 31.9$ m/s ; \pm error = 0.4 m/s
- Inner Circle: $\pm\sigma = 20.3$ m/s ; \pm error = 0.0 m/s
- Difference between Outer and Inner Circle: $\pm\sigma = 11.6$ m/s;
 \pm error = 0.4 m/s

This deviation is quite large when compared to the velocity deviations in the water column:

- Outer Circle: $\pm\sigma = 1$ m/s ; \pm error = 0.0 m/s
- Inner Circle: $\pm\sigma = 1$ m/s ; \pm error = 0.0 m/s
- The error in the deviation difference between the Outer and Inner Circle is negligible.

ii) The variation in the Absorption Coefficients indicates a similar trend for the Till Model:

- Outer Circle: $\pm\sigma = 0.074$ dB/m kHz; \pm error = 0.001 dB/m kHz
- Inner Circle: $\pm\sigma = 0.039$ dB/m kHz; \pm error = 0.000 dB/m kHz
- Difference between Outer and Inner Circle $\pm\sigma = 0.035$ dB/m kHz;
 \pm error = 0.001 dB/m kHz

The water column in comparison is characterized by:

- Outer Circle: $\pm\sigma = 0.0001$ dB/m kHz; \pm error = 0.0000 dB/m kHz
- Inner Circle: $\pm\sigma = 0.0001$ dB/m kHz; \pm error = 0.0000 dB/m kHz
- The error in the deviation difference between the Outer and Inner Circle is negligible.

iii) A Coefficient of Variation was accentuated non-linearly to emphasize the differences in value. A homogeneity classification scale was attempted using the variations as a base.

iv) The homogeneity variation using the property of velocity for the till model had an average variation of 63.0/100 while for the water column the average variation was 2.5/100. The average Absorption Coefficient variation for the till showed a level of 8.3 while for the water it was noted to be 1.0 (1.0 corresponds to 0.01 dB/m kHz).

v) Once sufficient field data is collected using a sea-going ASI then a homogeneity standard can be established. This standard could evolve into a sediment classification model.

8.4.3 The "Acoustic Core" Product

i) The data base was visually displayed as isolines. This spatially manifested the homogeneity distribution of the data in terms of bathymetry, thickness, velocity, and attenuation.

ii) The contour patterns outlined the internal structural properties of the pseudo glacial till model.

iii) The most striking feature observed is the velocity flow pattern around positions $B_1 \rightarrow C$. The shape of the velocity isolines conform to the density-porosity values that are expected or predicted for the model given the manner the material was laid in the tank.

iv) It is considered very significant that the internal flow patterns are mapped with such clarity.

v) The analytical modelling suggested that the ASI would be able to maintain a high degree of measurement sensitivity. This is supported by the experimental results.

vi) The distribution of the Absorption Coefficients is also revealing. While absorption is noted to be sensitive to density and porosity changes, it is also affected by grain size. There is a distinct anomaly observed in the D-zone. This anomaly is seen as a response to a higher accumulation or clustering of very large particulates. In real life this would represent a boulder field.

vii) Only through the synthesis of the velocity and attenuation data can this type of interpretation manifest itself.

The experimentation over the complex till model has demonstrated the uniqueness of the ASI concept in acquiring precise acoustic responses off a sedimentary medium. It is believed that the fundamental internal structural information defined in the "Acoustic Core" by the ASI cannot be attained using existing geophysical and geotechnical techniques.

8.5 Attenuation Loss Approach to Measure and Monitor Changes in Shear-Wave Velocity

The "Acoustic Sub-seabed Interrogation" may provide a means of defining geotechnical data using its calibrated acoustic response. In particular, the correlation of attenuation data with rigidity may provide an indirect but quantitative mensuration of shear-wave velocity. The arguments which support this hypothesis evolve from:

8.5.1 Elastic Equations

i) The derivation of shear modulus using estimations for bulk modulus is not very accurate since the bulk modulus is very much larger than the shear modulus.

ii) A more accurate assessment of shear modulus involves the shear-wave velocity.

iii) The measurement of shear-wave velocity is impractical to execute in an ocean-seabed environment using presently available technology.

8.5.2 Correlating Attenuation Losses with Rigidity

i) The results of Thomas and Pace (1980) study indicated that increases in the particle-particle contact area (solid friction loss) caused a decrease in both the sound attenuation and the dynamic rigidity.

ii) When porosity dropped below 35%, the dynamic rigidity component diminished in the total bulk modulus of the sand matrix. As the porosity values increased, the reverse occurred with rigidity becoming a more important contributor (see the footnote on page 265).

iii) Plotting attenuation loss data from Thomas and Pace (1980) against the shear-wave velocity of the rigidity factor denoted three key zones. Attenuation losses below 0.24 dB/m kHz produced a negligible shear-wave velocity. Attenuation levels between 0.23 and 0.35 dB/mkHz indicated a complex curve which possessed three discrete inflections. The third zone occurred beyond 0.35 dB/m kHz. In this region the shear-wave velocity peaked and the curve flattened at \approx 400 m/s. The shear-wave velocity remains constant providing that the sediment can support shear stresses.

iv) By reexpressing the middle zone using a mean slope, a maximum deviation was established which translated into an error of less than 5% (\approx 3%).

This curve is thought to be representative of a family of curves for other particulate sizes. Further experimentation is required on a wide range of soil types to verify the two extreme inflection points which establish the mean slope of the intermediate zone. A large statistical data base using the ASI laboratory simulator would validate the use of attenuation losses to derive a shear-wave velocity. However, the in-situ acquisition of attenuation losses using existing geophysical/geotechnical techniques lacks the precision to employ this correlation approach. Absorption values acquired through conventional

in-situ methods may not correlate well with elastic properties because of the high degree of uncertainty and error inherent in the measurements (J. Ross (1985) communication - refer to Appendix D - Volume II).

The significance of the "Acoustic Sub-seabed Interrogator" is that it should be able to make in-situ attenuation measurements with an unprecedented accuracy. The ASI's calibrated response may therefore provide the direction and confidence needed to translate acoustical energy into physical and elastic properties. It may also accommodate a continuous means of monitoring the dynamic changes in shear-wave velocity and modulus under cyclic loading.

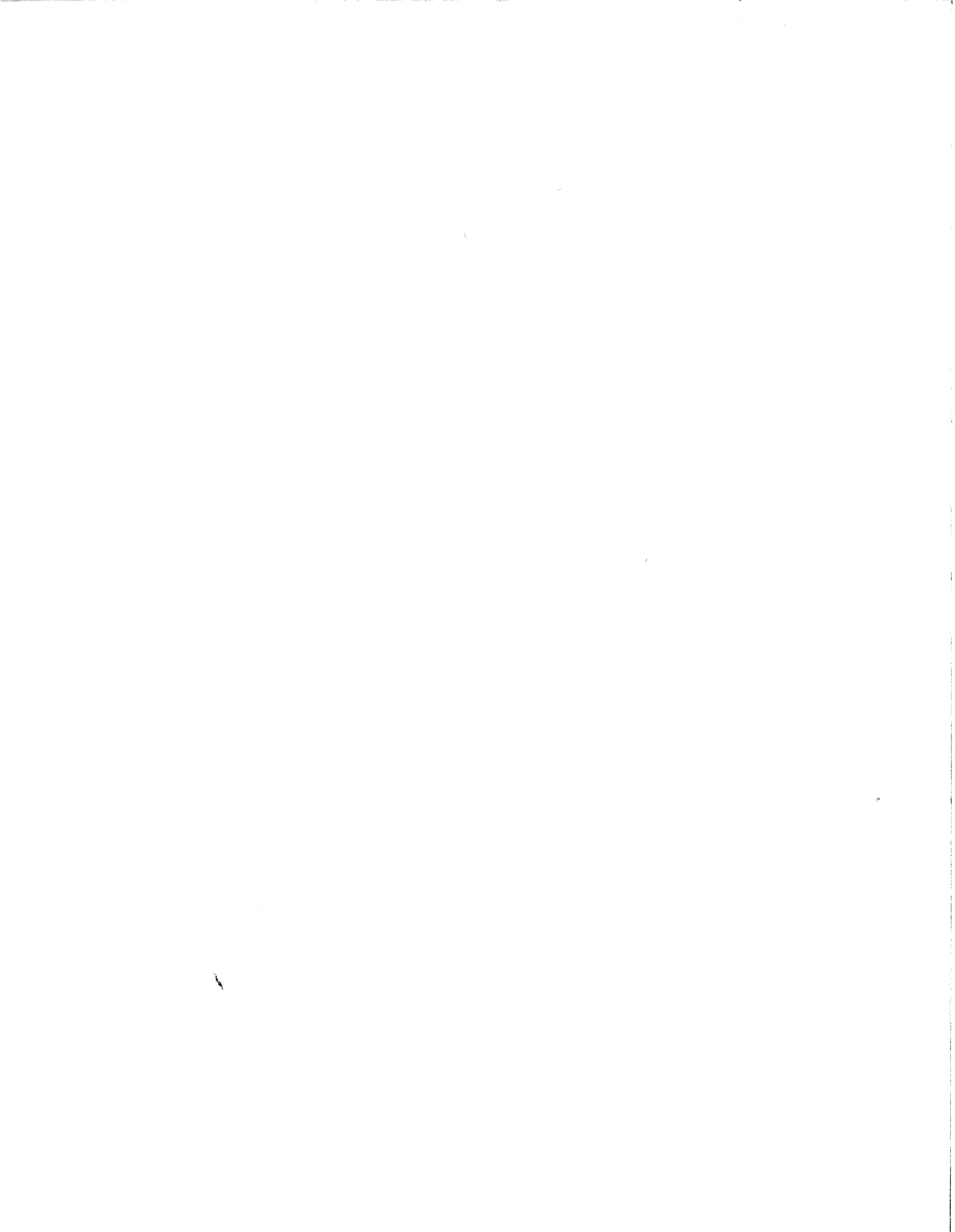
8.6 Future Direction

The ASI's remotely sensed calibrated response may provide a continuous means of monitoring the dynamic in-situ changes in shear-wave velocity and modulus under cyclic loading. Once an initial acoustic translation has been executed to establish the physical and elastic properties of a particular site, the resultant "Acoustic Core" product can then be transposed into a dedicated acoustic spot probe. The proposed tool for this monitoring phase would consist of a streamlined version of the ASI called a "Programmable Monitoring ASI" (PM-ASI)*. The PM-ASI would have a normal incident truncated Parametric Source, a calibrated hydrophone and a computer controlled data logger. The information contained in the "Acoustic Core" would dictate essentially which sub-seabed layer should have a continuous

recording of its pore pressure under changes in cyclic loads and it would also optimize the source configuration appropriately.

In support of this idea, the ASI laboratory research will be directed towards the quantification of acoustic and elastic properties of selected soils. A special battery of tests will map the effects of induced pore pressure changes on attenuation losses for controlled sediment types. If the correlations are as sensitive as what is hypothesized then the concepts of an "Acoustic Sub-seabed Interrogator" and a "Programmable Monitoring ASI" could revolutionize the current thinking on in-situ geotechnical mapping of sub-seabed soils.

*The "Programmable Monitoring ASI" or its abridged name PM-ASI, is a concept that is yet to be evaluated. A new phase of research which will follow the Ph.D program, will involve the acoustic monitoring of pore pressure changes to assess the feasibility of implementing the PM-ASI idea.

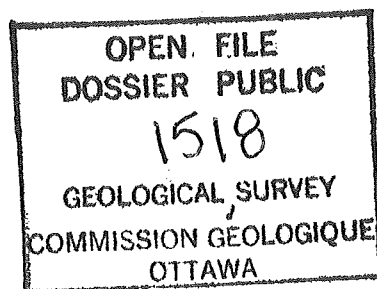


THE CONCEPT, DESIGN AND EXPERIMENTAL
EVALUATION OF AN
"ACOUSTIC SUB-SEABED INTERROGATOR"

VOLUME II

REFERENCES AND APPENDICES

JACQUES YVES GUIGNÉ



VOLUME II
REFERENCES AND APPENDICES

LIST OF REFERENCES

- Anderson, A. L., 1974, "Acoustic of Gas-Bearing Sediments" applied Research Laboratories Technical Report (ARL-TR-74-19). The University of Texas at Austin: Applied Research Laboratories.
- Anderson, V. C., 1979, "Variation of the Vertical Directionality of Noise with Depth in the North Pacific". J. Acoust. Soc. Am. 66 (S. J. Nov., (1416-1452)).
- Andrews, J. T., 1970, "A geomorphological study of post glacial uplift with particular reference to Arctic Canada". Inst. Br. Geog. Sp. Pub. 2.
- Bajpai, A. C., Mustoe, L. R., and Walker, D., 1982, Engineering Mathematics, John Wiley and Sons, (686-726).
- Berktay, H. O., 1967, "Some Finite Amplitude Effects in Underwater Acoustics" in V.M. Abers (ed), "Underwater Acoustics" Vol. 2 Chapt. 12, Plenum Press, New York.
- _____ 1971, "Near-field Effects in Parametric End-Fire Arrays. University of Birmingham, Department of Electronic and Electrical Engineering Memorandum No. 418.
- _____ and Muir, T.G., 1973, "Arrays of Parametric Receiving Arrays", J. Acoust. Soc. Am. 53, (1377-1383).
- _____ Smith, B. V., Cooper, B. S., Dunn, J. R., 1979, "Near-Field Effects in Non-Linear Acoustics". Proceedings Underwater Applications of Non-linear Acoustics, Institute of Acoustics.

- Biot, M. A., 1956a, - "Theory of Elastic Waves in a Fluid Saturated Porous Solid". I. (Low-Frequency Range). J. Acoustic Soc. Am., 28, (168-178).
- 1956b, - "Theory of Elastic Waves in a Fluid Saturated Porous Solid II. (Higher Frequency Range). J. Acoustic Soc. Am., 28, (179-191).
- Bjorno, L., 1977, - "Excitation of Selected Modes in Shallow Water Propagation". Proc. Ultrasonics International 1977, JPC Science and Technology Press Ltd. Guildford, England.
- Hatig, A., Jensen, H. H. and Larsen, P. N., 1979, "Parametric Acoustic Arrays in Temperature Stratified Shallow Water", Proc. Underwater Applications of Non Linear Acoustics - Institute of Acoustics.
- Blue, J. E. and McLeroy, E. G., 1968, "Attenuation of Sound in Suspensions and Gels". J. Acoust. Soc. Am. 44, (1145-1148).
- Brophy, J. J., 1983, Basic Electronics for Scientists, McGraw-Hill International Book Company, International Student Copy, (75-77).
- Brown, W. M. and Procello, L. J., 1962, "Theory of Coherent Systems", IRE Trans. Mil. Electron. 6, No. 2 special issue on "Signal Processing Radar", (187-196).
- Bruel and Kjaer, 1980 "Introduction to Underwater Acoustics", Application Notes: Hydrophones - their characteristics and applications.
- Buchan, S., McCann, D. M. and Taylor Smith, D., 1972, "Relations between the Acoustic and Geotechnical Properties of Marine Sediments". Quart. J. Eng. Geol. 5. No. 3 (265-284).

- Burg, J. P., 1969, "Maximum Entropy Spectral Analysis". Paper presented at the 37th Annual International SEC Meeting. Oklahoma.
- Ceen, R. V. and Pace, N. G., 1981, "Time Domain Study of the Terminated Transient Parametric Array", Proceedings Institute of Acoustics, Advances in Underwater Acoustics, AUWE Portland.
- Chatfield, C., 1976, Statistics for Technology, Chapman and Hall, (90-100).
- Clark, J., 1975; communications on the status of marine geotechnical research.
- Clay, S. C. and Medwin H., 1977, Acoustical Oceanography: Principles and Applications, Wiley - Interscience Publication.
- Cochrane, N. A. and Dunsiger, A. D., 1979, "Seabed Characterization from Broadband Acoustic Echolocation with Scattering Models" IEEE Journal of Oceanic Engineering Vo. OE-6, No. 3.
- Cuberston, C. R., 1979, "The Parametric Receiving Array in an Inhomogeneous Medium". Proceedings Underwater Applications of Non-linear Acoustics, Institute of Acoustics.
- Cultrona, L. J., Vivian, W. E., Leith, E. N. and Hall, G. O., 1961, "A High Resolution Radar Combat Surveillance System", IRE Trans. Mil. Electron. 5 (127-130).
- _____ Hall, G. O., 1962, "A Comparison of Techniques for Achieving Fine Azimuth Resolution," IRE Trans. Mil. Electron 6, (119-121).

- _____ Leith, E. N., Porcello, L. J., and Vivian, W. E., 1966, "On the Application of Coherent Optical Techniques to Synthetic Aperture Radar", Proc. IEEE 54 No. 8, (1026-1032).
- _____ 1970, "Synthetic Aperture Radar, in Radar Handbook (edited by M.I. Skolnik McGraw - Hill, New York 1970) Chap. 23.
- _____ 1975, "Comparison of Sonar System Performance Achievable Using Synthetic Aperature Techniques with the Performance Achievable by more Conventional Means" J. Acoust. Soc. Am., Vol. 58, No. 2.
- Dawe, C. R., 1984, M. Eng., Thesis - Memorial University of Newfoundland, private communications.
- des Vallieres, 1978, "Test of Various High Resolution Seismic Devices in Hard Bottom areas", Proc. OTC 10th Annual May 8-11.
- Dobrin, M. B., 1976, Introduction to Geophysical Prospecting, McGraw-Hill - Third Edition.
- Dodds, J. D., 1980, "Attenuation Estimates from High Resolution Sub-bottom Profiler Echos", In Bottom - Interacting Ocean Acoustics. Edited by W.A. Kuperman and F.B. Jensen. Plenum Publishing Corporation New York, NY.
- _____ 1981, "Surface and Volume Backscattering of Broadband Acoustic Pulses Normally Incident on the Seafloor: Observations and Models". Conf. on Mathematical and Computational Methods in the Exploration and Extraction of Deep Mineral Resources, Tucson, Arizona.

- Dreimainis, A. and Vagners, V. J., 1971, "Bimodal Distribution of Rock and Mineral fragments in Basal Till", In Goldthwait, R. P. (ed) Till symposium Ohio State Univ. Press (237-50).
- Duffy, J. and Mindlin, R. D., 1957, "Stress-Strain Relations of a Granular Media" J. appl. Mech. 24 (585-593).
- Easterbrook, D. J., 1964, "Void Ratios and Bulk Densities as means of Identifying Pleistocene Till" Bull. Geol. Soc. Am. 75 (8), (745-50).
- Ewing, M. and Donn, W. L., 1957, "A Theory of Ice Ages" Science 129 (463-465).
- Farnbach, A. S., 1975, "The Complex Envelope in Seismic Signal Analysis" S.S.A. Bull., V65(951-962).
- Flint, R. F. ,1971, Glacial and Quaternary Geology Wiley, New York.
- Flynn, H. G., 1964, Physics of Acoustic Cavitation in Liquids" in W. P. Mason Ed., Physical Acoustics, Vol. 1, Prt B, Academic Press, New York, (57-172).
- Foley, J. D. and Van Dam, A., 1982, Fundamentals of Interactive Computer Graphics, Addison - Wesley.
- Gerth, 1976, Labrador Sea Survey - Eastcan (proprietary).
- Geonautics Ltd., 1981, Boulder Detection Study, 81-1015 Canterra Energy Ltd. (proprietary).
- _____ 1983, Boulder Detection Study (Sonogram Acoustic Modelling) 81-1015 Canterra Energy Ltd. (proprietary).

- Goldthwait, R. P., 1971, "Introduction to Till, Today" In Goldthwait, R.P. (ed) Till a symposium Ohio State University Press (3-26).
- Goodell, H. G., 1968, "The Antarctic Glacial History Recorded in Sediments of the Southern Ocean". Palaeogeogr. Palaeoclimatol. Palaeoecol. 5 (41-62).
- Guigne, J. Y., 1984, "Comprehensive Geophysical Study of the Davis Strait Region - Loks Land to Edge of the Continental Shelf" in preparation.
- _____ Geonautics Ltd., 1983, Strait of Belle Isle Submarine Cable Crossing 1983 - Geophysical Program, Proprietary Report, ShawMont, Newfoundland Ltd.
- Hamilton, E. L., Shumway, G., Menard, H. W. and Shipek, G. J., 1956, "Acoustic and Other Physical Properties of Shallow-Water Sediments off San Diego". J. Acoust. Soc. Am., Volume 28, Number 1, (1-15), January.
- _____ 1956, "Low Sound Velocities in High Porosity Sediments" J. Acoust. Soc. Am. 28 (16-19).
- _____ 1961, "Stratigraphy of the Deep Sea Floor". In Oceanography. Edited by M. Sears. Washington D.C. American Association for the Advancement of Science.
- _____ 1970 (a), "Sound Velocity and Related Properties of Marine Sediments, North Pacific" J. Geophys Res., 75. (4423-4446).
- _____ 1970 (b), "Prediction of In-Situ Acoustic and Elastic Properties of Marine Sediments". Geophysics 36, (266-284).

- _____ 1972, "Compressional Wave Attenuation in Marine Sediments"
Geophysics 37 (620-646).
- Hampton, L. D., 1967, "Acoustic Properties of Sediments, J. Acoust. Soc. Am. 42, (882-890).
- Harger, R. O., 1970, Synthetic Aperture Radar Systems, Academic New York, 1970.
- Hartshorn, J. H. and Ashley, G. M., 1972, "Glacial Environment and Processes in Southeastern Alaska". Coastal Res. Center Tech. Rept. 4-CRC Univ. Massachussets (69 pp).
- Havlice, J. F., Kino, G. S., Kofol, J. S., Quate, C. F., 1974, "An Electronically Focused Acoustic Imaging Device", Acoustic Holography, ed. Green, Philips, Plenum Press, New York, (317-333).
- Hornbeck, R. W., 1975, Numerical Methods, Prentice-Hall, Inc. Englewood Cliffs, New Jersey Quantum Publishers, Inc., Page 154.
- Horton, C.W., 1974, "The Penetration of Highly Directional Acoustic Beams into a Sedimentary Bottom, Applied Research Lab/U. of Texas. Austin Report ARL-TR-74-28.
- Ikeda, O., and Sato, T., 1980, "Further Examination of Synthetic Aperature Sonar in a Turbulent Medium "J. Acoust. Soc. Am. 68 (2).
- Kanasewich, E. R., 1975, Time Sequence Analysis in Geophysics 2nd. Edition. University of Alberta Press.

- Keary, P., and Brooks, M., 1984, An Introduction to Geophysical Exploration, Blackwell Scientific Publications - Geoscience Texts, Volume 4, (57 - 101).
- Kinsler, L.E., Frey, A. R., Copens, A. B., and Sanders, J. V., 1982, Fundamentals of Acoustics, Third Edition, Wiley, London.
- Kirby, R.P., 1969, "Variation in Glacial Deposition in a Subglacial Environment: an Example from Midlothian", Scott J. Geol., 5 (49-53).
- Knudsen, V. O., Allford, R.S., and Emling, J. W., 1943, "Survey of Underwater Sound" No. 2 Sounds from Submarines Nat. Def. Res. Comm. Div. 6 sec. 61-NORC-1306.
- Konrad, W. L., 1979, "Applications of the Parametric Source" Proceedings of the conference, Underwater Applications on Non-Linear Acoustics Institute of Acoustics.
- Kritz, J., 1977, "Parametric Array Doppler Sonar", IEEE J. Ocean Eng. OE - 2(2), (190-200).
- Lanczos, C., 1956, Applied Analysis, Prentice-Hall.
- Lee, L. S., and Baecher, G. B., 1983, "Acoustic Data and Uncertainty in Geotechnical Site Characterization Offshore" MIT Report No. MITSG 83-13.
- Mayer, L. A., 1979, "The Origin of Fine Scale Acoustic Stratigraphy in Deep-Sea Carbonates", Jour. Geoph. Res., V. 84, n. B11, (6177-6184).

- _____ and LeBlanc, L. R., 1983, "The Chirp Sonar: A New Quantitative High-Resolution Profiling System", Acoustic and the Sea-Bed, Proceedings of an Institute of Acoustic Conference (April), University of Bath.
- McCann, D.M., 1968, Acoustic Properties of North Atlantic Cores". Vol. 1 Ph.D. thesis, University of Wales.
- McCann, C. and McCann, D.M., 1969, "The Attenuation of Compressional Waves in Marine Sediments" Geophysics, 34 No. 6, (882-892).
- _____ 1970 "Compressional Wave Attenuation in Concentrated Clay Suspensions", Acustica 22, (352-356).
- Merklinger, H. M, 1971, High Intensity Effects in the Non-Linear Acoustic Parametric End-Fire Array, Ph.D. thesis (unpublished), University of Birmingham.
- Moffett, M. B., Westerbelt, P. J., and Beyer, R. T., 1971, "Large-Amplitude Pulse Propagation - A Transient Effect II", J. Acoust. Soc. Amer., Vol. 49, No. 1 (Part 2) (339-343).
- Muir, T. G. and Blue, J. E., 1969, "Acoustic Modulation of Large Amplitude Waves", J. Acoust. Soc. Am., 46, (227-232).
- _____ and Willette, J. G., 1972, "Parametric Acoustic Transmitting Arrays", J. Acoust. Soc. Am. 52 (1481-1486).

- _____ 1973, "A Survey of Several Nonlinear Acoustic Experiments on Travelling Wave Fields", Finite-Amplitude Wave Effects in Fluids, Proceedings of the 1973 Symposium, Copenhagen.
- _____, White, R. L. and Clynch, J. R., 1974, "Experimental Model Studies of Nonlinear Effects in Normal Mode Propagation" In Sound Propagation in Shallow water. O.F. Hastrup and O.V. Olesen (EDS) Saclant ASW Center Conference Proceedings No. 14.
- _____ Clynch, J. R., 1975, "Application of Parametric Arrays to Shallow Water Propagation" J. Acoust. Soc. Amer. 57 (Sup. No. 1) (564).
- _____ Clynch, J. R., 1976, "Propagation of Parametric Waves in Shallow Water", Proceedings of the Conference. Recent Development in Underwater Acoustics, Institute of Acoustic, AUWE, Portland, April.
- _____ 1979, "Some Simple Propagation Models for Linear and Parametric Sources in Shallow Water" Proceedings of the Conference, Underwater Applications of Non-Linear Acoustics, Institute of Acoustics.
- Nafe, J. E. and Drake, C. L., 1957, "Variation with Depth in Shallow and Deep Waters Marine Sediments of Porosity, Density and the Velocities of Compressional and Shear Waves", Geophysics 18, (421-439).
- Newman, W. M. and Sproull, R. F., 1979, Principles of Interactive Computer Graphics, 2nd Edition, McGraw-Hill.

- Nolle, A. W., Hoyer, W. A., Misfud, J. F., Runyan, W. R., and Ward, M. B., 1963, "Acoustical Properties of Water-Filled Sands". J. Acoust. Soc. Am. 35. (1394-1408).
- Officer, C.B., 1958, Introduction to the Theory of Sound Transmission With Applications to the Ocean, McGraw-Hill, New York.
- Olauson, E., 1972, "Oceanographic Aspects of the Pleistocene of the Arctic Ocean", Inter-Nord 12 (151-170).
- Ong, L. H., 1978, "A Novel CCD for Time Delay Within - Pulse Sector Scanning Sonars". Proceedings of the Institute of Acoustics Conference on Transducer Arrays and Array Processing, (61-70).
- _____ 1979, "A Special Theory of Beam Scanning in the Time Domain", Progression Sector Scanning Sonar, Proceedings of the Conference, Institute of Acoustics, (December)(107-114).
- Pace, N. G. and Ceen, R. V., 1980, "Acoustic Propagation in Sedimentary Material" Progress Report, School of Physics, University of Bath, December 1980.
- _____ 1982, "The Terminated Transient Array" School of Physics, University of Bath, August 1982.
- Parrott, D. R., Dodds, D. J., King, L. H. and Simpkin, P. G., "Measurement and Evaluation of the Acoustic Reflectivity of the Sea Floor" Canadian Journal of Earth Sciences Vol. 17, No. 6 (722-737).

- Prest, V. K., 1968, "Nomenclature of Moraines and Ice-Flow Features as Applied to the Glacial Map of Canada", Geol. Surv. Pap. Can. 67-57 (32 pp.).
- Quazi, A. H., Vicione, D.M., Lackoff, M.R. and Kurth, R.R., 1977, "Results of High Data Rate Underwater Acoustic Communications Experiments", in 9th International Congress on Acoustics, Modrid, Spain, July 04-09.
- Robinson, E. A. and Treital, S., 1980, Geophysical Signal Analysis, Prentice-Hall-London.
- Rogers, D. F. and Adams, J. A., 1976, Mathematical Elements for Computer Graphics, McGraw-Hill.
- Ross, J. M. and Bluy, O. Z., 1976, DREA Research
Note - Informal Communication
- Rusby, J. S. M., 1970, "The Inset of Sound Wave Distortion and Cavitation in Seawater", J. Sound Vib., 13(257-267).
- Sabin, 1984, communications: Gauss Quadrature Software Modifications.
- Sampson, R. J., 1978, "Surface II Graphics System", Computer Services Section, Kansas Geological Survey, Lawrence, Kansas.
- Sato, T., Veda, M. and Fukuda, S., 1973, "Synthetic Aperature Sonar", J. Acoust. Soc. Am. 54, (799-802).
- _____ Ikeda, O., 1977, "Sequential Synthetic Aperature Sonar System", IEEE Trans. Sonics Ultrason., 24, (253-259).

- Schulkin, M. and March, H. W., 1962, "Sound Absorption in Sea Water",
J. Acoust. Soc. Am. 34 (864).
- _____ 1963, "Absorption of Sound in Sea Water" J. Brit. IRE, 25
(493).
- Sheriff, R. E., (1978), A First Course in Geophysical Exploration and
Interpretation, International Human Resources Development
Corporation, Boston, (122-125).
- _____ 1980, Seismic Stratigraphy International Human
Resources Development Corporation Boston.
- Shirmer, F., 1970, "Schallausbreitung in Schlick", Dept. Hydrog. Z 23
H.1, (24-30).
- Shumway, G., 1958, "Sound Velocity vs. Temperature in Water Saturated
Sediments", Geophysics 23. (494-505).
- _____ 1960, "Sound Speed and Absorption Studies of Marine Sediments
by a Resonance Method". (Part I and Part II) Geophysics
25. (451-467) and (659-682).
- Simpkin, P., 1975, Geophysical Investigation of Marine Sediments under
In-Situ Conditions Ph.D. thesis - University of Wales.
- Stockhausen, J. H., 1975, "Ambient Noise Directionality - A Useful
Empirical Model", presented at the 90th Meeting of the
Acoustical Society of America.
- Stoll, R.D. and Bryan, G.M., 1970, "Wave Attenuation in Saturated
Sediments", J. Acoust. Soc. Am., 47, No. 5,
(1440-1447).

- Sugden, D.E. and John, B.S., 1976, "Glaciers and Landscape: Geomorphological Approach Edward Arnold.
- Taner, M. T. and Sheriff, R. E., 1977, "Application of Amplitude, Frequency, and other Attributes to Stratigraphic Hydrocarbon Exploration", C. E. Payton, Ed., AAPG MEMOIR 26, Tulsa, Am. Assn. Petroleum Geologists, (310, 327).
- Taner, M. T., Koehler, F. and Sheriff, R. E., 1978, "Complex Trace Analysis, Geophysics, Vol. 44, No. 6, June (1041 - 1063).
- Taylor Smith, D., 1968, "Physics and Sea-Floor Minerals". Contemp. Phys., Vol. 9, No. 6 (565-585).
- _____ 1974, "Acoustic and Mechanical Loading of Marine Sediments", in L. L. Hampton, Ed., Physics of Sound in Marine Sediments, Plenum Press, New York (41-62).
- Thomas, P. R., and Pace, N. G., 1980, "Broadband Measurements of Acoustic Attenuation in Water-saturated Sands", Ultrasonics, January (13-17).
- Tucker, D. G., 1965, "The Exploitation of Non-Linearity in Underwater Acoustics", J. Sound Vib., 2(4) (429-434).
- Urlick, R. J., 1947, "A Sound Velocity Method for Determining Compressibility of Finely Divided Substances", J. Appl. Phys. 18, (983-987).
- _____ 1948, "Absorption of Sound in Suspension of Irregular Particles", J. Acoust. Soc. Am. 20 (283-289).
- _____ 1975, Principles of Underwater Sound, 2nd Edition McGraw-Hill Book Company.
- Van Overeem, A. J. A., 1977, "Shallow-Penetration, High Resolution Sub-bottom Profiling", Marine Geotechnology, Volume 3, Number 1.

- Vetter, W. J., 1984, Signal Concepts, The One-Dimensional Medium Model and Basics of Seismic Trace Processing, draft of course notes. Prepared at PP PG 1983/84 for courses GEO 565 and GEO 566.
- Wagstaff, R. A., 1980, "Horizontal Directionality Estimation Considering Array Tilt and Noise Field Vertical Arrival Structure", J. Acoust. Soc. Am. 67(4), April, (1287-1294).
- Wenz, G. M., 1962, "Acoustic Ambient Noise in the Ocean: Spectra and Sources", J. Acoust. Soc. Amer., 34, (1936-1956).
- Westervelt, P. J., 1957, "Scattering of Sound by Sound", J. Acoust. Soc. Am., 25 (199-203).
- _____ 1963, "Parametric Acoustic Array", J. Acoust. Soc. Am. 35 (535-537).
- White, J. E., and Sengbush, R. L., 1953, "Velocity Measurements in Near-Surface Formations", Geophysics 18, (54-69).
- Wood, A. B., 1940, A Textbook of Sound Bell, London.
- Wyllie, M. R. J., Gregory, A.R. and Gardiner, L.W., 1966, "Elastic Wave Velocities in Heterogeneous and Porous Media", Geophysics, 21 (41-70).
- Yates, 1970, "The Principle of Orthogonality and Confounding in Replicated Experiments", Experimental Design: selected papers of Frank Yates, London, Griffin, 1970 (3).
- Yuen, C. K., Beauchamp, K. G. and Robinson, G. P. S., 1982, Microprocessor System and Their Application to Signal Processing, Academic Press, New York, (286-290).

APPENDIX A

SUMMARY OF CONCLUSIONS
OF THE GEONAUTICS'
BOULDER DETECTION STUDY

(by permission
Geonautics 1981)

Conclusions and Recommendations

The following conclusions and recommendations resulted from the assessment of the BIO-Open File data, site survey data and the 1976 Labrador Sea Soil Survey.

- 1) The high resolution sparker (16 kilojoule) data may provide useful information on till thickness if thicknesses exceed 50 metres. In general the systems tested have not exhibited resolution required to define the shallow glacial tills either in thickness or in content.
- 2) The mini-sleeve exploder data have exhibited limited resolution of near-bottom conditions. This resolution may be improved by either better field operations or processing. The data recorded at 1/4 msec. warrant additional processing to determine if resolution can be increased either by sampling rate, by better deconvolution, by automatic statics or by closely spaced velocity analysis.
- 3) The NSRF data have exhibited limited anomalies which could be interpreted as bouldery sequences. The single line at Finnbogi suggests that boulders are more likely to the north. This interpretation may be a result of interference with a multiple but diffractive energy to the north does not appear to result from this interference.

At Raleigh, data in the northwest subarea suggest that there are bouldery and non-bouldery areas (Lines R-2, 3, 4, 6, 7, 8). The Hekja data show no anomalous zones that could be interpreted as boulder without preconceived knowledge. In all areas the presence of excessive sparker interference severely reduces data quality. Data recorded without this interference may illustrate variations in gray level due to backscattering in differing types of glacial tills. Further systems evaluation is therefore recommended.

- 4) The Huntec Deeptow (BIO-Open File) data illustrate apparent variations in backscattering. 'White-out' areas suggest an absence of boulders while dark areas suggest boulders. These areas may warrant further evaluations by sonogram analysis and also may be suitable for test drilling.

- 5) The airgun data have exhibited substantial penetration in thick till and bedrock units. The 25 ms. bubble pulse has severely reduced resolution capabilities of the system. The use of digital recording and post survey processing may provide higher quality data (ie. better near-bottom resolution) and the system may therefore warrant additional testing.
- 6) The 1976 Labrador Sea Soil Surveys included recommendations for various sources. Through personal communications with other operators, comparisons of the mini-sleeve exploder and mini-Flexichoc sources have shown the former system superior in both resolution and penetration (1980 surveys).
- 7) Multi-electrode sparkers have shown good intermediate penetration (150 - 200 ms on Labrador Banks) with resolution of up to 4 ms. Additional evaluation of this source is recommended.

APPENDIX B

DIFFERENCE FREQUENCY PRESSURE

The difference frequency pressure in the frequency domain as a function of range and angle for $R \gg L$ may be obtained from an expression given in reference (*).

$$P(\omega) = P_o^2 \omega d^2 \sqrt{2\pi} \frac{a^2 \ell}{R} \cdot \frac{J_1(x_1)}{x_1} \cdot \frac{\text{Sin}(x_2)}{x_2} \cdot \frac{\beta}{8\pi\rho c^4} \quad (\text{B.1})$$

The on-axis far field pressure, reduced to a unit distance is

$$P(\omega,1) = \frac{P_o^2 \omega^2 d^2 \sqrt{2\pi} a^2 \ell \beta}{8\pi\rho c^4} \quad (\text{B.2})$$

If we let the power radiated W equal $\frac{P_o^2 a^2 \pi}{2\rho c}$ then

$$P(\omega,1) = \frac{W\omega d^2 \ell \beta}{c^3 \pi \sqrt{2\pi}} \quad (\text{B.3})$$

The Source Level of the difference frequency in the farfield will be $20 \log (P(\omega,1))$ or SLd. Therefore:

$$\text{SLd} = 144.88 - 60 \log c + 40 \log f_d + 20 \log W + 20 \log \ell \quad (\text{B.4})$$

* The Penetration of a Water - Sediment Interface by a Parametric Array
 Ph.D Thesis: D. J. Wingham 1984 University of Bath - School of
 Physics, England.

APPENDIX C

EXPERIMENTAL DATA DIGEST FOR THE OUTER AND INNER SCANNING CIRCLES

- PLATES 1A to 1d₁ : Pre-measurement Settings

- PLATES 2A to 2d₁ : Time History Data

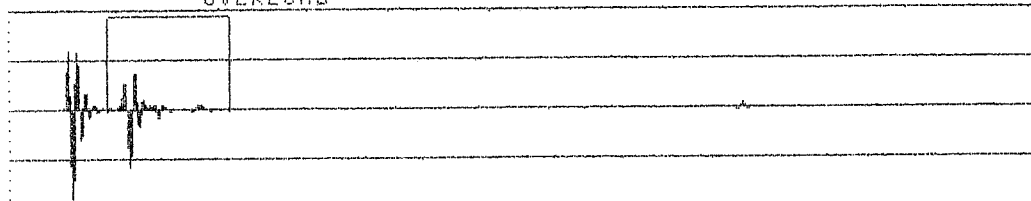
- PLATES 3A to 3d₁ : Envelope of the Time Signals
(using the Hilbert Transform)

- PLATES 4A to 4d₁ : Instantaneous Frequency
(Using the Hilbert Transform)

PLATES 1A TO 1D₁
PRE-MEASUREMENT SETTINGS

PLATE 1A - OUTER SCANNING CIRCLE PRE-MEASUREMENT SETTINGS

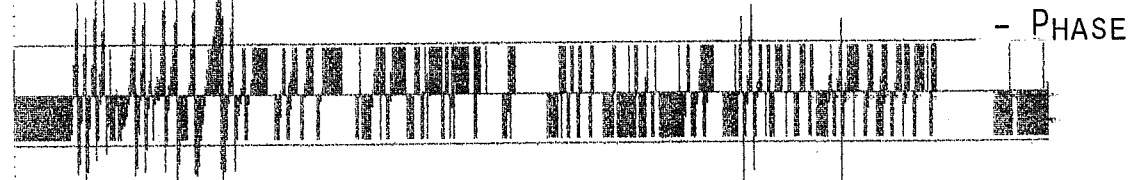
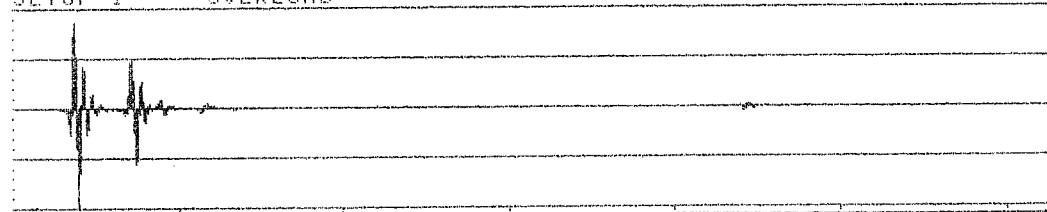
01 TIME CH.A REAL INPUT DELT Y: 19.5E-9U
 Y: 11.8U X: 0.000ms/C + 31.3ms/C X: 0.000ms/C
 X: 0.000ms/C + 31.3ms/C ΔX: 0.000ms/C - REAL PART
 OVERLOAD



SETUP 1
 MEASUREMENT: DUAL SPECTRUM AVERAGING - SETTINGS
 TRIGGER: FREE RUN
 DELAY: CH.A+B: 0.000ms/C
 AVERAGING: EXP 10 OVERLAP: 0%

FREQ SPAN: 25.6kHz*0 ΔF: 32Hz*0 T: 31.3ms/C ΔT: 15.30us/C
 CENTER FREQ: BASEBAND C = EXT SAMPL FREQ: 65536Hz
 WEIGHT CH.A: TRANSIENT SHIFT: 2.944ms/C LENGTH: 3.738ms/C
 WEIGHT CH.B: TRANSIENT SHIFT: 21.469ms/C LENGTH: 1.129ms/C
 CH.A: 10V + 3Hz DIR FILT: 25.6kHz 250mV/PA
 CH.B: 10V + 3Hz DIR FILT: 25.6kHz 250mV/PA
 GENERATOR: DISABLED
 SPECIAL PARAMETER : #100: 200H KEY DEC VALUE: 1

01 TIME CH.A IMAG MAIN Y: 34.2mU - IMAGINARY PART
 Y: 10.7U X: 0.000ms/C + 31.3ms/C X: 0.000ms/C
 SETUP 1 OVERLOAD



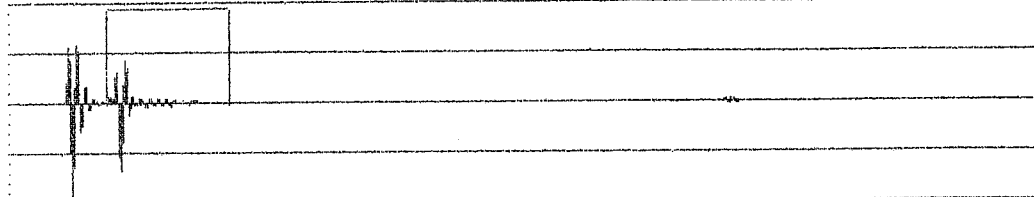
01 TIME CH.A PHASE INPUT MAIN Y: 90.0DEG
 Y: -200 TO +200 DEG X: 0.000ms/C + 31.3ms/C X: 0.000ms/C
 SETUP 1 OVERLOAD

C=30.52 (0.5μs EXTERNAL SAMPLING RATE)

PLATE 1A₁ - OUTER SCANNING CIRCLE

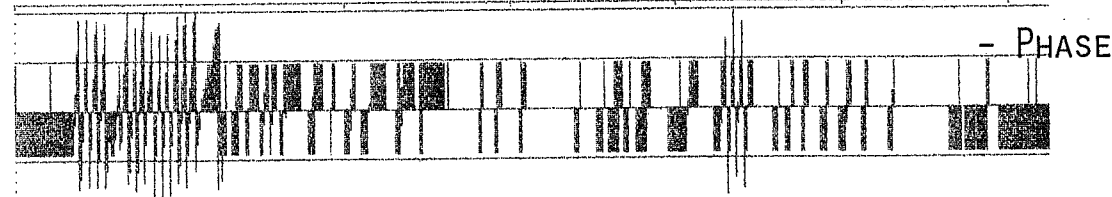
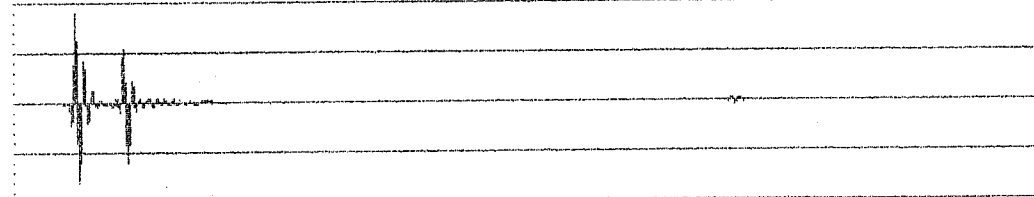
PRE-MEASUREMENT SETTINGS

CH1 TIME CH.A REAL INPUT MAIN Y: 18.6E-9U
 Y: 9.66U X: 0.000ms/C + 31.3ms/C
 OVERLOAD FLEX : 0.00000000 - REAL PART



SETUP 1 PH.D EXPERIMENTAL STUDY... 1985
 TIME HISTORY DATA LTH613N0103
 MEASUREMENT: DUAL SPECTRUM AVERAGING - SETTINGS
 TRIGGER: FREE RUN
 DELAY: CH.A+B: 0.000ms/C
 AVERAGING: EXP 10 OVERLAP: 0%
 FREQ SPAN: 25.6kHz*C ΔF: 32Hz*C T: 31.3ms/C ΔT: 15.3us/C
 CENTER FREQ: BASEBAND C = EXT SAMPL FREQ/65536Hz
 WEIGHT CH.A: TRANSIENT SHIFT: 2.944ms/C LENGTH: 3.738ms/C
 WEIGHT CH.B: TRANSIENT SHIFT: 21.469ms/C LENGTH: 1.129ms/C
 CH.A: 10V + 3Hz DIR FILT: 25.6kHz 250mV/PA
 CH.B: 10V + 3Hz DIR FILT: 25.6kHz 250mV/PA
 GENERATOR: DISABLED
 SPECIAL PARAMETER #100: ZOOM KEY 0 DEC VALUE: 1

CH1 TIME CH.A IMAG INPUT MAIN Y: 39.1mU - IMAGINARY PART
 Y: 9.66U X: 0.000ms/C + 31.3ms/C
 OVERLOAD FLEX : 0.00000000

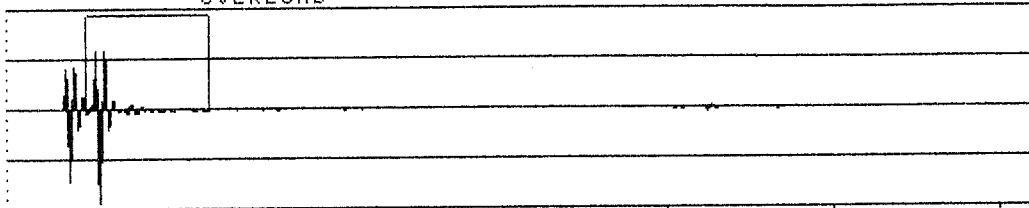


CH1 TIME CH.A PHASE DELT Y: 90.0DEG
 Y: -200 TO +200 DEG X: 0.000ms/C
 X: 0.000ms/C + 31.3ms/C ΔX: 0.000ms/C
 SETUP 1 OVERLOAD

C=30.52 (0.5μs EXTERNAL SAMPLING RATE).

PLATE 1B - OUTER SCANNING CIRCLE PRE-MEASUREMENT SETTINGS

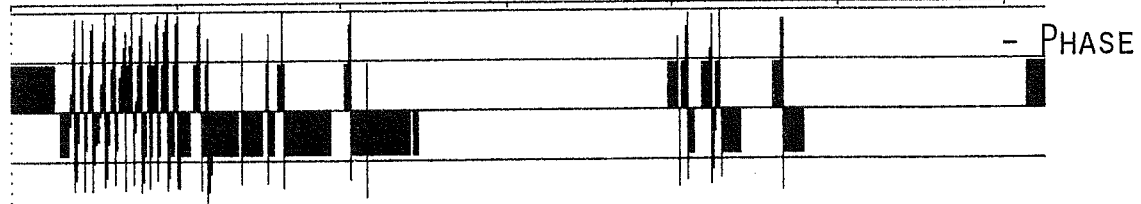
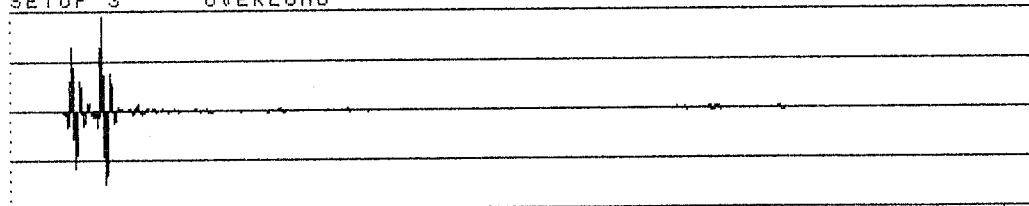
W1 TIME CH.A REAL INPUT MAIN Y: 46.6E-9U - REAL PART
 Y: 13.0U X: 0.000ms/C + 31.3ms/C
 X: 0.000ms/C + 31.3ms/C OVERLOAD



SETUP 3

MEASUREMENT: DUAL SPECTRUM AVERAGING - SETTINGS
 TRIGGER: FREE RUN
 DELAY: CH.A→B: 0.000ms/C
 AVERAGING: EXP 10 OVERLAP: 0%
 FREQ SPAN: 25.6kHz* C ΔF : 32Hz* C T: 31.3ms/C ΔT : 15.3 μs /C
 CENTER FREQ: BASEBAND C = EXT SAMPL FREQ: 65536Hz
 WEIGHT CH.A: TRANSIENT SHIFT: 2.395ms/C LENGTH: 3.738ms/C
 WEIGHT CH.B: TRANSIENT SHIFT: 20.889ms/C LENGTH: 1.129ms/C
 CH.A: 10V + 3Hz DIR FILT: 25.6kHz 100mV/PA
 CH.B: 10V + 3Hz DIR FILT: 25.6kHz 100mV/PA
 GENERATOR: DISABLED
 SPECIAL PARAMETER #100: ZOOM KEY DEC VALUE: 1

W1 TIME CH.A IMAG MAIN Y: 18.3mU - IMAGINARY PART
 Y: 13.0U X: 0.000ms/C + 31.3ms/C
 X: 0.000ms/C + 31.3ms/C OVERLOAD



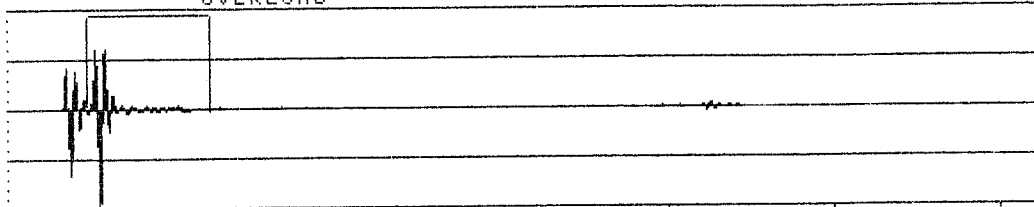
W1 TIME CH.A PHASE INPUT MAIN Y: -200 TO +200 DEG
 Y: -200 TO +200 DEG X: 0.000ms/C + 31.3ms/C
 X: 0.000ms/C + 31.3ms/C OVERLOAD

C=30.52 (0.5 μs EXTERNAL SAMPLING RATE)

PLATE 1B₁ - OUTER SCANNING CIRCLE PRE-MEASUREMENT SETTINGS

01 TIME CH.A REAL INPUT MAIN Y: 46.6E-9U
 Y: 17.0U X: 0.000ms/C + 31.3ms/C
 X: 0.000ms/C OVERLOAD

- REAL PART



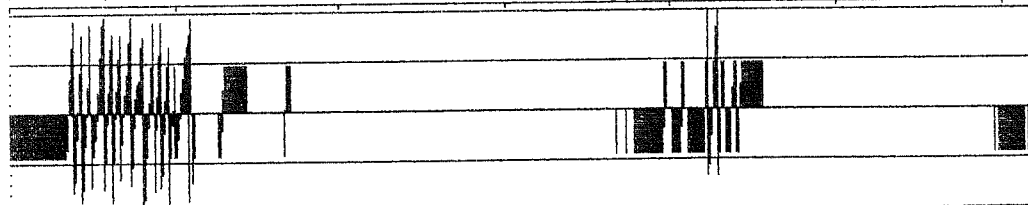
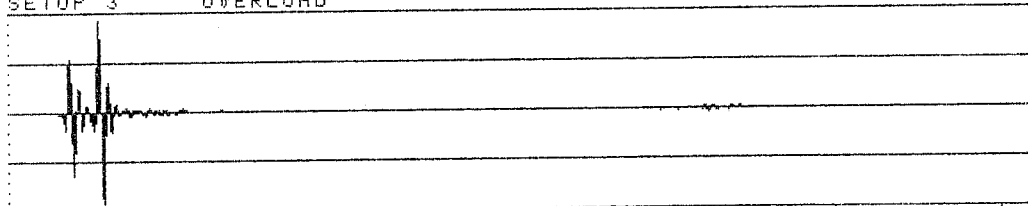
SETUP 3

- SETTINGS

MEASUREMENT: DUAL SPECTRUM AVERAGING
 TRIGGER: FREE RUN
 DELAY: CH.A+B: 0.000ms/C
 AVERAGING: EXP 10 OVERLAP: 0%
 FREQ SPAN: 25.6kHz*C ΔF: 32Hz*C T: 31.3ms/C ΔT: 15.3μs/C
 CENTER FREQ: BASEBAND C = EXT SAMPL FREQ/65536Hz
 WEIGHT CH.A: TRANSIENT SHIFT: 2.395ms/C LENGTH: 3.738ms/C
 WEIGHT CH.B: TRANSIENT SHIFT: 20.889ms/C LENGTH: 1.129ms/C
 CH.A: 10V + 3Hz DIR FILT: 25.6kHz 100mV/PA
 CH.B: 10V + 3Hz DIR FILT: 25.6kHz 100mV/PA
 GENERATOR: DISABLED
 SPECIAL PARAMETER #100: ZOOM KEY DEC VALUE: 1

W1 TIME CH.A IMAG MAIN Y: -24.4mU
 Y: 17.0U X: 0.000ms/C + 31.3ms/C
 X: 0.000ms/C OVERLOAD

- IMAGINARY PART



- PHASE

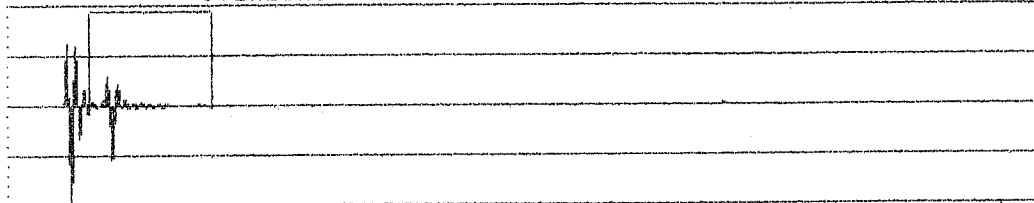
01 TIME CH.A PHASE INPUT MAIN Y: -90.00DEG
 Y: -200 TO +200 DEG X: 0.000ms/C + 31.3ms/C
 X: 0.000ms/C OVERLOAD

C=30.52 (0.5μs EXTERNAL SAMPLING RATE)

PLATE 1C - OUTER SCANNING CIRCLE PRE-MEASUREMENT SETTINGS

#1 TIME CH.A REAL INPUT DELT Y: 18.6E-9U
 Y: 10.5U X: 0.000ms/C + 31.3ms/C
 OVERLOAD ΔX: 0.000ms/C

- REAL PART



SETUP 2

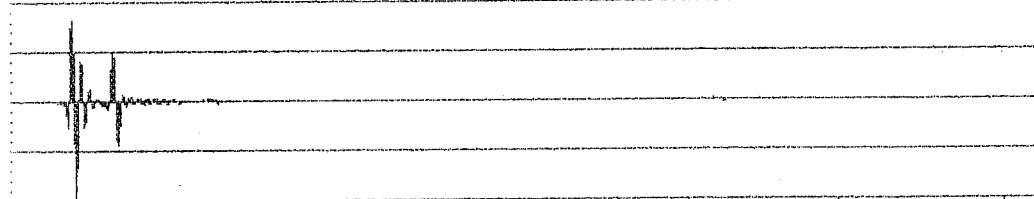
MEASUREMENT: DUAL SPECTRUM AVERAGING
 TRIGGER: FREE RUN
 DELAY: CH.A→B: 0.000ms/C
 AVERAGING: EXP 10 OVERLAP: 0%

- SETTINGS

FREQ SPAN: 25.6kHz*C ΔF: 32Hz*C T: 31.3ms/C AT: 15.3μs/C
 CENTER FREQ: BASEBAND C = EXT SAMPL FREQ/65536Hz
 HEIGHT CH.A: TRANSIENT SHIFT: 2.456ms/C LENGTH: 3.738ms/C
 HEIGHT CH.B: TRANSIENT SHIFT: 20.751ms/C LENGTH: 1.129ms/C
 CH.A: 10V + 3Hz DIR FILT: 25.6kHz 250mV/PA
 CH.B: 10V + 3Hz DIR FILT: 25.6kHz 250mV/PA
 GENERATOR: DISABLED
 SPECIAL PARAMETER : #100: ZOOM KEY DEC VALUE: 1

#1 TIME CH.A IMAG INPUT MAIN Y: -9.77mU
 Y: 10.5U X: 0.000ms/C + 31.3ms/C
 OVERLOAD FLEX : 0.00000000

- IMAGINARY PART



SETUP 2 OVERLOAD

- PHASE

#1 TIME CH.A PHASE DELT Y: -90.0DEG
 Y: -200 TO +200 DEG X: 0.000ms/C
 X: 0.000ms/C + 31.3ms/C ΔX: 0.000ms/C
 SETUP 2 OVERLOAD

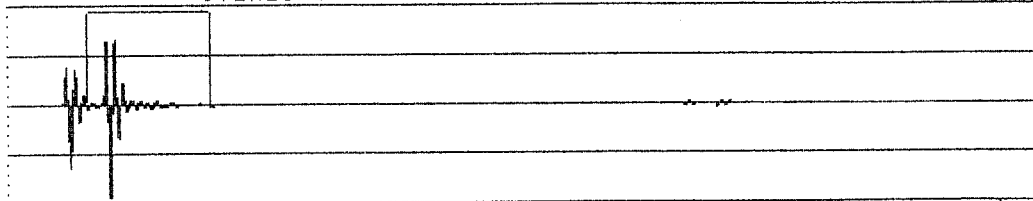
C=30.52 (0.5μs EXTERNAL SAMPLING RATE)

PLATE 1C₁- OUTER SCANNING CIRCLE

PRE-MEASUREMENT SETTINGS

1 TIME CH.A REAL INPUT MAIN Y: 46.6E-9U
 Y: 17.5U X: 0.000ms/C + 31.3ms/C
 OVERLOAD X: 0.000ms/C

- REAL PART



SETUP 3

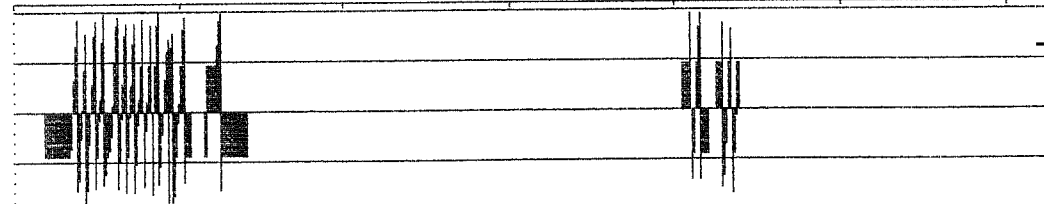
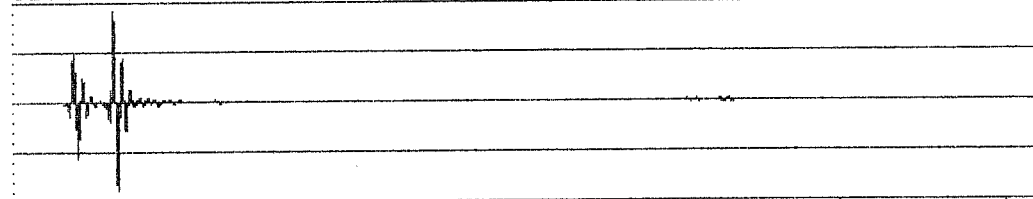
MEASUREMENT: DUAL SPECTRUM AVERAGING
 TRIGGER: FREE RUN
 DELAY: CH.A+B: 0.000ms/C
 AVERAGING: EXP 10 OVERLAP: 0%

- SETTINGS

FREQ SPAN: 25.6kHz*C ΔF: 32Hz*C T: 31.3ms/C ΔT: 15.3us/C
 CENTER FREQ: BASEBAND C = EXT SAMPL FREQ/65536Hz
 WEIGHT CH.A: TRANSIENT SHIFT: 2.395ms/C LENGTH: 3.738ms/C
 WEIGHT CH.B: TRANSIENT SHIFT: 20.889ms/C LENGTH: 1.129ms/C
 CH.A: 10V + 3Hz DIR FILT: 25.6kHz 100mV/PA
 CH.B: 10V + 3Hz DIR FILT: 25.6kHz 100mV/PA
 GENERATOR: DISABLED
 SPECIAL PARAMETER : #100: ZOOM KEY DEC VALUE: 1

1 TIME CH.A IMAG INPUT MAIN Y: 46.6E-9U
 Y: 19.0U X: 0.000ms/C + 31.3ms/C
 OVERLOAD X: 0.000ms/C

- IMAGINARY PART



- PHASE

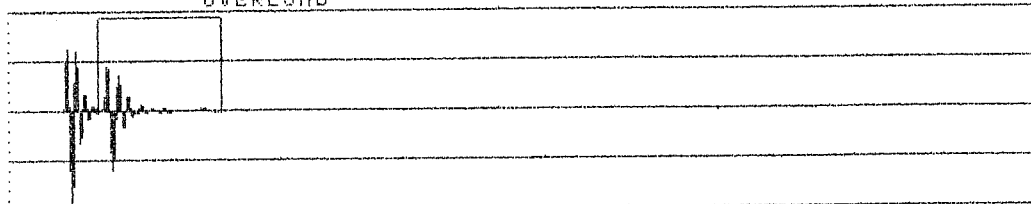
1 TIME CH.A PHASE
 Y: -200 TO +200 DEG
 X: 0.000ms/C + 31.3ms/C
 OVERLOAD

MAIN Y:
 X: 0.000ms/C

C=30.52 (0.5μs EXTERNAL SAMPLING RATE)

PLATE 1D - OUTER SCANNING CIRCLE PRE-MEASUREMENT SETTINGS

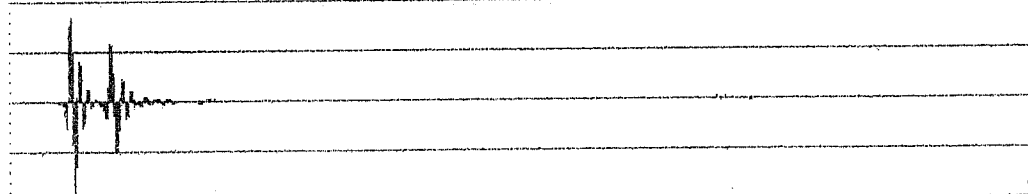
01 TIME CH.A REAL INPUT DELT Y: 18.6E-9U
 Y: 11.3U X: 0.000ms/C + 31.3ms/C X: 0.000ms/C
 X: 0.000ms/C + 31.3ms/C ΔX: 0.000ms/C
- REAL PART



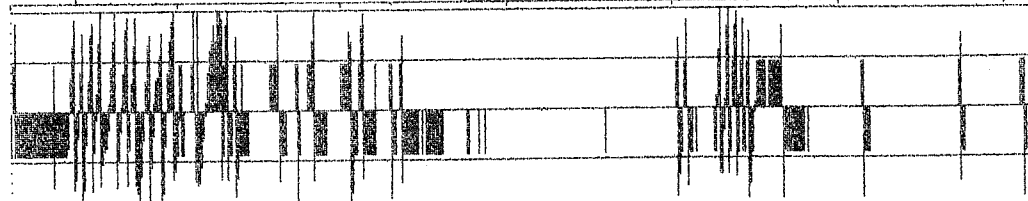
SETUP 2

MEASUREMENT: DUAL SPECTRUM AVERAGING - SETTINGS
 TRIGGER: FREE RUN
 DELAY: CH.A+B: 0.000ms/C
 AVERAGING: EXP 10 OVERLAP: 0%
 FREQ SPAN: 25.6kHz*0 AF: 32Hz*0 T: 31.3ms/C ΔT: 15.3μs/C
 CENTER FREQ: BASEBAND C = EXT SAMPL FREQ/65536Hz
 WEIGHT CH.A: TRANSIENT SHIFT: 2.716ms/C LENGTH: 3.738ms/C
 WEIGHT CH.B: TRANSIENT SHIFT: 21.209ms/C LENGTH: 1.129ms/C
 CH.A: 10V + 3Hz DIR FILT: 25.6kHz 250mV/PA
 CH.B: 10V + 3Hz DIR FILT: 25.6kHz 250mV/PA
 GENERATOR: DISABLED
 SPECIAL PARAMETER : #100: ZOOM KEY DEC VALUE: 1

01 TIME CH.A IMAG INPUT MAIN Y: -4.88mU
 Y: 11.0U X: 0.000ms/C + 31.3ms/C X: 0.000ms/C
 X: 0.000ms/C + 31.3ms/C
 SETUP 2 OVERLOAD
- IMAGINARY PART



- PHASE

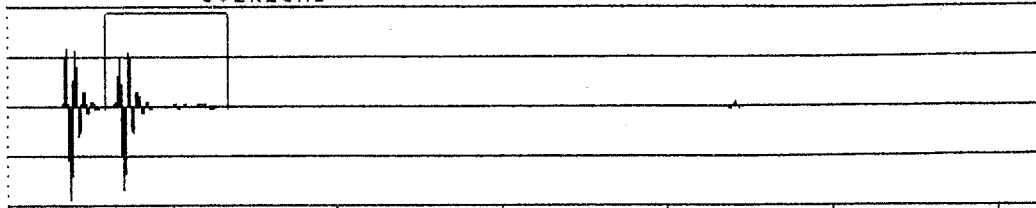


01 TIME CH.A PHASE DELT Y:
 Y: -200 TO +200 DEG X: 0.000ms/C
 X: 0.000ms/C + 31.3ms/C ΔX: 0.000ms/C
 SETUP 2 OVERLOAD

C=30.52 (0.5μs EXTERNAL SAMPLING RATE)

PLATE 1D₁ - OUTER SCANNING CIRCLE PRE-MEASUREMENT SETTINGS

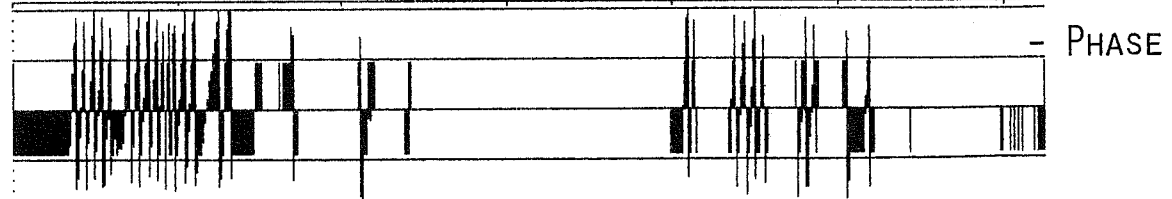
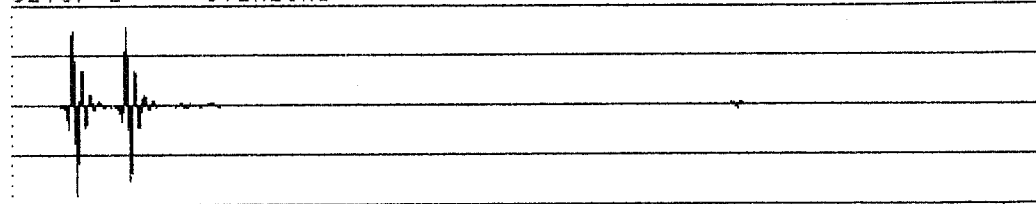
W1 TIME CH.A REAL INPUT MAIN Y: 18.5E-9U - REAL PART
Y: 12.0U X: 0.000ms/C + 31.3ms/C
X: 0.000ms/C OVERLOAD



SETUP 2

MEASUREMENT: DUAL SPECTRUM AVERAGING - SETTINGS
TRIGGER: FREE RUN
DELAY: CH.A+B: 0.000ms/C
AVERAGING: EXP 10 OVERLAP: 0%
FREQ SPAN: 25.6kHz*C ΔF: 32Hz*C T: 31.3ms/C ΔT: 15.3μs/C
CENTER FREQ: BASEBAND C = EXT SAMPL FREQ/65536Hz
WEIGHT CH.A: TRANSIENT SHIFT: 2.944ms/C LENGTH: 3.738ms/C
WEIGHT CH.B: TRANSIENT SHIFT: 21.606ms/C LENGTH: 1.129ms/C
CH.A: 10V + 3Hz DIR FILT: 25.6kHz 250mV/PA
CH.B: 10V + 3Hz DIR FILT: 25.6kHz 250mV/PA
GENERATOR: DISABLED
SPECIAL PARAMETER #100: ZOOM KEY DEC VALUE: 1

W1 TIME CH.A IMAG MAIN Y: -4.88mU - IMAGINARY PART
Y: 12.0U X: 0.000ms/C + 31.3ms/C
X: 0.000ms/C OVERLOAD



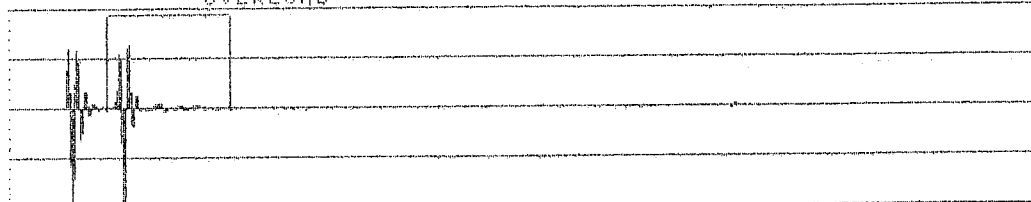
W1 TIME CH.A PHASE INPUT MAIN Y: -200 TO +200 DEG
Y: -200 TO +200 DEG X: 0.000ms/C + 31.3ms/C
X: 0.000ms/C OVERLOAD

C=30.52 (0.5μs EXTERNAL SAMPLING RATE)

PLATE 1A - INNER SCANNING CIRCLE PRE-MEASUREMENT SETTINGS

W1 TIME CH.A REAL INPUT DELT Y: 18.6E-9U
 Y: 11.3U X: 0.000ms/C + 31.3ms/C
 X: 0.000ms/C OVERLOAD

- REAL PART



SETUP 3

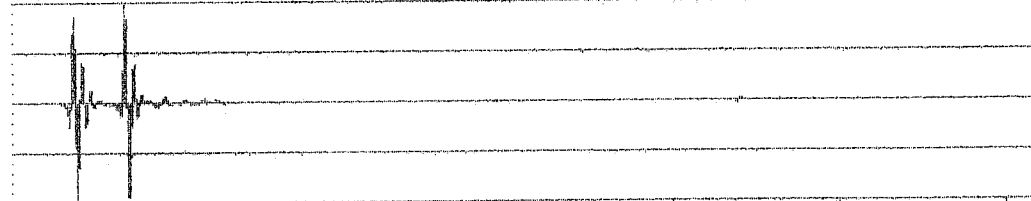
MEASUREMENT: DUAL SPECTRUM AVERAGING
 TRIGGER: FREE RUN
 DELAY: CH.A+B: 0.000ms/C
 AVERAGING: EXP 10 OVERLAP: 0%

- SETTINGS

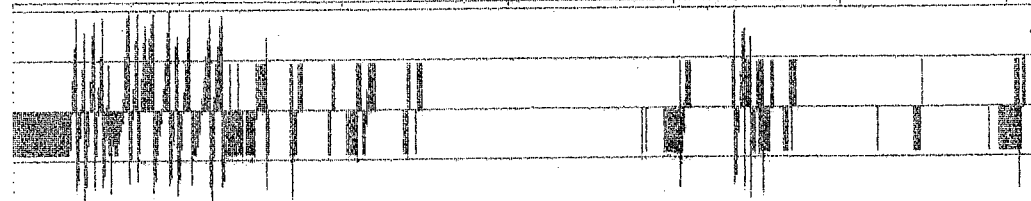
FREQ SPAN: 25.6kHz*C ΔF: 32Hz*C T: 31.3ms/C AT: 15.3us/C
 CENTER FREQ: BASEBAND C = EXT SAMPL FREQ/65536Hz
 WEIGHT CH.A: TRANSIENT SHIFT: 2.944ms/C LENGTH: 3.738ms/C
 WEIGHT CH.B: TRANSIENT SHIFT: 21.652ms/C LENGTH: 1.129ms/C
 CH.A: 10V + 3Hz DIR FILT: 25.6kHz 250mV/PA
 CH.B: 10V + 3Hz DIR FILT: 25.6kHz 250mV/PA
 GENERATOR: DISABLED
 SPECIAL PARAMETER : #100: ZOOM KEY DEC VALUE: 1

W1 TIME CH.A IHAG INPUT MAIN Y: 2.44mU
 Y: 10.7U X: 0.000ms/C + 31.3ms/C
 X: 0.000ms/C OVERLOAD

- IMAGINARY PART



- PHASE



W1 TIME CH.A PHASE
 Y: -200 TO +200 DEG
 X: 0.000ms/C + 31.3ms/C
 SETUP 3 OVERLOAD

MAIN Y:
 X: 0.000ms/C

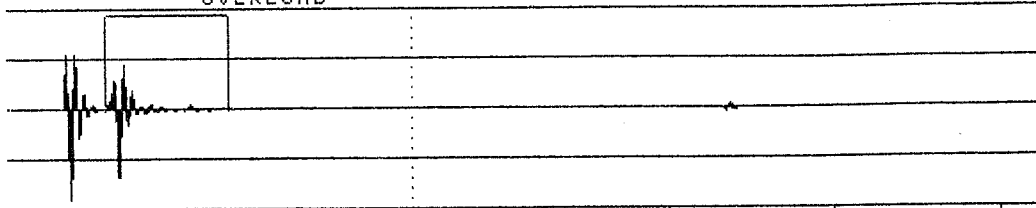
C=30.52 (0.5μs EXTERNAL SAMPLING RATE)

PLATE 1A₁ - INNER SCANNING CIRCLE

PRE-MEASUREMENT SETTINGS

W1 TIME CH.A REAL INPUT DELT Y: 18.6E-9U
 Y: 12.0U X: 12.207ms/C
 X: 0.000ms/C + 31.3ms/C ΔX: 26.367ms/C
 OVERLOAD

- REAL PART



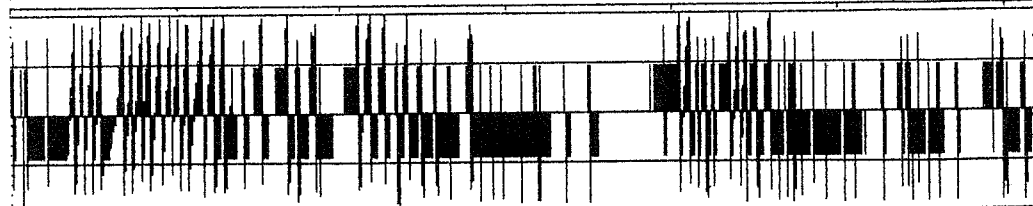
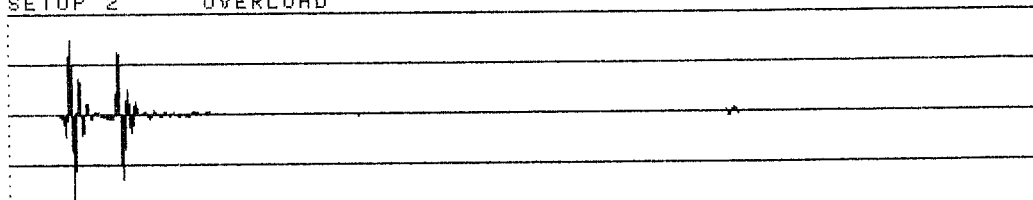
SETUP 2

MEASUREMENT: DUAL SPECTRUM AVERAGING
 TRIGGER: FREE RUN
 DELAY: CH.A+B: 0.000ms/C
 AVERAGING: EXP 10 OVERLAP: 0%
 FREQ SPAN: 25.6kHz* C ΔF: 32Hz* C T: 31.3ms/ C ΔT: 15.3us/ C
 CENTER FREQ: BASEBAND C = EXT SAMPL FREQ/65536Hz
 WEIGHT CH.A: TRANSIENT SHIFT: 2.944ms/ C LENGTH: 3.738ms/ C
 WEIGHT CH.B: TRANSIENT SHIFT: 21.575ms/ C LENGTH: 1.129ms/ C
 CH.A: 10V + 3Hz DIR FILT: 25.6kHz 250mV/PA
 CH.B: 10V + 3Hz DIR FILT: 25.6kHz 250mV/PA
 GENERATOR: DISABLED
 SPECIAL PARAMETER : #100: ZOOM KEY DEC VALUE: 1

- SETTINGS

W1 TIME CH.A IMAG MAIN Y: 7.33mU
 Y: 12.0U X: 0.000ms/C
 X: 0.000ms/C + 31.3ms/C
 SETUP 2 OVERLOAD

- IMAGINARY PART



- PHASE

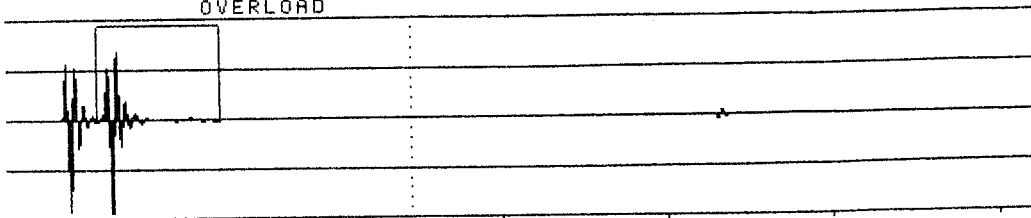
W1 TIME CH.A PHASE INPUT MAIN Y:
 Y: -200 TO +200 DEG X: 0.000ms/C
 X: 0.000ms/C + 31.3ms/C
 SETUP 2 OVERLOAD

C=30.52 (0.5μs EXTERNAL SAMPLING RATE)

PLATE 1B - INNER SCANNING CIRCLE PRE-MEASUREMENT SETTINGS

1 TIME CH.A REAL INPUT DELT Y: -78.2mV
 Y: 12.0U X: 12.207ms/C
 X: 0.000ms/C + 31.3ms/C ΔX: 26.367ms/C
 OVERLOAD

- REAL PART



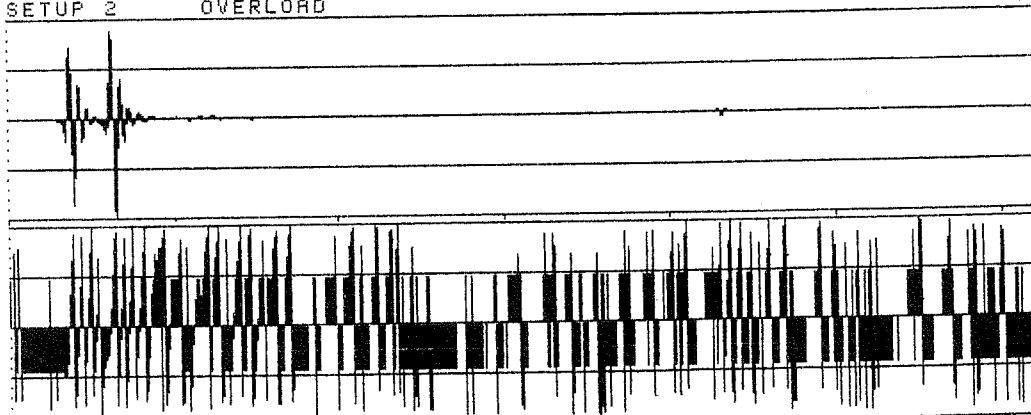
SETUP 2

MEASUREMENT: DUAL SPECTRUM AVERAGING
 TRIGGER: FREE RUN
 DELAY: CH.A→B: 0.000ms/C
 AVERAGING: EXP 10 OVERLAP: 0%
 FREQ SPAN: 25.6kHz*C ΔF: 32Hz*C T: 31.3ms/C ΔT: 15.3μs/C
 CENTER FREQ: BASEBAND C = EXT SAMPL FREQ/65536Hz
 WEIGHT CH.A: TRANSIENT SHIFT: 2.716ms/C LENGTH: 3.738ms/C
 WEIGHT CH.B: TRANSIENT SHIFT: 21.209ms/C LENGTH: 1.129ms/C
 CH.A: 10V + 3Hz DIR FILT: 25.6kHz 250mV/PA
 CH.B: 10V + 3Hz DIR FILT: 25.6kHz 250mV/PA
 GENERATOR: DISABLED
 SPECIAL PARAMETER : #100: ZOOM KEY DEC VALUE: 1

- SETTINGS

1 TIME CH.A IMAG INPUT MAIN Y: 2.44mV
 Y: 12.0U X: 0.000ms/C
 X: 0.000ms/C + 31.3ms/C
 SETUP 2 OVERLOAD

- IMAGINARY PART



- PHASE

1 TIME CH.A PHASE
 Y: -200 TO +200 DEG
 X: 0.000ms/C + 31.3ms/C
 SETUP 2 OVERLOAD

MAIN Y:
 X: 0.000ms/C

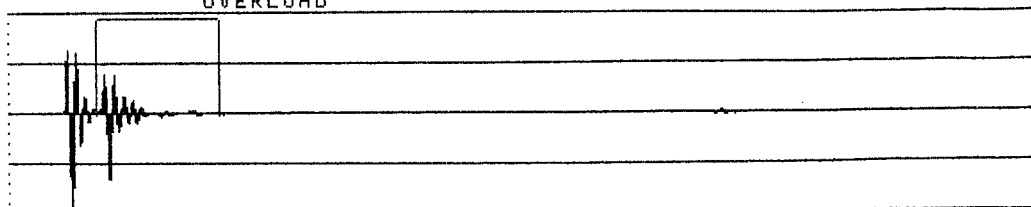
C=30.52 (0.5μs EXTERNAL SAMPLING RATE)

PLATE J_{B1} - INNER SCANNING CIRCLE

PRE-MEASUREMENT SETTINGS

#1 TIME CH.A REAL INPUT MAIN Y: 18.6E-9U
 Y: 12.0U X: 0.000ms/C + 31.3ms/C
 OVERLOAD

- REAL PART



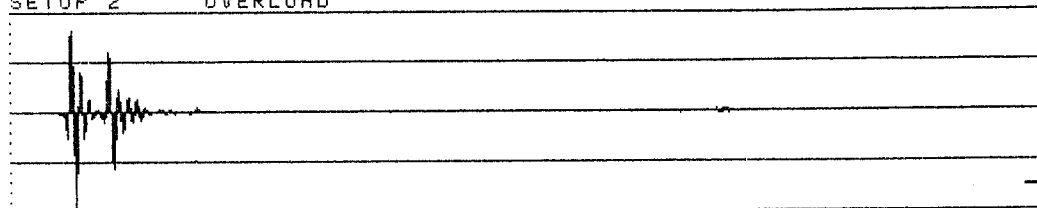
SETUP 2

MEASUREMENT: DUAL SPECTRUM AVERAGING
 TRIGGER: FREE RUN
 DELAY: CH.A+B: 0.000ms/C
 AVERAGING: EXP 10 OVERLAP: 0%
 FREQ SPAN: 25.6kHz*C ΔF: 32Hz*C T: 31.3ms/C AT: 15.3us/C
 CENTER FREQ: BASEBAND C = EXT SAMPL FREQ/65536Hz
 WEIGHT CH.A: TRANSIENT SHIFT: 2.670ms/C LENGTH: 3.738ms/C
 WEIGHT CH.B: TRANSIENT SHIFT: 21.163ms/C LENGTH: 1.129ms/C
 CH.A: 10V + 3Hz DIR FILT: 25.6kHz 250mV/PA
 CH.B: 10V + 3Hz DIR FILT: 25.6kHz 250mV/PA
 GENERATOR: DISABLED
 SPECIAL PARAMETER : #100: ZOOM KEY DEC VALUE: 1

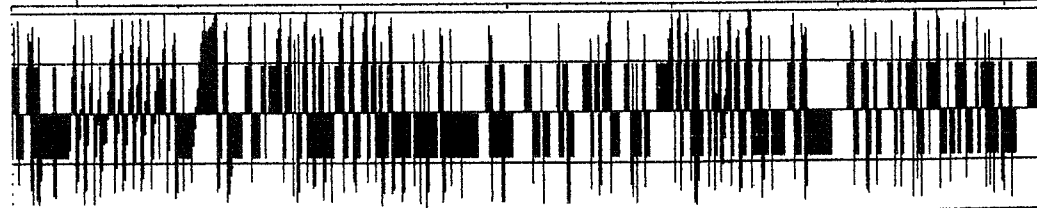
- SETTINGS

#1 TIME CH.A IMAG MAIN Y: -22.0mU
 Y: 12.0U X: 0.000ms/C + 31.3ms/C
 SETUP 2 OVERLOAD

- IMAGINARY PART



- PHASE

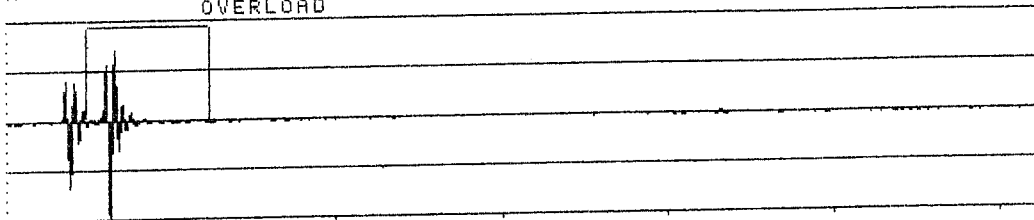


#1 TIME CH.A PHASE INPUT MAIN Y: -90.0DEG
 Y: -200 TO +200 DEG X: 0.000ms/C + 31.3ms/C
 SETUP 2 OVERLOAD

C=30.52 (0.5 μ s EXTERNAL SAMPLING RATE)

PLATE 1c - INNER SCANNING CIRCLE PRE-MEASUREMENT SETTINGS

M1 TIME CH.A REAL INPUT MAIN Y: 46.6E-9U
 Y: 16.2U X: 0.000ms/C + 31.3ms/C
 X: 0.000ms/C OVERLOAD - REAL PART

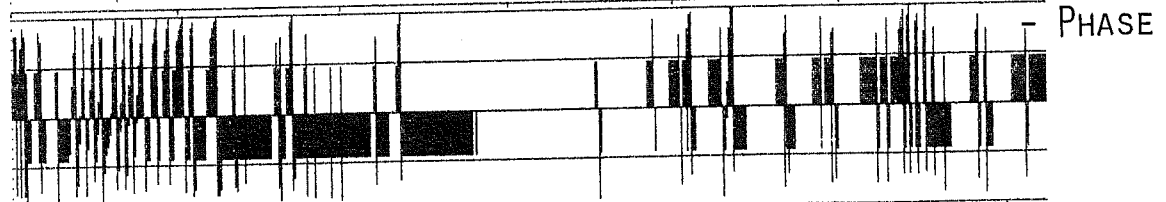
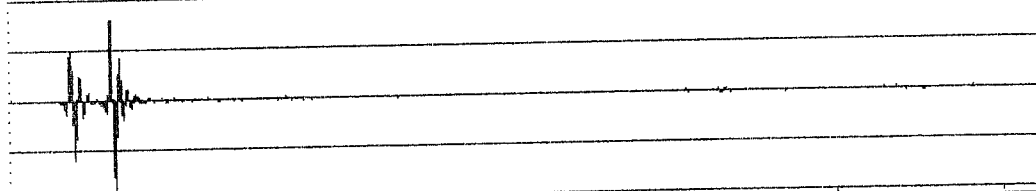


SETUP 3
 MEASUREMENT: DUAL SPECTRUM AVERAGING
 TRIGGER: FREE RUN
 DELAY: CH.A+B: 0.000ms/C
 AVERAGING: EXP 10 OVERLAP: 0% - SETTINGS

FREQ SPAN: 25.6kHz* C ΔF : 32Hz* C T: 31.3ms/ C AT: 15.3us/ C
 CENTER FREQ: BASEBAND C = EXT SAMPL FREQ/65536Hz
 WEIGHT CH.A: TRANSIENT SHIFT: 2.395ms/ C LENGTH: 3.738ms/ C
 WEIGHT CH.B: TRANSIENT SHIFT: 20.889ms/ C LENGTH: 1.129ms/ C

CH.A: 10V + 3Hz DIR FILT: 25.6kHz 100mV/PA
 CH.B: 10V + 3Hz DIR FILT: 25.6kHz 100mV/PA
 GENERATOR: DISABLED
 SPECIAL PARAMETER : #100: ZOOM KEY DEC VALUE: 1

M1 TIME CH.A IMAG MAIN Y: 73.3mU
 Y: 17.5U X: 0.000ms/C + 31.3ms/C
 X: 0.000ms/C OVERLOAD - IMAGINARY PART



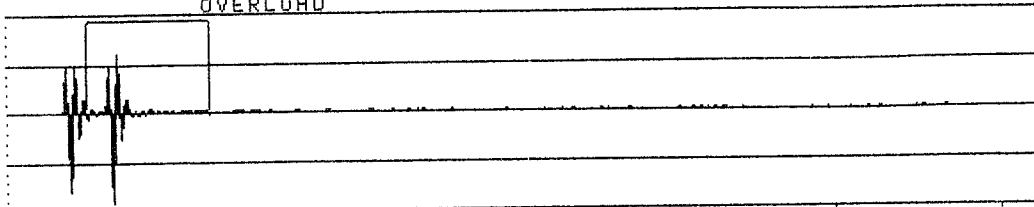
M1 TIME CH.A PHASE INPUT MAIN Y: 90.0DEG
 Y: -200 TO +200 DEG X: 0.000ms/C + 31.3ms/C
 X: 0.000ms/C OVERLOAD

C=30.52 (0.5 μ s EXTERNAL SAMPLING RATE)

PLATE 1c₁ - INNER SCANNING CIRCLE

PRE-MEASUREMENT SETTINGS

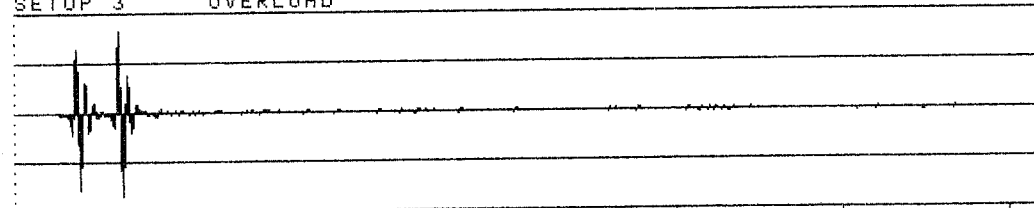
W1 TIME CH.A REAL INPUT MAIN Y: 46.6E-9U - REAL PART
 Y: 13.0U X: 0.000ms/C + 31.3ms/C
 OVERLOAD



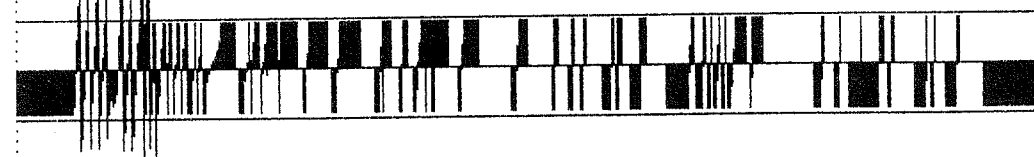
SETUP 3

MEASUREMENT: DUAL SPECTRUM AVERAGING - SETTINGS
 TRIGGER: FREE RUN
 DELAY: CH.A→B: 0.000ms/C
 AVERAGING: EXP 10 OVERLAP: 0%
 FREQ SPAN: 25.6kHz*C ΔF: 32Hz*C T: 31.3ms/C ΔT: 15.3μs/C
 CENTER FREQ: BASEBAND C = EXT SAMPL FREQ/65536Hz
 WEIGHT CH.A: TRANSIENT SHIFT: 2.395ms/C LENGTH: 3.738ms/C
 WEIGHT CH.B: TRANSIENT SHIFT: 20.889ms/C LENGTH: 1.129ms/C
 CH.A: 10V + 3Hz DIR FILT: 25.6kHz 100mV/PA
 CH.B: 10V + 3Hz DIR FILT: 25.6kHz 100mV/PA
 GENERATOR: DISABLED
 SPECIAL PARAMETER : #100: ZOOM KEY DEC VALUE: 1

W1 TIME CH.A IMAG INPUT MAIN Y: -48.8mU - IMAGINARY PART
 Y: 13.0U X: 0.000ms/C + 31.3ms/C
 OVERLOAD



SETUP 3 OVERLOAD - PHASE



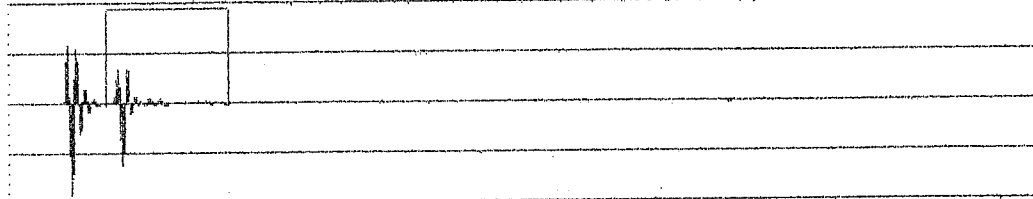
W1 TIME CH.A PHASE MAIN Y: -90.0DEG
 Y: -200 TO +200 DEG X: 0.000ms/C + 31.3ms/C
 OVERLOAD

C=30.52 (0.5μs EXTERNAL SAMPLING RATE)

PLATE 1D - INNER SCANNING CIRCLE PRE-MEASUREMENT SETTINGS

CH1 TIME CH.A REAL INPUT DELT Y: 18.8E-9U
 Y: 12.00 X: 0.000ms/C + 31.3ms/C
 X: 0.000ms/C OVERLOAD

- REAL PART



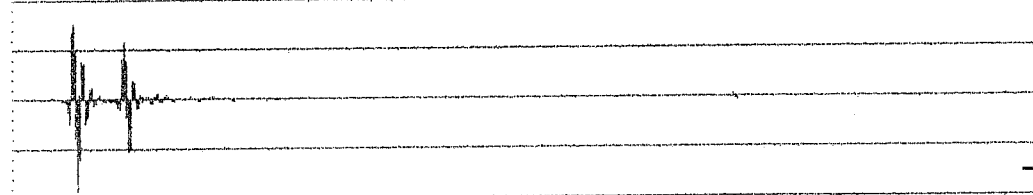
SETUP 1

MEASUREMENT: DUAL SPECTRUM AVERAGING
 TRIGGER: FREE RUN
 DELAY: CH.A+B: 0.000ms/C
 AVERAGING: EXP 10 OVERLAP: 0%
 FREQ SPAN: 25.6kHz*0 ΔF: 32Hz*0 T: 31.3ms/C ΔT: 15.3us/C
 CENTER FREQ: BASEBAND C = EXT SAMPL FREQ/65536Hz
 WEIGHT CH.A: TRANSIENT SHIFT: 2.944ms/C LENGTH: 3.738ms/C
 WEIGHT CH.B: TRANSIENT SHIFT: 21.469ms/C LENGTH: 1.129ms/C
 CH.A: 10V + 3Hz DIR FILT: 25.6kHz 250mV/PA
 CH.B: 10V + 3Hz DIR FILT: 25.6kHz 250mV/PA
 GENERATOR: DISABLED
 SPECIAL PARAMETER #100: ZOOM KEY DEC VALUE: 1

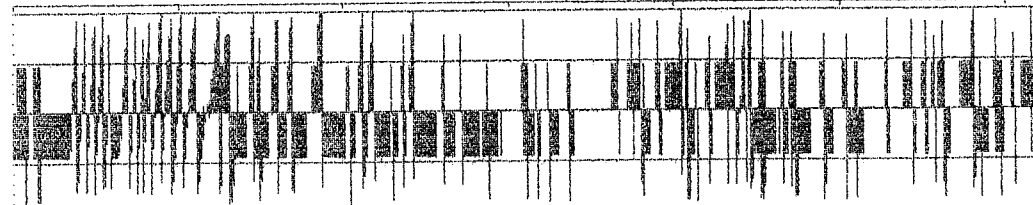
- SETTINGS

CH1 TIME CH.A IMAG INPUT MAIN Y: -2.44mU
 Y: 11.50 X: 0.000ms/C + 31.3ms/C
 X: 0.000ms/C OVERLOAD

- IMAGINARY PART



- PHASE



CH1 TIME CH.A PHASE MAIN Y:
 Y: -200 TO +200 DEG X: 0.000ms/C
 X: 0.000ms/C + 31.3ms/C
 SETUP 1 OVERLOAD

C=30.52 (0.5μs EXTERNAL SAMPLING RATE)

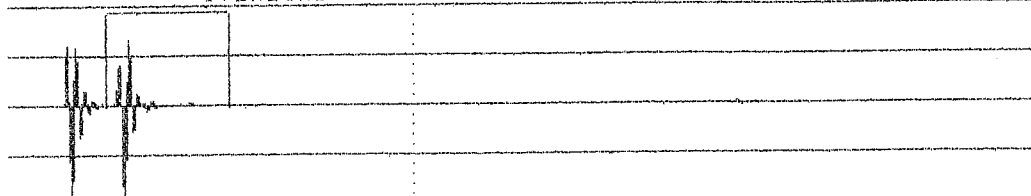
PLATE 1D₁ - INNER SCANNING CIRCLE

PRE-MEASUREMENT SETTINGS

```

001 TIME CH.A      REAL      INPUT      DELT Y: 18.6E-9U
Y: 11.5U          X: 12.207ms/C
X: 0.000ms/C + 31.3ms/C  ΔX: 26.367ms/C
OVERLOAD
    
```

- REAL PART



SETUP 1

```

MEASUREMENT: DUAL SPECTRUM AVERAGING
TRIGGER: FREE RUN
DELAY: CH.A+B: 0.000ms/C
AVERAGING: EXP 10 OVERLAP: 0%

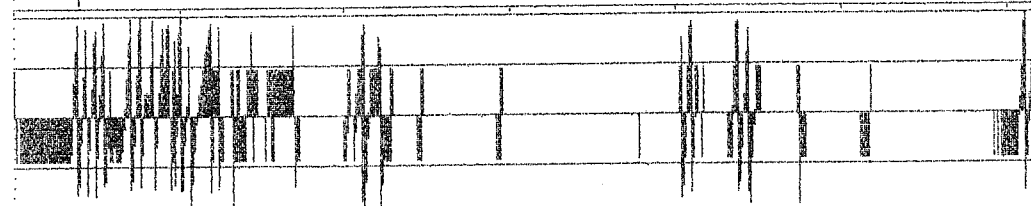
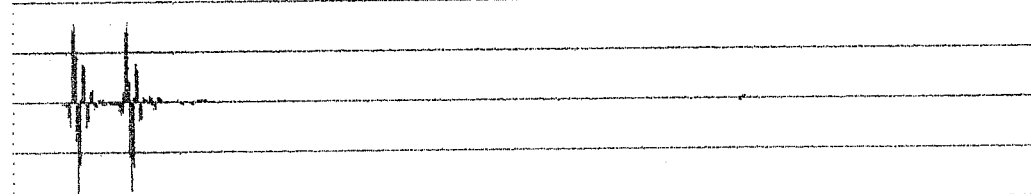
FREQ SPAN: 25.6kHz#C ΔF: 32Hz#C T: 31.3ms/C ΔT: 15.3us/C
CENTER FREQ: BASEBAND C = EXT SAMPL FREQ/65536Hz
WEIGHT CH.A: TRANSIENT SHIFT: 2.944ms/C LENGTH: 3.738ms/C
WEIGHT CH.B: TRANSIENT SHIFT: 21.469ms/C LENGTH: 1.129ms/C
CH.A: 10V + 3Hz DIR FILT: 25.6kHz 250mV/PA
CH.B: 10V + 3Hz DIR FILT: 25.6kHz 250mV/PA
GENERATOR: DISABLED
SPECIAL PARAMETER #100: ZOOM KEY DEC VALUE: 1
    
```

- SETTINGS

```

001 TIME CH.A      IMAG      INPUT      MAIN Y: 2.44mU
Y: 11.5U          X: 0.000ms/C
X: 0.000ms/C + 31.3ms/C
SETUP 1 OVERLOAD
    
```

- IMAGINARY PART



- PHASE

```

001 TIME CH.A      PHASE      MAIN Y:
Y: -200 TO +200 DEG X: 0.000ms/C
X: 0.000ms/C + 31.3ms/C
SETUP 1 OVERLOAD
    
```

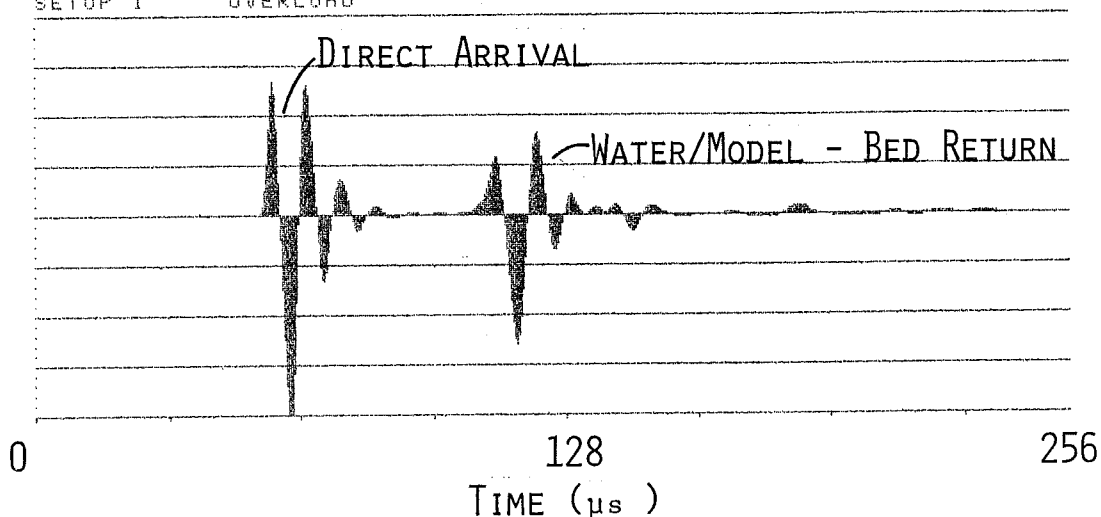
C=30.52 (0.5μs EXTERNAL SAMPLING RATE)

PLATES 2A TO 2D₁

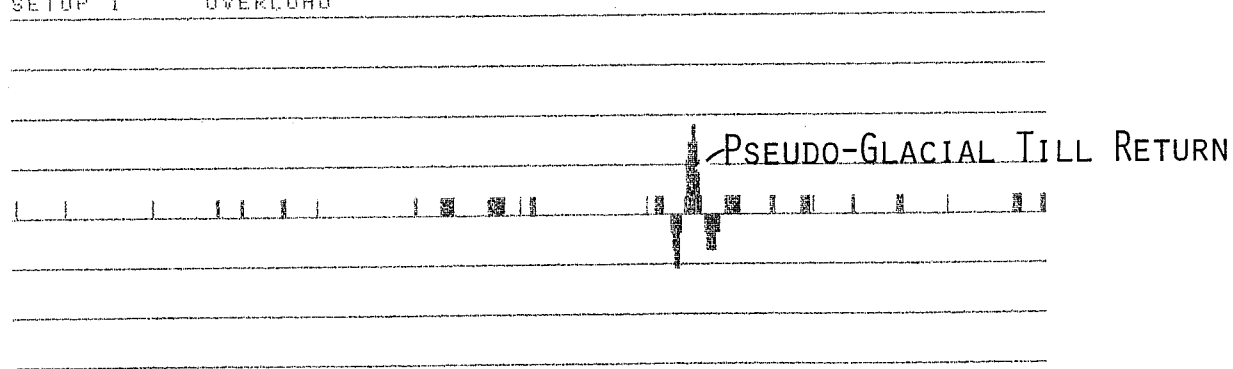
TIME HISTORY DATA

PLATE 2A - OUTER SCANNING CIRCLE
TIME HISTORY DATA

01 TIME CH.B REAL INPUT MAIN Y: 18.6E-9U
Y: 10.6U X: 0.000ms/C + 7.81ms/C
X: 0.000ms/C
SETUP 1 OVERLOAD



01 TIME CH.A REAL INPUT MAIN Y: 18.6E-9U
Y: 969mU X: 17.028ms/C + 7.81ms/C
X: 0.000ms/C
SETUP 1 OVERLOAD



558

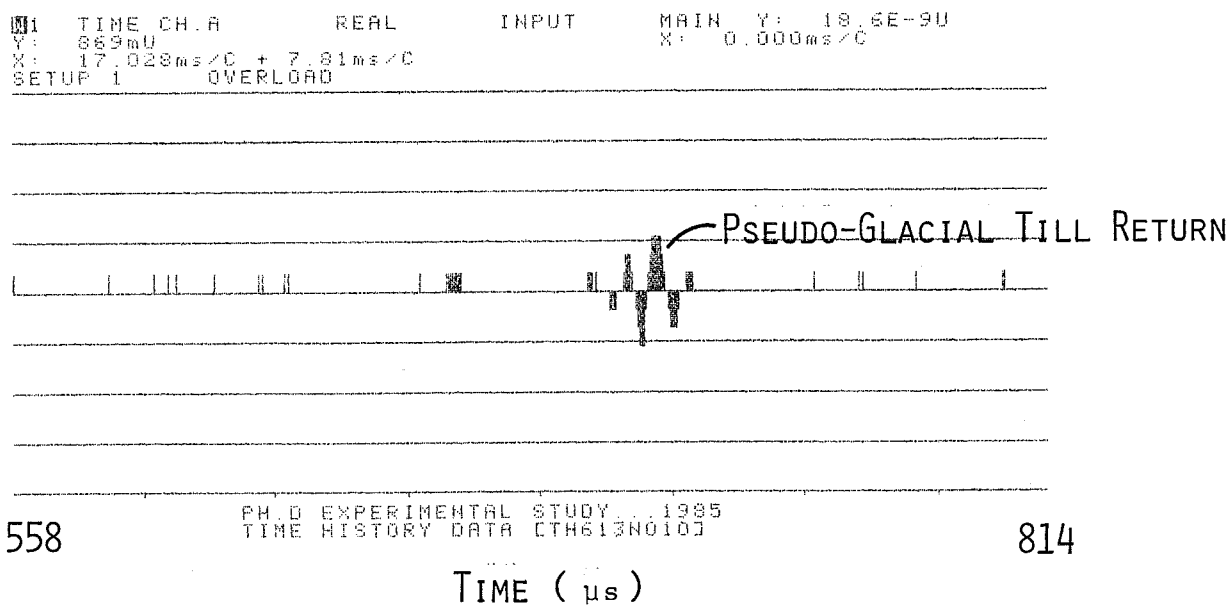
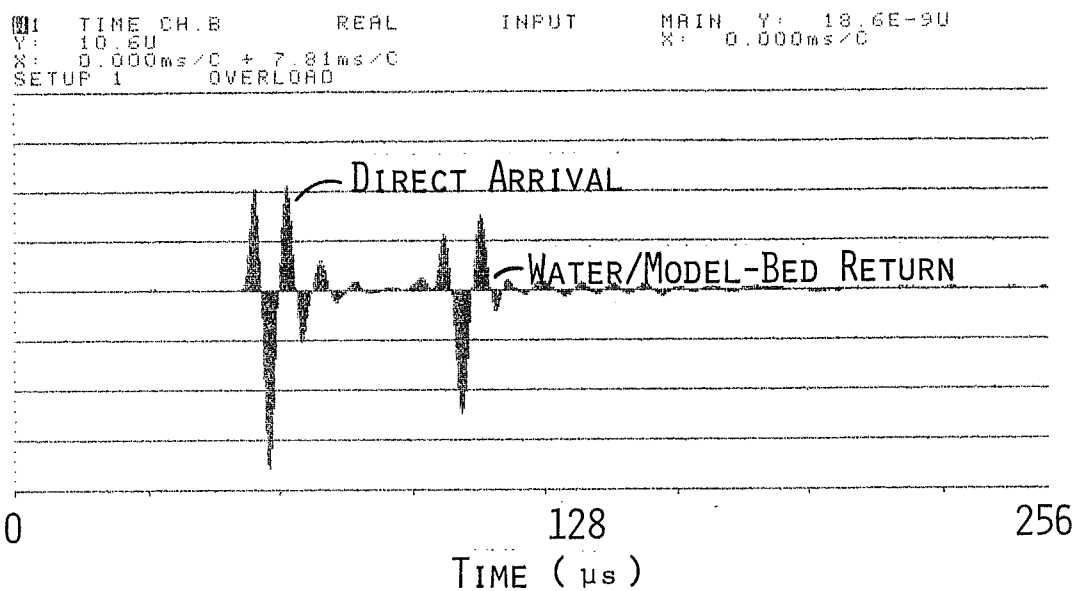
PH.D EXPERIMENTAL STUDY, 1985
TIME HISTORY DATA CTH613N0021

814

TIME (μs)

C=30.52 (0.5μs EXTERNAL SAMPLING
RATE)

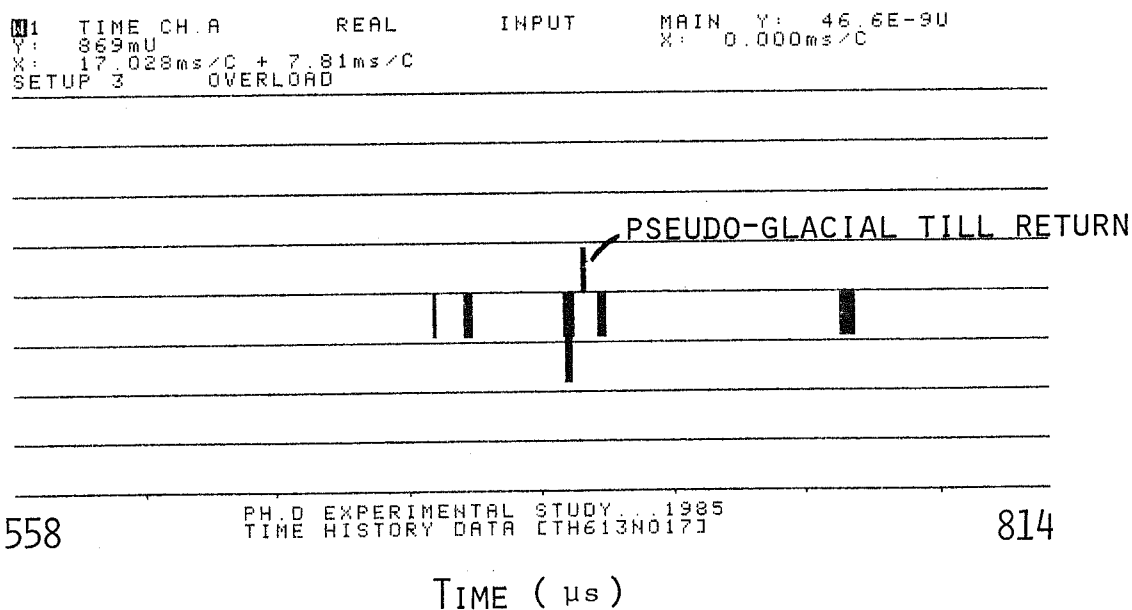
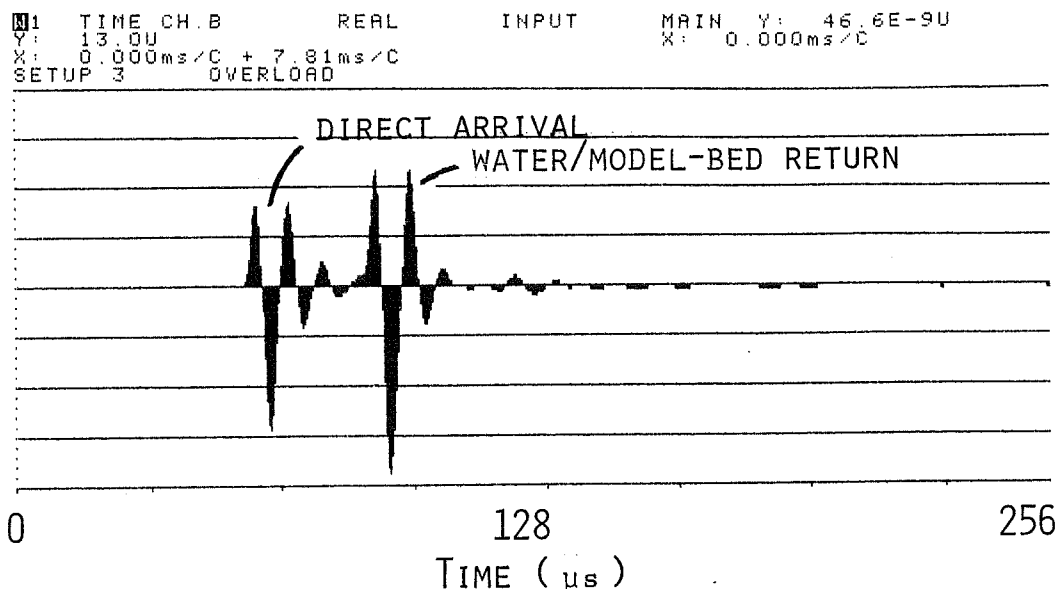
PLATE 2A₁ - OUTER SCANNING CIRCLE
TIME HISTORY DATA



PH.D EXPERIMENTAL STUDY ... 1985
TIME HISTORY DATA CTH613N010J

C=30.52 (0.5μs EXTERNAL SAMPLING RATE)

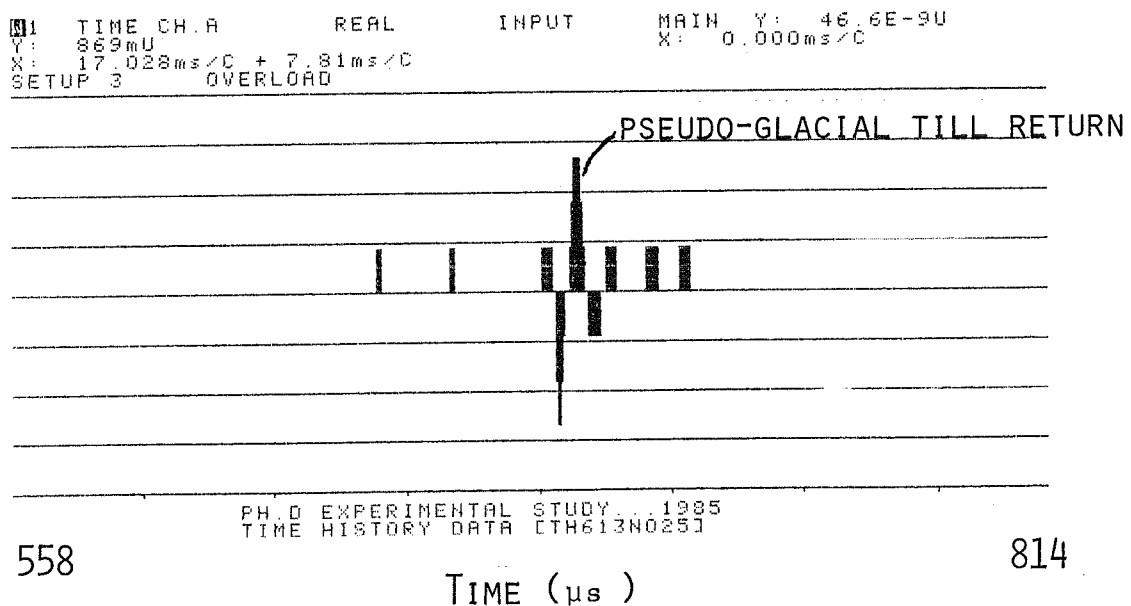
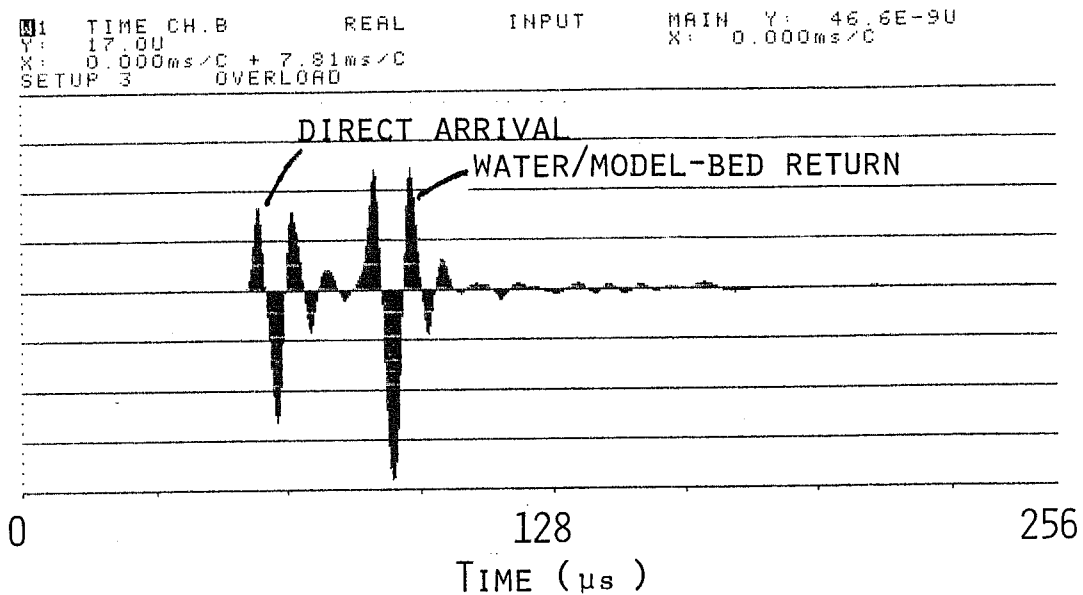
PLATE 2B - OUTER SCANNING CIRCLE
TIME HISTORY DATA



PH.D EXPERIMENTAL STUDY... 1985
TIME HISTORY DATA [TH613N017]

C=30.52 (0.5μs EXTERNAL SAMPLING RATE)

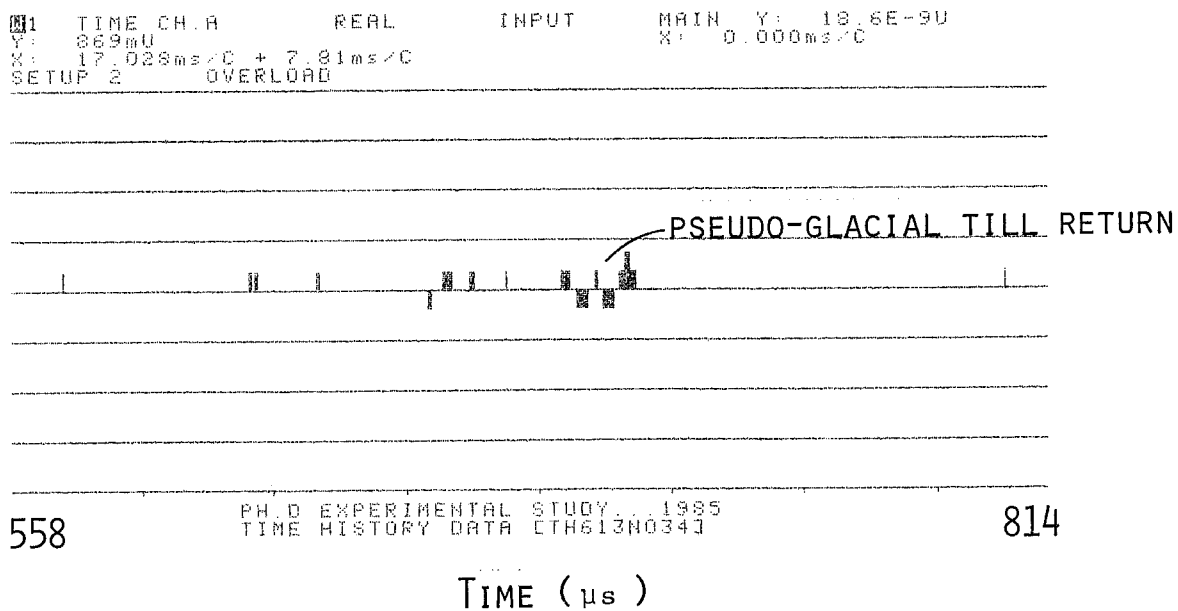
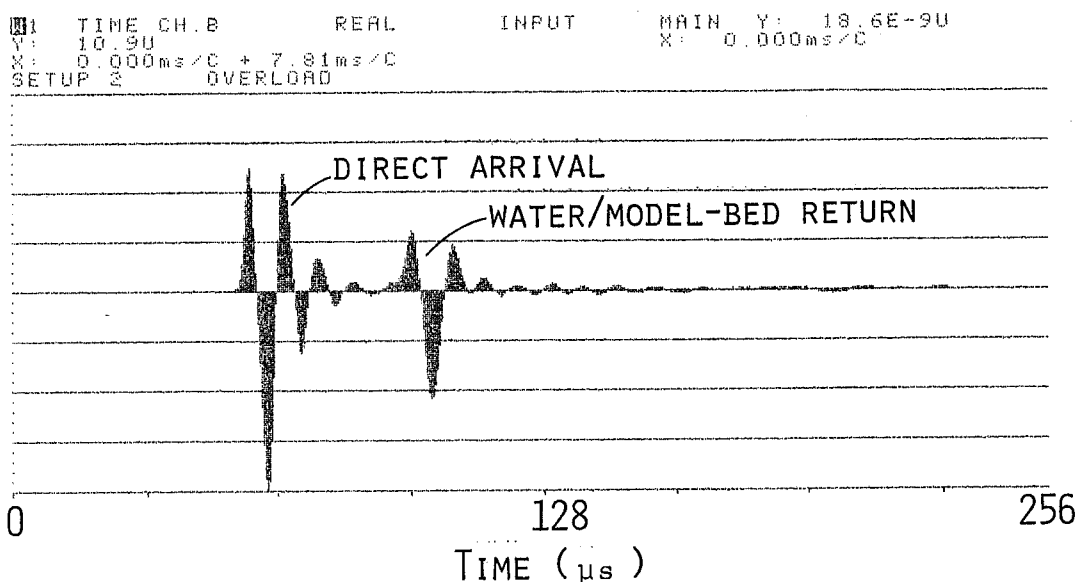
PLATE 2B₁ - OUTER SCANNING CIRCLE
 TIME HISTORY DATA



PH.D EXPERIMENTAL STUDY... 1985
 TIME HISTORY DATA [TH613N025]

C=30.52 (0.5 μs EXTERNAL SAMPLING RATE)

PLATE 2C - OUTER SCANNING CIRCLE
TIME HISTORY DATA



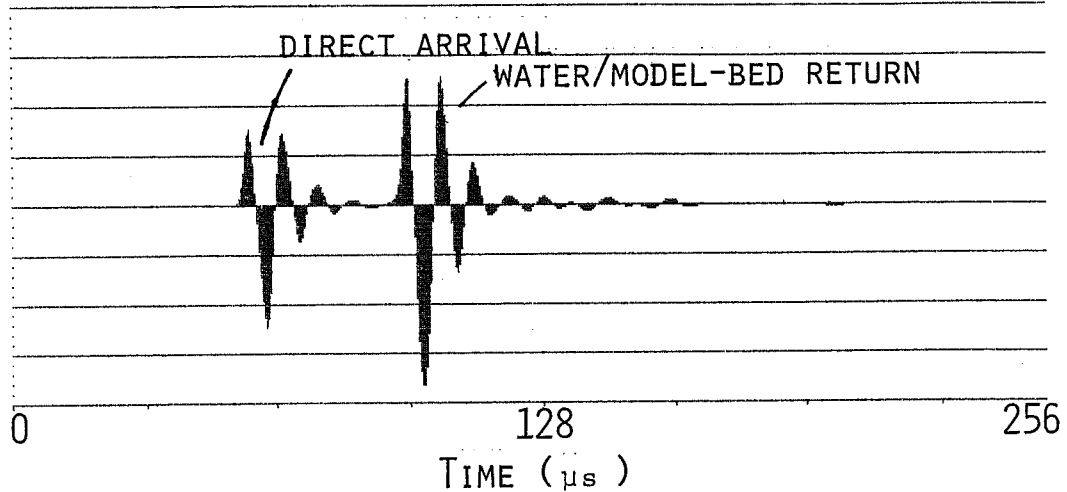
PH.D EXPERIMENTAL STUDY... 1985
TIME HISTORY DATA ETH613N034J

C=30.52 (0.5 μs EXTERNAL SAMPLING RATE)

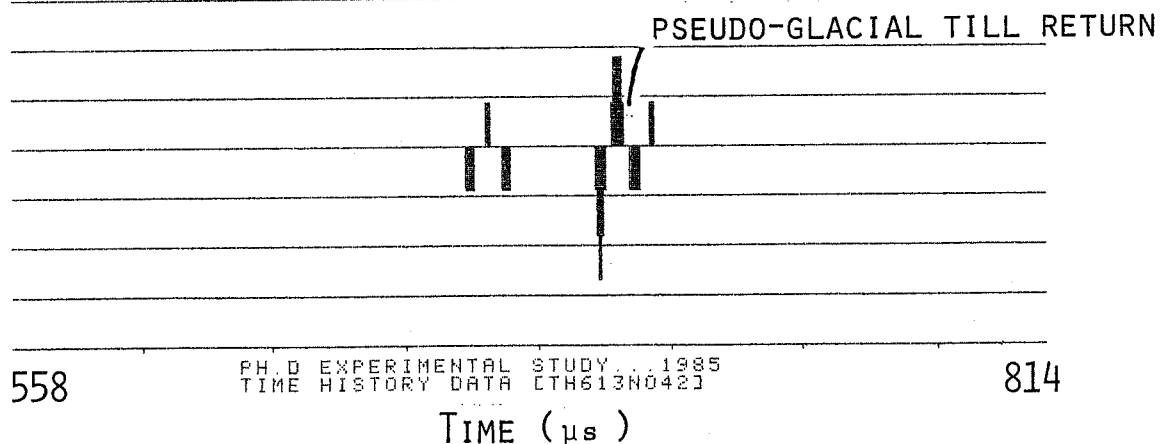
PLATE 2C₁ - OUTER SCANNING CIRCLE

TIME HISTORY DATA

1 TIME CH.B REAL INPUT MAIN Y: 46.6E-9U
 Y: 18.0U X: 0.000ms/C + 7.81ms/C
 SETUP 3 OVERLOAD X: 0.000ms/C

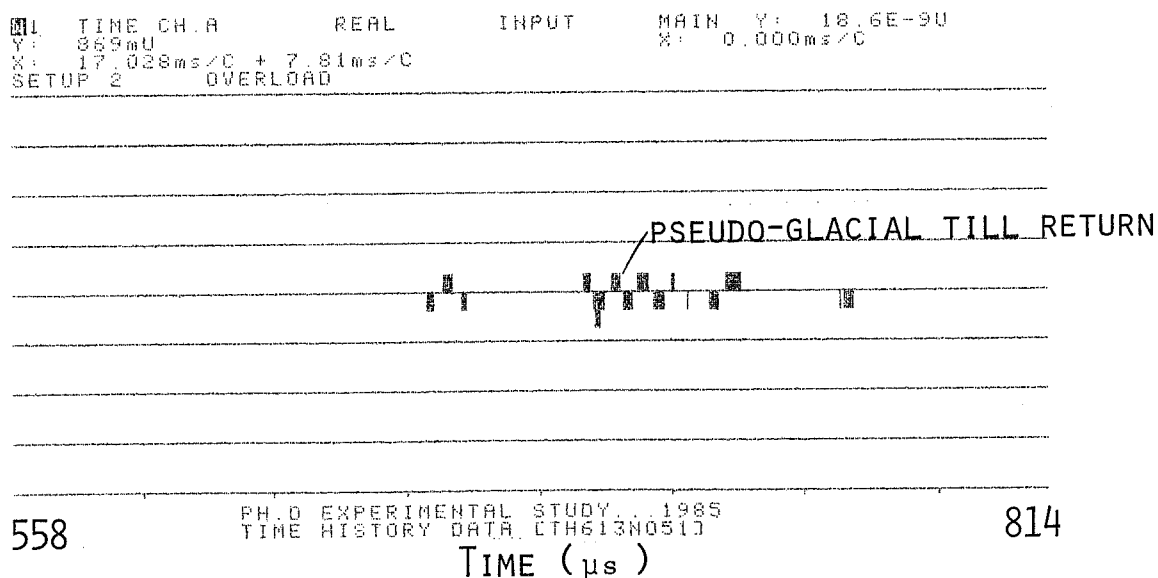
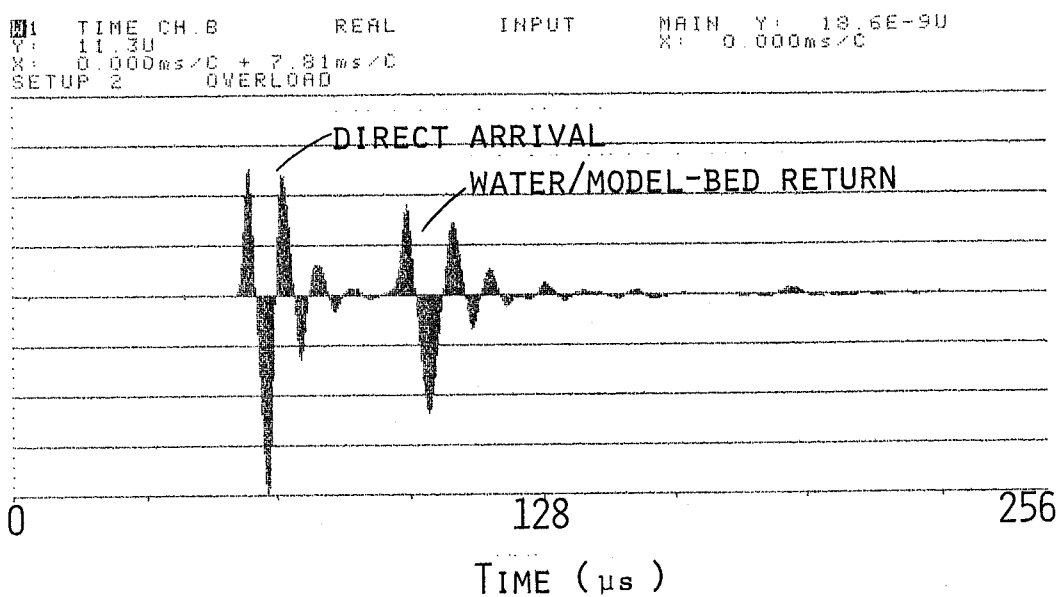


1 TIME CH.A REAL INPUT MAIN Y: 46.6E-9U
 Y: 869mU X: 17.028ms/C + 7.81ms/C
 SETUP 3 OVERLOAD X: 0.000ms/C



C=30.52 (0.5 μ s EXTERNAL SAMPLING
 RATE)

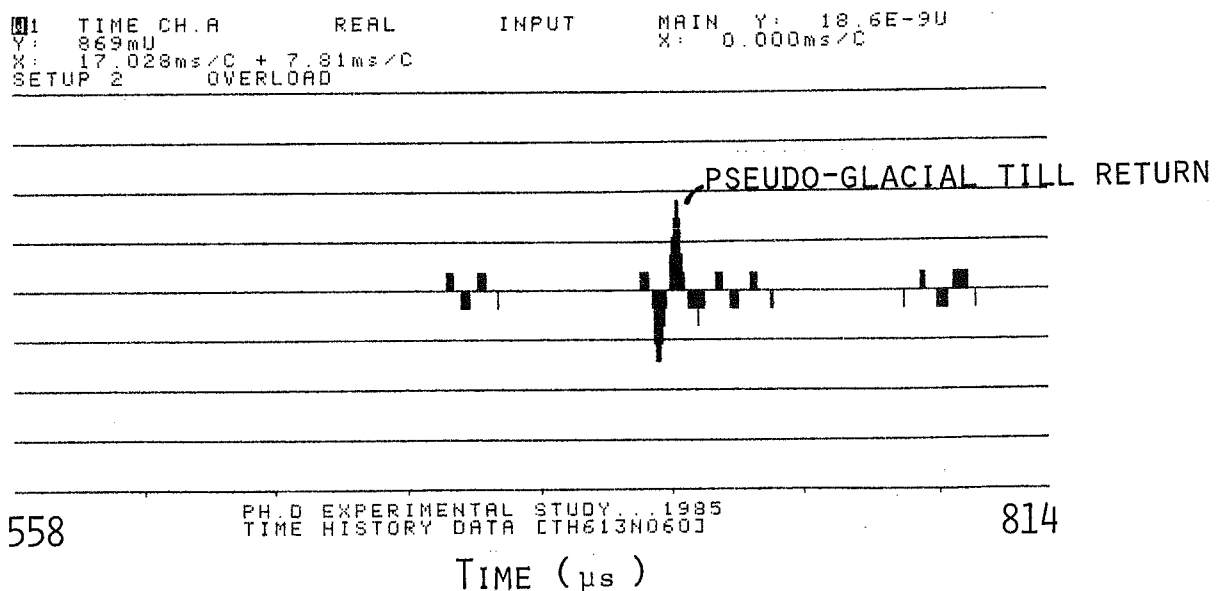
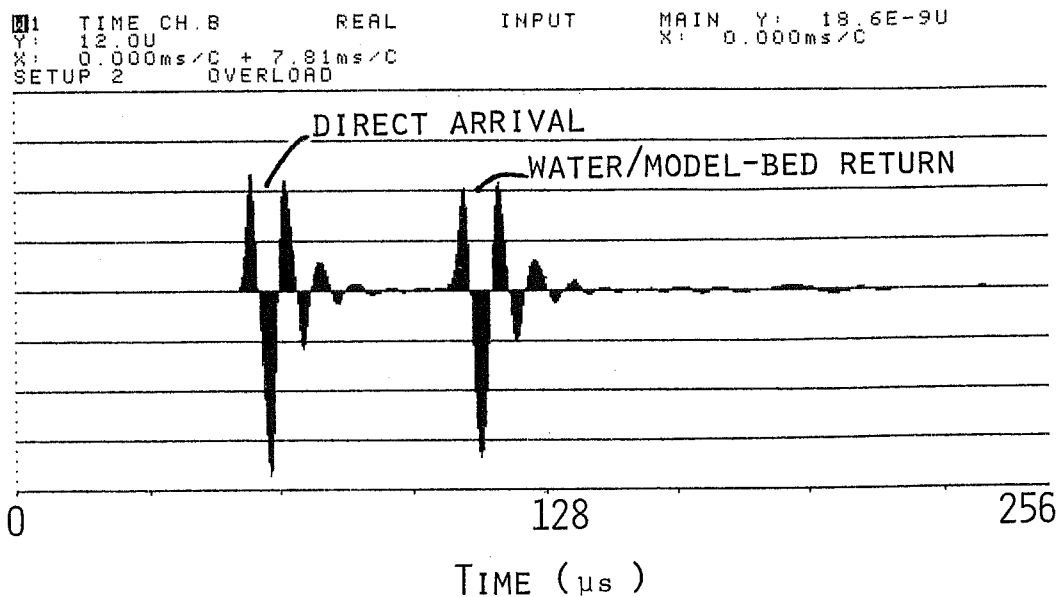
PLATE 2D - OUTER SCANNING CIRCLE
TIME HISTORY DATA



PH.D EXPERIMENTAL STUDY, 1985
TIME HISTORY DATA, ETH613N0513

C=30.52 (0.5 μ s EXTERNAL SAMPLING RATE)

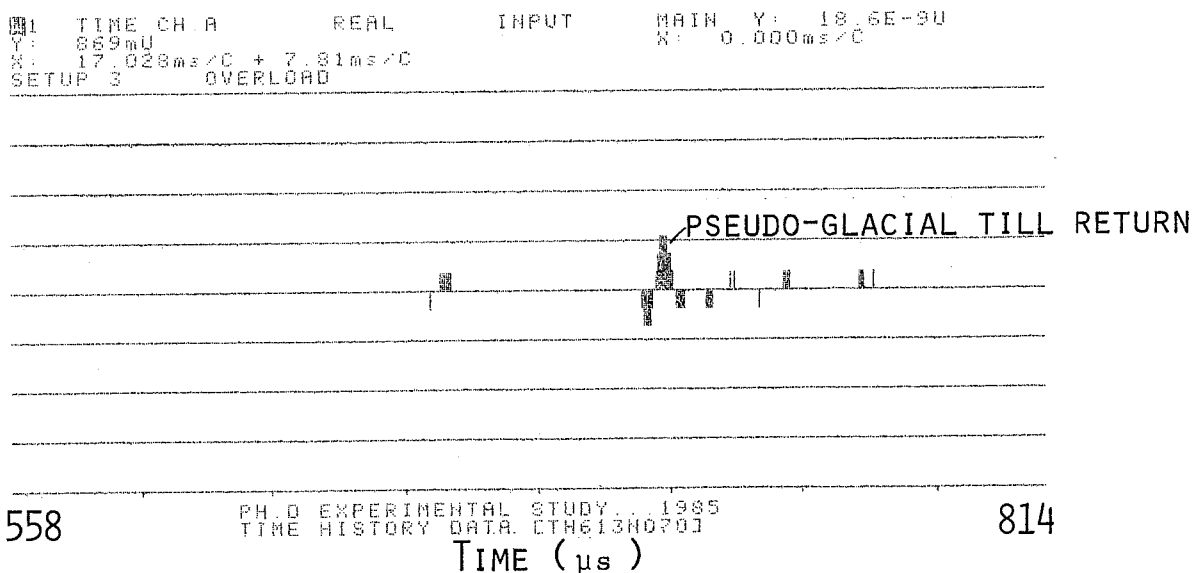
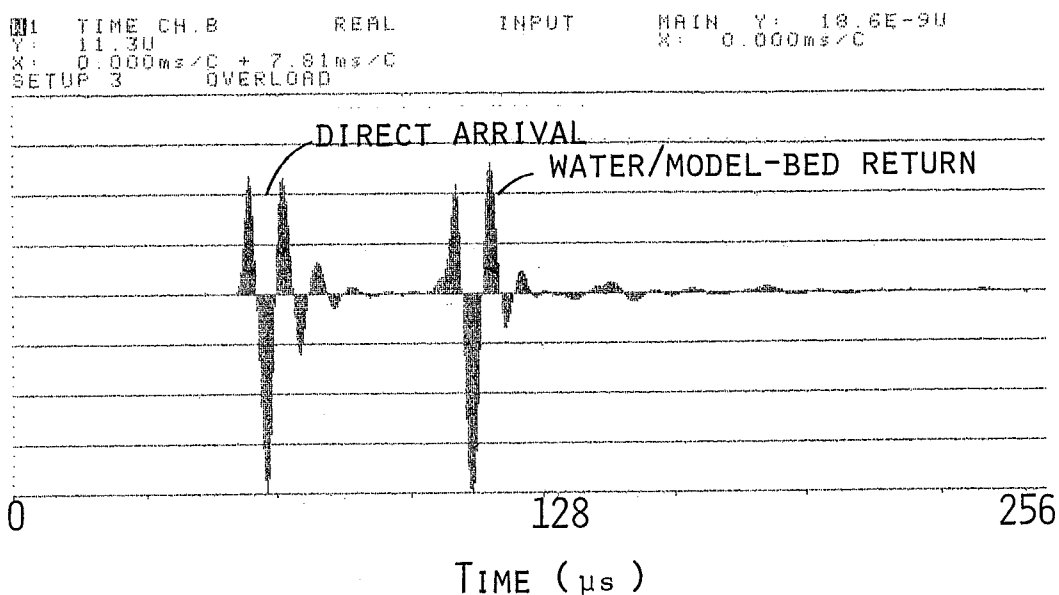
PLATE 2D₁ - OUTER SCANNING CIRCLE
TIME HISTORY DATA



PH.D EXPERIMENTAL STUDY... 1985
TIME HISTORY DATA LTH613N060J

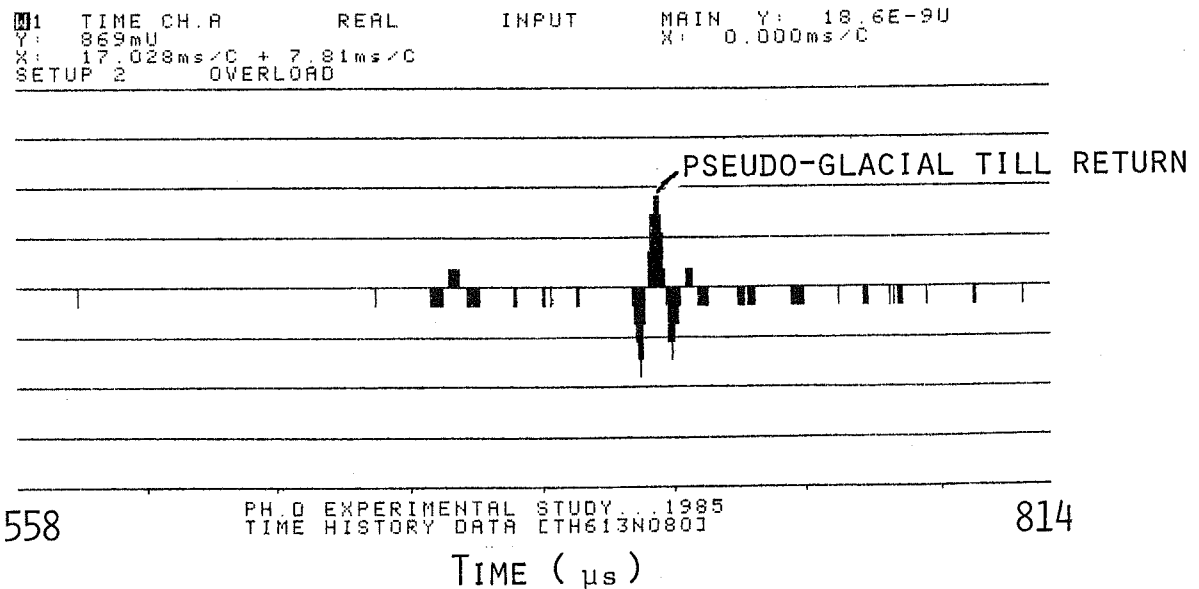
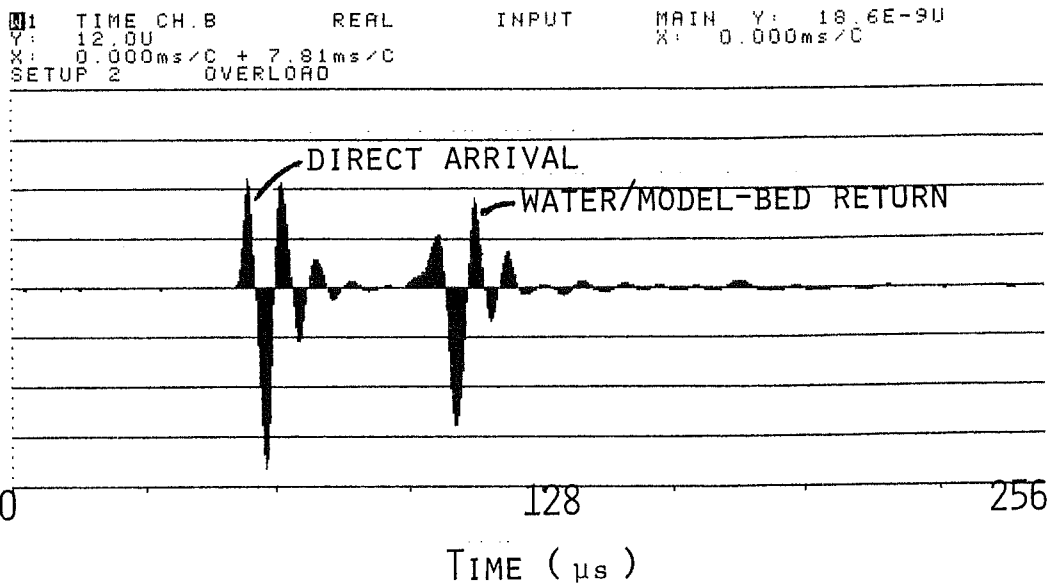
C=30.52 (0.5 μs EXTERNAL SAMPLING RATE)

PLATE 2A - INNER SCANNING CIRCLE TIME HISTORY DATA



C=30.52 (0.5 μs EXTERNAL SAMPLING RATE)

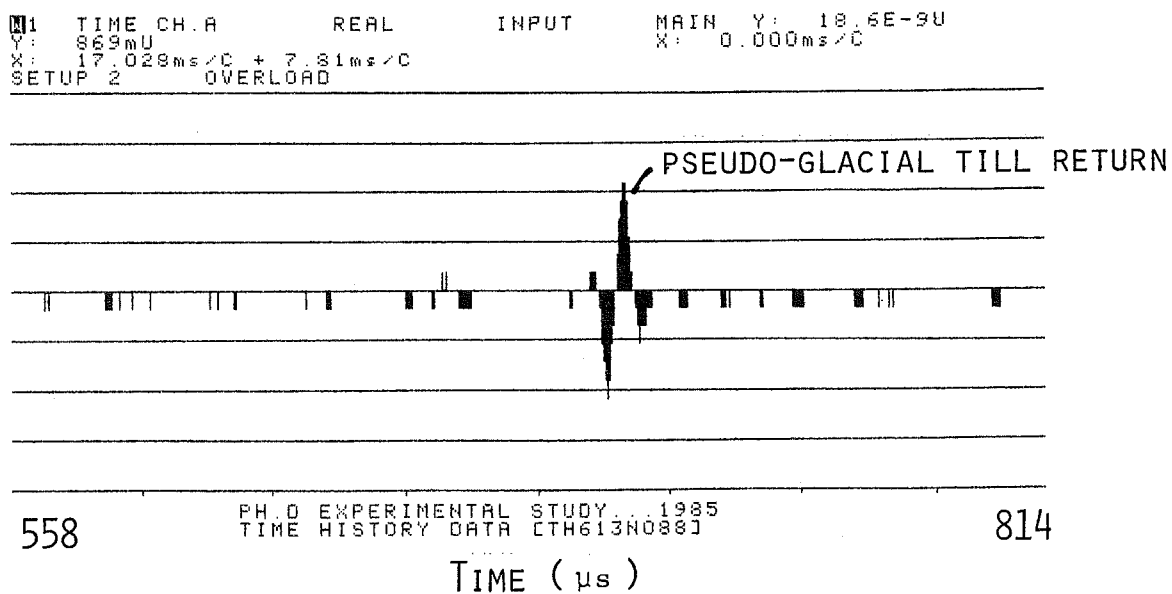
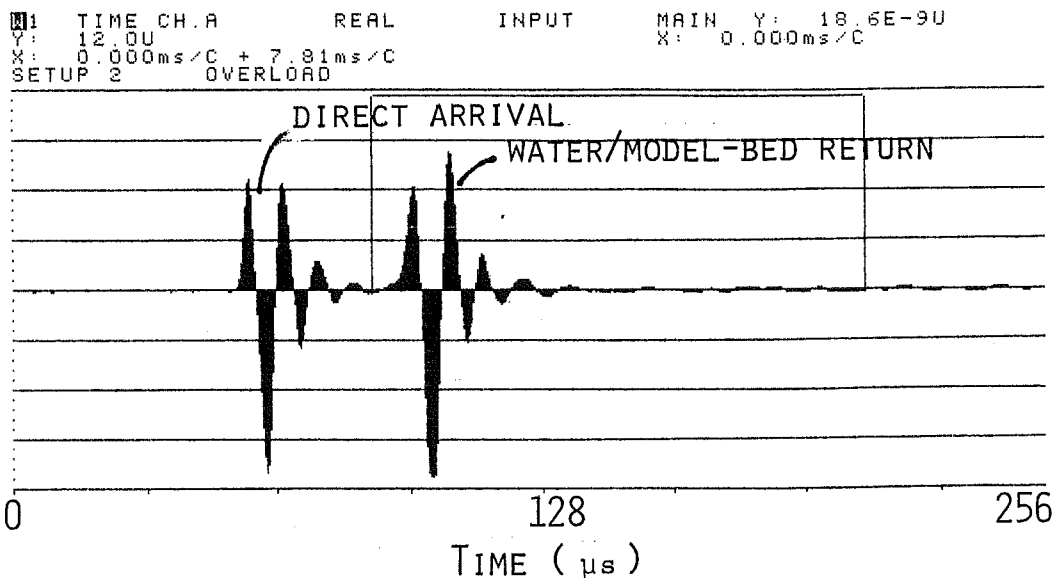
PLATE 2A₁ - INNER SCANNING CIRCLE
 TIME HISTORY DATA



PH.D EXPERIMENTAL STUDY... 1985
 TIME HISTORY DATA CTH613N0801

C=30.52 (0.5µs EXTERNAL SAMPLING RATE)

PLATE 2B₁- INNER SCANNING CIRCLE
TIME HISTORY DATA



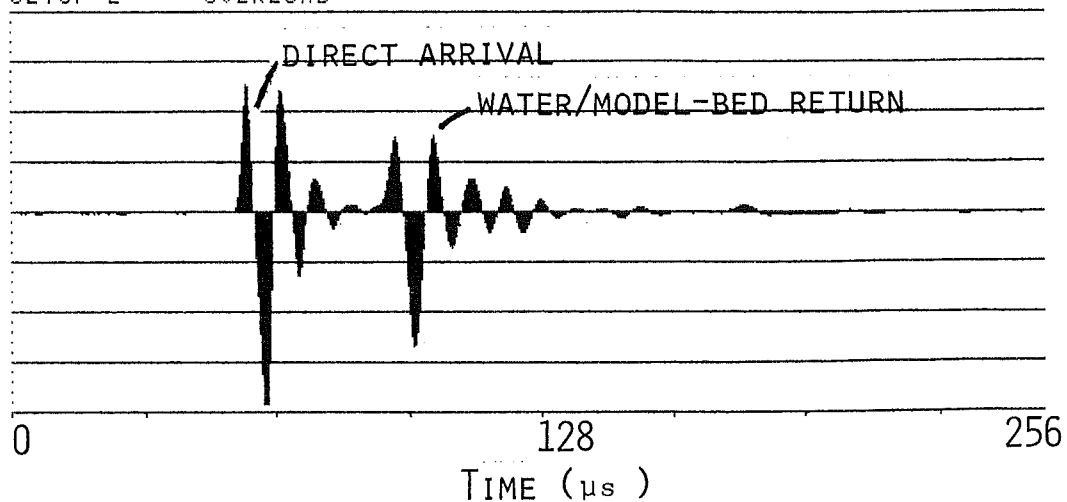
PH.D EXPERIMENTAL STUDY... 1985
TIME HISTORY DATA [TH613N088]

C=30.52 (0.5 µs EXTERNAL SAMPLING RATE)

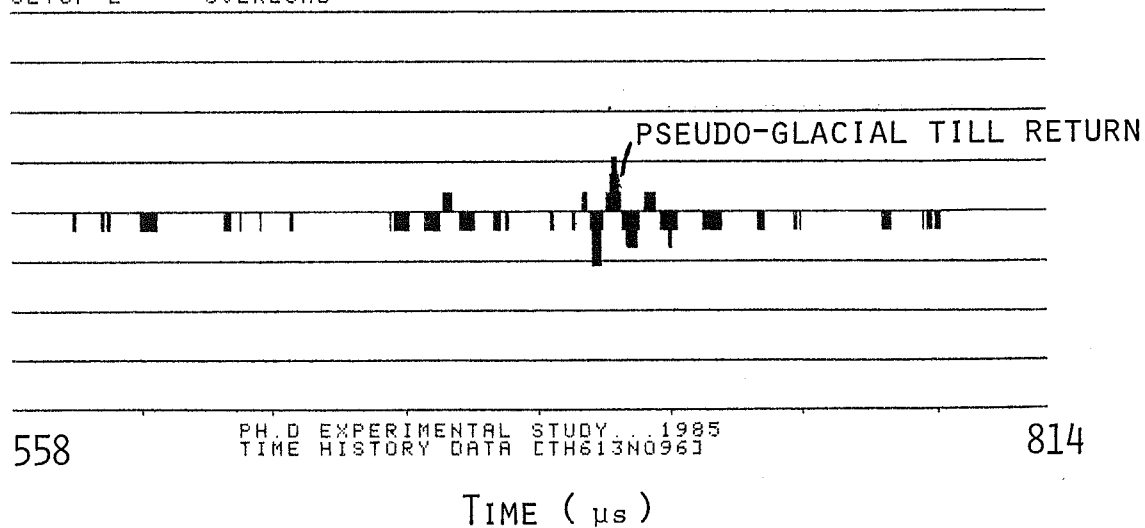
PLATE 2B₁ - INNER SCANNING CIRCLE

TIME HISTORY DATA

01 TIME CH.B REAL INPUT MAIN Y: 18.6E-9U
 Y: 12.0U X: 0.000ms/C + 7.81ms/C
 SETUP 2 OVERLOAD X: 0.000ms/C



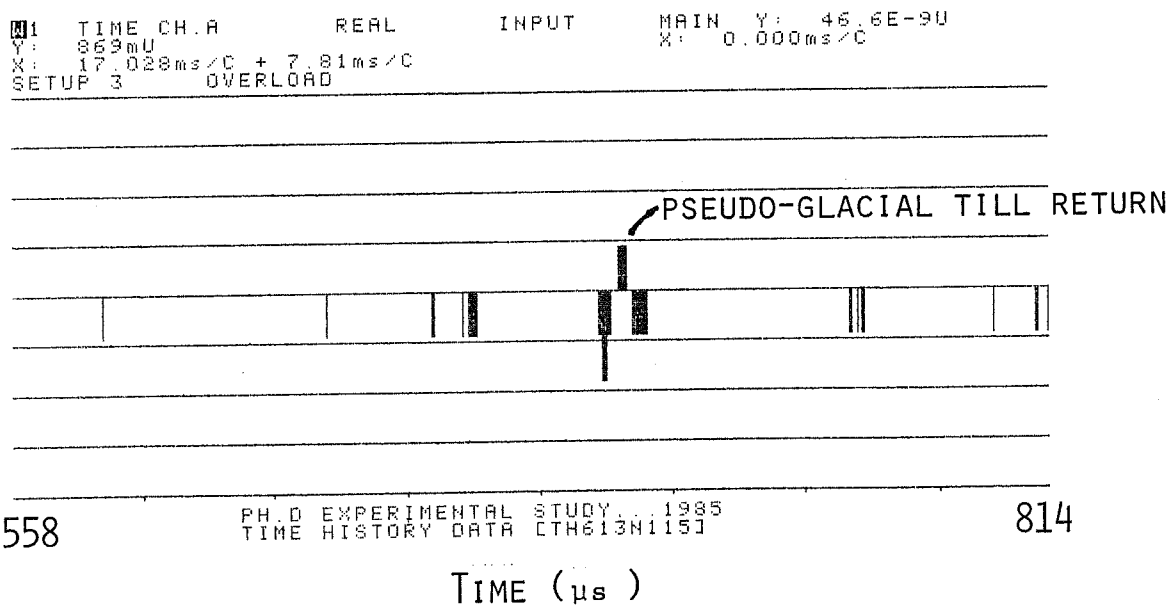
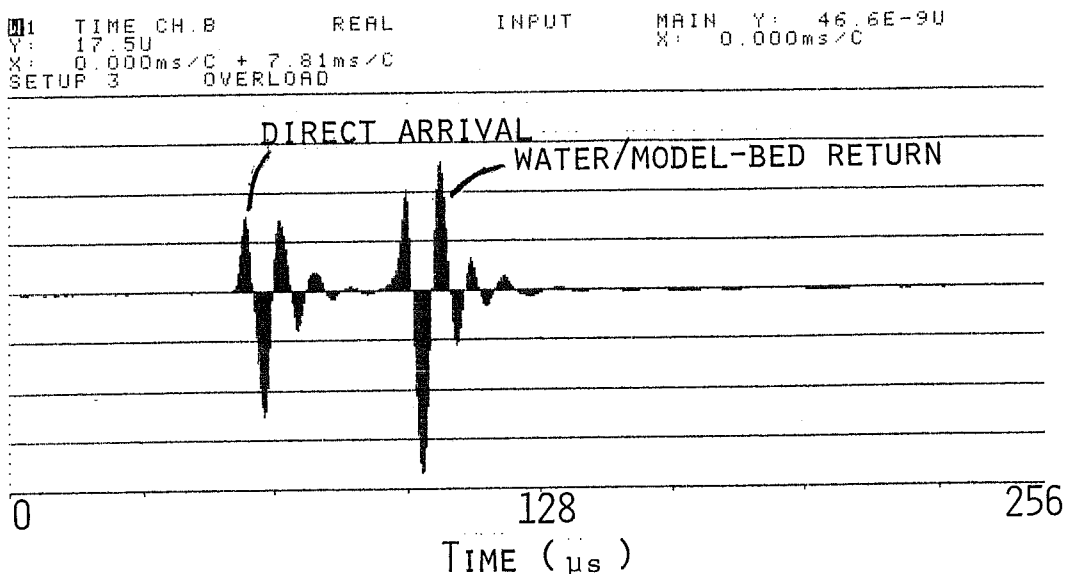
01 TIME CH.A REAL INPUT MAIN Y: 18.6E-9U
 Y: 863mU X: 17.028ms/C + 7.81ms/C
 SETUP 2 OVERLOAD X: 0.000ms/C



PH.D EXPERIMENTAL STUDY... 1985
 TIME HISTORY DATA [TH613N096]

C=30.52 (0.5μs EXTERNAL SAMPLING RATE)

PLATE 2c - INNER SCANNING CIRCLE TIME HISTORY DATA



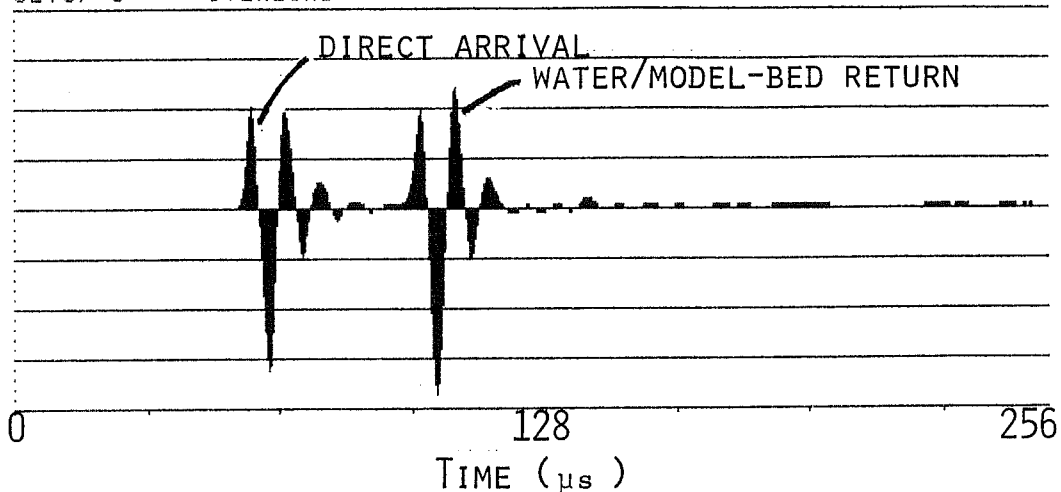
PH.D EXPERIMENTAL STUDY... 1985
TIME HISTORY DATA [TH613N115]

C=30.52 (0.5μs EXTERNAL SAMPLING RATE)

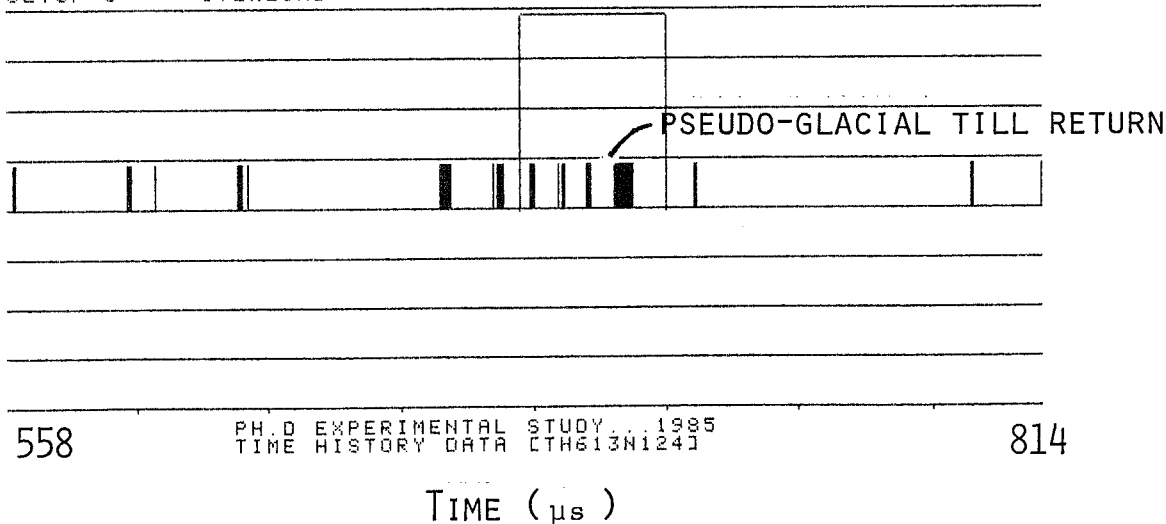
PLATE 2C₁ - INNER SCANNING CIRCLE

TIME HISTORY DATA

01 TIME CH.B REAL INPUT MAIN Y: 46.6E-9U
 Y: 13.0U X: 0.000ms/C + 7.81ms/C
 SETUP 3 OVERLOAD



01 TIME CH.B REAL INPUT MAIN Y: 46.6E-9U
 Y: 869mU X: 17.028ms/C + 7.81ms/C
 SETUP 3 OVERLOAD



PH.D EXPERIMENTAL STUDY... 1985
 TIME HISTORY DATA [LTH613N124]

C=30.52 (0.5 μs EXTERNAL SAMPLING RATE)

PLATE 2D - INNER SCANNING CIRCLE
TIME HISTORY DATA

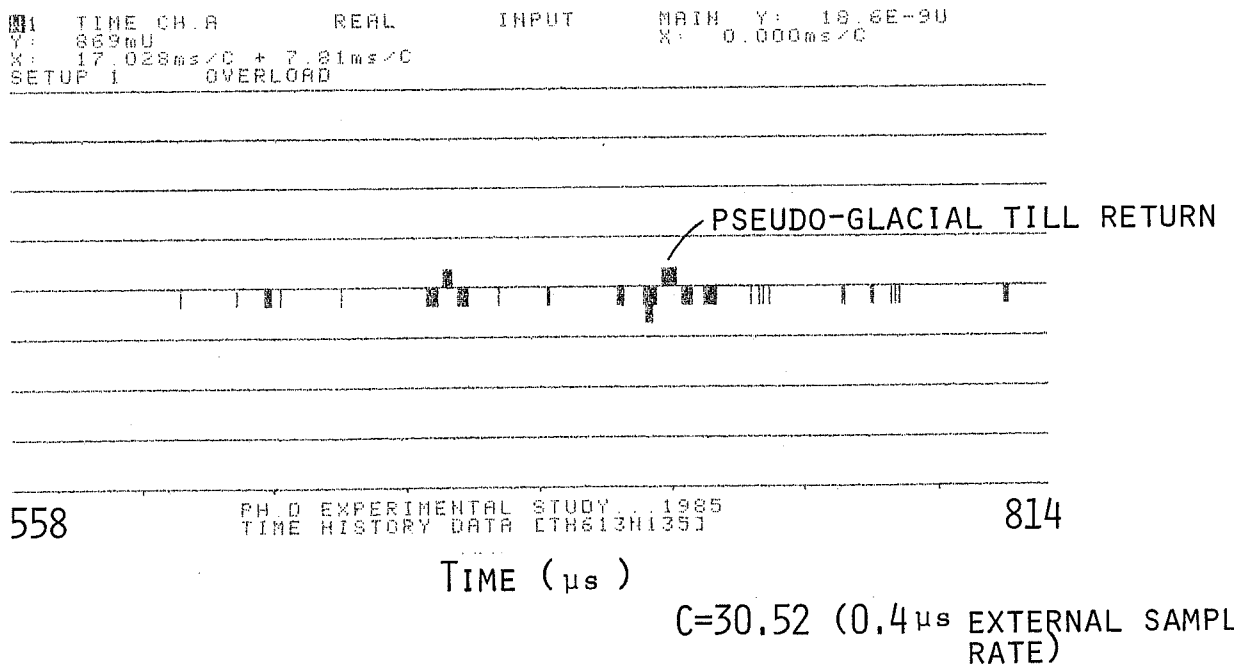
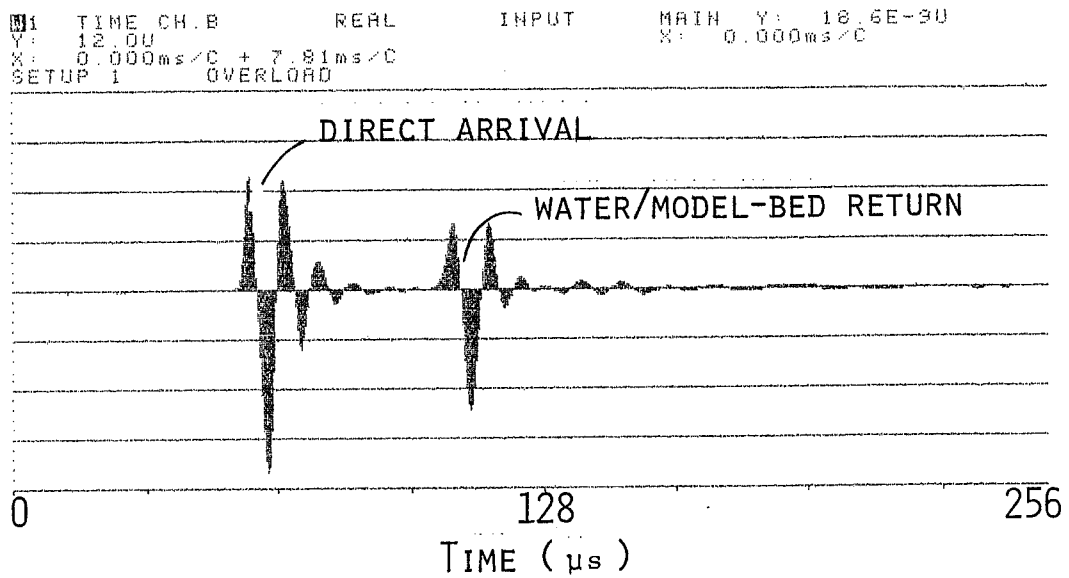
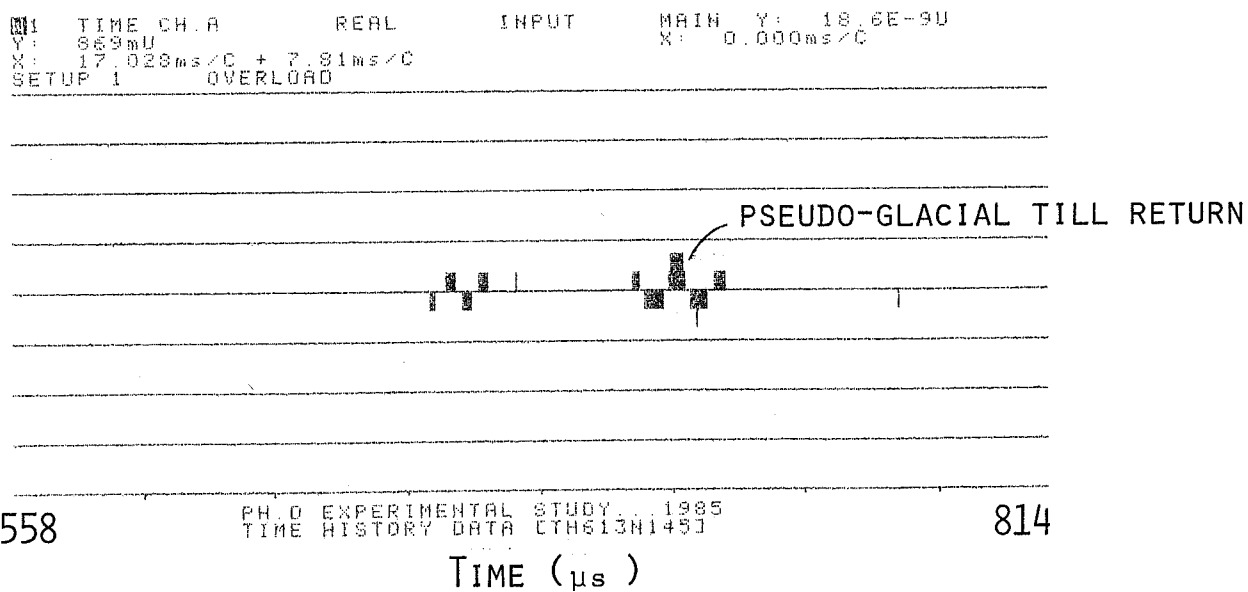
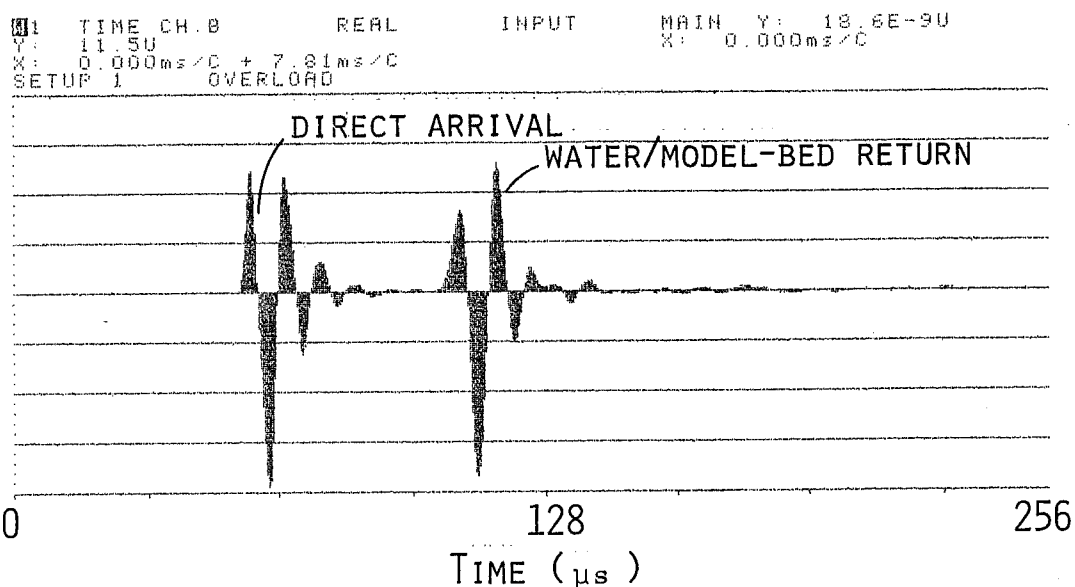


PLATE 2D₁ - INNER SCANNING CIRCLE
TIME HISTORY DATA

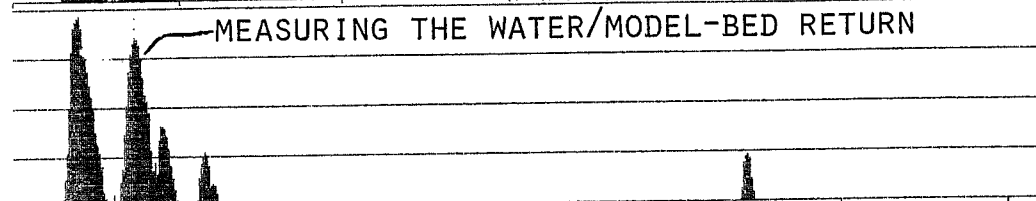
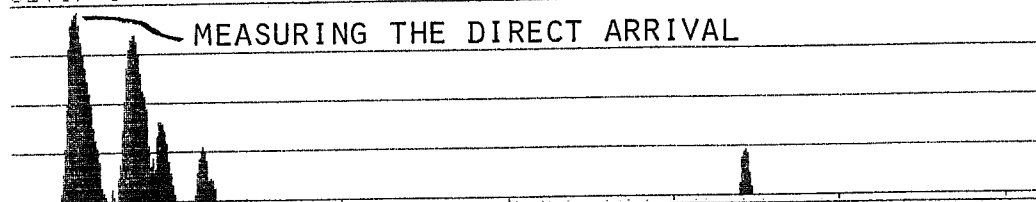


C=30.52 (0.5 μs EXTERNAL SAMPLING RATE)

PLATES 3A TO 3D₁
ENVELOPE OF THE TIME SIGNALS
(USING THE HILBERT TRANSFORM)

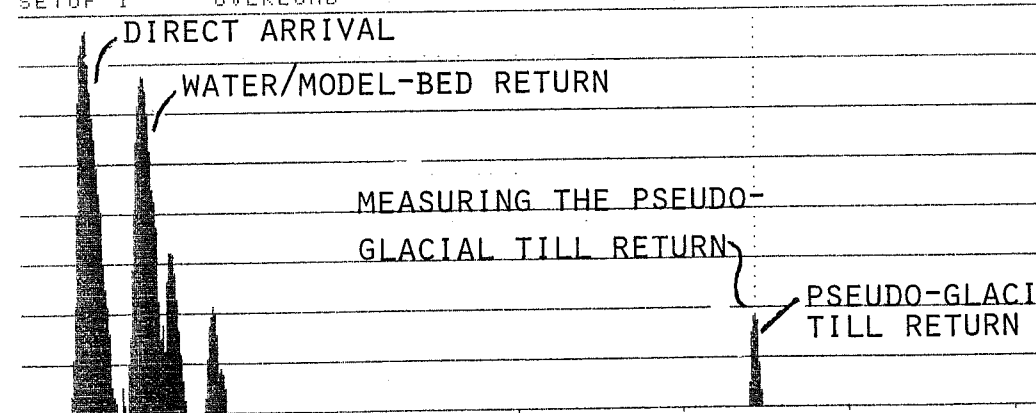
PLATE 3A - OUTER SCANNING CIRCLE ENVELOPE OF THE TIME SIGNALS (USING THE HILBERT TRANSFORM)

W1 TIME CH.A MAG Y: 143.0dB / 1.00uV 40dB X: 0.000ms/C + 31.3ms/C SETUP 1 OVERLOAD	MAIN Y: 141.4dB X: 1.953ms/C FLEX : 0.06396873
---------------------------------------------------------------------------------------------	------------------------------------------------------



W1 TIME CH.A MAG Y: 143.0dB / 1.00uV 40dB X: 0.000ms/C + 31.3ms/C SETUP 1 OVERLOAD	INPUT REF Y: 136.8dB X: 3.646ms/C ΔX: 1.693ms/C ΔY : -4.6dB
---------------------------------------------------------------------------------------------	----------------------------------------------------------------------

W1 TIME CH.A MAG Y: 143.0dB / 1.00uV 40dB X: 0.000ms/C + 31.3ms/C SETUP 1 OVERLOAD	INPUT REF Y: 112.2dB X: 22.186ms/C ΔX: 18.539ms/C ΔY : -24.6dB
---------------------------------------------------------------------------------------------	-------------------------------------------------------------------------



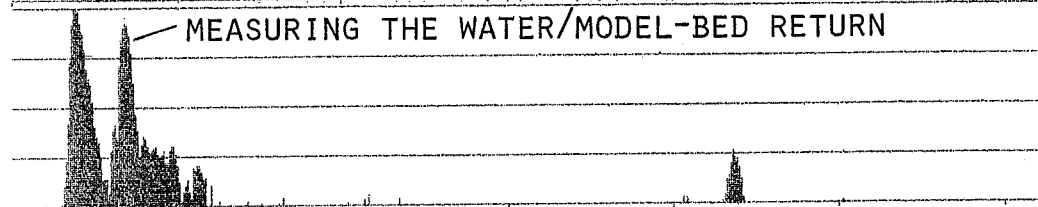
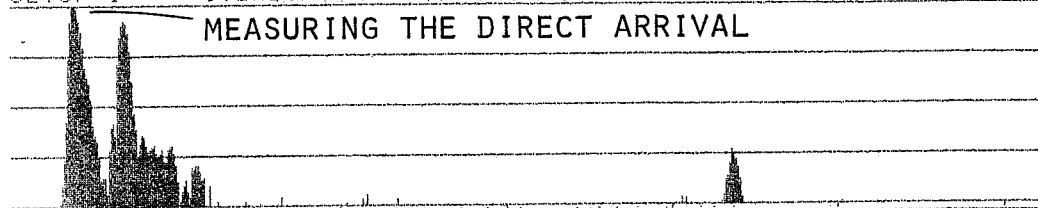
0 PH.D EXPERIMENTAL STUDY... 1985 TIME HISTORY DATA [TH613N002] 1000

TIME (μs)

C=30.52 (0.5μs EXTERNAL SAMPLING RATE)

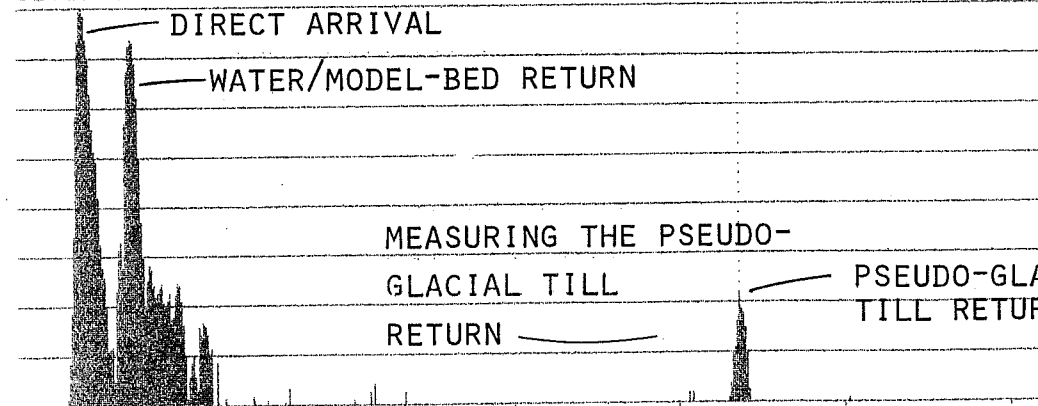
PLATE 3A₁ - OUTER SCANNING CIRCLE
 ENVELOPE OF THE TIME SIGNALS
 (USING THE HILBERT TRANSFORM)

W1 TIME CH.A MAG MAIN Y: 139.7dB
 Y: 139.7dB /1.00uV 40dB X: 1.907ms/C
 X: 0.000ms/C + 31.3ms/C FLEX: 0.06246946
 SETUP 1 OVERLOAD



W1 TIME CH.A MAG INPUT REF Y: 136.5dB
 Y: 139.7dB /1.00uV 40dB X: 3.387ms/C
 X: 0.000ms/C + 31.3ms/C ΔX: 1.480ms/C
 SETUP 1 OVERLOAD ΔY: -3.3dB

W1 TIME CH.A MAG INPUT REF Y: 110.6dB
 Y: 139.7dB /1.00uV 40dB X: 21.804ms/C
 X: 0.000ms/C + 31.3ms/C ΔX: 18.417ms/C
 SETUP 1 OVERLOAD ΔY: -25.9dB

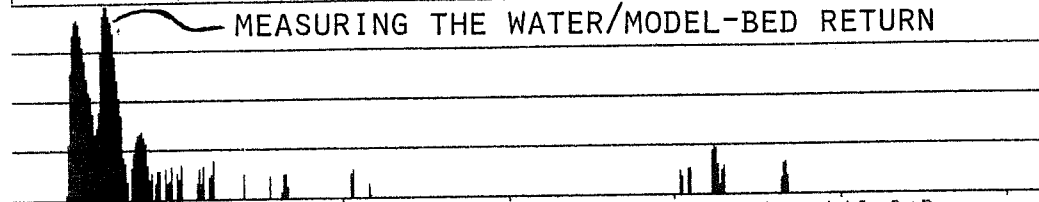
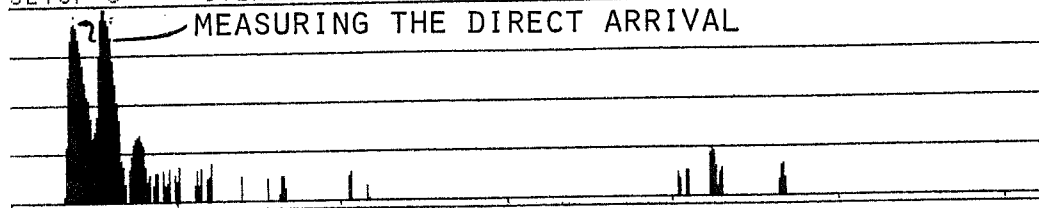


0 PH.D EXPERIMENTAL STUDY, 1985 TIME HISTORY DATA ETH613H0103 1000
 TIME (μs)

C=30.52 (0.5μs EXTERNAL SAMPLING RATE)

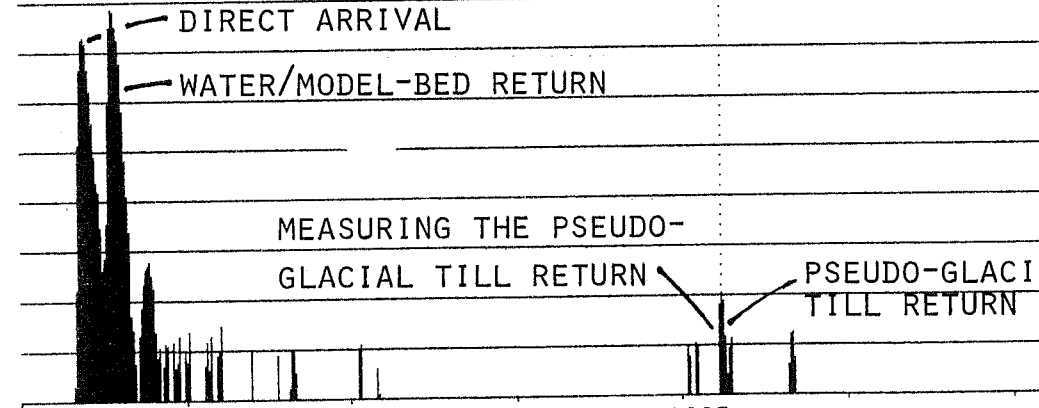
PLATE 3B - OUTER SCANNING CIRCLE
 ENVELOPE OF THE TIME SIGNALS
 (USING THE HILBERT TRANSFORM)

W1 TIME CH.A MAG MAIN Y: 139.5dB
 Y: 143.0dB / 1.00uV 40dB X: 1.892ms / C
 X: 0.000ms / C + 31.3ms / C FLEX : 0.06196971
 SETUP 3 OVERLOAD



W1 TIME CH.A MAG INPUT REF Y: 142.2dB
 Y: 143.0dB / 1.00uV 40dB X: 2.792ms / C
 X: 0.000ms / C + 31.3ms / C ΔX: 0.900ms / C
 SETUP 3 OVERLOAD ΔY : 2.7dB

W1 TIME CH.A MAG INPUT REF Y: 113.2dB
 Y: 143.0dB / 1.00uV 40dB X: 21.224ms / C
 X: 0.000ms / C + 31.3ms / C ΔX: 18.432ms / C
 SETUP 3 OVERLOAD ΔY : -29.0dB



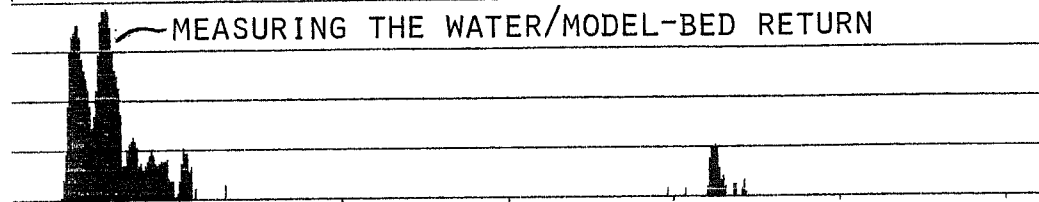
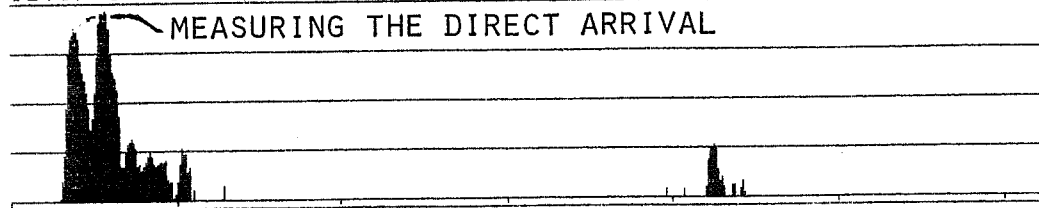
0 PH.D EXPERIMENTAL STUDY... 1985 TIME HISTORY DATA [TH613N017] 1000

TIME (μs)

C=30.52 (0.5μs EXTERNAL SAMPLING RATE)

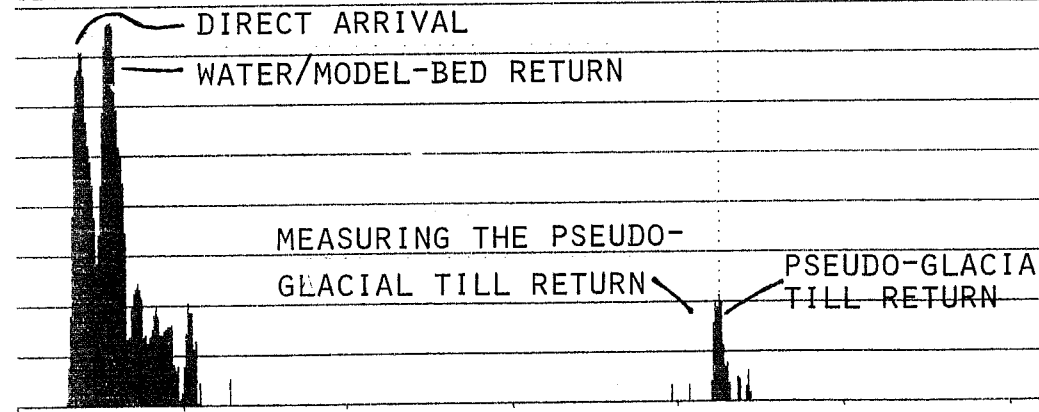
PLATE 3B₁ - OUTER SCANNING CIRCLE
 ENVELOPE OF THE TIME SIGNALS
 (USING THE HILBERT TRANSFORM)

W1 TIME CH.A MAG MAIN Y: 141.4dB
 Y: 146.0dB / 1.00uU 40dB X: 1.953ms/C
 X: 0.000ms/C + 31.3ms/C FLEX : 0.06396873
 SETUP 3 OVERLOAD



W1 TIME CH.A MAG INPUT REF Y: 144.4dB
 Y: 146.0dB / 1.00uU 40dB X: 2.822ms/C
 X: 0.000ms/C + 31.3ms/C ΔX: 0.869ms/C
 SETUP 3 OVERLOAD ΔY : 3.0dB

W1 TIME CH.A MAG INPUT REF Y: 116.6dB
 Y: 146.0dB / 1.00uU 40dB X: 21.255ms/C
 X: 0.000ms/C + 31.3ms/C ΔX: 18.432ms/C
 SETUP 3 OVERLOAD ΔY : -27.8dB



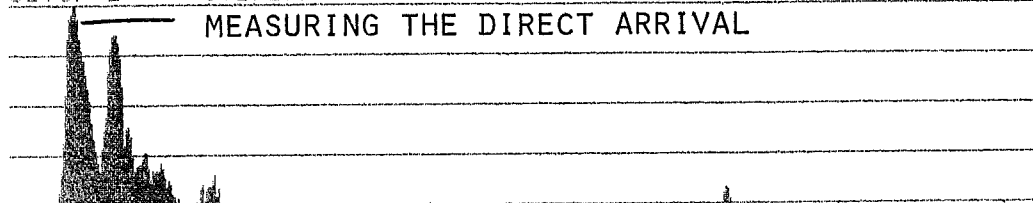
0 PH.D EXPERIMENTAL STUDY 1985 TIME HISTORY DATA ETH613N0253 1000

TIME (μs)

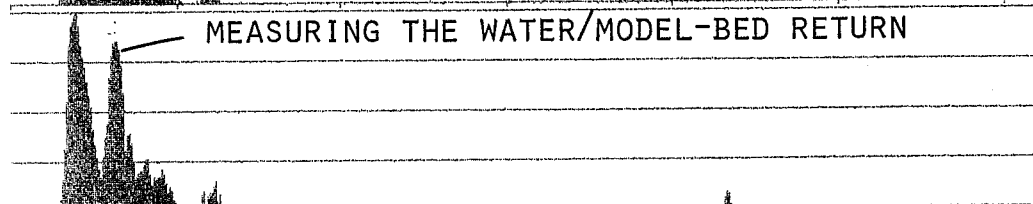
C=30.52 (0.5 μs EXTERNAL SAMPLING RATE)

PLATE 3C - OUTER SCANNING CIRCLE
 ENVELOPE OF THE TIME SIGNALS
 (USING THE HILBERT TRANSFORM)

W1 TIME CH.A MAG MAIN Y: 141.1dB
 Y: 141.4dB / 1.00uU 40dB X: 1.937ms/C
 X: 0.000ms/C + 31.3ms/C
 SETUP 2 OVERLOAD FLEX.: 0.06346897

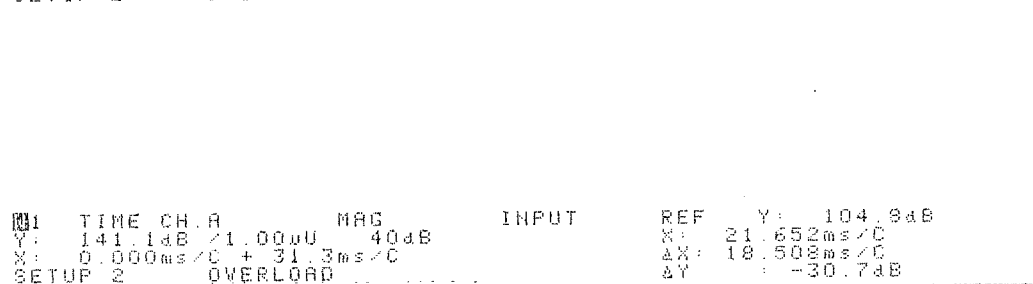


MEASURING THE DIRECT ARRIVAL

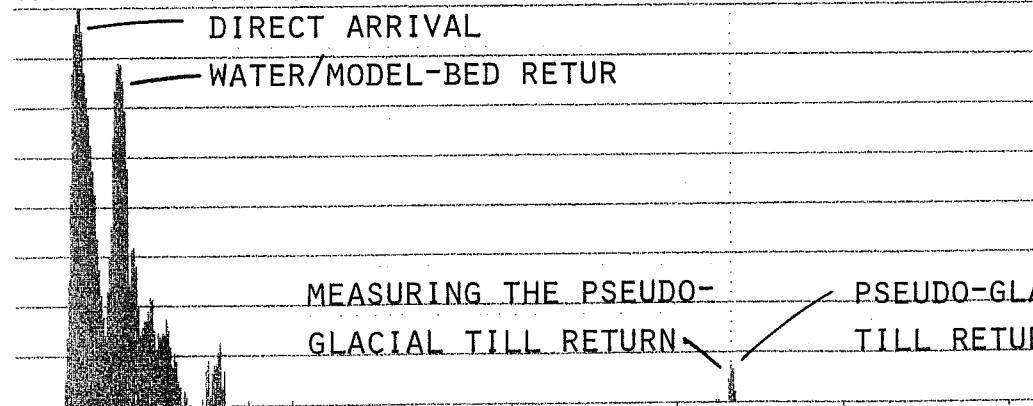


MEASURING THE WATER/MODEL-BED RETURN

W1 TIME CH.A MAG INPUT REF Y: 135.5dB
 Y: 141.4dB / 1.00uU 40dB X: 3.143ms/C
 X: 0.000ms/C + 31.3ms/C ΔX: 1.205ms/C
 SETUP 2 OVERLOAD ΔY: -5.6dB



DIRECT ARRIVAL
 WATER/MODEL-BED RETURN
 MEASURING THE PSEUDO-GLACIAL TILL RETURN
 PSEUDO-GLACIAL TILL RETURN

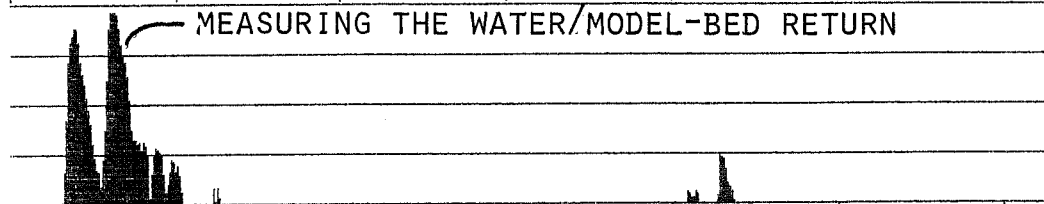
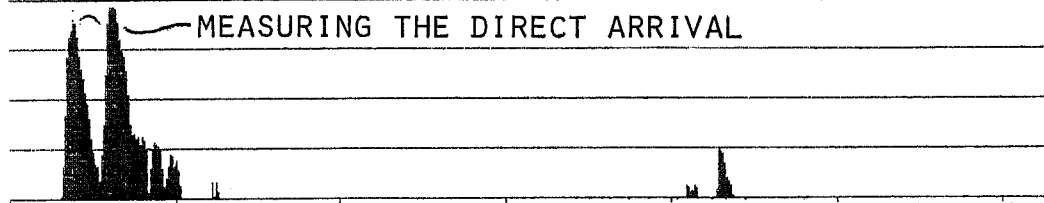


0 PH.D EXPERIMENTAL STUDY 1985
 TIME HISTORY DATA LTH813H034J 1000
 TIME (μs)

C=30.52 (0.5μs EXTERNAL SAMPLING RATE)

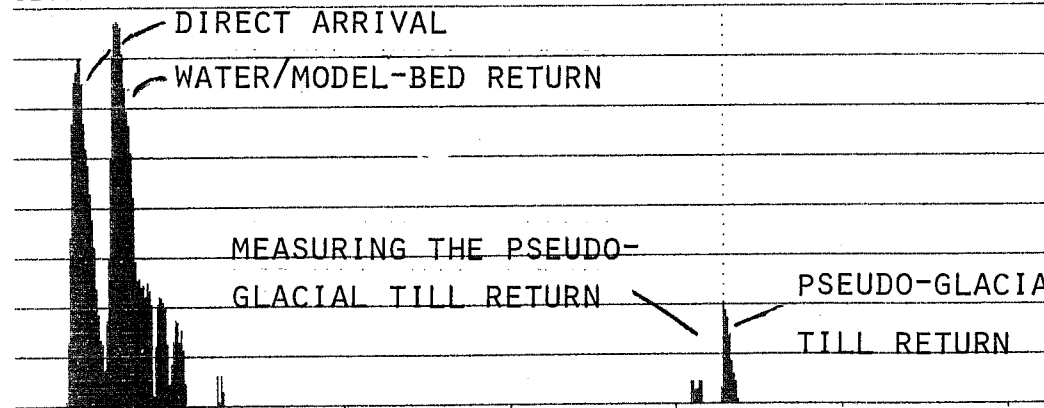
PLATE 3C₁ - OUTER SCANNING CIRCLE
 ENVELOPE OF THE TIME SIGNALS
 (USING THE HILBERT TRANSFORM)

W1	TIME	CH.A	MAG	MAIN	Y:	141.1dB
Y:	146.0dB	/1.00uU	40dB	X:	1.937ms/C	
X:	0.000ms/C	+ 31.3ms/C		FLEX	:	0.06346897
SETUP	3	OVERLOAD				



W1	TIME	CH.A	MAG	INPUT	REF	Y:	144.4dB
Y:	146.0dB	/1.00uU	40dB	X:	3.097ms/C		
X:	0.000ms/C	+ 31.3ms/C		ΔX:	1.159ms/C		
SETUP	3	OVERLOAD		ΔY	:	3.3dB	

W1	TIME	CH.A	MAG	INPUT	REF	Y:	116.1dB
Y:	146.0dB	/1.00uU	40dB	X:	21.469ms/C		
X:	0.000ms/C	+ 31.3ms/C		ΔX:	18.371ms/C		
SETUP	3	OVERLOAD		ΔY	:	-28.2dB	



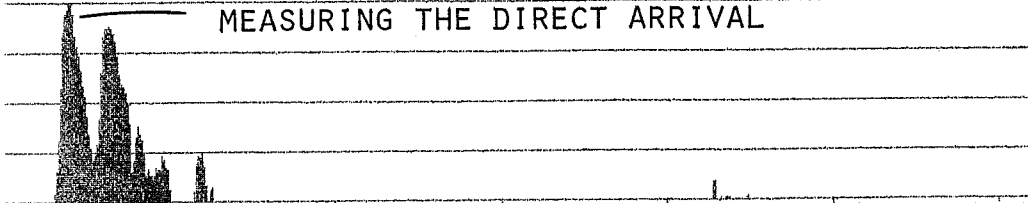
0 PH.D EXPERIMENTAL STUDY... 1985 TIME HISTORY DATA ETH613N0423 1000
 TIME (μs)

C=30.52 (0.5μs EXTERNAL SAMPLING RATE)

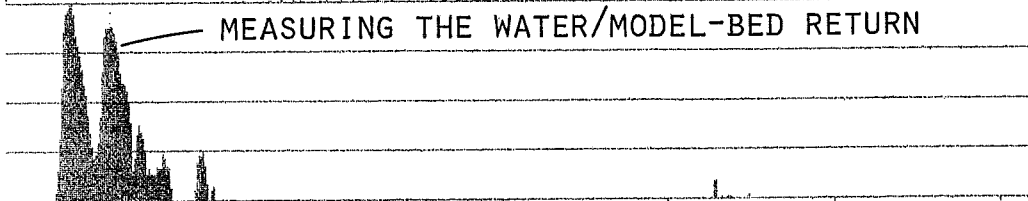
PLATE 3D - OUTER SCANNING CIRCLE
 ENVELOPE OF THE TIME SIGNALS
 (USING THE HILBERT TRANSFORM)

W1 TIME CH.A MAG INPUT MAIN Y: 141.6dB
 Y: 141.4dB / 1.00uV 40dB X: 1.953ms/C
 X: 0.000ms/C + 31.3ms/C
 SETUP 2 OVERLOAD FLEX : 0.06396873

MEASURING THE DIRECT ARRIVAL



MEASURING THE WATER/MODEL-BED RETURN

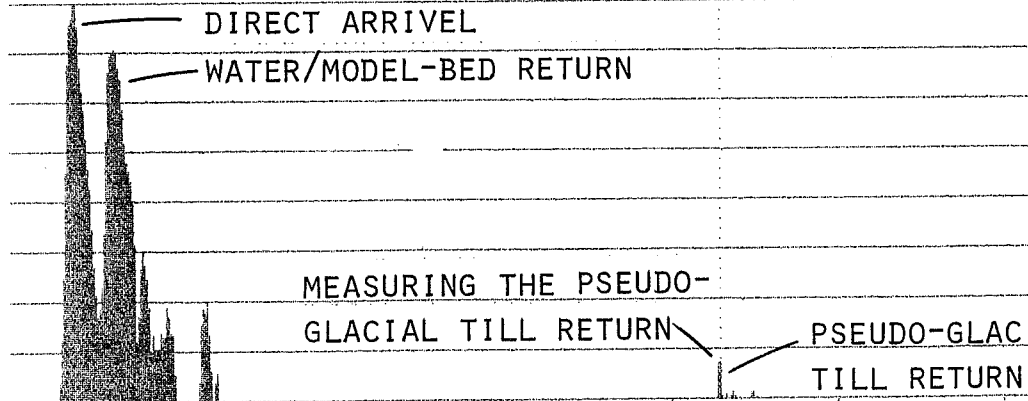


W1 TIME CH.A MAG REF Y: 135.6dB
 Y: 141.4dB / 1.00uV 40dB X: 3.143ms/C
 X: 0.000ms/C + 31.3ms/C ΔX: 1.190ms/C
 SETUP 2 OVERLOAD ΔY : -5.0dB

W1 TIME CH.A MAG INPUT REF Y: 105.1dB
 Y: 141.4dB / 1.00uV 40dB X: 21.423ms/C
 X: 0.000ms/C + 31.3ms/C ΔX: 18.280ms/C
 SETUP 2 OVERLOAD ΔY : -31.5dB

DIRECT ARRIVEL

WATER/MODEL-BED RETURN



MEASURING THE PSEUDO-
 GLACIAL TILL RETURN

PSEUDO-GLACIAL
 TILL RETURN

0

PH.D EXPERIMENTAL STUDY... 1985
 TIME HISTORY DATA ETH613N0511

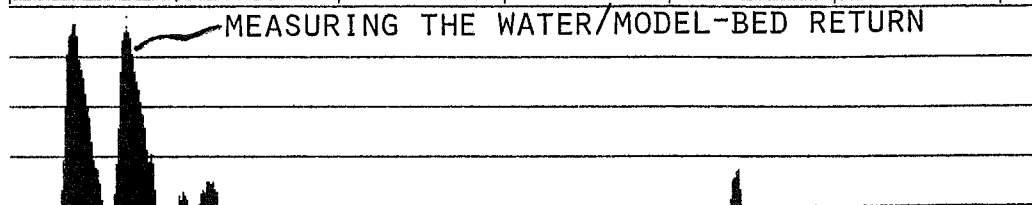
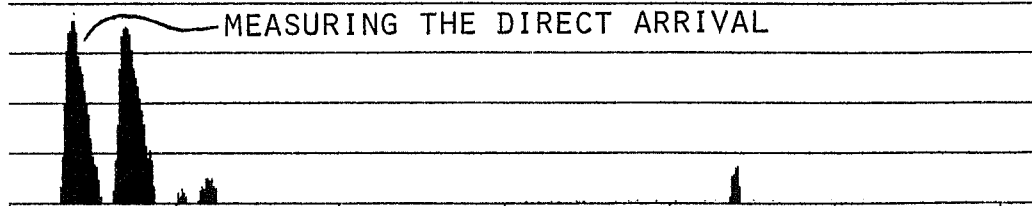
1000

TIME (μs)

C=30.52 (0.5 μs EXTERNAL SAMPLING
 RATE)

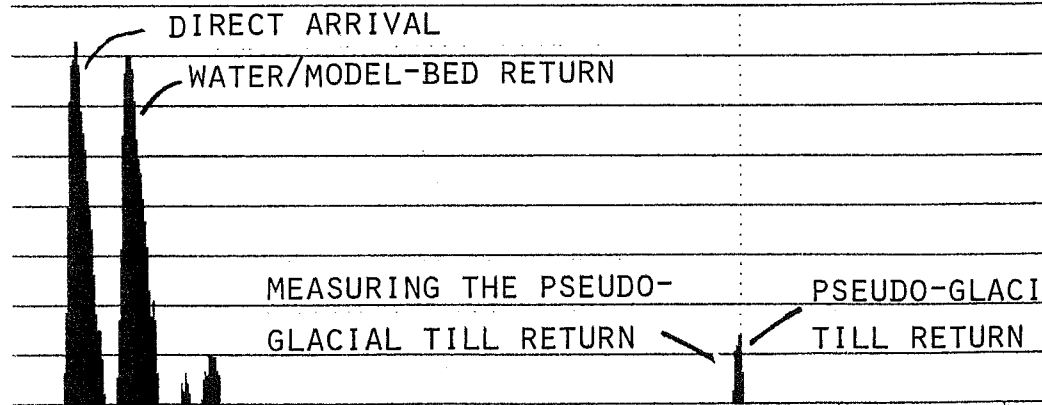
PLATE 3D₁ - OUTER SCANNING CIRCLE
 ENVELOPE OF THE TIME SIGNALS
 (USING THE HILBERT TRANSFORM)

W1 TIME CH.A MAG MAIN Y: 141.5dB
 Y: 145.0dB / 1.00uV 40dB X: 1.953ms/C
 X: 0.000ms/C + 31.3ms/C FLEX : 0.06396872
 SETUP 2 OVERLOAD



W1 TIME CH.A MAG INPUT REF Y: 140.1dB
 Y: 145.0dB / 1.00uV 40dB X: 3.509ms/C
 X: 0.000ms/C + 31.3ms/C ΔX: 1.556ms/C
 SETUP 2 OVERLOAD ΔY: -1.4dB

W1 TIME CH.A MAG INPUT REF Y: 112.1dB
 Y: 145.0dB / 1.00uV 40dB X: 22.033ms/C
 X: 0.000ms/C + 31.3ms/C ΔX: 18.524ms/C
 SETUP 2 OVERLOAD ΔY: -28.0dB

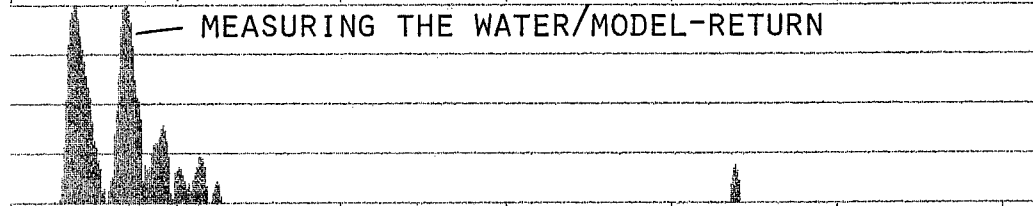
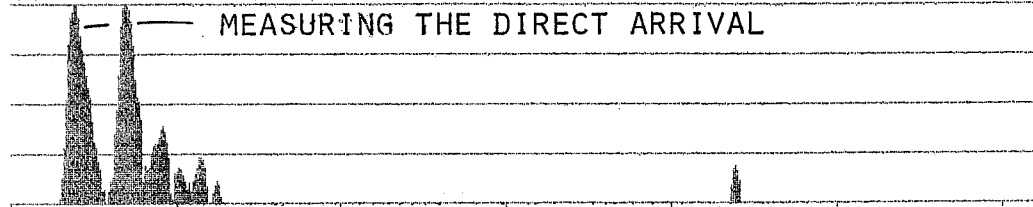


0 PH.D EXPERIMENTAL STUDY... 1985 TIME HISTORY DATA LTH613N060J 1000
 TIME (μs)

C=30.52 (0.5μs EXTERNAL SAMPLING RATE)

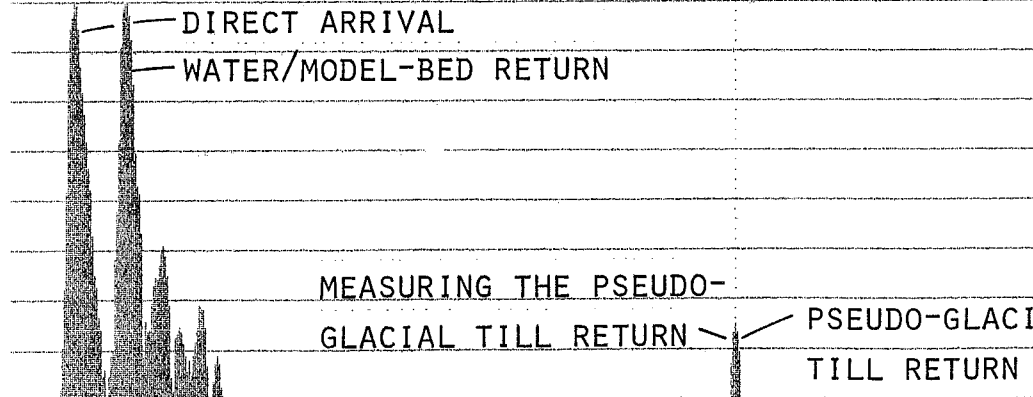
PLATE 3A - INNER SCANNING CIRCLE
 ENVELOPE OF THE TIME SIGNALS
 (USING THE HILBERT TRANSFORM)

M1 TIME CH.A MAG INPUT MAIN Y: 141.14B
 Y: 141.4dB /1.00uV 40dB X: 1.937ms/C
 X: 0.000ms/C + 31.3ms/C
 SETUP 3 OVERLOAD FLEX : 0.06346897



M1 TIME CH.A MAG REF Y: 141.4dB
 Y: 141.4dB /1.00uV 40dB X: 3.433ms/C
 X: 0.000ms/C + 31.3ms/C ΔX: 1.495ms/C
 SETUP 3 OVERLOAD ΔY: 0.2dB

M1 TIME CH.A MAG INPUT REF Y: 108.84B
 Y: 141.4dB /1.00uV 40dB X: 21.986ms/C
 X: 0.000ms/C + 31.3ms/C ΔX: 18.493ms/C
 SETUP 3 OVERLOAD ΔY: -32.54B

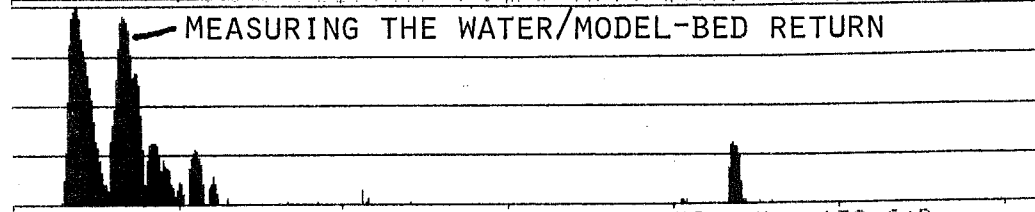
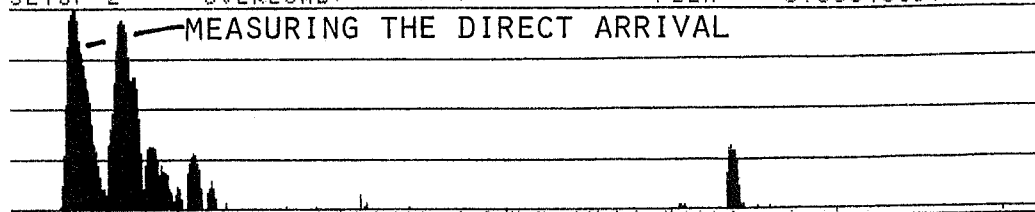


0 PH.D EXPERIMENTAL STUDY... 1985 TIME HISTORY DATA ETH613N0703 1000
 TIME (μs)

C=30.52 (0.5μs EXTERNAL SAMPLING RATE)

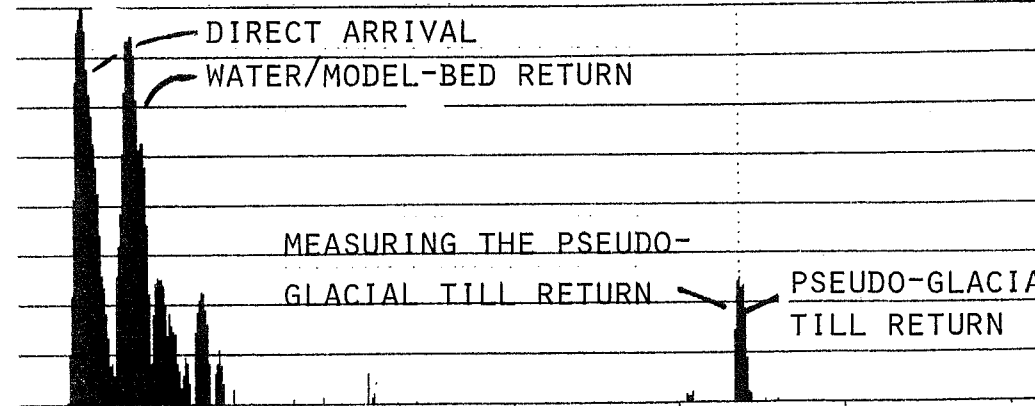
PLATE 3A₁ - INNER SCANNING CIRCLE
 ENVELOPE OF THE TIME SIGNALS
 (USING THE HILBERT TRANSFORM)

W1 TIME CH.A MAG MAIN Y: 140.9dB
 Y: 140.9dB / 1.00uU 40dB X: 1.937ms/C
 X: 0.000ms/C + 31.3ms/C FLEX : 0.06346897
 SETUP 2 OVERLOAD



M1 TIME CH.A MAG INPUT REF Y: 139.6dB
 Y: 140.9dB / 1.00uU 40dB X: 3.326ms/C
 X: 0.000ms/C + 31.3ms/C ΔX: 1.388ms/C
 SETUP 2 OVERLOAD ΔY: -2.4dB

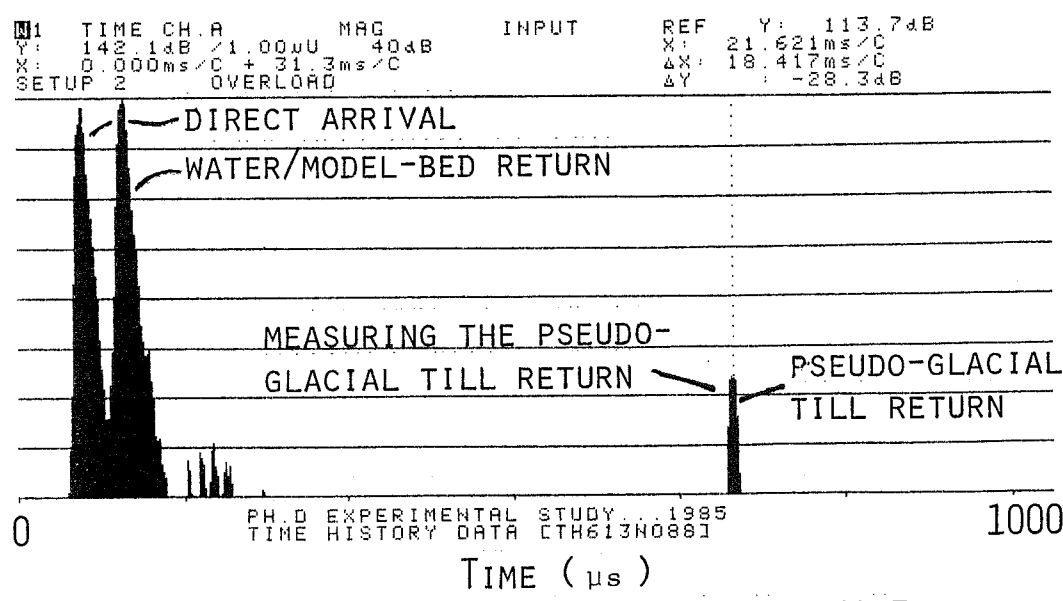
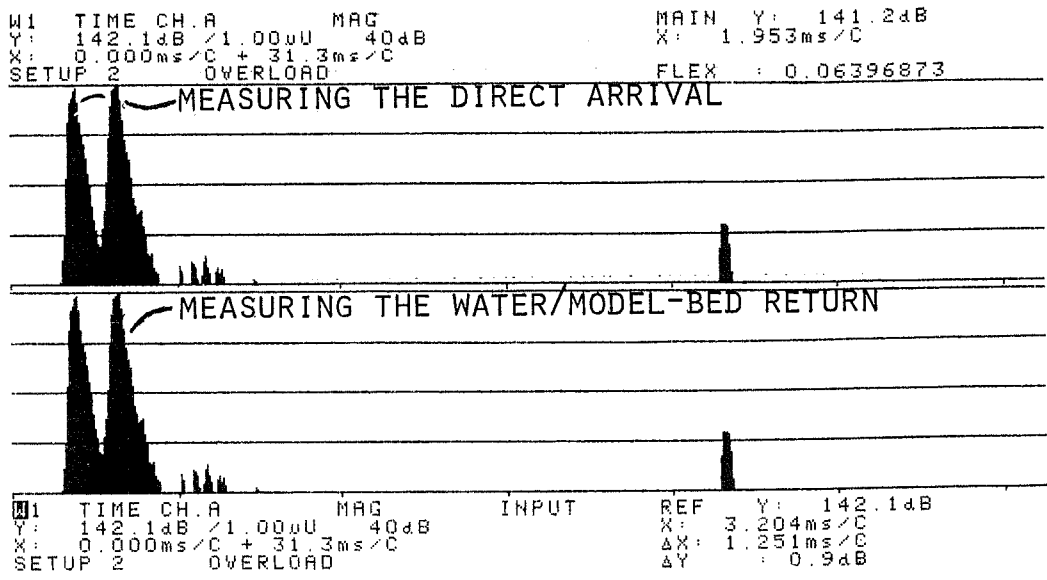
M1 TIME CH.A MAG INPUT REF Y: 113.2dB
 Y: 140.9dB / 1.00uU 40dB X: 21.804ms/C
 X: 0.000ms/C + 31.3ms/C ΔX: 18.478ms/C
 SETUP 2 OVERLOAD ΔY: -25.3dB



0 PH.D EXPERIMENTAL STUDY... 1985 TIME HISTORY DATA [TH613N0801] 1000
 TIME (μs)

C = 30.52 (0.5μs EXTERNAL SAMPLING RATE)

PLATE 3B - INNER SCANNING CIRCLE
 ENVELOPE OF THE TIME SIGNALS
 (USING THE HILBERT TRANSFORM)

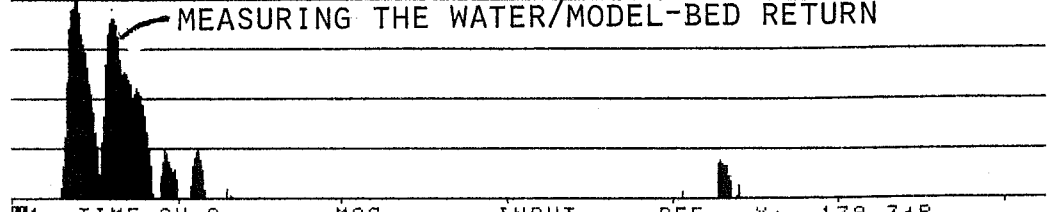
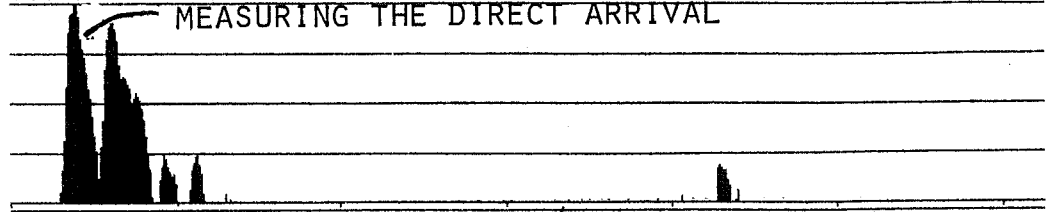


PH.D EXPERIMENTAL STUDY...1985
 TIME HISTORY DATA CTH613N0881

C=30.52 (0.5μs EXTERNAL SAMPLING RATE)

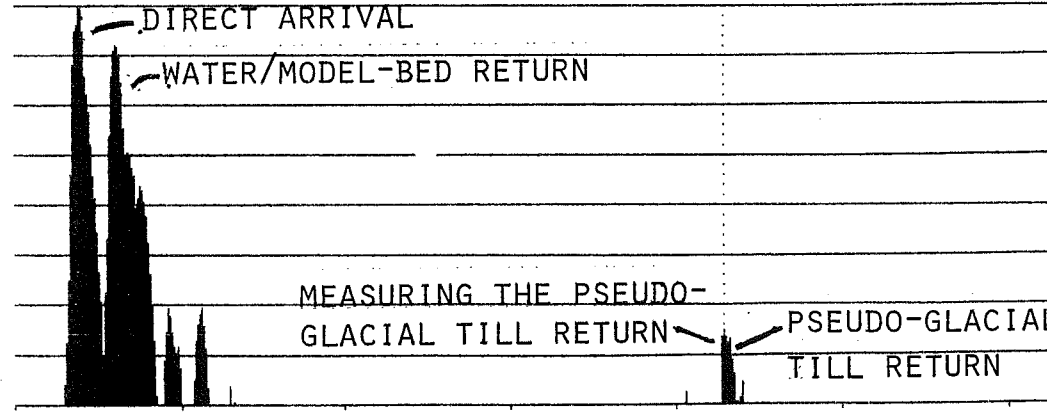
PLATE 3B₁ - INNER SCANNING CIRCLE
 ENVELOPE OF THE TIME SIGNALS
 (USING THE HILBERT TRANSFORM)

W1 TIME CH.A MAG MAIN Y: 141.4dB
 Y: 142.2dB / 1.00uU 40dB X: 1.907ms/C
 X: 0.000ms/C + 31.3ms/C FLEX : 0.06246946
 SETUP 2 OVERLOAD



W1 TIME CH.A MAG INPUT REF Y: 139.3dB
 Y: 142.2dB / 1.00uU 40dB X: 3.021ms/C
 X: 0.000ms/C + 31.3ms/C ΔX: 1.113ms/C
 SETUP 2 OVERLOAD ΔY : -3.1dB

W1 TIME CH.A MAG INPUT REF Y: 109.7dB
 Y: 142.2dB / 1.00uU 40dB X: 21.469ms/C
 X: 0.000ms/C + 31.3ms/C ΔX: 18.447ms/C
 SETUP 2 OVERLOAD ΔY : -28.6dB

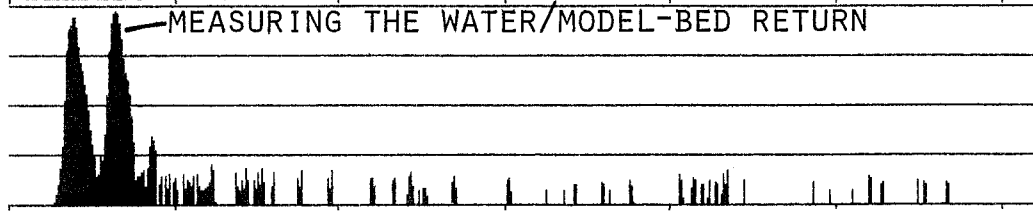
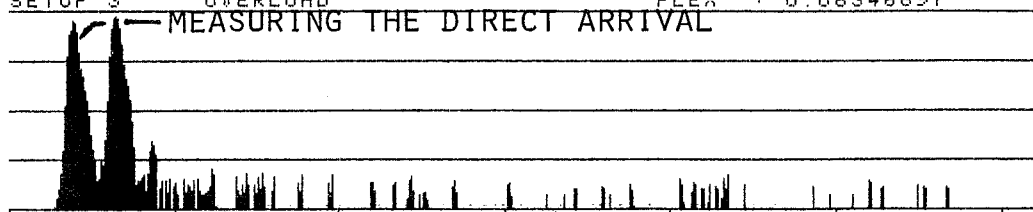


0 PH.D EXPERIMENTAL STUDY... 1985 TIME HISTORY DATA [TH613N096] 1000
 TIME (μs)

C=30.52 (0.5μs EXTERNAL SAMPLING RATE)

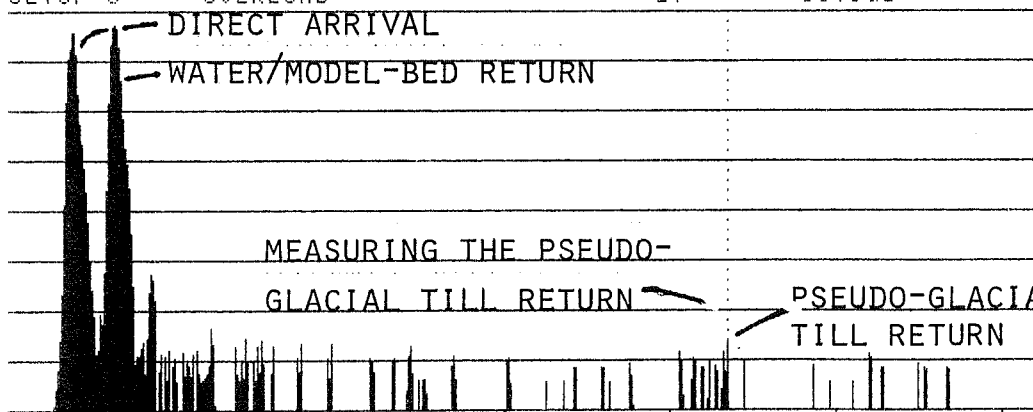
PLATE 3c₁ - INNER SCANNING CIRCLE
 ENVELOPE OF THE TIME SIGNALS
 (USING THE HILBERT TRANSFORM)

W1 TIME CH.A MAG MAIN Y: 140.8dB
 Y: 143.0dB / 1.00uU 40dB X: 1.937ms/C
 X: 0.000ms/C + 31.3ms/C FLEX : 0.06346897
 SETUP 3 OVERLOAD



W1 TIME CH.A MAG INPUT REF Y: 141.7dB
 Y: 143.0dB / 1.00uU 40dB X: 3.189ms/C
 X: 0.000ms/C + 31.3ms/C ΔX: 1.251ms/C
 SETUP 3 OVERLOAD ΔY : 0.9dB

W1 TIME CH.A MAG INPUT REF Y: 109.8dB
 Y: 143.0dB / 1.00uU 40dB X: 21.743ms/C
 X: 0.000ms/C + 31.3ms/C ΔX: 18.554ms/C
 SETUP 3 OVERLOAD ΔY : -31.9dB

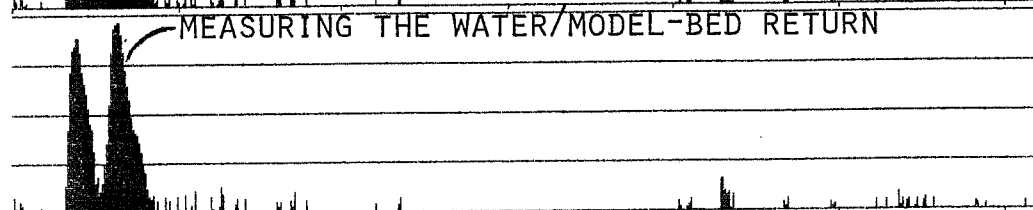
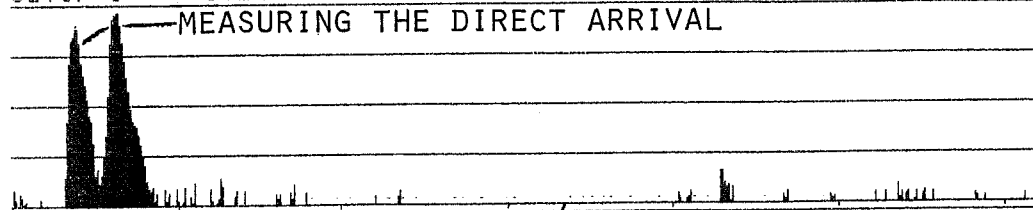


0 PH.D EXPERIMENTAL STUDY... 1985 TIME HISTORY DATA [LTH613N124J] 1000
 TIME (μs)

C = 30.52 (0.5 μs EXTERNAL SAMPLING RATE)

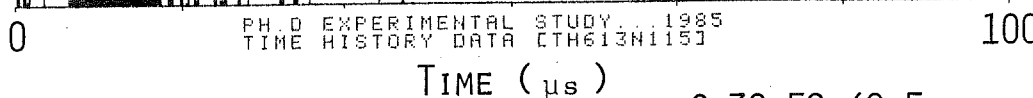
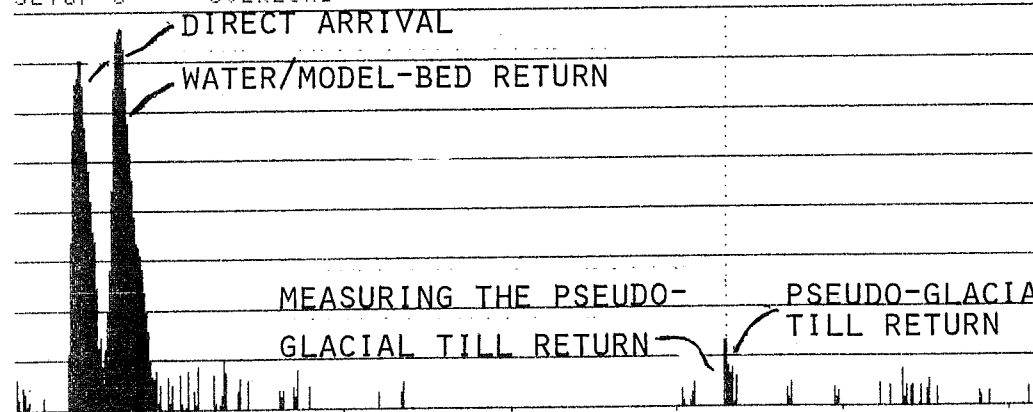
PLATE 3c - INNER SCANNING CIRCLE
 ENVELOPE OF THE TIME SIGNALS
 (USING THE HILBERT TRANSFORM)

W1 TIME CH.A MAG MAIN Y: 141.1dB
 Y: 146.0dB / 1.00uU 40dB X: 1.937ms/C
 X: 0.000ms/C + 31.3ms/C FLEX : 0.06346897
 SETUP 3 OVERLOAD



W1 TIME CH.A MAG INPUT REF Y: 144.5dB
 Y: 146.0dB / 1.00uU 40dB X: 3.143ms/C
 X: 0.000ms/C + 31.3ms/C ΔX: 1.205ms/C
 SETUP 3 OVERLOAD ΔY : 3.3dB

W1 TIME CH.A MAG INPUT REF Y: 112.6dB
 Y: 146.0dB / 1.00uU 40dB X: 21.499ms/C
 X: 0.000ms/C + 31.3ms/C ΔX: 18.356ms/C
 SETUP 3 OVERLOAD ΔY : -31.9dB



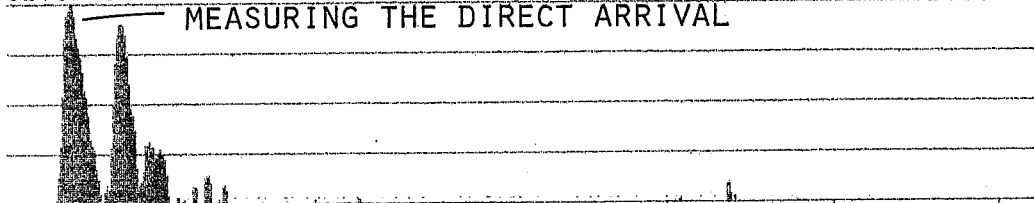
0 PH.D EXPERIMENTAL STUDY...1985 1000
 TIME HISTORY DATA CTH613N1153
 TIME (μs)

C=30.52 (0.5μs EXTERNAL SAMPLING RATE)

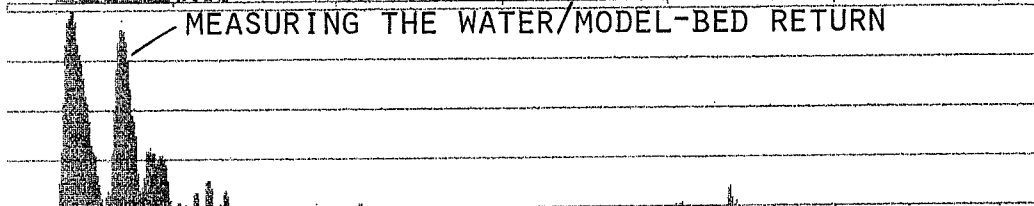
PLATE 3d - INNER SCANNING CIRCLE
 ENVELOPE OF THE TIME SIGNALS
 (USING THE HILBERT TRANSFORM)

W1 TIME CH.A MAG INPUT MAIN Y: 141.3dB
 Y: 141.3dB / 1.00uV 40dB X: 1.937ms / C
 X: 0.000ms / C + 31.3ms / C FLEX: 0.06346897
 SETUP 1 OVERLOAD

MEASURING THE DIRECT ARRIVAL



MEASURING THE WATER/MODEL-BED RETURN

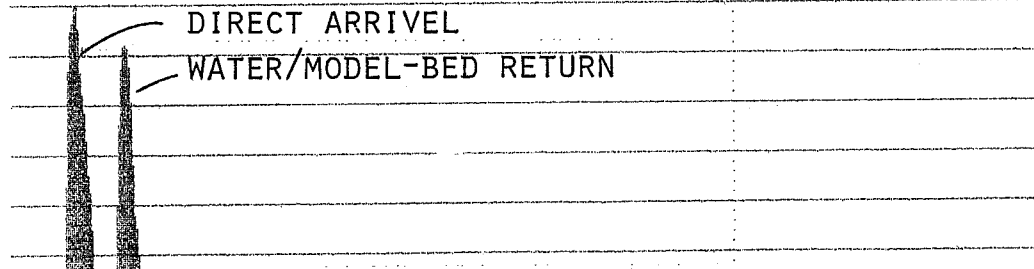


W1 TIME CH.A MAG INPUT REF Y: 137.4dB
 Y: 141.3dB / 1.00uV 40dB X: 3.433ms / C
 X: 0.000ms / C + 31.3ms / C ΔX: 1.498ms / C
 SETUP 1 OVERLOAD ΔY: -3.8dB

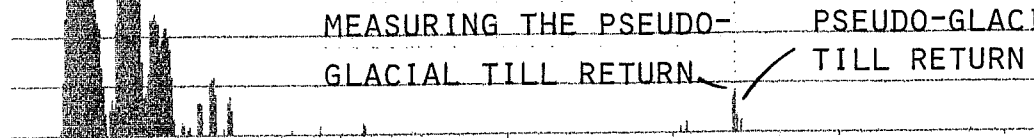
W1 TIME CH.A MAG INPUT REF Y: 105.4dB
 Y: 141.3dB / 1.00uV 40dB X: 21.850ms / C
 X: 0.000ms / C + 31.3ms / C ΔX: 18.417ms / C
 SETUP 1 OVERLOAD ΔY: -32.0dB

DIRECT ARRIVEL

WATER/MODEL-BED RETURN



MEASURING THE PSEUDO-GLACIAL TILL RETURN PSEUDO-GLACIAL TILL RETURN

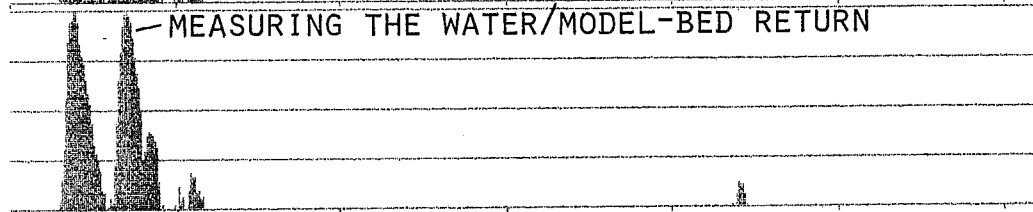
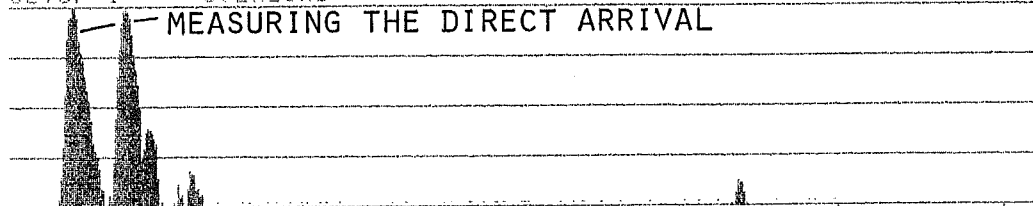


0 PH.D EXPERIMENTAL STUDY... 1985 TIME HISTORY DATA LTH613N135J 1000
 TIME (μs)

C=30.52 (0.5μs EXTERNAL SAMPLING RATE)

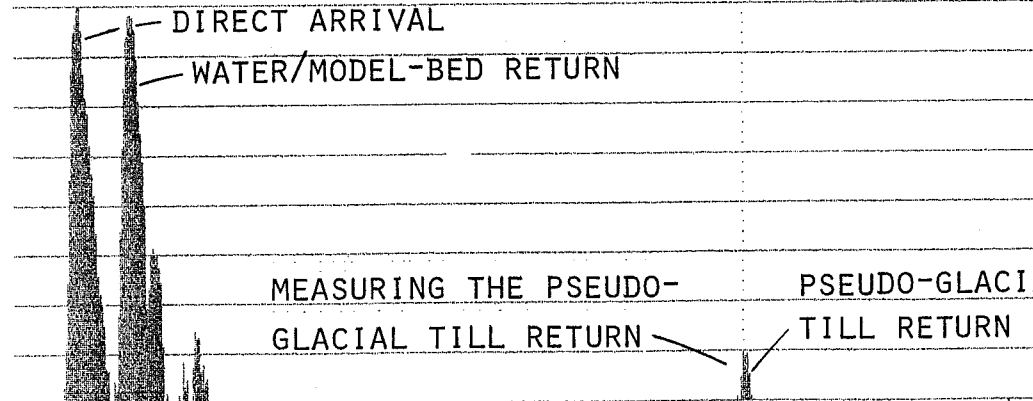
PLATE 3D₁ - INNER SCANNING CIRCLE
 ENVELOPE OF THE TIME SIGNALS
 (USING THE HILBERT TRANSFORM)

W1 TIME CH.A MAG MAIN Y: 141.5dB
 Y: 141.5dB / 1.000U 40dB X: 1.953ms/C
 X: 0.000ms/C + 31.3ms/C FLEX : 0.06396873
 SETUP 1 OVERLOAD



W1 TIME CH.A MAG INPUT REF Y: 140.6dB
 Y: 141.5dB / 1.000U 40dB X: 3.479ms/C
 X: 0.000ms/C + 31.3ms/C ΔX: 1.525ms/C
 SETUP 1 OVERLOAD ΔY : -0.9dB

W1 TIME CH.A MAG INPUT REF Y: 106.3dB
 Y: 141.5dB / 1.000U 40dB X: 21.972ms/C
 X: 0.000ms/C + 31.3ms/C ΔX: 18.493ms/C
 SETUP 1 OVERLOAD ΔY : -34.3dB



0 PH.D EXPERIMENTAL STUDY... 1985
 TIME HISTORY DATA CTH613N1451 1000
 TIME (μs)

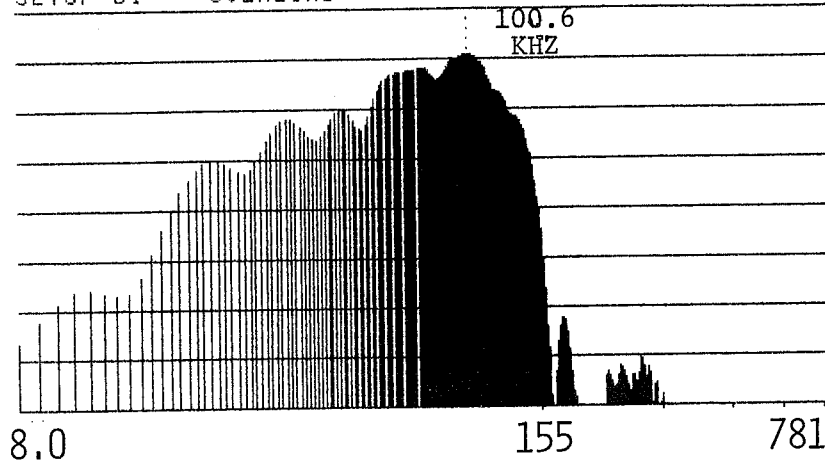
C=30.52 (0.5μs EXTERNAL SAMPLING RATE)

PLATES 4A TO 4D₁

INSTANTANEOUS FREQUENCY
(USING THE HILBERT TRANSFORM)

PLATE 4A - OUTER SCANNING CIRCLE
 INSTANTANEOUS FREQUENCY
 (USING THE HILBERT TRANSFORM)

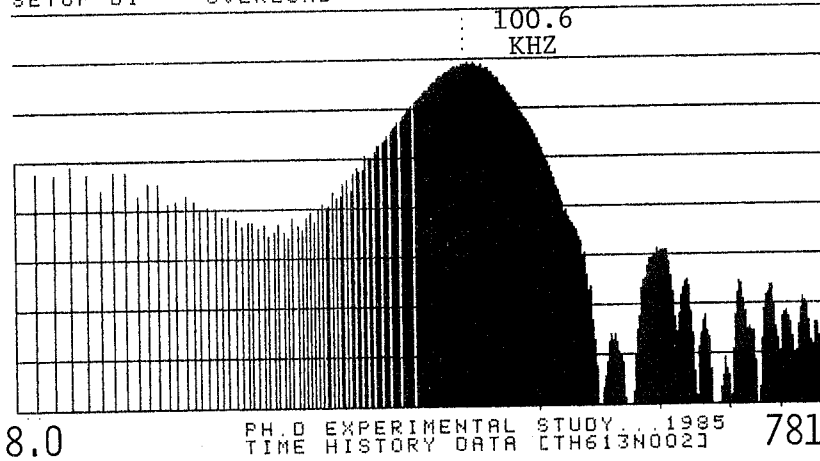
#1 INST SPEC CH.A MAG INPUT MAIN Y: 95.5dB
 Y: 100.0dB /1.00E-12U2 PWR 40dB X: 3296Hz*C
 X: 256Hz*C TO 25.6kHz*C LOG TOTAL : 113.1dB/YREF
 SETUP D1 OVERLOAD



WATER/MODEL-BED
 RETURN

FREQUENCY (IN KHZ)

#1 INST SPEC CH.B MAG INPUT MAIN Y: 69.4dB
 Y: 75.0dB /1.00E-12U2 PWR 40dB X: 3296Hz*C
 X: 256Hz*C TO 25.6kHz*C LOG TOTAL : 87.3dB/YREF
 SETUP D1 OVERLOAD



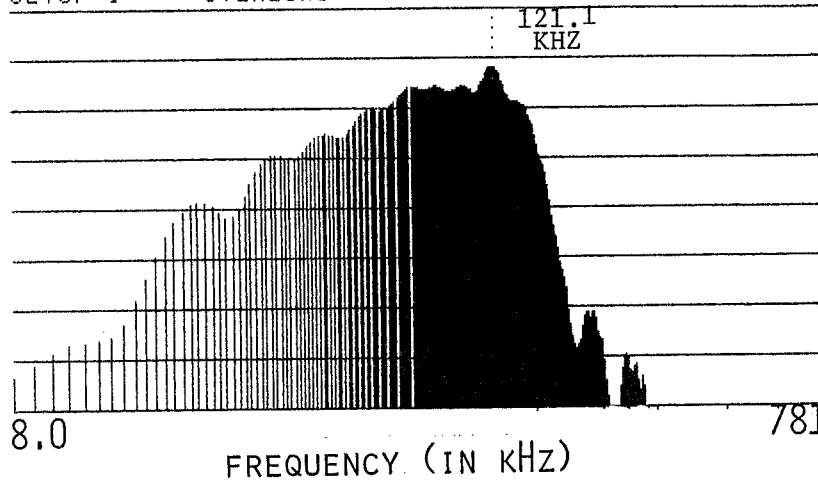
BOTTOM REFLECTION
 PSEUDO-GLACIAL TILL

PH.D EXPERIMENTAL STUDY...1985
 TIME HISTORY DATA [TH613N002] 781
 FREQUENCY (IN KHZ)

C=30.52 (0.5 μ s EXTERNAL SAMPLING RATE)

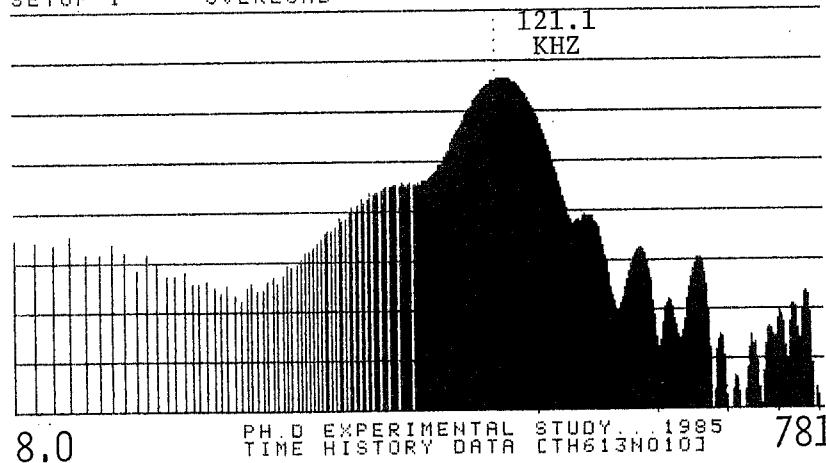
PLATE 4A₁- OUTER SCANNING CIRCLE
 INSTANTANEOUS FREQUENCY
 (USING THE HILBERT TRANSFORM)

M1 INST SPEC CH.A MAG INPUT MAIN Y: 94.1dB
 Y: 100.0dB /1.00E-12U² PWR 40dB X: 3968Hz*C
 X: 256Hz*C TO 25.6kHz*C LOG TOTAL : 112.0dB/YREF
 SETUP 1 OVERLOAD



WATER/MODEL-BED
 RETURN

M1 INST SPEC CH.B MAG INPUT MAIN Y: 68.0dB
 Y: 75.0dB /1.00E-12U² PWR 40dB X: 3968Hz*C
 X: 256Hz*C TO 25.6kHz*C LOG TOTAL : 85.8dB/YREF
 SETUP 1 OVERLOAD

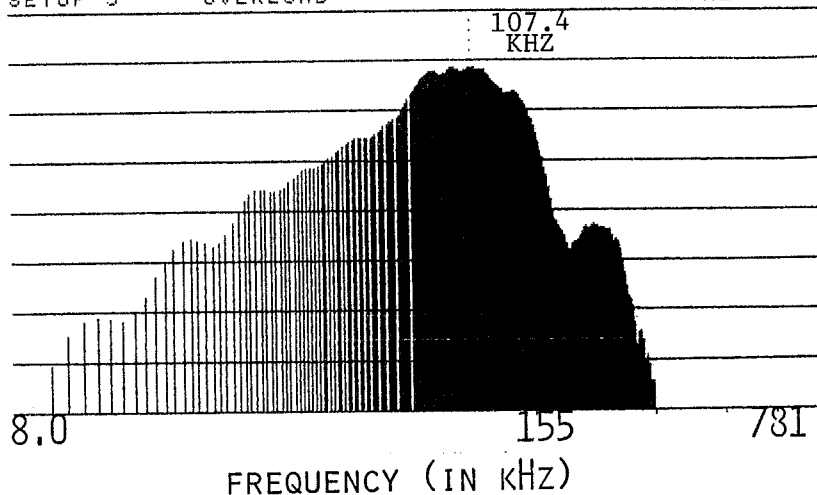


BOTTOM REFLECTION
 PSEUDO-GLACIAL TILL

C=30.52 (0.5 μ s EXTERNAL SAMPLING RATE)

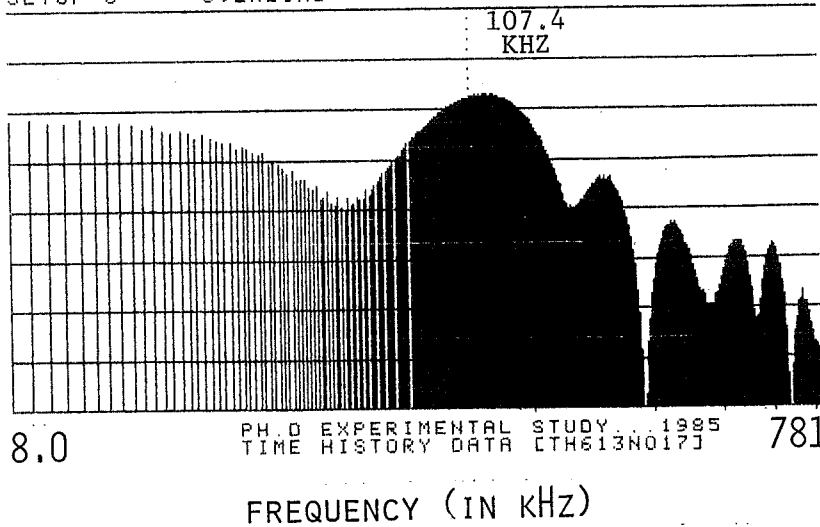
PLATE 4B - OUTER SCANNING CIRCLE
INSTANTANEOUS FREQUENCY
(USING THE HILBERT TRANSFORM)

M1 INST SPEC CH.A MAG INPUT MAIN Y: 99.2dB
 Y: 105.0dB /1.00E-12U² PWR 40dB X: 3520Hz*C
 X: 256Hz*C TO 25.6kHz*C LOG TOTAL : 117.7dB/YREF
 SETUP 3 OVERLOAD



WATER/MODEL-BED
RETURN

M1 INST SPEC CH.B MAG INPUT MAIN Y: 66.2dB
 Y: 75.0dB /1.00E-12U² PWR 40dB X: 3520Hz*C
 X: 256Hz*C TO 25.6kHz*C LOG TOTAL : 86.7dB/YREF
 SETUP 3 OVERLOAD



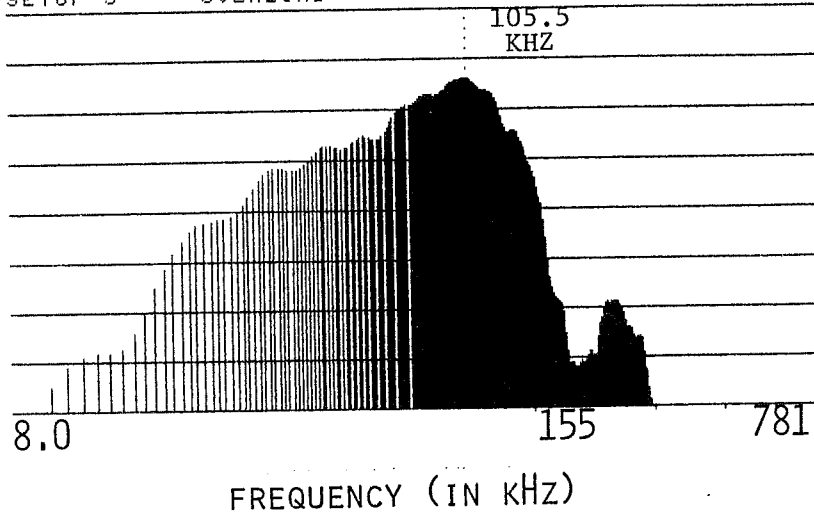
BOTTOM REFLECTION
PSEUDO-GLACIAL TILL

PH.D EXPERIMENTAL STUDY... 1985
TIME HISTORY DATA [TH613N017]

C=30.52 (0.5 μ s EXTERNAL SAMPLING
RATE)

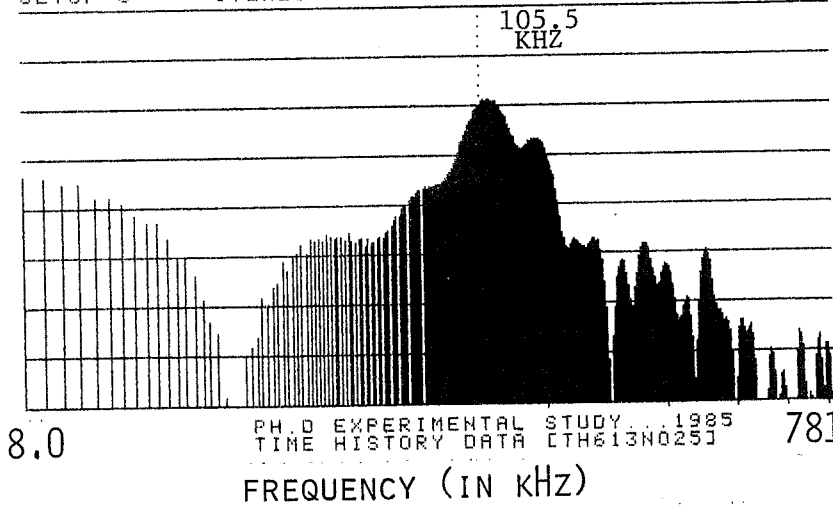
PLATE 4B₁- OUTER SCANNING CIRCLE
 INSTANTANEOUS FREQUENCY
 (USING THE HILBERT TRANSFORM)

01 INST SPEC CH.A MAG INPUT MAIN Y: 103.1dB
 Y: 110.0dB / 1.00E-12U² PWR 40dB X: 3456Hz* π C
 X: 256Hz* π C TO 25.6kHz* π C LOG TOTAL : 120.8dB/YREF
 SETUP 3 OVERLOAD



WATER/MODEL-BED
 RETURN

01 INST SPEC CH.B MAG INPUT MAIN Y: 75.0dB
 Y: 85.0dB / 1.00E-12U² PWR 40dB X: 3456Hz* π C
 X: 256Hz* π C TO 25.6kHz* π C LOG TOTAL : 92.6dB/YREF
 SETUP 3 OVERLOAD



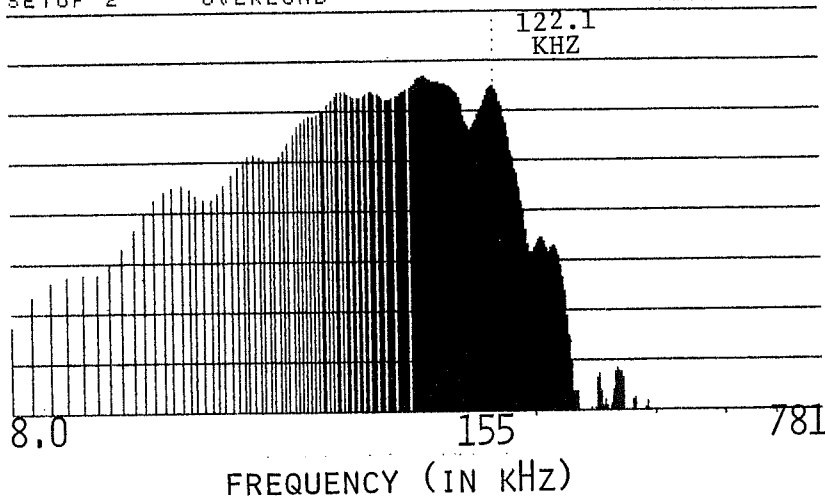
BOTTOM REFLECTION
 PSEUDO-GLACIAL TILL

PH.D EXPERIMENTAL STUDY... 1985
 TIME HISTORY DATA LTH613N025J

C=30.52 (0.5 μ s EXTERNAL SAMPLING
 RATE)

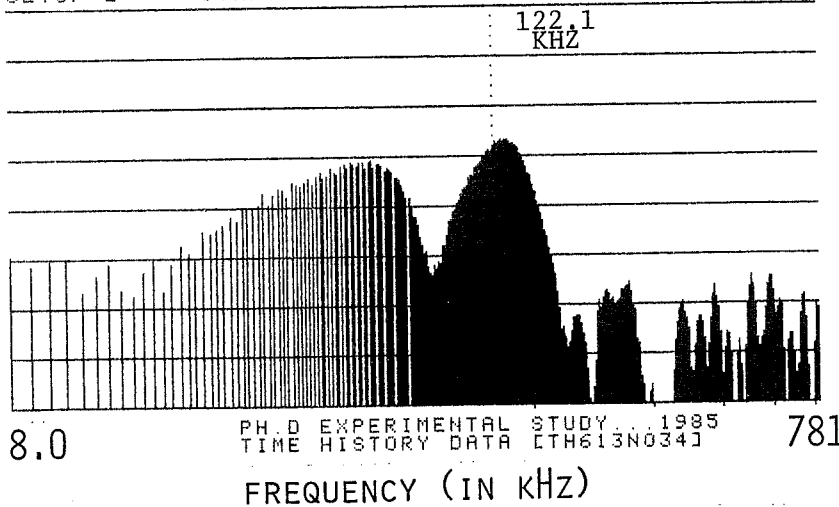
PLATE 4C - OUTER SCANNING CIRCLE
 INSTANTANEOUS FREQUENCY
 (USING THE HILBERT TRANSFORM)

01 INST SPEC CH.A MAG INPUT MAIN Y: 92.4dB
 Y: 100.0dB / 1.00E-12U² PWR 40dB X: 4000Hz*C
 X: 256Hz*C TO 25.6kHz*C LOG TOTAL : 111.5dB/YREF
 SETUP 2 OVERLOAD



WATER/MODEL-BED
 RETURN

01 INST SPEC CH.B MAG INPUT MAIN Y: 60.7dB
 Y: 75.0dB / 1.00E-12U² PWR 40dB X: 4000Hz*C
 X: 256Hz*C TO 25.6kHz*C LOG TOTAL : 80.1dB/YREF
 SETUP 2 OVERLOAD



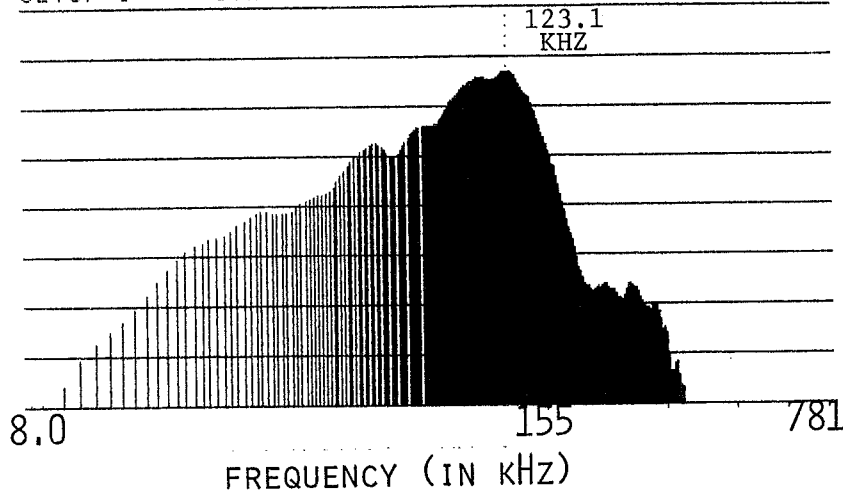
BOTTOM REFLECTION
 PSEUDO-GLACIAL TILL

PH.D EXPERIMENTAL STUDY... 1985
 TIME HISTORY DATA ETH613N0341

C=30.52 (0.5 μ s EXTERNAL SAMPLING
 RATE)

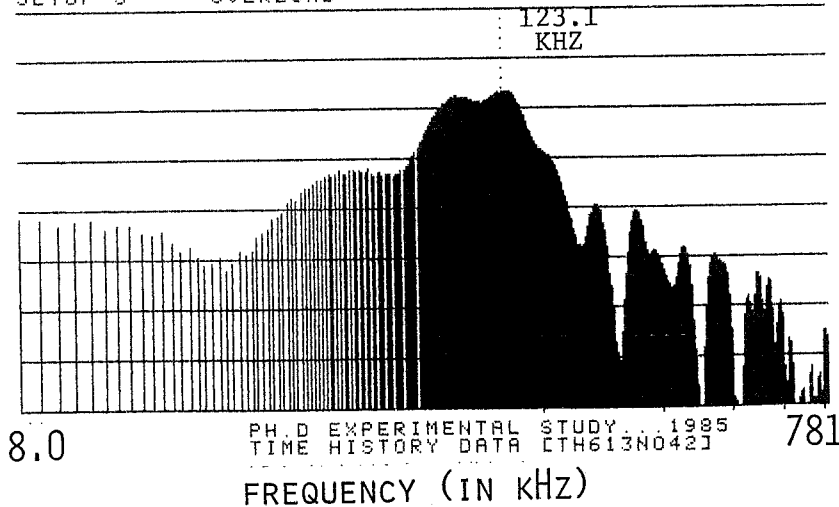
PLATE 4C₁ - OUTER SCANNING CIRCLE
 INSTANTANEOUS FREQUENCY
 (USING THE HILBERT TRANSFORM)

01 INST SPEC CH.A MAG INPUT MAIN Y: 103.4dB
 Y: 110.0dB /1.00E-12U² PWR 40dB X: 4032Hz*C
 X: 256Hz*C TO 25.6kHz*C LOG TOTAL : 121.1dB/YREF
 SETUP 3 OVERLOAD



WATER/MODEL-BED
 RETURN

01 INST SPEC CH.B MAG INPUT MAIN Y: 71.7dB
 Y: 80.0dB /1.00E-12U² PWR 40dB X: 4032Hz*C
 X: 256Hz*C TO 25.6kHz*C LOG TOTAL : 90.4dB/YREF
 SETUP 3 OVERLOAD



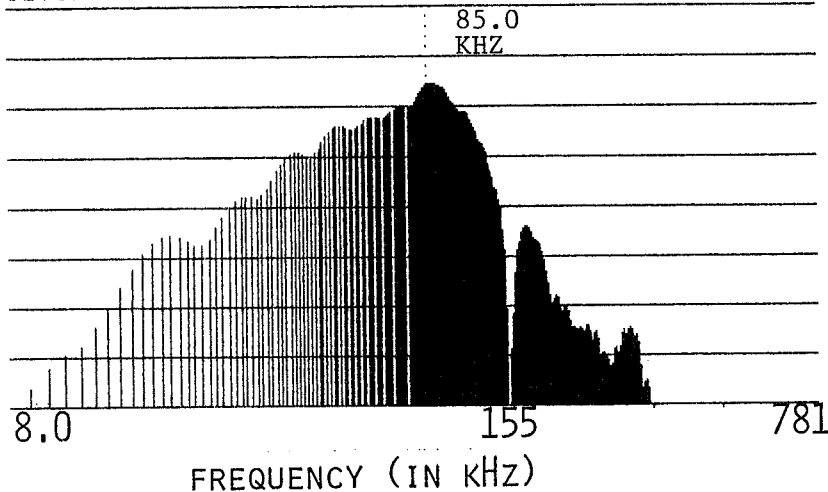
BOTTOM REFLECTION
 PSEUDO-GLACIAL TILL

PH.D EXPERIMENTAL STUDY... 1985
 TIME HISTORY DATA [LTH613N042]

C=30.52 (0.5 μ s EXTERNAL SAMPLING
 RATE)

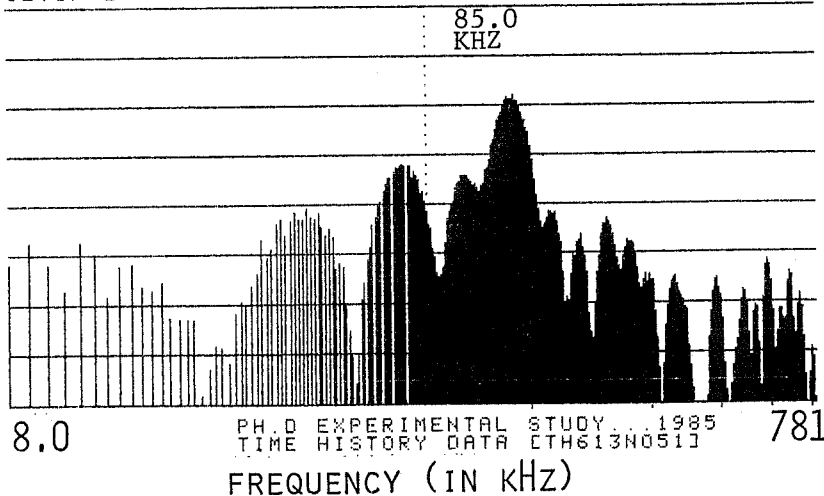
PLATE 4D - OUTER SCANNING CIRCLE
INSTANTANEOUS FREQUENCY
(USING THE HILBERT TRANSFORM)

01 INST SPEC CH.A MAG INPUT MAIN Y: 97.2dB
 Y: 105.0dB / 1.00E-12U² PWR 40dB X: 2784Hz*C
 X: 256Hz*C TO 25.6kHz*C LOG TOTAL : 113.9dB/YREF
 SETUP 2 OVERLOAD



WATER/MODEL-BED
RETURN

01 INST SPEC CH.B MAG INPUT MAIN Y: 54.1dB
 Y: 75.0dB / 1.00E-12U² PWR 40dB X: 2784Hz*C
 X: 256Hz*C TO 25.6kHz*C LOG TOTAL : 81.6dB/YREF
 SETUP 2 OVERLOAD



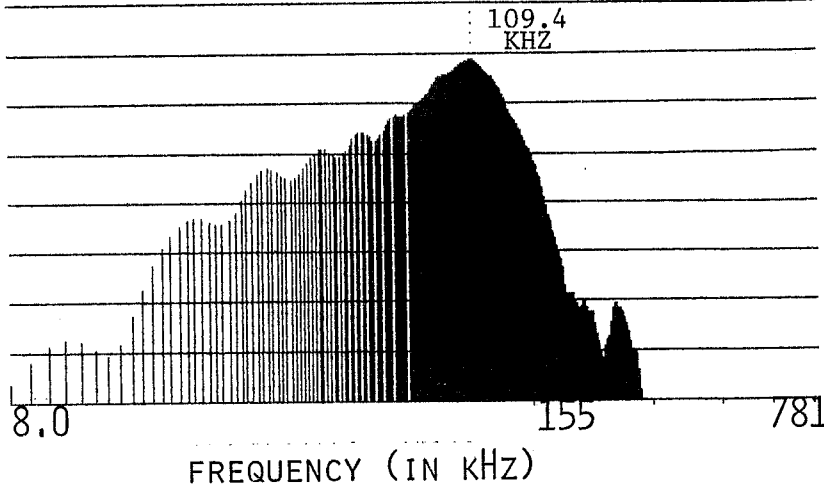
BOTTOM REFLECTION
PSEUDO-GLACIAL TILL

PH.D EXPERIMENTAL STUDY... 1985
TIME HISTORY DATA ETH613N0513

C=30.52 (0.5μs EXTERNAL SAMPLING
RATE)

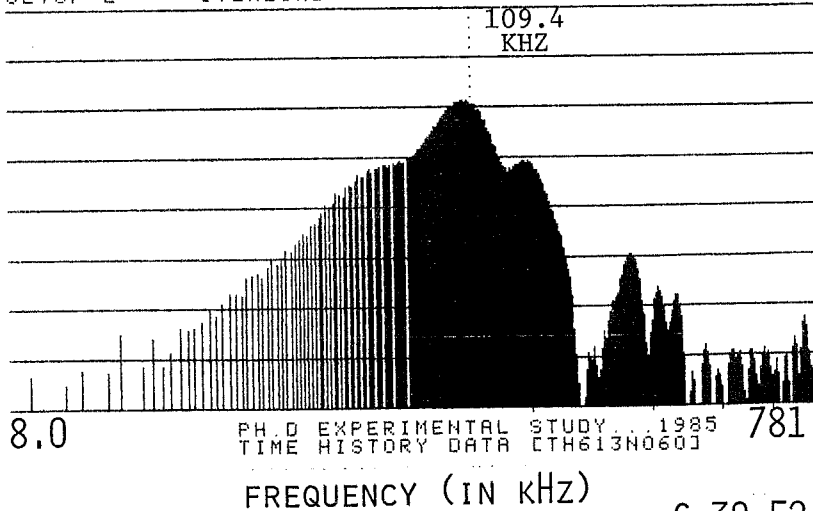
PLATE 4D₁ - OUTER SCANNING CIRCLE
 INSTANTANEOUS FREQUENCY
 (USING THE HILBERT TRANSFORM)

01 INST SPEC CH.A MAG INPUT MAIN Y: 99.3dB
 Y: 105.0dB / 1.00E-12U² PWR 40dB X: 3584Hz*C
 X: 256Hz*C TO 25.6kHz*C LOG TOTAL : 116.5dB/YREF
 SETUP 2 OVERLOAD



WATER/MODEL-BED
 RETURN

01 INST SPEC CH.B MAG INPUT MAIN Y: 70.2dB
 Y: 80.0dB / 1.00E-12U² PWR 40dB X: 3584Hz*C
 X: 256Hz*C TO 25.6kHz*C LOG TOTAL : 87.7dB/YREF
 SETUP 2 OVERLOAD



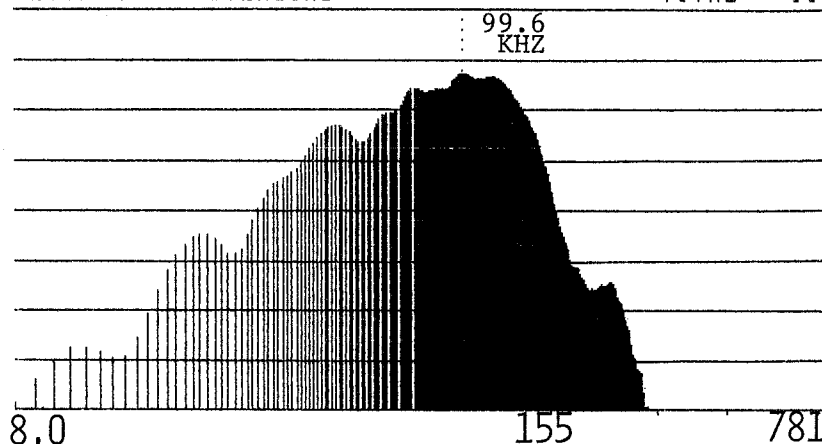
BOTTOM REFLECTION
 PSEUDO-GLACIAL TILL

PH.D EXPERIMENTAL STUDY... 1985
 TIME HISTORY DATA [TH613N060]

C=30.52 (0.5_μs EXTERNAL SAMPLING
 RATE)

PLATE 4A - INNER SCANNING CIRCLE
 INSTANTANEOUS FREQUENCY
 (USING THE HILBERT TRANSFORM)

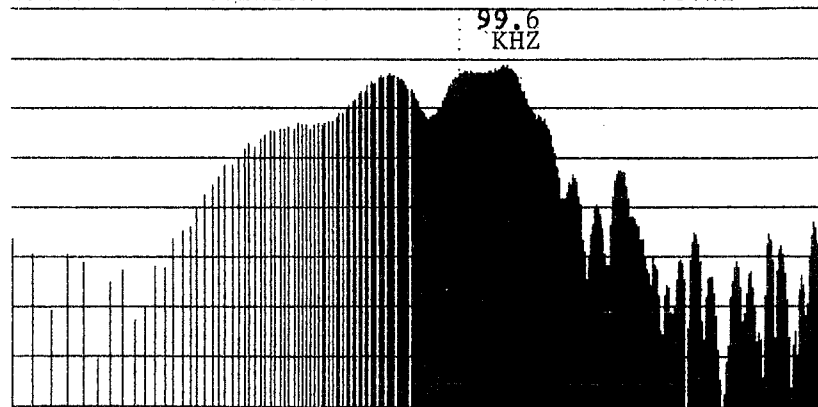
01 INST SPEC CH.A MAG INPUT MAIN Y: 98.7dB
 Y: 105.0dB /1.00E-12U² PWR 40dB X: 3264Hz*C
 X: 256Hz*C TO 25.6kHz*C LOG TOTAL : 117.1dB/YREF
 SETUP 2 OVERLOAD



WATER/MODEL-BED
 RETURN

FREQUENCY (IN KHZ)

01 INST SPEC CH.B MAG INPUT MAIN Y: 63.4dB
 Y: 70.0dB /1.00E-12U² PWR 40dB X: 3264Hz*C
 X: 256Hz*C TO 25.6kHz*C LOG TOTAL : 83.6dB/YREF
 SETUP 2 OVERLOAD



BOTTOM REFLECTION
 PSEUDO-GLACIAL TILL

PH.D EXPERIMENTAL STUDY... 1985
 TIME HISTORY DATA CTH613NO70J

8.0

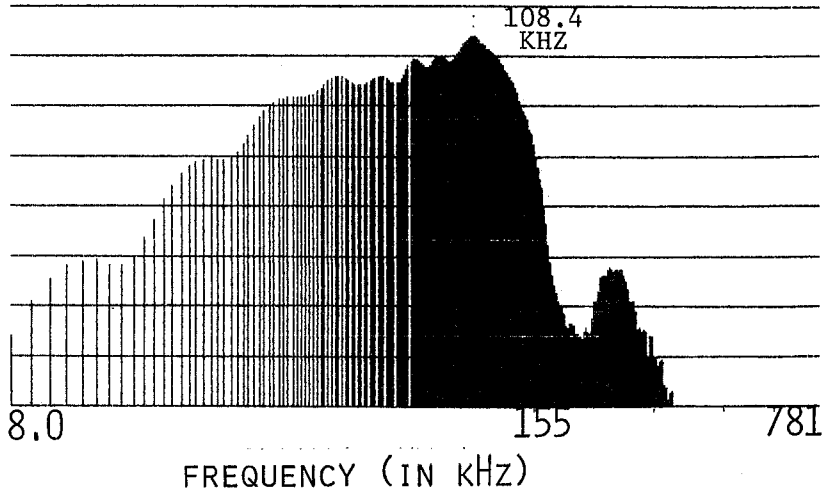
781

FREQUENCY (IN KHZ)

C=30.52 (0.5 μ s EXTERNAL SAMPLING
 RATE)

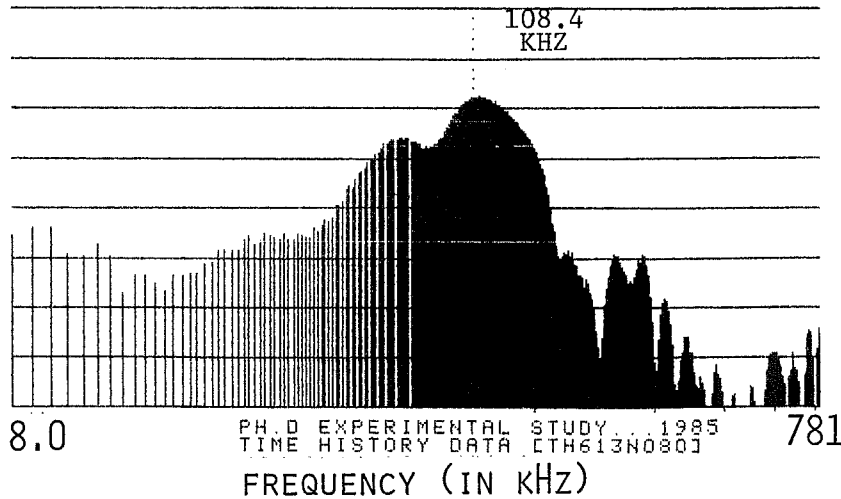
PLATE 4A₁ - INNER SCANNING CIRCLE
 INSTANTANEOUS FREQUENCY
 (USING THE HILBERT TRANSFORM)

01 INST SPEC CH.A MAG INPUT MAIN Y: 97.0dB
 Y: 100.0dB / 1.00E-12U² PWR 40dB X: 3552Hz*C
 X: 256Hz*C TO 25.6kHz*C LOG TOTAL : 114.7dB/YREF
 SETUP 2 OVERLOAD



WATER/MODEL-BED
 RETURN

01 INST SPEC CH.B MAG INPUT MAIN Y: 71.0dB
 Y: 80.0dB / 1.00E-12U² PWR 40dB X: 3552Hz*C
 X: 256Hz*C TO 25.6kHz*C LOG TOTAL : 89.2dB/YREF
 SETUP 2 OVERLOAD

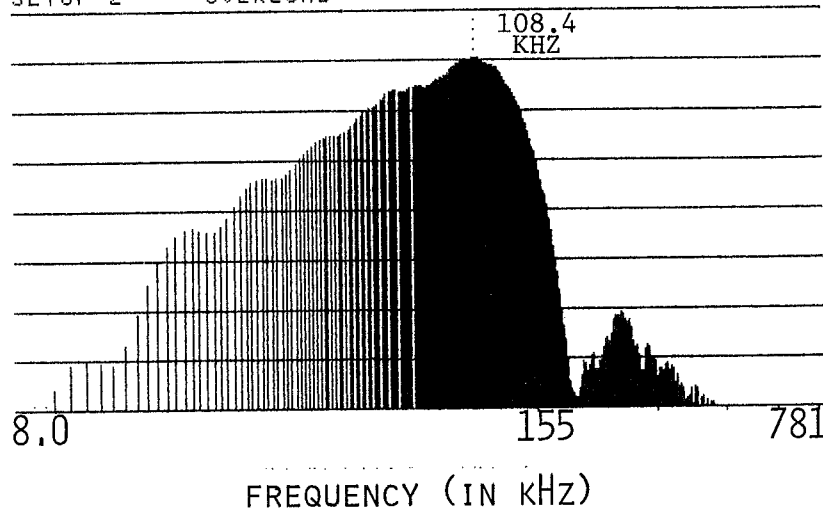


BOTTOM REFLECTION
 PSEUDO-GLACIAL TILL

C=30.52 (0.5μs EXTERNAL SAMPLING
 RATE)

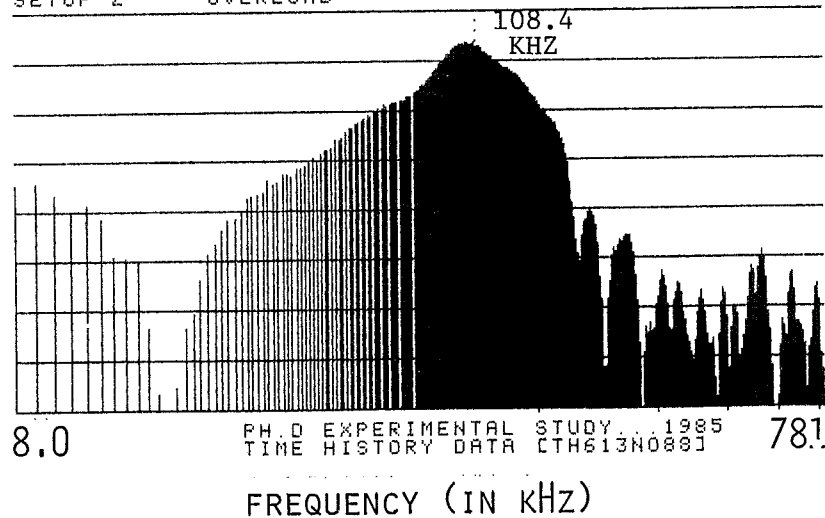
PLATE 4B - INNER SCANNING CIRCLE
INSTANTANEOUS FREQUENCY
(USING THE HILBERT TRANSFORM)

[1] INST SPEC CH.A MAG INPUT MAIN Y: 100.3dB
 Y: 105.0dB / 1.00E-12U² PWR 40dB X: 3552Hz*C
 X: 256Hz*C TO 25.6kHz*C LOG TOTAL : 118.1dB/YREF
 SETUP 2 OVERLOAD



WATER/MODEL-BED
RETURN

[1] INST SPEC CH.B MAG INPUT MAIN Y: 71.5dB
 Y: 75.0dB / 1.00E-12U² PWR 40dB X: 3552Hz*C
 X: 256Hz*C TO 25.6kHz*C LOG TOTAL : 89.7dB/YREF
 SETUP 2 OVERLOAD



BOTTOM REFLECTION OF
PSEUDO-GLACIAL TILL

PH.D EXPERIMENTAL STUDY... 1985
TIME HISTORY DATA CTH613N0883

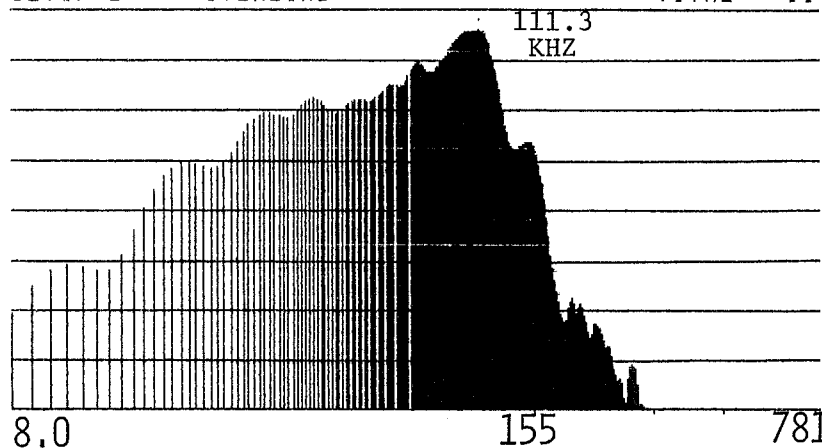
C=30.52 (0.5 μ s EXTERNAL SAMPLING
RATE)

PLATE 4B₁ - INNER SCANNING CIRCLE

INSTANTANEOUS FREQUENCY

(USING THE HILBERT TRANSFORM)

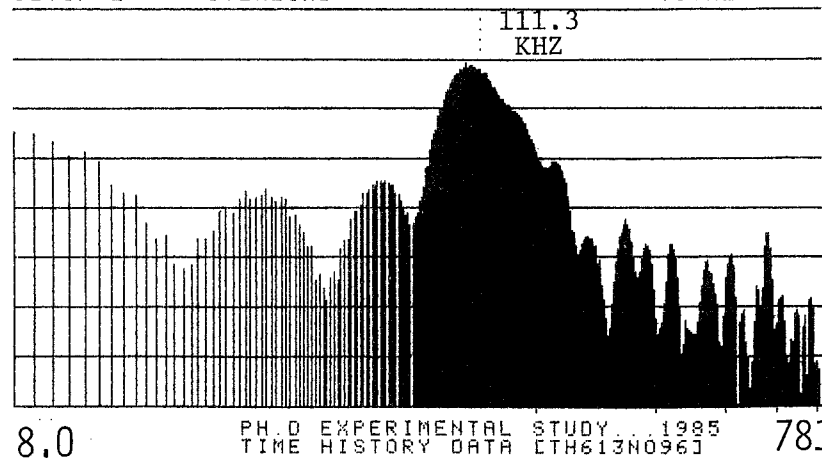
1 INST SPEC CH.A MAG INPUT MAIN Y: 97.9dB
 Y: 100.0dB / 1.00E-12U² PWR 40dB X: 3649Hz*²
 X: 256Hz*² TO 25.6kHz*² LOG TOTAL : 114.7dB/YREF
 SETUP 2 OVERLOAD



WATER/MODEL-BED
RETURN

FREQUENCY (IN KHZ)

1 INST SPEC CH.B MAG INPUT MAIN Y: 69.1dB
 Y: 75.0dB / 1.00E-12U² PWR 40dB X: 3649Hz*²
 X: 256Hz*² TO 25.6kHz*² LOG TOTAL : 86.3dB/YREF
 SETUP 2 OVERLOAD



BOTTOM REFLECTION
PSEUDO-GLACIAL TILL

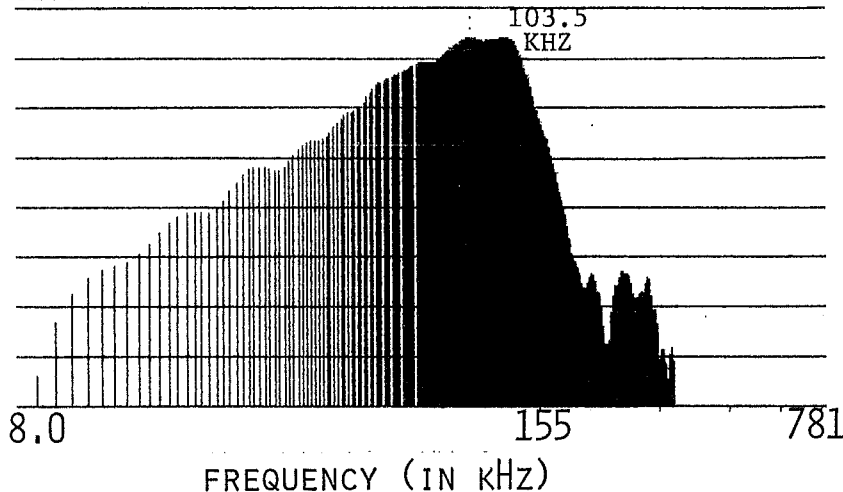
FREQUENCY (IN KHZ)

C=30.52 (0.5 μ s EXTERNAL SAMPLING RATE)

PH.D EXPERIMENTAL STUDY 1985
TIME HISTORY DATA LTH613N096J

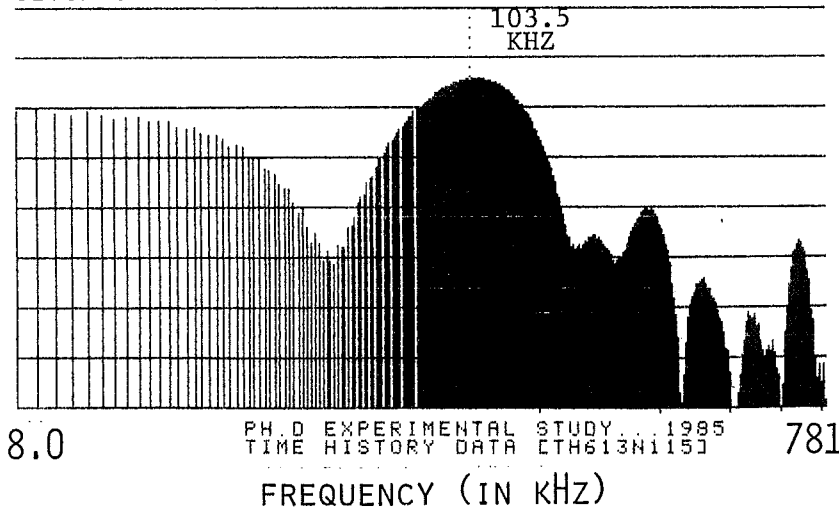
PLATE 4c - INNER SCANNING CIRCLE
 INSTANTANEOUS FREQUENCY
 (USING THE HILBERT TRANSFORM)

01 INST SPEC CH.A MAG INPUT MAIN Y: 102.1dB
 Y: 105.0dB / 1.00E-12U² PWR 40dB X: 3392Hz* π C
 X: 256Hz* π C TO 25.6kHz* π C LOG TOTAL : 120.6dB/YREF
 SETUP 3 OVERLOAD



WATER/MODEL-BED
 RETURN

01 INST SPEC CH.B MAG INPUT MAIN Y: 67.7dB
 Y: 75.0dB / 1.00E-12U² PWR 40dB X: 3392Hz* π C
 X: 256Hz* π C TO 25.6kHz* π C LOG TOTAL : 87.1dB/YREF
 SETUP 3 OVERLOAD

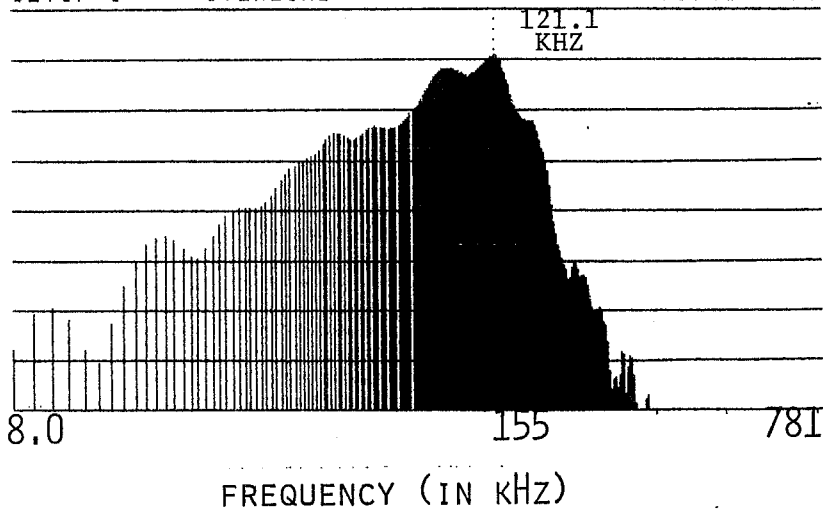


BOTTOM REFLECTION
 PSEUDO-GLACIAL TILL

C=30.52 (0.5 μ s EXTERNAL SAMPLING
 RATE)

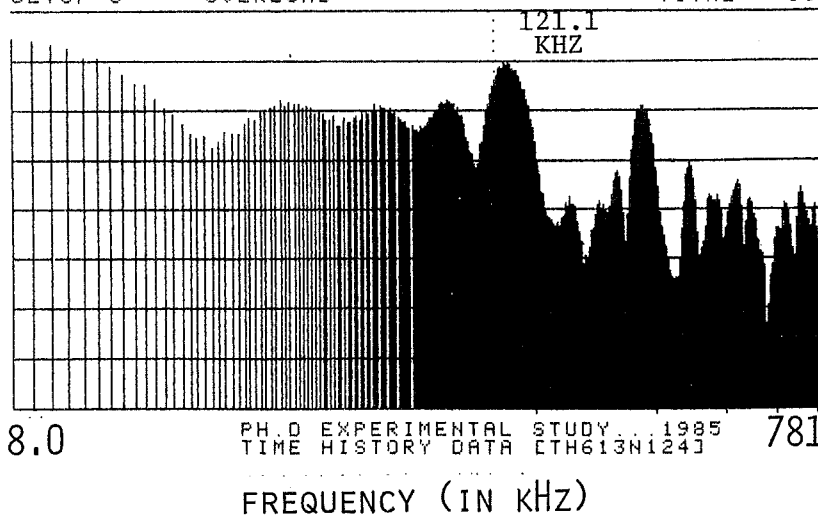
PLATE 4A - INNER SCANNING CIRCLE
 INSTANTANEOUS FREQUENCY
 (USING THE HILBERT TRANSFORM)

M1 INST SPEC CH.A MAG INPUT MAIN Y: 100.3dB
 Y: 105.0dB /1.00E-12U² PWR 40dB X: 3968Hz* C
 X: 256Hz* C TO 25.6kHz* C LOG TOTAL : 117.7dB/YREF
 SETUP 3 OVERLOAD



WATER/MODEL-BED
 RETURN

M1 INST SPEC CH.B MAG INPUT MAIN Y: 62.9dB
 Y: 70.0dB /1.00E-12U² PWR 40dB X: 3968Hz* C
 X: 256Hz* C TO 25.6kHz* C LOG TOTAL : 85.0dB/YREF
 SETUP 3 OVERLOAD



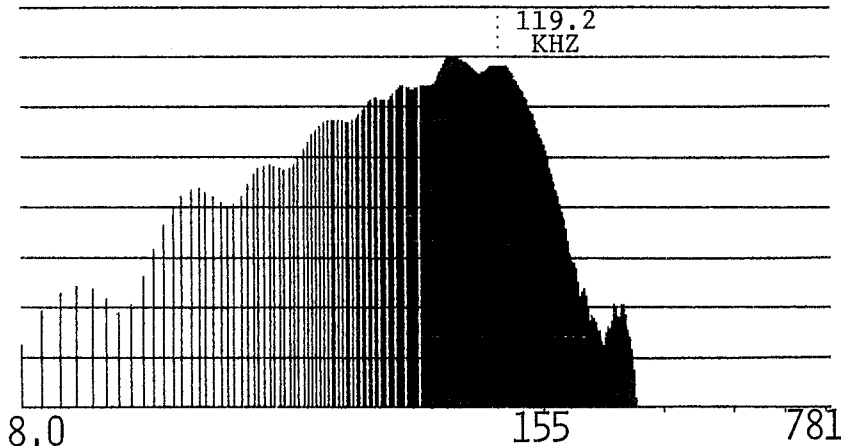
BOTTOM REFLECTION OF
 PSEUDO-GLACIAL TILL

PH.D EXPERIMENTAL STUDY... 1985
 TIME HISTORY DATA ETH613N1243

C=30.52 (0.5 μ s EXTERNAL SAMPLING RATE)

PLATE 4D - INNER SCANNING CIRCLE
 INSTANTANEOUS FREQUENCY
 (USING THE HILBERT TRANSFORM)

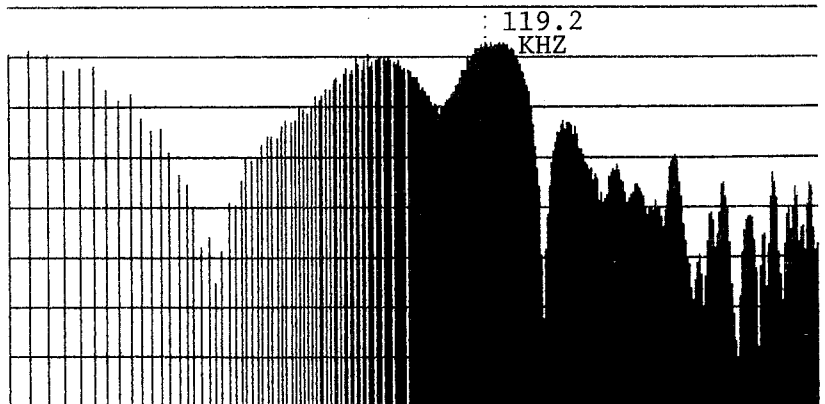
01 INST SPEC CH A MAG INPUT MAIN Y: 94.0dB
 Y: 100.0dB / 1.00E-12U² PWR 40dB X: 3904Hz*C
 X: 256Hz*C TO 25.6kHz*C LOG TOTAL : 113.1dB/YREF
 SETUP 1 OVERLOAD



WATER/MODEL-BED
 RETURN

FREQUENCY (IN KHZ)

01 INST SPEC CH B MAG INPUT MAIN Y: 61.5dB
 Y: 65.0dB / 1.00E-12U² PWR 40dB X: 3904Hz*C
 X: 256Hz*C TO 25.6kHz*C LOG TOTAL : 81.2dB/YREF
 SETUP 1 OVERLOAD



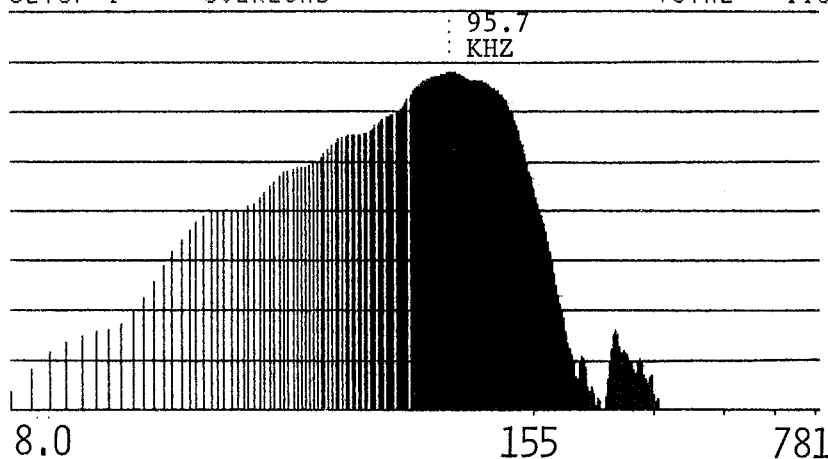
BOTTOM REFLECTION
 PSEUDO-GLACIAL TILL

PH.D EXPERIMENTAL STUDY... 1985
 TIME HISTORY DATA [TH613N135] 781
 FREQUENCY (IN KHZ)

C=30.52 (0.5 μs EXTERNAL SAMPLING
 RATE)

PLATE 4D₁ - INNER SCANNING CIRCLE
 INSTANTANEOUS FREQUENCY
 (USING THE HILBERT TRANSFORM)

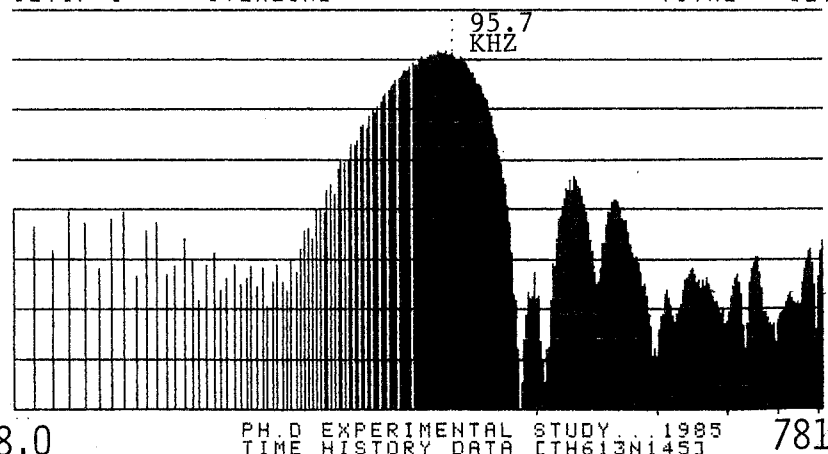
M1 INST SPEC CH.A MAG INPUT MAIN Y: 99.0dB
 Y: 105.0dB / 1.00E-12U² PWR 40dB X: 3136Hz* π C
 X: 256Hz* π C TO 25.6kHz* π C LOG TOTAL : 116.9dB/YREF
 SETUP 1 OVERLOAD



WATER/MODEL-BED
 RETURN

FREQUENCY (IN KHZ)

M1 INST SPEC CH.B MAG INPUT MAIN Y: 65.6dB
 Y: 70.0dB / 1.00E-12U² PWR 40dB X: 3136Hz* π C
 X: 256Hz* π C TO 25.6kHz* π C LOG TOTAL : 82.4dB/YREF
 SETUP 1 OVERLOAD



BOTTOM REFLECTION
 PSEUDO-GLACIAL TILL

PH.D EXPERIMENTAL STUDY... 1985
 TIME HISTORY DATA [TH613N145]

FREQUENCY (IN KHZ)

C=30.52 (0.5 μ s EXTERNAL SAMPLING
 RATE)

APPENDIX D

CONFIDENCE LEVELS ASSOCIATED WITH
IN-SITU ATTENUATION MEASUREMENTS

- Letter from Dr. John Ross
Director, Industry and
University Programs
National Defense - Canada



National Defence

Défense nationale

National Defence Headquarters
Ottawa, Canada
K1A 0K2

Quartier général de la Défense nationale
Ottawa, Canada
K1A 0K2

From: Dr J.M. Ross
Director, Industry and University Programs

25 November 1985

Mr Jacques Guigne
Centre for Cold Ocean Resource
Engineering
Memorial University
St John's
Newfoundland
A1B 3X5

Dear Jacques:

You asked me for some comment on the accuracy of conventional acoustic attenuation measurements in sediments. I am responding from memory since most of the relevant material to which I might refer is still in packing boxes.

Basically there is a wide spread in conventional measurements of seabed attenuation. The major cause for the spread is found in a number of factors:

- a. variations in the physical properties of the sediments;
- b. uncertainties in the velocity of sound necessary to establish sediment layer thickness;
- c. differences in sediment porosity which can have a marked influence on both sediment velocity and attenuation; and
- d. experimental error.

Because of the lack of experimental control for in situ direct seabed sediment attenuation measurements, the literature shows quite a spread in values. Hamilton's measurements of the late '60s and early '70s were thought by many in the scientific community to be on the high side. Certainly my experience, at DREA, measuring attenuation indirectly by obtaining the value which gave the best fit for propagation loss measurements fitted to normal mode propagation loss models produced attenuation estimates lower than those of Hamilton for the "same" material.

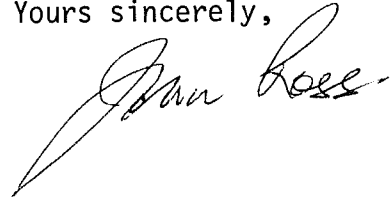
.../2

Canada

In conclusion, it is difficult to estimate the accuracy of many acoustic sediment attenuation measurements, given the variables listed above.

I think what can be said about your work is that it tells the story of the manner in which the experimental sediment bed was formed which correlates well with reality. The fact that the sediment was poured into one area and distributed by someone standing in another area using a rake and that these areas can be identified from the velocity and attenuation measurements is, in my view, the most convincing evidence of the sensitivity and validity of your approach.

Yours sincerely,

A handwritten signature in cursive script, appearing to read "John Ross". The signature is written in black ink and is positioned to the right of the typed name "John Ross".

